博士論文

Building and District Energy Optimization using Metaheuristics and Machine Learning

（メタヒューリスティクスおよび機械学習を用いた

建物・地域エネルギーシステムの最適化に関する研究）

池田 伸太郎

Building and District Energy Optimization using Metaheuristics and Machine Learning

by

Shintaro Ikeda

A dissertation submitted in partial satisfaction of the
requirements for the degree of
Doctor of Philosophy

in

Department of Architecture

in the

Graduate School of Engineering
of the
UNIVERSITY OF TOKYO

February 2018

Table of Contents

LIST OF FIGURES

LIST OF TABLES

NOMENCLATURE

A	Area [m^2] and action of Q-learning
C	Capacity
c	Amount of consumption such as electricity and gas [kW] or [m^3/h]
D	Demand [kW]
f	Objective function value
H	Pump pressure [kPa]
I	Solar radiation [kW/m^2]
L	Length [m]
m	Mass flow rate [m^3/s]
N	Number of something
P	Power output and thermal output [kW]
p	Price
R	Ratio [-]
r	Radius [m] and reward of Q-learning
S	Stored electricity in a battery and heat in thermal energy storage [kWh], and state of Q-learning
T	Temperature [°C]
U	Overall heat transfer coefficient [W/(m^2·K)]
V	Volume [m^3]
v	Velocity
w	Inertia weight factor
x	Individual of metaheuristic optimization methods
α	Coefficient and parameter [-]
γ	Heat capacity [J/(m^3·K)] and discount rate of Q-learning
κ	Volumetric heat capacity [MJ/(m^3·K)]
λ	Thermal conductivity [W/(m·K)]
μ	Efficiency [-]
ρ	Density [kg/m^3]
τ	Fouling and loss rate [-]
φ	Constraint violation

ψ	Frequency [Hz]
$\mathcal{N}$	Gaussian distributed random number
$\mathcal{R}$	Random number with a specific standard deviation
$\mathcal{U}$	Uniformly distributed random number

Superscript

child	Child individual
donor	Donor individual
g	Generation
HS	Heat source side of TES
L	Load side of TES

Subscript

atm	Atmosphere
b	Borehole
c	Charge
cirw	Circulating water of GSHP
cl	Cooling
co	Cooling water
cv	Crossover
cw	Chilled water
d	Discharge
ds	Discrete
dv	Decision variable
E	Electricity
fs	feasible
G	Gas
g	Generation
gb	Global best
gw	Global worst
hs	High side
ht	Heating
hw	Hot water

in	Inlet
lb	Lower bound
lr	Load rate
ls	Low side
max	Maximum value
mt	Mutation
min	Minimum value
oc	Operating costs
out	Outlet
$p1, p2, p3$	Individual numbers
pb	Personal best
pd	Purchased
pe	Primary energy consumption
pop	Population in metaheuristic optimization methods
pw	Public water
req	Required value
Rd	Rated value of machine's specification
s	Thermal resistance
sd	Sold
sl	Selection
th	Time horizon
ub	Upper bound
wb	Wet bulb
XtoY	Machine or device X to Y

Abbreviation

ANN	Artificial neural network
AR	Absorption refrigerator
ASHP	Air-source heat pump
BA	Bat algorithm
BEMS	Building energy management system
BHE	Borehole heat exchanger
BHEP	Pump for borehole heat exchanger

CDA	Crowding distance algorithm
CEMS	Community energy management system
CHP	Combined heat and power
COP	Coefficient of performance
CR	Centrifugal refrigerator
CS	Cuckoo search
CT	Cooling tower
CTP	Cooling tower pump
DE	Differential evolution
DHC	District heating and cooling
DP	Dynamic programming
DR	Demand response
EG	Electricity grid
EMS	Energy management system
FIT	Feed-in-tariff
FP	Primary pump for heat source machine
GA	Genetic algorithm
GB	Gas boiler
GHP	Gas heat pump
GSHP	Ground source heat pump
HEX	Heat exchanger
HRAR	Heat recovered absorption refrigerator
HVAC	Heating, ventilation, and air conditioning system
LCEM	Life cycle energy management
LiB	Lithium-ion battery
LP	Linear programming
MINLP	Mixed-integer nonlinear programming
MILP	Mixed-integer linear programming
MPC	Model predictive control
NaS	Sodium-sulfur battery
NDS	Non-dominated sorting
NiMH	Nickel-metal hydride battery
NLP	Nonlinear programming

PC	Power conditioning system
PEFC	Polymer electrolyte fuel cell
PSO	Particle swarm optimization
PV	Photovoltaic system
RB	Rechargeable battery
RH	Recovered heat
RJ	Random jumping
SC	Solar collector
SCOP	System coefficient of performance
SL	Self-learning
SM	Splitter and mixture
SOFC	Solid oxide fuel cell
TES	Stratified water thermal energy storage
TtsR	Two-time steps recalculation

CHAPTER 1

Introduction

1.1 Recent status of building and district energy systems

1.1.1 Fundamentals of energy systems

Domestic energy systems are composed of electricity, space cooling and heating, and hot water systems. The electricity system is composed of an electricity grid (EG), a rechargeable battery (RB), and power generation equipment. The major types of RBs for building and district energy systems are lithium-ion batteries (LiB), nickel-metal hydride (NiMH) batteries, sodium-sulfur (NaS) batteries, and redox flow batteries. LiBs and NiMH batteries mainly serve building energy needs, while NaS and redox flow batteries are primarily used in district energy systems.

Major power generation equipment includes photovoltaic (PV) devices, wind turbine equipment, combined heat and power (CHP) equipment, geothermal power equipment, and other renewable energy sources. For building energy systems, PV devices and CHP equipment have been commonly used in recent years. The capacity of a PV device is 3–10 kW for ordinary residential and office buildings in Japan. In particular, the PV capacity for residential buildings has increased from 3.3 kW to 4.5 kW in recent years [1]. In accordance with the Japanese government's policies, total installed capacity will continue to increase in the near future [2] and PV will play a significant role in building energy systems.

CHP systems are categorized into fuel cells and gas turbines. Fuel cells are often used in small residential buildings. The cumulative number of installed polymer electrolyte fuel cells (PEFCs) increased from 2,550 units in 2009 to 142,837 units in 2015 [3] in Japan. PEFCs can be easily used to generate electricity and utilize waste heat due to their relatively small capacity (5–20 kW), making them suitable for small residential buildings.

Solid oxide fuel cells (SOFCs), another CHP type, have become increasingly popular in recent years. The cumulative number of the installed SOFCs increased from 324 units in 2011 to 11,208 units in 2015 [3]. The typical temperature of the waste heat generated by SOFCs is 800–900 °C, higher than the corresponding value for PEFCs, as is the power generation efficiency. As a result, SOFCs are mostly used in condominiums. Hence, PEFCs and SOFCs are key emerging technologies for power generation systems in residential buildings. In large buildings such as offices, hotels, and hospitals, gas-turbine-type CHP systems are mostly used because of their large capacity (300–1,200 kW) and high efficiency. CHP systems have attracted significant attention, especially in Japan after the 2011 earthquake, with regard to business continuity planning (BCP). For example, the Roppongi Hills in Tokyo, managed by Mori Building Corporation, is recognized as a state-of-the-art building with regard to the energy supply using a gas turbine instead of a commercial electricity grid [4,5]. Hence, large-

size CHP systems will also be key technologies to improve the energy resilience of buildings and the urban energy infrastructure.

Space cooling and heating systems can be primarily categorized as central cooling and heating systems, or individually packaged heating, ventilation, and air conditioning (HVAC) systems. The packaged HVAC system [6,7] is often installed in small- and medium-sized buildings. In contrast, central cooling and heating systems are often installed in buildings in terms of installation costs and payback period. The central system has been widely used not only in office buildings but also in residential buildings in the U.S. for more than 60 years [8]. In terms of system optimization, the central system can be controlled optimally compared to the packaged system because the occupants have no access to set point controls in the former case.

The central system consists of heat source machines such as air-source heat pumps (ASHPs), centrifugal refrigerators (CRs). Thermal energy storage (TES) systems are used to charge or discharge thermal energy. In addition, some pumps are installed to circulate fluids from the heat source machines to a secondary system such as air-conditioned rooms. In particular, the energy system optimization focuses on the heat source machines and pumps, and is called a primary system. The optimization is used to determine when the machines will be operated and how much heat will be generated.

A central and an individual system are typically used in domestic hot water systems as well. The individual system is composed of instantaneous water heaters and is used in ordinary residential buildings in Japan. Central hot water systems are used in large buildings such as hotels and hospitals that have sufficient demand for hot water. The central system often consists of a gas boiler (GB), and waste heat is generated by other equipment such as the CHP equipment and double-bundle centrifugal refrigerators.

Energy systems can also be categorized by size, that is, for buildings or districts (Fig. 1-1). District energy systems can further be divided into two systems: district heating and cooling (DHC), and shared energy systems such as smart grids [9] and heat sharing networks [10].
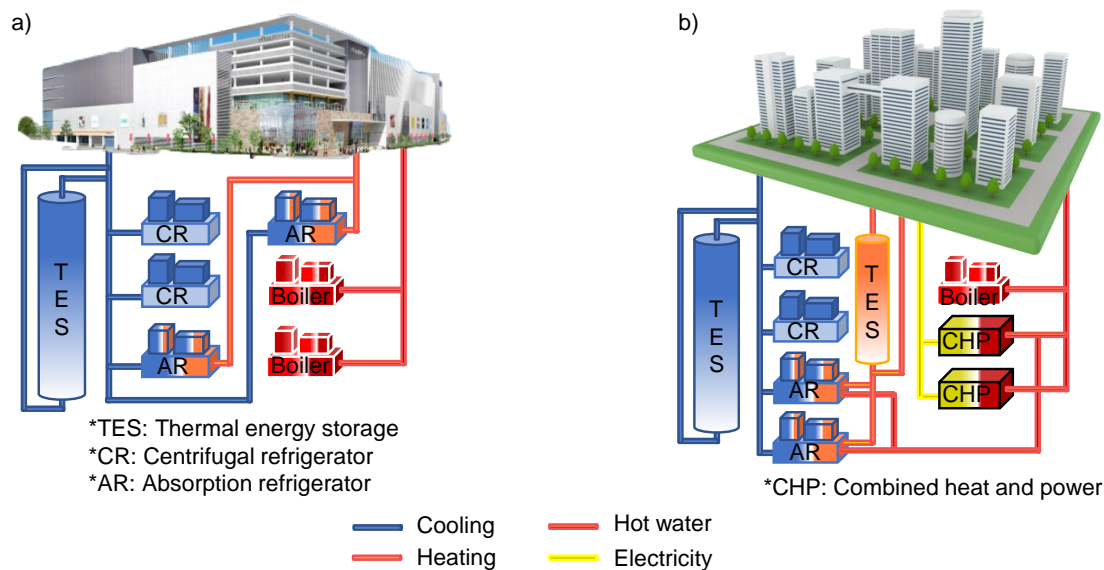
Fig. 1-1 | Conceptual diagram of system configurations: a) building energy system, b) DHC system.

1.1.2 Green grid management and associated problems

The number of renewable energy installations has globally increased in recent years. In particular, solar energy utilization such as PV and solar collectors have significantly increased due to the adoption of feed-in-tariff (FIT) in many countries. However, the installation of some systems causes problems in the control of a commercial electricity grid. According to a report by the California Independent System Operator [11], a globally recognized grid manager, a duck curve is the most pressing issue of concern (Fig. 1-2). The electricity demand during the daytime drastically decreases compared to that in the morning hours (6 a.m. to 8 a.m.) because of the power generation by the PV system. After the power generation decreases as the amount of sunlight reduces, electricity demand increases sharply. Hence, there are two peak demand periods, the morning and evening hours. Although flexible electricity plants such as pumped-storage hydroelectricity plants and oil-fired electricity plants could theoretically meet the electricity balance, their operation is not easy to predict.

The same issue is encountered in Japan, especially in the Kyushu region [12]. As a result, storage equipment, such as RBs and TES, has been increasingly used to achieve peak-shift and peak-cut control.
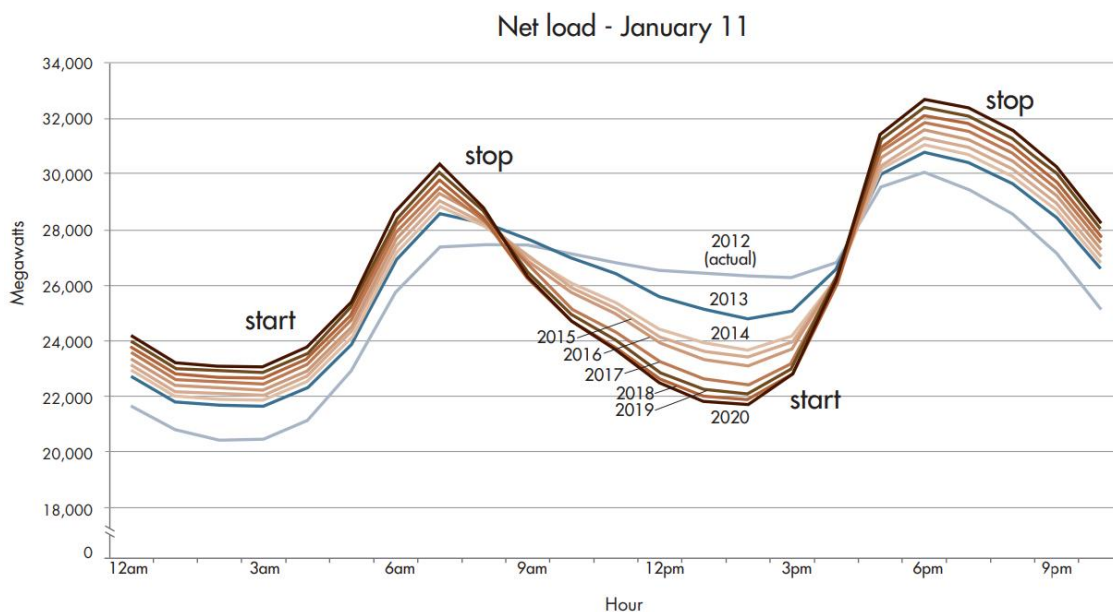
Fig. 1-2 | Duck curve of electricity demand in California Independent System Operator [11].

1.1.3 Present state of FIT and dynamic pricing

FIT is a significant policy to promote the installation of renewable energy, which is used in many countries including Japan, the U.S., the U.K., Germany, and France. The installed capacity of PV equipment has increased from approximately 500 MW in 2011 to 2,500 MW in 2014 in Japan [12] due to the FIT system. Although a surplus electricity purchasing system was implemented in 2009 before FIT came into force, the latter became a more attractive option for many users. As the amount of installed capacity increased, the electricity sale price generated from PV equipment is forecasted to decrease from 42 yen/kWh in 2012 to 24 yen/kWh in 2019 for capacities less than 10 kW.

Although FIT can achieve green energy power generation, it leads to issues, as indicated by the duck curves. Demand response (DR) is another significant policy to maintain the electricity balance. DR is mainly divided into two categories: dynamic pricing and demand-side management. The demand-side management controls the amount of electricity consumption in accordance with an order from grid operators or aggregators to managers in targeted buildings. Hence, the managers should decrease or increase the electricity consumption to meet the designated value. For proper management, it is important to determine how much incentive should be provided in DR.

The dynamic pricing system is intended to vary the price of purchased electricity at every time step, basically, one hour, or three or four times a day. The NordPool [13] in the Scandinavia region and the PJM Electricity Exchange [14] in eastern U.S. have adopted a typical dynamic pricing system.
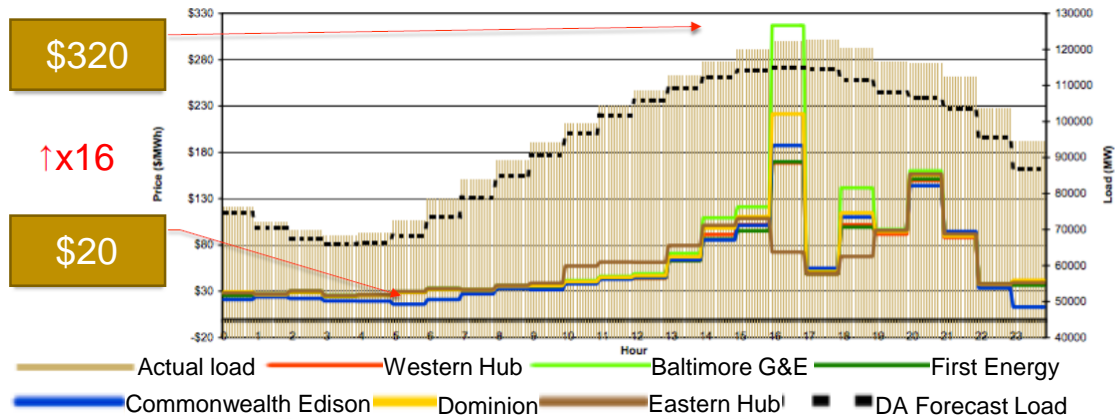
Fig. 1-3 | Price variations of purchased electricity at peak day for the PJM [15].

Fig. 1-3 shows the price variations of purchased electricity on a peak day for the PJM [15]. The price at the peak time (4 p.m.) was 16 times as high as the price at the off-peak time (5 a.m.). Hence, the empirical operation of an energy system using fixed-rate operations will be not suitable in the near future, and optimal control will be needed to handle the demand-side management and the dynamic pricing system.

1.1.4 Progress and application of information and communication technologies

It is vital to achieve optimal operation using management tools that collect data from many measurement points (e.g., chillers, pumps, and PV equipment). In fact, some tools have already been used in actual systems. A building energy management system (BEMS) consists of a central monitor and many sensors. Although BEMS is a platform to monitor dynamic variations in electricity consumption, temperature, and mass flow rate of the building energy system, it can be used with an optimization software for daily or hourly optimizations. BEMS has already been a consolidated technology based on some international standards such as ISO 16484-2 for its hardware, ISO 16484-3 for its function, and ISO 16484-5 for its data protocol. BEMS, which is basically an energy management system (EMS), will be applied to a larger district energy system called the community energy management system (CEMS) in Japan (Fig. 1-4).

The physical elements required to achieve the optimal operation have already been used in an actual system in Japan. However, a sophisticated and flexible software that can handle almost all energy system configurations has yet to be developed for integration into an EMS.
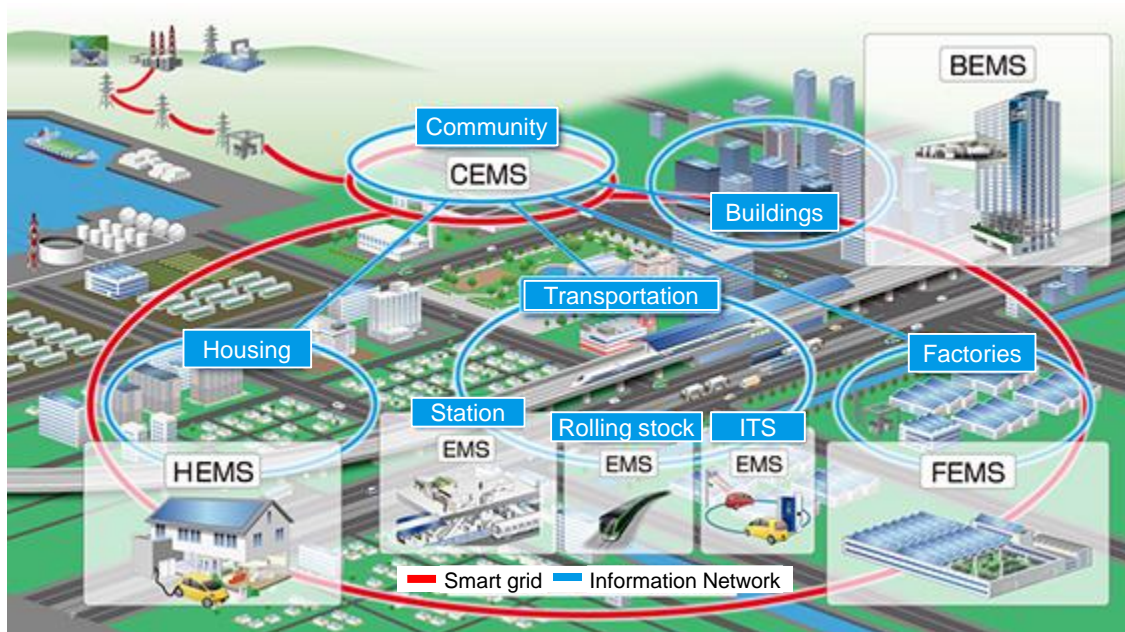
Fig. 1-4 | Conceptual diagram of the community energy management system (CEMS) [16].

1.1.5 Three phases for daily optimization of operating schedules

The software for daily optimization consists of three phases: 1) a prediction phase, 2) a day-ahead optimization phase, and 3) real-time control phase.

The prediction phase is to predict the elements that affect the demand curves and machine efficiency. Typical elements are outdoor temperature, outdoor humidity, demand, the price of purchased electricity under dynamic pricing, solar radiation, and wind velocity. In particular, the demand for electricity, cooling, heating, and domestic hot water directly depends on occupants' behavior. The occupants' schedule might also be the most valuable prediction target.

The day-ahead optimization phase is to optimize the operating schedule of each heat source machine for 24 h because the outdoor prediction and price variation are determined for the next day. This phase is more important when the system includes time-dependent equipment such as RBs and TES because the operating schedule of time-dependent equipment should be optimized during the day to minimize daily operating costs and primary energy consumption. When the system uses only flexible heat source machines such as heat pumps, it is sufficient to optimize the operating schedule for each time step, to minimize hourly operating costs and consumption.

The real-time control phase is intended to recalculate the operating schedule and meet a temperature constraint of secondary systems, because the predicted value used in the day-ahead

optimization phase is not always the same as the actual values. When the tolerance between the predicted and actual values is not acceptable for the system, the operating schedule should be modified to meet the conditions.

1.2 Literature review

1.2.1 Development of prediction methods and their applications

The development of prediction methods for electricity price and demand is a popular research area. There are many proposed methods that can be categorized as follows: 1) mathematical technique-based methods, 2) neural network technique-based methods, and 3) classical statistical-technique based methods.

Mathematical technique-based methods have been studied by Xu et al. [17] for predicting the dynamic cooling load of a building. Xu et al. [17] created a mathematical model to predict the load as a quadratic polynomial exponential smooth equation. The golden section algorithm (0.618 algorithm) [18] was used to minimize the predicted sum of squared errors. The mathematical model predicted the load every 20 min while updating a coefficient of the equation. As a result, the mean square error (MSE) of the mathematical model was 0.0539, and the error of the static model for the day-ahead prediction without the use of any updating methods was 0.0605. The mean absolute error (MAE) of the proposed prediction method was 0.3034 and of the static model was 0.3660. Laouafi [19] proposed a Hampel filtering method to predict very short-term electricity demand. The method (HFCM-TM) showed the best results with 0.37–0.64% of the mean absolute percentage error (MAPE) compared to other seven methods including back-propagation neural network (BPNN), and adaptive neuro-fuzzy inference system (ANFIS).

The neural network technique-based approaches have been used by Laouafi et al. [20] to create a two-stage prediction technique that includes a first prediction method such as the feed-forward BPNN, nonlinear autoregressive neural network with external input (NARX), and ANFIS. The second prediction methods were the wavelet packet decomposition and the k-Nearest Neighbors algorithm to predict the peak load. They used the absolute percentage error (APE) and MAPE. The hybrid methods could forecast the peak load within 1.879% of tolerance on normal days and 3.283% of tolerance on public holidays.

Liu [21] evaluated various methods such as autoregressive integrated moving average (ARIMA), support vector regression (SVR), BPNN, radial basis function neural network (RBFNN), general regression neural network (GRNN), fuzzy ARTMAP (FA), wavelet transform (WT) with BPNN (WT+BPNN), WT with RBFNN, WT with GRNN, WT with FA, WT with the firefly algorithm (FF)

and FA, WT with two-stage mutual information (MI-MI) and neural networks. Finally, they proposed a novel shark smell optimization (NSSO) algorithm with an improved Elman neural network (IENN). These methods were used to predict building electricity load. As a result, MAPE of the proposed method, NSSO, was the best outcome with 0.87–1.12% compared to 15.21–16.43% for SVR.

Lahouar [22] used the random forest method, a machine learning technique, to predict the district electricity load in Tunisia. The random forest method was superior at predicting the electricity demand of the Tunisia power system and the PJM market compared to other methods such as ANN and SVM because of its accuracy (MAPE: 0.96–6.80%). Abedinia [23] proposed a new training method for optimizing the weights of combinational neural networks (CNNs) to predict electricity price variations after referring to the PJM market. They used weekly mean error (WME) and weekly peak error (WPE) to evaluate the proposed method and other methods such as ARIMA, ANN, and MI-MI. The WME of the proposed method was 3.97–4.12%, which was superior to those of the other techniques (e.g., the WME of ARIMA was 34.32–55.81%). Other studies [24–27] also applied ANN to predict loads.

Classical statistical models are also used to predict electricity demand. Short [28] integrated an open software to predict the price of electricity and loads using an exponentially weighted extended recursive least squares (EWE-RLS) method based on Kalman filter and to optimize the operating schedule of CHP using mixed integer linear programming (MILP). They also used MAPE to evaluate the accuracy of the prediction model. EWE-RLS could predict within 7.85% when the forecasting time horizon was one hour and 4.67% when the horizon was 23 h.

Rasmussen [29] used the RLS model to predict the electricity demand of a supermarket. Weather data used to predict the demand were provided by Danish Meteorological Institute. The prediction time horizon was 42 h and the business hour and off-business hour periods were separately predicted. The RMSE of the proposed method was 1.41 for 24 h prediction and 1.73 for 42 h prediction. However, the peak demand prediction caused more than 6 kW (25%) of tolerance.

Kaur [30] compared several classical statistical models including SVR and autoregressive model with exogenous input (ARX) to predict the time series of solar power and the net load demand based on the actual data from the University of California, Merced (UCM). MAPE of SVR was 30.47–349.08% and that of ARX was 4.60%. The ARX was also used by Dahl [31] to predict the heat load of a district energy system. Other studies [32–34] adopted classical models (e.g., ARX) to predict not only loads but also fault detections.

1.2.2 Development of day-ahead optimization methods and their applications

The day-ahead optimization methods can be categorized as follows: 1) scenario-based methods, 2) mathematical optimization methods, and 3) statistical or stochastic optimization methods.

The scenario-based methods are often used when a target system is complex and the energy system simulation software such as TRNSYS, EnergyPlus™, and Rhinoceros® is integrated because the detailed simulation is computationally expensive and it is difficult to conduct iterative calculations to find the optimal solution. There are many studies on scenario-based methods [35–51]. Dufo-López [36] targeted a grid-connected storage system in a district. The study aimed to optimize the size and control of the storage to minimize the net present cost and levelized cost of energy under the real-time pricing system. Oliveira [37] compared the following four scenarios to minimize the operating costs of generating hot water with electricity: 1) an ideal case, 2) maximum storage policy, 3) simple variable storage, and 4) optimal variable storage. Cui [43] integrated TRNSYS and scenario-based optimization to control a hybrid ground source heat pump (GSHP) system. In general, TRNSYS or other simulation software is used in the GSHP system because the temperature variations of the circulating fluid significantly affect the efficiency of GSHP. The decision variables include the fixed load ratio (FLR) of the hybrid system and the auxiliary cooling ratio (ACR) of the cooling tower. Five ACR values (10%, 30%, 50%, 70%, and 90%) and four FLR values (0, 0.3, 0.4, and 0.5) were tested.

The mathematical technique-based optimization methods have often been used in previous studies because of their ability to find the optimal solution and their low computational cost. Wakui [52] attempted to optimize two residential buildings that included thermal storage, combined heat and power, and gas boilers. The two buildings shared electricity and heat through connection pipes. Due to the low computational cost of mixed integer linear programming (MILP), Wakui could also run annual energy simulations for 20 residential buildings [53]. MILP is one of the most commonly used optimization methods in the field of the energy system optimization. Many studies [52–66] optimized energy systems with MILP using major solvers such as CPLEX® [67] and GAMS [68]. Ameri [60] and Ashouri [57] used MILP to simultaneously optimize the design and operation of a district and a building.

In contrast, some studies used mixed integer nonlinear programming (MINLP) or nonlinear programming (NLP) [69–75] to make the machine's characteristics nonlinear. MINLP and NLP are based on mathematical techniques, especially defferentiating an objective function such as Newton's method and the steepest decent method. Although MINLP and NLP have limitations of use, they are suitable to realistically express the characteristics compared to MILP.

Dynamic programming (DP), also a mathematical theorem-based method, is a common optimization technique to determine the optimal combination of thermal and power outputs of devices. Some studies [76–81] used it because of its ability to optimize target systems without any limitations of use. Ranaweera [77] used the method to optimize the operating schedules of PV power generation and a rechargable battery. The system had nonlinear characteristics such as the efficiency of the power electronic converter and the open-circuit voltage of an LiB. DP requires discrete decision variables and an actual energy system usually has discrete set points.

Stochastic optimization methods are one of the most popular methods because of their flexibility and adaptability. In particular, metaheuristic optimization methods, also called metaheuristics and nature-inspired optimization techniques, are the most common methods in this field. Metaheuristics include many different types of methods such as particle swarm optimization (PSO), genetic algorithm (GA), bat algorithm (BA), differential evolution (DE), and cuckoo search (CS). Previous studies used PSO [82–90] and GA [91–100] to optimize energy systems. Tsukada [83] used PSO to optimize a CHP operation. The results of PSO could reduce total daily operating costs compared to a conventional method. A extended PSO (binary PSO, BPSO) was proposed by Elsied [84] to optimize the operating schedule of a wind generator, a fuel cell, and a PV in a microgrid. In fact, there are many extended models of PSO described in the next chapter.

BA [101,102], DE [103–109], and CS [110–114] were also used in some optimization studies, although these methods have been developed in recent years. Other metaheuristic methods were utilized in several studies [115–118]. Camargo [115] compared six different types of metaheuristics including the extended PSO and DE models for the optimization of hydrothermal system operation. Deihimi [116] proposed a new method, a multi-objective uniform water cycle algorithm, to minimize the operating costs and pollutant emissions of distributed generation in a microgrid.

Many methods can be used in the second phase, namely, the day-ahead optimization. They can be categorized into three approaches: deterministic with linear, deterministic with nonlinear, and stochastic regardless of the system configuration and machine's characteristics. Although each method has unique advantages and disadvantages, we need to determine whether the algorithm is suitable for solving the target optimization problem.

1.2.3 Development of real-time control methods and their applications

A real-time control method aims to recalculate or revise the operating schedule determined in the second phase consistent with the tolerance of the predicted value and the actual measurement value [119–130]. In recent years, the model predictive control (MPC) has been used to achieve real-time control. Hasikos [119] integrated the radial basis function artificial neural network (RBF-NN) and MPC to control fuel cells. RBF-NN predicted the net power and oxygen excess ratio using input data such as the stack current and the compressor voltage of the fuel cell. Although they used the dynamic matrix control (DMC) to realize the real-time control, DMC was based on the same concept as MPC. In the DMC procedure, an operating schedule was updated iteratively with system dynamic predictions using RBF-NN.

Schirror [122] applied the MPC procedure, called a modular MPC (MMPC), to an actual building located in Vienna, Austria. The time-dependent characteristics were important because this building had the cooling and heating system of thermally activated building systems (TABS). They used a linear approximation model to reduce the computational complexity because the MPC procedure required an optimization for the operating schedule during several time intervals. Although the nonlinear behavior should be handled as a nonlinear approximation, the linear approximation technique was used in other studies, for instance in [126]. Sanjari [130] compared the day-ahead and hour-ahead optimized scheduling with demand forecast error in grid-connected residential buildings. They used a hyper-spherical search algorithm to find the optimal electricity dispatch.

1.3   State-of-the-art projects with optimal operating management

1.3.1 District cooling plant in Marina Bay, Singapore

A district cooling plant including Plant No. 1 and No. 2 at Marina Bay in Singapore has been operated by Mitsubishi Heavy Industries [131]. In this area, the Singapore Government requested that the system coefficient of performance (SCOP) be more than 5.4 (0.65 kW/USRT). Thus, an optimization method is used to accomplish this goal. The cooling capacity of Plant No. 1 is 20,000 USRT and that of Plant No. 2 is 25,000 USRT. In addition, these two plants share the generated heat while considering a pressure balance of pipes. A specific feature of optimization for operating schedules of the energy system is to realize the online optimization by a software, which has two tasks: online and offline. In the online task, a central monitoring system collects real-time operating data. The system also provides measured data to an arithmetic unit and a control unit every 15 min. The arithmetic unit determines the combination of thermal outputs of each heat source machine and the fan speed of the cooling tower.

To control these thermal energy tasks, two different operating strategies are applied: 1) peak-cutting and 2) constant discharge. However, the electricity market in Singapore uses a real-time pricing system, which means the electricity price is determined by real-time trading every 30 min. Thus, determining the day-ahead operating schedule of TES is difficult because the price changes every 30 min.

The operation of heat source machines is optimized by PSO, which identifies the quasi-optimal combination of thermal outputs of each heat source machine. The computation time to determine the thermal output combination by PSO was only 10 s. Fig. 1-5 shows the search performance of PSO. To minimize energy consumption, the combination of load rates of each heat source varied as the number of calculation steps increased.
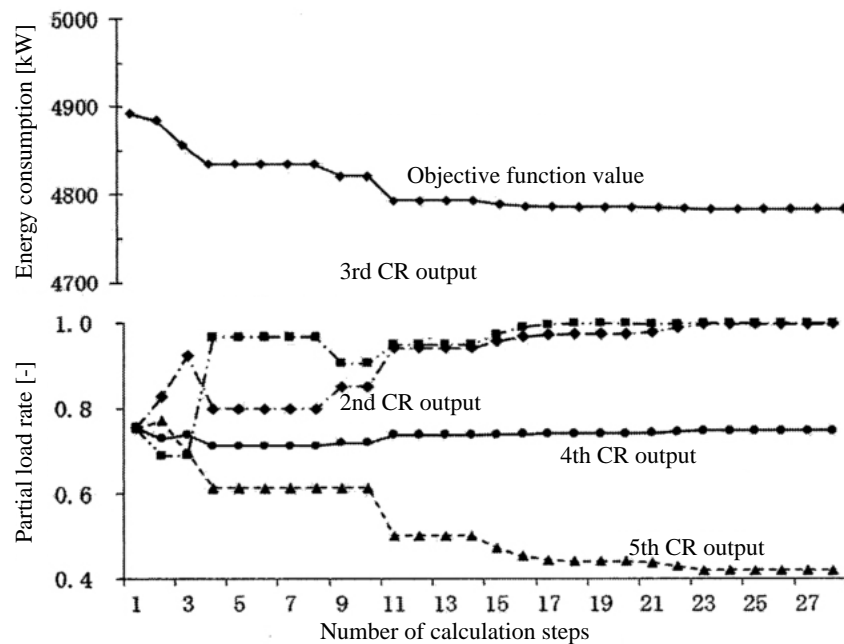
Fig. 1-5 | Performance of the optimal solution search by PSO (translated in English from [132])

In the final calculation step, as per the quasi-optimal combination, the second and third CRs generated cooling heat at the rated capacity. CR No. 1 is not shown in Fig. 1-5 because the machine is designed to remain inactive to prevent the overworking of a specific machine, especially the most efficient one. The optimization could reduce the electricity consumption by 5.1% compared to the actual operation [132].

1.3.2 Comprehensive real-time optimization for building operations in Tokyo

Takenaka Corporation, one of the giant construction companies in Japan, developed an optimization structure, I. Smart Energy Management (I.SEM), to properly control electricity, space cooling, and heating systems (Fig. 1-6). They used I.SEM to comprehensively optimize three buildings located in Toyocho, Tokyo. I.SEM included a demand prediction unit and an optimization unit for machine operation. The prediction unit could forecast electricity and cooling/heating demands within 5% of tolerance. The optimization unit could determine an optimal operation for the next 30 min to meet the forecasted demand. It can also be used in terms of DR because DR often requires a proper operation for 30 min. These units are controlled in a cloud platform.
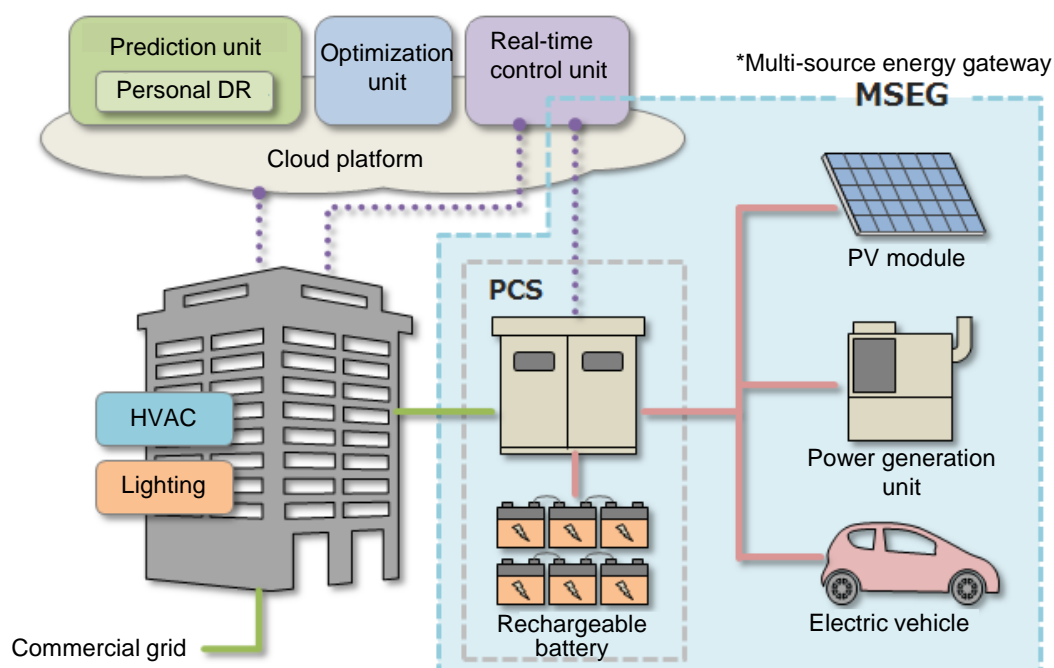
Fig. 1-6 | Structure of I.SEM (translated in English from [133])

1.3.3 Other projects aiming energy optimization

SmartWatt contributed to the optimization of building and district energy systems in actual cases [134] (e.g., Coast College District with building automation technology). An energy system of the Yau Ma Tei Specialist Clinic at Queen Elizabeth Hospital [135] was optimized by PowerBox™, which could monitor and analyze the energy system online. The Pacific Northwest Smart Grid Demonstration Project [136] was a notable project supported by the U.S. Department of Energy.

For the development of an optimization software to achieve operational optimization, the TEMOA project [137–139] proposed an energy simulation tool. The tool has a protocol for problem formulation such as an objective function and constraints and also requires some linear programming such as CPLEX® and Gurobi™ to be integrated [140]. REopt™, which stands for renewable energy integration and optimization, is a techno-economic decision support model proposed by the National Renewable Energy Laboratory (NREL) [141] and also required the MILP model to simplify target models. The model could optimize the operation of an electricity system using PV equipment and RBs, to minimize life-cycle costs [142]. NREL also developed BEopt™ (building energy optimization) [143], supported by the U.S. Department of Energy, to minimize the life-cycle cost of target buildings integrated with EnergyPlus™.

1.4   Current issues

Linear programming (LP) including MILP has strict limitations of use because it requires a linear configuration. Although MILP and LP can find an optimal solution rapidly and allow users to conduct long-term (annual and life-cycle) building energy simulations, the linearization of the system configuration is not easy to be conducted in dynamic or real-time controls. In addition, LP cannot be applied to a discrete optimization problem and MILP should consider the combinations of decision variables in the discrete problem, although actual systems consist of discrete set points.

DP can directly handle discrete variables and nonlinear configurations. However, the computational complexity of the method depends on the number of decision variables and resolution of discrete variables. Although the method is suitable for use in simple energy systems, it is not appropriate for complex energy systems.

More efficient methods should be developed and applied to complex systems. Deterministic optimization methods such as MILP and dynamic programming without any simplifications are computationally expensive (e.g., linearization and large size resolution of the discrete variables). Hence, other optimization approaches such as stochastic methods are strongly needed. Such stochastic methods, e.g., metaheuristics, were introduced in Section 1.2.2. Classical metaheuristic methods, such as GA, PSO, and DE, cannot always solve problems efficiently because of the various complex factors such as nonlinear configurations, discrete conditions, and many constraints.

This thesis proposes a new optimization method with a realistic computational cost, to solve the complicated issue of achieving day-ahead and real-time optimizations for complex building and district energy systems. In addition, a novel optimization strategy for the schedule recalculation in the real-time control is proposed.

1.5   Structure of the thesis

This thesis is organized as follows. Chapter 2 introduces the basics of components and optimization methods. Detailed characteristics of each component and algorithms of some methods often used in previous studies are described. Chapter 3 describes the optimization of the operating schedules of a complex building energy system composed of electricity, space cooling, and domestic hot water systems. The system also consists of three different storage equipment such as RB, TES for cooling, and TES for hot water. An efficient multi-objective optimization method is proposed to minimize daily operating costs and primary energy consumption at once. Chapter 4 describes a new index to determine the optimal operating schedules of PV systems and RBs under various purchased electricity prices. The index allows users to easily determine the optimal operation without using any optimization

methods. Chapter 5 describes the development of a re-optimization framework for the uncertainty in demand and PV power generation. The framework is called two-time step recalculation (TtsR), which is used in the third phase for real-time control. Chapter 6 describes an improved robust optimization method and its application to the multiple GSHP systems. Although the GSHP system requires high computational costs to calculate temperature variations in circulating fluid, the proposed method can easily optimize the operating schedule of the GSHP system. Chapter 7 describes a hybrid technique of the optimization method proposed in Chapter 6 and machine learning such as artificial neural network (ANN) to minimize the daily operating costs of an energy system composed of multiple renewable energy systems. Chapter 8 aims to minimize the daily operating costs of the DHC system with the proposed hybrid method. Chapter 9 discusses the minimization of the daily operating costs of heat sharing network system with the proposed hybrid method. Chapter 10 presents the conclusions of this research and proposes ideas for future studies.

CHAPTER 2

Basic theory

2.1 Description of components

This section describes the characteristics of components such as heat source machines and pumps using mathematical models. The mathematical equations of the following machines are in accordance with the life cycle energy management (LCEM) tool provided by the Ministry of Land, Infrastructure, Transport, and Tourism, Japan [144]: centrifugal refrigerator, absorption refrigerator, heat recovered absorption refrigerator, air-source heat pump, gas heat pump, and ground source heat pump. These models in the LCEM tool use not only physical equations, but also empirical coefficients that were determined using actual machine data. Hence, these models have an advantage in simulating the actual phenomenon of energy system components.

2.1.1 Centrifugal refrigerator

A centrifugal refrigerator (CR) typically has a larger capacity and more efficient performance than other machines such as air-source heat pumps and absorption refrigerators. Hence, CRs are often used in large buildings that have high cooling demands. Although there are many types of CR, a CR with inverter technology was used in this research as it has become increasingly popular in actual energy systems owing to its high part-load performance. The model is in accordance with the excel file "RC-XX1-310L200-500_Ver310.xls" in the LCEM tool, which contains six capacities, as listed in Table 2-1.

Table 2-1 | Rated specification of CR in the LCEM tool

Cooling capacity [kW]	703	879	1,090	1,231	1,582	1,828
Mass flow rate of cooling water [L/min]	2,400	3,000	3,683	4,200	5,367	6,167
Electricity consumption of CR itself [kW]	131	156	186	221	272	304
Electricity consumption of sub-machine [kW]	0.75	0.75	0.75	0.75	1.20	1.20
COP*	5.34	5.62	5.83	5.54	5.79	5.99

*COP: coefficient of performance

This model has following constraints:

1) Partial load rate: 20–100%

2) Inlet temperature of cooling water: 12–32 °C

Although the LCEM tool has discrete capacities, a continuous capacity could be considered with trend-lines as shown in Fig. 2-1. The horizontal and the left and right vertical axes are rated cooling capacity, rated electricity consumption, and rated mass flow rate of cooling water, respectively.
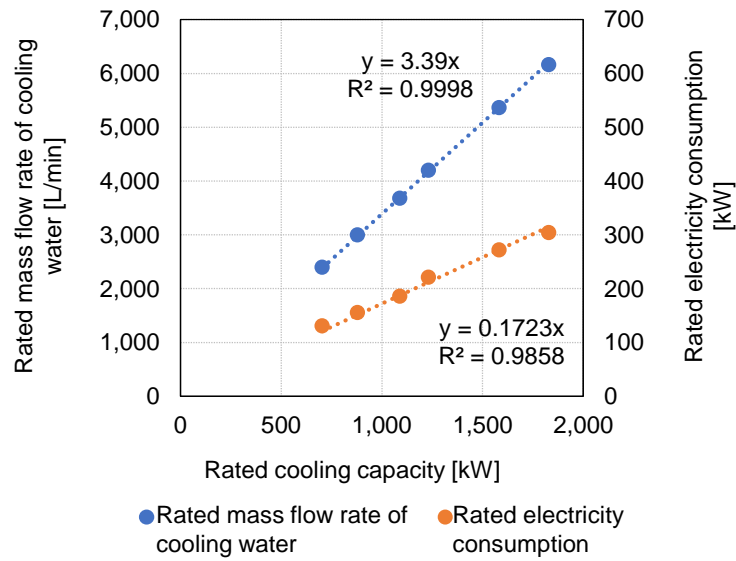
Fig. 2-1 | Relationship of rated cooling capacity to rated electricity consumption and mass flow rate of cooling/chilled water.

In contrast, a rated mass flow rate of chilled water could be determined using the temperature difference of inlet and outlet and the rated capacity.

The electricity consumption of the CR was calculated as shown in Eq. (2-1).

$$c_E = c_{E,rd} \prod_i^5 \alpha_{i,CR} \tag{2-1}$$

where, c_E is the electricity consumption [kW], $c_{E,rd}$ is the rated electricity consumption of the CR itself [kW], and $\alpha_{i,CR}$ the coefficient with which to determine the CR's performance. Each $\alpha_{i,CR}$ is defined as follows:

$$
\begin{aligned}
\alpha_{1,CR} = {} & 17.9046644869913 R_{lr}{}^6 - 67.0573761220053 R_{lr}{}^5 \\
& + 101.123764585813 R_{lr}{}^4 - 77.8739337726255 R_{lr}{}^3 \\
& + 32.5714403900183 R_{lr}{}^2 - 6.61431800228766 R_{lr} \\
& + 0.945477028090787
\end{aligned}
\tag{2-2}
$$

$$\begin{aligned}
\alpha_{2,\mathrm{CR}} = {} & -1.16416709971475 \times 10^{-8} T_{\mathrm{in,co}}^{6} - 7.37922244873432 \times 10^{-7} T_{\mathrm{in,co}}^{5} \\
& + 0.000141564520003781 T_{\mathrm{in,co}}^{4} - 0.00639083378124009 T_{\mathrm{in,co}}^{3} \\
& + 0.13274935442347 T_{\mathrm{in,co}}^{2} - 1.30336858289761 T_{\mathrm{in,co}} \\
& + 5.00901140248692
\end{aligned} \tag{2-3}$$

$$\alpha_{3,\mathrm{CR}} = 0.413955451708935 R_{\mathrm{cw}}^{2} - 1.04486182259178 R_{\mathrm{cw}} + 1.63090637088285 \tag{2-4}$$

$$\alpha_{4,\mathrm{CR}} = 0.0032169 T_{\mathrm{out,cw}}^{2} - 0.0815249 T_{\mathrm{out,cw}} + 1.412122 \tag{2-5}$$

$$\alpha_{5,\mathrm{CR}} = -0.00081712 R_{\mathrm{co}}^{2} + 0.02150023 R_{\mathrm{co}} + 0.97945391 \tag{2-6}$$

where, R_{lr} is the partial load rate [-], $T_{\mathrm{in,co}}$ is the inlet temperature of the cooling water [°C], R_{co} is the ratio of the current mass flow rate to the rated mass flow rate of the cooling water [-], $T_{\mathrm{out,cw}}$ is the outlet temperature of the chilled water [°C], and R_{cw} is the ratio of the chilled water [-].

2.1.2 Absorption refrigerator

An absorption refrigerator (AR) is based on gas energy and has a relatively high capacity for both cooling and heating compared to heat pump machines. Thus, AR has been widely used, particularly to meet cooling and heating demands in large buildings. In addition, AR has been adopted together with electrical heat source machines, such as CR, to improve the flexibility of energy systems. The characteristics of AR are in accordance with the excel file with "RC-XX5-310A_150-500_Ver310.xls" in the LCEM tool, which contains ten capacities, as listed in Table 2-2.

This model has the following constraints:

1) Partial load rate: 25% to 100%

2) Inlet temperature of cooling water: 20–32 °C

To continuously determine specifications such as rated heating capacity, rated mass flow rate of cooling water, rated electricity, and gas consumption, trend-lines were created as shown in Fig. 2-2.

Table 2-2 | Rated specification of AR in the LCEM tool.

Cooling capacity [kW]	527	633	738	879	985	1,125	1,266	1,407	1,582	1,758
Heating capacity [kW]	348	418	487	580	650	743	835	928	1,044	1,160
Mass flow rate of cooling water [L/min]	2,500	3,000	3,500	4,170	4,670	5,330	5,770	6,410	7,210	8,010
Electricity consumption for cooling [kW]	5.18	6.13	6.13	7.08	7.08	7.92	11.98	12.95	14.67	14.67
Electricity consumption for heating [kW]	4.55	5.49	5.49	6.45	6.45	7.28	11.35	11.35	13.07	13.07
Gas consumption for cooling [m³/h]	31.3	37.5	43.8	52.1	58.3	66.6	75.0	83.4	93.8	104.2
Gas consumption for heating [m³/h]	31.9	38.3	44.6	53.2	59.5	68.1	76.6	85.0	95.7	106.3
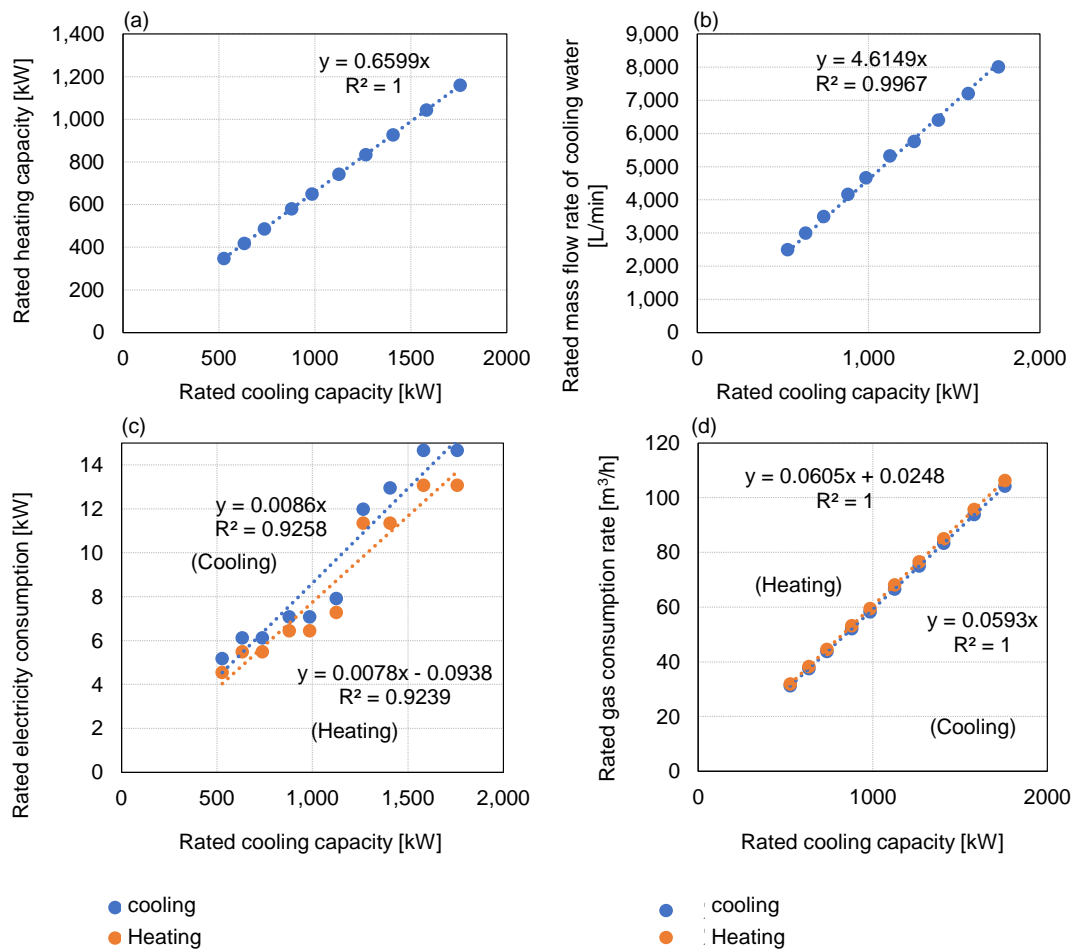
Fig. 2-2 | Relationship of rated cooling capacity to the following specifications: a) rated heating capacity, b) rated mass flow rate of cooling water, c) rated electricity consumption, d) rated gas consumption rate.

Electricity consumption was calculated using the following linear equation, Eq. (2-7).

$$c_{E,AR} = c_{E,rd,AR} R_{lr} \tag{2-7}$$

where, $c_{E,AR}$ is the electricity consumption [kW] and $c_{E,rd,AR}$ the rated electricity consumption [kW].

In contrast, the gas consumption was calculated using the following nonlinear equations.

$$c_{G,AR} = c_{G,rd,AR} \prod_i^4 \alpha_{i,AR} \tag{2-8}$$

where, $c_{G,AR}$ represents the gas consumption [m³/h], $c_{G,rd,AR}$ the rated gas consumption [m³/h], and $\alpha_{i,AR}$ the coefficients determined by testing an actual machine. Each coefficient was determined mathematically as follows:

$$\alpha_{1,AR} = \frac{7.6R_{lr}^2 + 91.27R_{lr} + 1}{100} \tag{2-9}$$

$$\alpha_{2,AR} = \frac{0.0212T_{in,co}^2 - 0.1103T_{in,co} + 81.727}{100} \tag{2-10}$$

$$\alpha_{3,AR} = \frac{15R_{co}^2 - 38.08R_{co} + 122.81}{100} \tag{2-11}$$

$$\alpha_{4,AR} = \frac{-T_{out,cw} + 107}{100} \tag{2-12}$$

where, $T_{in,co}$ is the inlet temperature of the cooling water [°C], R_{co} the ratio of the current mass flow rate to the rated mass flow rate of the cooling water [-], and $T_{out,cw}$ the outlet temperature of the chilled water [°C].

2.1.3 Heat recovered absorption refrigerator

A heat recovered absorption refrigerator (HRAR) is a state-of-the-art technology to improve machine efficiency through the utilization of waste heat; in particular, gas consumption for cooling could be reduced.

The characteristics of HRAR (Fig. 2-3) are in accordance with the excel file "RJ-XX1-310H_120-500_Ver310.xls" in the LCEM tool, which contains five capacities, as listed in Table 2-3. This model has the following constraints:

1) Partial load rate: 25% to 100%

2) Inlet temperature of cooling water: 20–32 °C

Table 2-3 | Rated specification of HRAR in the LCEM tool

Cooling capacity [kW]	422	738	949	1,407	1,758
Heating capacity [kW]	338	591	844	912	1,140
Mass flow rate of cooling water [L/min]	2,000	3,500	4,500	6,667	8,333
Recovered heat [kW]	130	227	292	433	541
Electricity consumption for cooling and heating [kW]	6.6	8.5	10.6	12.3	12.3
Gas consumption for cooling [m³/h]	25.1	43.9	56.4	83.6	104.5
Gas consumption for heating [m³/h]	30.9	54.1	77.3	83.6	104.5
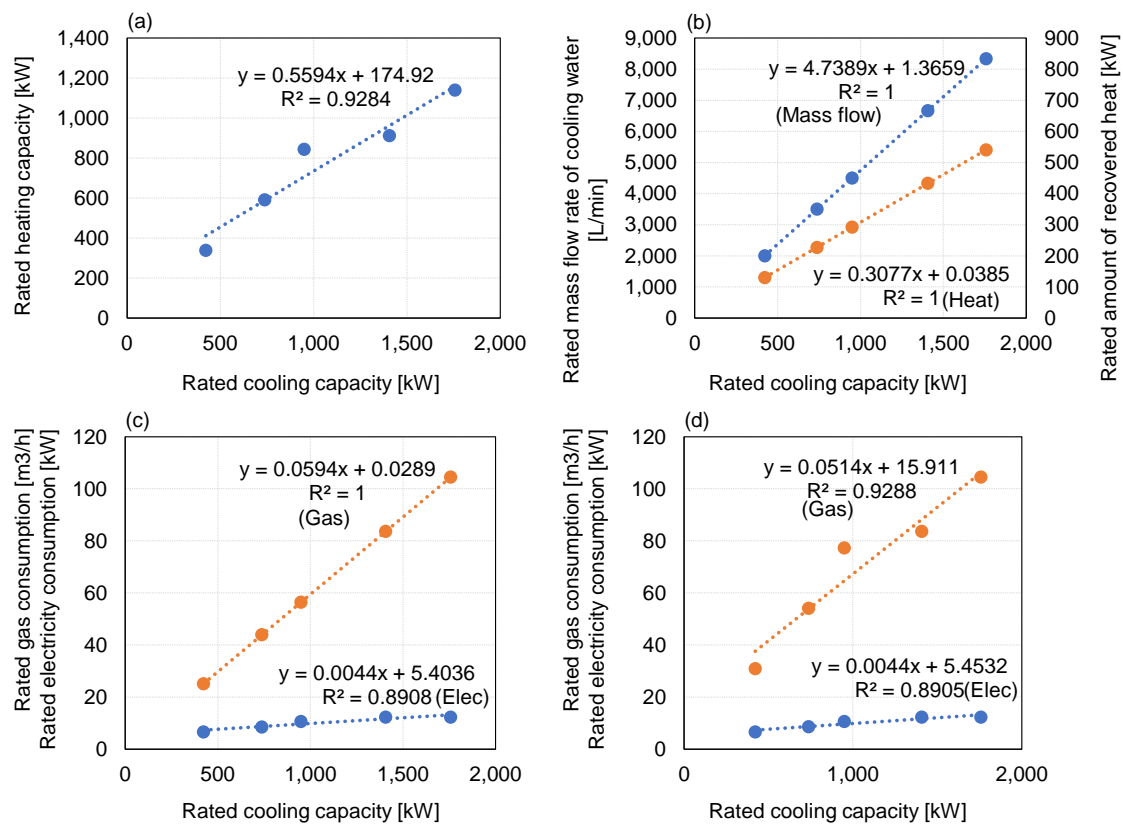
Fig. 2-3 | Relationship of various specification values to the rated cooling capacity: a) rated heating capacity, b) rated mass flow rate of cooling water and rated amount of recovered heat, c) rated gas and electricity consumption for cooling, d) rated gas and electricity consumption for heating.

3) Inlet temperature of recovered heat: less than 95 °C

HRAR is generally used with a combined heat and power (CHP) system because the temperature of waste heat from a common type of CHP is less than 95 °C. To make the specification continuous, the following figures show trend-lines that indicate the relationships of the rated cooling capacity to various parameters.

The electricity consumption was calculated linearly as follows:

$$c_{E,HRAR} = c_{E,rd,HRAR}(0.1R_{lr} + 0.9) \tag{2-13}$$

In contrast, the gas consumption had nonlinear characteristics as follows:

$$c_{G,HRAR_{cl}} = c_{G,rd,HRAR_{cl}}R_{G,HRAR_{cl}} - \frac{0.8P_{RH}R_{G,HRAR_{cl}}c_{G,rd,HRAR_{cl}}}{P_{HRAR_{cl}}} \tag{2-14}$$

$$c_{G,HRAR_{ht}} = c_{G,rd,HRAR_{ht}}R_{G,HRAR_{ht}} \tag{2-15}$$

where, $c_{G,HRAR_{cl}}$, and $c_{G,HRAR_{ht}}$ represent the gas consumption of cooling and heating [kW], respectively; $c_{G,rd,HRAR_{cl}}$ and $c_{G,rd,HRAR_{ht}}$ are the rated gas consumption of cooling and heating [kW], respectively; $R_{G,HRAR_{cl}}$ and $R_{G,HRAR_{ht}}$ denote the gas consumption ratio of cooling and heating to the rated value [-], respectively; P_{RH} is the amount of recovered heat [kW]; and $P_{HRAR_{cl}}$ denotes thermal output of HRAR for cooling [kW]. When P_{RH} is large and $c_{G,HRAR_{cl}}$ is negative, $c_{G,HRAR_{cl}}$ should be zero. As shown in Eq. (2-14), P_{RH} can reduce the gas consumption.

$R_{G,HRAR_{cl}}$ and $R_{G,HRAR_{ht}}$ are the gas consumption ratios for cooling and heating, respectively, to the rated gas consumption. These are calculated as follows:

$$
\begin{aligned}
R_{G,HRAR_{cl}} = {}& (0.1R_{lr}^2 + 0.8576R_{lr} + 0.042672) \times (0.000084T_{in,co}^2 + 0.006028T_{in,co} \\
& + 0.72107)\frac{100}{0.074533R_{co} + 92.545} \\
& \times \frac{100}{0.001814T_{out,cw}^2 + 1.258145T_{out,cw} + 91.104} \\
& \times \frac{100}{-0.013758R_{cw} + 101.379}
\end{aligned} \tag{2-16}
$$

$$R_{G,HRAR_{ht}} = R_{lr} \tag{2-17}$$

where, $T_{in,co}$ represents the inlet temperature of the cooling water [°C], and R_{co} and R_{cw} are the ratios of mass flow rate to the rated values of cooling water and chilled water [-], respectively. $R_{G,HRARc}$ has nonlinear characteristics, but $R_{G,HRAR_{ht}}$ is linearly equal to the partial load rate.

2.1.4 Air-source heat pump

An air-source heat pump (ASHP) is a common heat source machine used for both cooling and heating. In general, a unit of ASHP is not large (e.g., 3.5 kW). Hence, many units were gathered to

Table 2-4 | Rated specification of ASHP

Cooling capacity [kW]	255	340	425	510	595	680	765	850	935
Heating capacity [kW]	270	360	450	540	630	720	810	900	990
Electricity consumption for cooling and heating [kW]	71.1	94.8	119	142	166	190	213	237	261
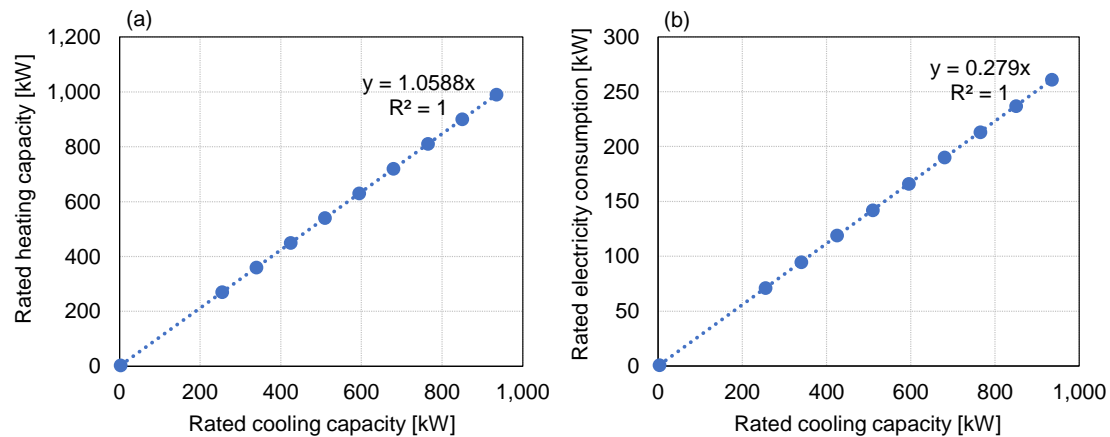
Fig. 2-4 | Relationship of various specification values to the rated cooling capacity: a) rated heating capacity, and b) rated electricity consumption for cooling and heating.

generate a large amount of heat. In addition, the time interval required to initiate heat generation using ASHP is shorter than that for other machines such as CR and AR. Thus, ASHP is suitable for use in buildings with highly variable cooling or heating demand.

The characteristics of ASHP is in accordance with the excel file "RR-XX5-310S_225-1020_Ver310" in the LCEM tool, which contains nine capacity models, as listed in Table 2-4.

This model has the following constraints:

1) Partial load rate: 10% to 100%

2) Outdoor temperature: -5–40 °C

To make the specification relationship continuous, trend-lines were generated, as shown in the following figures (Fig. 2-4); they indicate the relationship of the rated cooling capacity to various parameters.

The maximum cooling and heating capacities are dependent on the outdoor temperature as follows:

$$
\begin{aligned}
P_{\text{max,ASHP}_{\text{cl}}} = P_{\text{rd,ASHP}_{\text{cl}}}(&-0.000000123T_{\text{out,cw}}^2 T_{\text{atm}}^2 + 0.0000010278T_{\text{out,cw}}T_{\text{atm}}^2 \\
&- 0.00031152T_{\text{atm}}^2 + 0.0000096773T_{\text{out,cw}}^2 T_{\text{atm}} \\
&+ -0.00041981T_{\text{atm}}T_{\text{out,cw}} + 0.0071877T_{\text{atm}} - 0.00099621T_{\text{out,cw}}^2 \\
&+ 0.058391T_{\text{out,cw}} + 0.86301)
\end{aligned}
\tag{2-18}
$$

$$
\begin{aligned}
P_{\text{max,ASHP}_{\text{ht}}} = P_{\text{rd,ASHP}_{\text{ht}}}(&-0.000000422T_{\text{out,hw}}^2 T_{\text{atm}}^2 + 0.000016544T_{\text{out,hw}}T_{\text{atm}}^2 \\
&+ 0.000057912T_{\text{atm}}^2 + 0.000015522T_{\text{out,hw}}^2 T_{\text{atm}} \\
&- 0.00098337T_{\text{atm}}T_{\text{out,hw}} + 0.034725T_{\text{atm}} - 0.00017832T_{\text{out,hw}}^2 \\
&+ 0.011552T_{\text{out,hw}} + 0.69076)
\end{aligned}
\tag{2-19}
$$

where, $P_{\text{max,ASHP}_{\text{cl}}}$ and $P_{\text{max,ASHP}_{\text{ht}}}$ are the maximum capacity for cooling and heating, respectively; $P_{\text{Rd,ASHP}_{\text{cl}}}$ and $P_{\text{Rd,ASHP}_{\text{ht}}}$ the rated capacity for cooling and heating, respectively; and T_{atm}, $T_{\text{out,cw}}$, and $T_{\text{out,hw}}$ the atmosphere temperature [°C], and the outlet temperature of the chilled and hot water [°C], respectively.

The electricity consumption is calculated as follows:

$$
\begin{aligned}
c_{\text{E,ASHP}_{\text{cl}}} = c_{\text{E,rd,ASHP}_{\text{cl}}}(&-0.00000013T_{\text{out,cw}}^2 T_{\text{atm}}^2 + 0.000002019T_{\text{out,cw}}T_{\text{atm}}^2 \\
&+ 0.0005665T_{\text{atm}}^2 + 0.000005159T_{\text{out,cw}}T_{\text{atm}} \\
&- 0.00005125T_{\text{out,cw}}T_{\text{atm}} - 0.01236T_{\text{atm}} - 0.0002398T_{\text{out,cw}}^2 \\
&+ 0.01162T_{\text{out,cw}} + 0.6608) \times (0.3021R_{\text{lr}}^3 - 0.2442R_{\text{lr}}^2 + 0.9516R_{\text{lr}} \\
&- 0.0003)
\end{aligned}
\tag{2-20}
$$

$$
\begin{aligned}
c_{\text{E,ASHP}_{\text{ht}}} = c_{\text{E,rd,ASHP}_{\text{ht}}}(&-0.00000019T_{\text{out,hw}}^2 T_{\text{atm}}^2 + 0.00001592T_{\text{out,hw}}T_{\text{atm}}^2 \\
&- 0.0002736T_{\text{atm}}^2 + 0.000001611T_{\text{out,hw}}^2 T_{\text{atm}} \\
&- 0.0001121T_{\text{out,hw}}T_{\text{atm}} + 0.004077T_{\text{atm}} + 0.0002619T_{\text{out,hw}}^2 \\
&- 0.001682T_{\text{out,hw}} + 0.5267) \times (0.243R_{\text{lr}}^3 - 0.2903R_{\text{lr}}^2 + 1.0531R_{\text{lr}} \\
&- 0.0022)
\end{aligned}
\tag{2-21}
$$

where, $c_{\text{E,ASHP}_{\text{cl}}}$ and $c_{\text{E,ASHP}_{\text{ht}}}$ represent the electricity consumption for cooling and heating [kW], respectively; and $c_{\text{E,rd,ASHP}_{\text{cl}}}$ and $c_{\text{E,rd,ASHP}_{\text{ht}}}$ the rated electricity consumption for cooling and heating [kW], respectively.

2.1.5 Gas heat pump

A gas heat pump (GHP) is a heat pump technology based on gas energy. The characteristics of GHP are in accordance with the excel file "GHPCA-XX1-310_20-25_Ver310.xls" in the LCEM tool, which contains two capacities, as listed in Table 2-5.

This model has the constraint that the partial load rate should be between 25% and 100%. To make the specification continuous, trend-lines were generated in the following figures (Fig. 2-5); these represent the relationship of the rated cooling capacity to various parameters.

The electricity consumption was calculated linearly as follows:

$$c_{\text{E,GHP}} = c_{\text{E,rd,GHP}} R_{\text{lr}} \tag{2-22}$$

where, $c_{\text{E,GHP}}$ and $c_{\text{E,rd,GHP}}$ are the electricity consumption [kW] and rated electricity consumption [kW], respectively. Gas consumption was calculated nonlinearly as follows:

$$c_{\text{G,GHP}} = c_{\text{G,rd,GHP}} \prod_{i}^{3} \alpha_{i,\text{GHP}} \tag{2-23}$$

Table 2-5 | Rated specification of GHP

Cooling capacity [kW]	50	71
Heating capacity [kW]	60	80
Electricity consumption for cooling [kW]	1.37	1.92
Electricity consumption for heating [kW]	1.13	1.36
Gas consumption for cooling [m³/h]	3.48	5.12
Gas consumption for heating [m³/h]	3.68	5.36
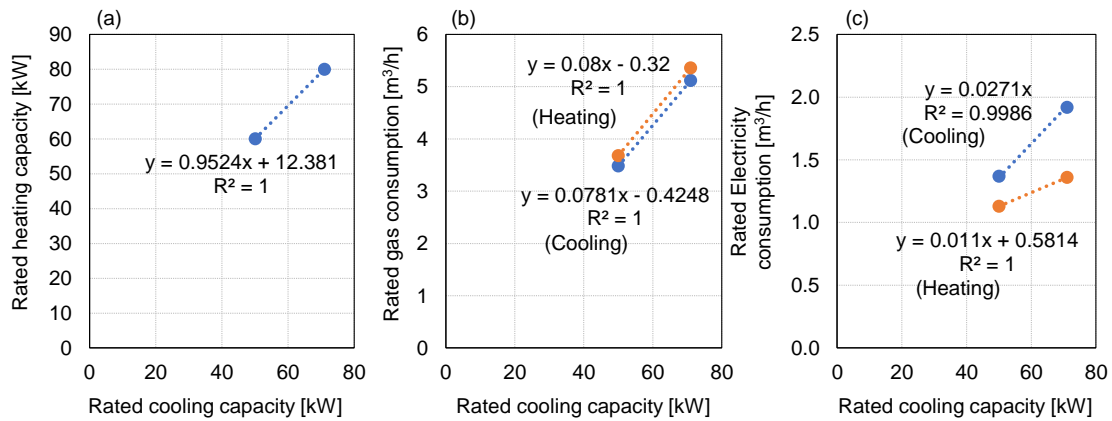
Fig. 2-5 | Relationship of various specification values to the rated cooling capacity: a) rated heating capacity, b) rated gas consumption for cooling and heating, and c) rated electricity consumption for cooling and heating.

where, $c_{\mathrm{G,GHP}}$ and $c_{\mathrm{G,rd,GHP}}$ are the gas consumption [m³/h] and rated gas consumption [m³/h], respectively; $\alpha_{i,\mathrm{GHP}}$ the coefficient with which to determine the gas consumption. Different coefficients are used for the cooling and heating operations; these are determined as follows:

$$\alpha_{1,\mathrm{GHP_{cl}}} = \frac{100R_{\mathrm{lr}}}{300R_{\mathrm{lr}}^3 - 770R_{\mathrm{lr}}^2 + 570R_{\mathrm{lr}} - 0.0002} \tag{2-24}$$

$$\alpha_{2,\mathrm{GHP_{cl}}} = \frac{0.0941T_{\mathrm{out,cw}}^2 - 2.5414T_{\mathrm{out,cw}} + 113.1789}{100} \tag{2-25}$$

$$\alpha_{3,\mathrm{GHP_{cl}}} = \frac{0.0939T_{\mathrm{atm}}^2 - 4.8649T_{\mathrm{atm}} + 155.244}{100} \tag{2-26}$$

$$\alpha_{1,\mathrm{GHP_{ht}}} = \frac{100R_{\mathrm{lr}}}{300R_{\mathrm{lr}}^3 - 737R_{\mathrm{lr}}^2 + 536R_{\mathrm{lr}} + 0.9998} \tag{2-27}$$

$$\alpha_{2,\mathrm{GHP_{ht}}} = \frac{0.0491T_{\mathrm{out,hw}}^2 - 2.4509T_{\mathrm{out,hw}} + 110.863}{100} \tag{2-28}$$

$$\alpha_{3,\mathrm{GHP_{ht}}} = \frac{0.0092T_{\mathrm{atm}}^3 - 0.0226T_{\mathrm{atm}}^2 - 1.8024T_{\mathrm{atm}} + 109.6408}{100} \tag{2-29}$$

where, $\alpha_{1-3,\mathrm{GHP_{cl}}}$ and $\alpha_{1-3,\mathrm{GHP_{ht}}}$ are the coefficients for cooling and heating, respectively.

2.1.6 Ground source heat pump

GSHP is applicable to for both cooling and heating operations and is a notable technology due to its high performance [145]. GSHP is used in conjunction with a borehole heat exchanger (BHE) to inject heat into ground. The characteristics of GSHP are in accordance with the excel file "HB(VP)-XX1-310_80-1000_Ver310.xls," which contains the following model.

The rated cooling and heating capacity are 51.32 and 46.62 kW, respectively. In addition, the rated electricity consumption for cooling and heating are 10.8 and 15.2 kW, respectively. However, the maximum capacity of GSHP and the electricity consumption depend particularly on the temperature of the water circulating through the BHE. The maximum capacity for cooling and heating are determined as follows:

$$\begin{aligned} P_{\mathrm{max,GSHP_{cl}}} = {} & 0.02251T_{\mathrm{out,cw}}^2 - 0.01407T_{\mathrm{out,cw}}T_{\mathrm{in,cirw}} - 0.00126T_{\mathrm{in,cirw}}^2 \\ & + 1.738T_{\mathrm{out,cw}} - 0.305T_{\mathrm{in,cirw}} + P_{\mathrm{R,GSHP_{cl}}} \end{aligned} \tag{2-30}$$

$$P_{\text{max,GSHP}_{\text{ht}}} = -0.001352T_{\text{out,hw}}^2 - 0.008325T_{\text{out,hw}}T_{\text{in,cirw}} + 0.02112T_{\text{in,cirw}}^2$$
$$+ 0.03779T_{\text{out,hw}} + 1.445T_{\text{in,cirw}} + P_{\text{R,GSHP}_{\text{ht}}} \tag{2-31}$$

where, $P_{\text{max,GSHP}_{\text{cl}}}$ and $P_{\text{max,GSHP}_{\text{ht}}}$ are the maximum cooling and heating capacities, respectively. The electricity consumption can be calculated as follows:

$$c_{\text{E,GSHP}_{\text{cl}}} = \left(-0.001418T_{\text{out,cw}}^2 + 0.005793T_{\text{out,cw}}T_{\text{in,cirw}} - 0.0001034T_{\text{in,cirw}}^2\right.$$
$$\left. - 0.1244T_{\text{out,cw}} + 0.2912T_{\text{in,cirw}} + 3.218\right) \tag{2-32}$$
$$\times \left(4.899R_{\text{lr}}^4 - 12.81R_{\text{lr}}^3 + 12.05R_{\text{lr}}^2 - 3.792R_{\text{lr}} + 0.6557\right)$$

$$c_{\text{E,GSHP}_{\text{ht}}} = \left(-0.0001136T_{\text{out,hw}}^2 + 0.005796T_{\text{out,hw}}T_{\text{in,cirw}} - 0.001418T_{\text{in,cirw}}^2\right.$$
$$\left. + 0.264T_{\text{out,hw}} - 0.1393T_{\text{in,cirw}} + 2.48\right) \tag{2-33}$$
$$\times \left(1.804R_{\text{lr}}^4 - 4.428R_{\text{lr}}^3 + 3.858R_{\text{lr}}^2 - 0.4286R_{\text{lr}} + 0.1962\right)$$

where, $c_{\text{E,GSHP}_{\text{cl}}}$ and $c_{\text{E,GSHP}_{\text{ht}}}$ are the electricity consumption [kW] for cooling and heating, respectively; and $T_{\text{in,cirw}}$ the inlet temperature of the circulating water. Fig. 2-6 shows the variations in rated capacity and COP for inlet temperatures in the range of 2 °C to 40 °C.
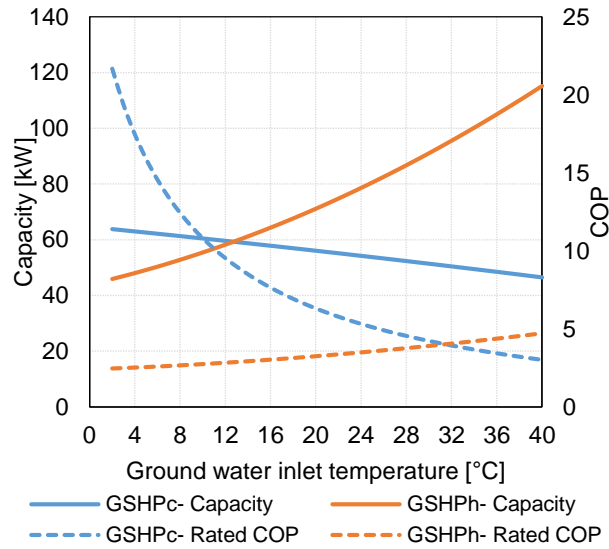
Fig. 2-6 | Capacity and COP variation as a function of the inlet temperature of the circulating water.

2.1.7 Gas boiler

GB is used to generate hot water using gas energy. The characteristics of GB are in accordance with the excel file "HB(VP)-XX1-310_80-1000_Ver310.xls," which contains twelve capacity models, as listed in Table 2-6. To make the specification continuous, various trend-lines were generated in the following figures (Fig. 2-7); these indicate the relationship of the rated cooling capacity to various parameters.

Table 2-6 | Rated specification of GB in the LCEM tool

Heating capacity [kW]	93	116	151	186	233	291	349	465	581	756	930	1,163
Electricity consumption of fan [kW]	0.45	0.45	0.46	0.61	0.61	0.61	0.66	1.15	1.15	2.08	2.08	2.08
Electricity consumption of other equipment [kW]	0.11	0.11	0.11	0.11	0.11	0.11	0.13	0.13	0.13	0.70	0.70	0.70
Gas consumption [m³/h]	9.0	11.2	14.8	18.0	22.7	28.1	34.4	45.4	56.1	73.8	89.8	114
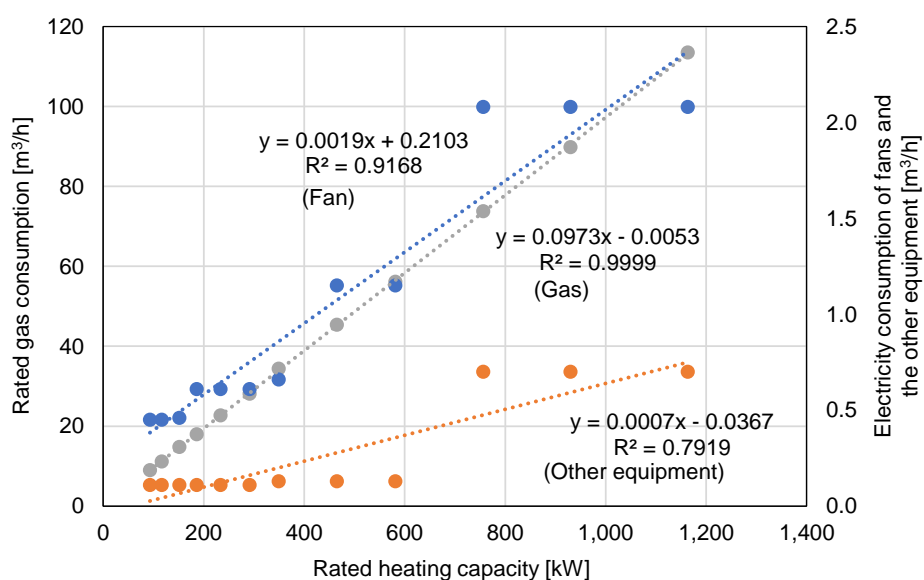
Fig. 2-7 | Relationship of the rated cooling capacity to various specifications such as rated gas consumption, and electricity consumption of fans and other equipment.

The electricity consumption of GB ($c_{E,GB}$) was calculated linearly as follows:

$$c_{E,GB} = c_{E,rd,FAN} + c_{E,rd,other}R_{lr} \tag{2-34}$$

where, $c_{E,rd,FAN}$ and $c_{E,rd,other}$ are the electricity consumption [kW] of the fans and other equipment. The gas consumption was calculated linearly as follows:

$$c_{G,GB} = c_{G,rd,GB}R_{lr} \tag{2-35}$$

2.1.8 Combined heat and power

CHP can generate electricity and heat energy simultaneously using gas energy. The rated efficiency of power generation and heat recovery are set to 40.5% and 34.5%, respectively. The power generation efficiency ($\mu_{E,CHP}$) is determined using Eq. (2-36).

$$\mu_{E,CHP} = -0.216R_{lr}^2 + 0.434R_{lr} + 0.187 \tag{2-36}$$

The gas consumption can be determined using the aforementioned rated gas consumption and power generation efficiency as follows:

$$c_{G,CHP} = \frac{3.6R_{lr}}{45\mu_{E,CHP}} \tag{2-37}$$

Third, the heat recovery efficiency ($\mu_{ht,CHP}$) i calculated as follows:

$$\mu_{ht,CHP} = 0.216R_{lr}^2 - 0.434R_{lr} + 0.563 \tag{2-38}$$

Finally, the amount of recovered heat (P_{RH} [kW]) can be calculated as follows:

$$P_{RH} = \frac{45c_{G,CHP}\mu_{ht,CHP}}{3.6} \tag{2-39}$$

2.1.9 Photovoltaic system

A photovoltaic system (PV) is widely used globally to utilize solar energy efficiently. Although PV systems have a complex technology to improve their performance, such as maximum power point tracking (MPPT), the calculation of PV power generation is simplified in this research as follows:

$$P_{PV} = A_{PV}I_{total}\mu_{PV}\mu_{PC} \tag{2-40}$$

where, P_{PV} denotes the power generation of PV [kW], A_{PV} is the PV area PV [m^2]; I_{total} the total solar radiation [kW/m^2]; and μ_{PV} and μ_{PC} indicate the conversion efficiency of the PV panel and power conditioner, respectively. A_{PV} is set to 500 m^2, and μ_{PV} and μ_{PC} to 0.13 and 0.97, respectively.

2.1.10   Solar thermal system

A solar thermal system consists of a solar collector (SC) and circulating pumps, and is used to generate hot water using solar energy. The characteristics of SC are in accordance with the excel file "SCOL-XX-303XX-01_Ver303.xls" in the LCEM tool. The parameters of the solar thermal system are fixed in this research as follows:

Location: Tokyo, Japan (35.69° N, 139.76° E)

Panel angle: 35° to ground

Panel area: 100 m^2

Fouling factor of the panel (τ): 3%

The heat available for collection can be calculated as follows:

$$P_{SC} = A_{SC} I_{total} \left(1 - \frac{\tau}{100}\right) \mu_{SC} \tag{2-41}$$

where, P_{SC} denotes the thermal output of SC [kW], A_{SC} is the area of the SC [m^2], τ the fouling factor [-], and μ_{SC} the conversion efficiency of SC [-]. μ_{SC} can be calculated as follows:

$$\mu_{SC} = \frac{-338.4 \left\{\frac{\Delta T}{I_{total}(1 - \tau/100)860}\right\} + 84}{100} \tag{2-42}$$

where, ΔT is the temperature difference between the inlet and outlet circulating fluids of SC.

2.1.11   Battery

The rechargeable Battery (RB) is becoming increasingly popular to reduce electricity costs and to achieve peak-shifting. Although many types of batteries have been developed in recent years, a Li-ion chargeable battery was applied in this research because it has advantages compared to other types; these include a low self-discharge rate and memory effects [146].

Although the battery undergoes chemical change during charging and discharging operations, which is difficult to model, a simple linear model was adopted in this research. The remaining battery charge [kWh] at a certain time step can be formulated as follows:

$$S_{\mathrm{RB}}^t = (1 - \tau_{\mathrm{RB}})S_{\mathrm{RB}}^{t-1} + P_{\mathrm{RB,c}} - P_{\mathrm{RB,d}} \tag{2-43}$$

where, S_{RB}^t is the remaining battery charge [kWh] at time step t; τ_{RB} the self-discharge rate which is fixed to 2 [%/h]; and $P_{\mathrm{RB,c}}$ and $P_{\mathrm{RB,d}}$ the power of the charge and discharge [kW], respectively.

2.1.12   Stratified water thermal energy storage

A stratified water thermal energy storage (TES) is used to improve system efficiency and realize peak-shifting operations. The characteristics of TES are in accordance with Ref [147]. According to the reference paper, a stratified TES can be modeled as a multi-node model. The temperature variation of each node can be calculated using the following differential equation.

$$
\begin{aligned}
V_i \frac{\mathrm{d}T_{\mathrm{TES},i}}{\mathrm{d}t} = {} & \left(\frac{UA_{\mathrm{TES}}}{\gamma}\right)_{\mathrm{i}} \left(T_{\mathrm{atm}} - T_{\mathrm{TES,i}}\right) + \alpha_i^{\mathrm{HS}} m^{\mathrm{HS}}\left(T_{\mathrm{in,c}} - T_{\mathrm{TES,i}}\right) \\
& + \alpha_i^{\mathrm{L}} m^{\mathrm{HS}}\left(T_{\mathrm{in,d}} - T_{\mathrm{TES,i}}\right) \\
& + \begin{cases} m_{\mathrm{net},i}\left(T_{\mathrm{TES},i-1} - T_{\mathrm{TES},i}\right) & \text{if } m_{\mathrm{net},i} > 0 \\ m_{\mathrm{net},i+1}\left(T_{\mathrm{TES},i} - T_{\mathrm{TES},i+1}\right) & \text{if } m_{\mathrm{net},i+1} < 0 \end{cases}
\end{aligned}
\tag{2-44}
$$

where, V_i is the volume of each node [m³], U the overall heat transfer coefficient [W/m²/K] which is fixed to 0.5, γ the heat capacity [J/m³·K], $T_{\mathrm{TES,i}}$ the water temperature of node i, α_i^{HS} and α_i^{L} the coefficients as shown below; m^{HS} and m^{L} the mass flow rate of the heat source and load side circulating fluid [m³/s], respectively; $T_{\mathrm{in,c}}$ and $T_{\mathrm{in,d}}$ the inlet water temperature of the charging and discharging fluid [°C], respectively; $m_{\mathrm{net},i}$ the net mass flow rate during simultaneous charging and discharging operations; $m_{\mathrm{net},i}$ indicates the vertical direction of heat transfer within TES; α_i^{HS} is a binary number; α_i^{HS} is one at the node with the diffuser inlet during the charging operation and zero at the other node. In contrast, α_i^{L} is one at the node with the diffuser inlet during the discharging operation and zero at the other node as in α_i^{HS}. In this research, the diffuser inlets during charging and discharging operations are the bottom and top node, respectively. Hence, when there are a total 20 nodes (N_{node}), only $\alpha_{20}^{\mathrm{HS}}$ and α_1^{L} are one. $m_{\mathrm{net},i}$ is calculated using α_i^{HS} and α_i^{L} as follows:

$$m_{\mathrm{net},i} = m^{\mathrm{HS}} \sum_{j=1}^{i-1} \alpha_j^{\mathrm{HS}} - m^{\mathrm{L}} \sum_{j=i+1}^{N_{\mathrm{node}}} \alpha_j^{\mathrm{L}} \tag{2-45}$$

The 4th Runge-Kutta method was adopted to solve the differential equation. The time interval of the method was set to ten seconds to avoid unpredicted errors.

2.1.13   Cooling tower

Cooling towers (CT) are used with some refrigerators, such as CR and AR, to reduce the cooling water temperature. CT has a fan which consumes electricity. According to the LCEM tool, the electricity consumption of the fan can be calculated as follows:

$$c_{E,CT} = \frac{T_{in,cw} - T_{out,cw}}{T_{in,cw} - T_{out,lb,cw}} c_{E,rd,CT} \tag{2-46}$$

where, $c_{E,CT}$ is the electricity consumption of CT [kW]; $c_{E,rd,CT}$ the rated electricity consumption [kW]; $T_{in,cw}$ and $T_{out,cw}$ the inlet and outlet temperatures, respectively, of the cooling water from CT [°C]; and $T_{out,lb,cw}$ the lower bound of the outlet temperature of the cooling water from CT [°C] which was fixed at   13 °C. $T_{out,cw}$ is determined as follows:

$$
\begin{aligned}
T_{out,cw} = \{&(-0.000004721794474 T_{in,cw}^2 + 0.00029751111532 T_{in,cw} \\
&+ 0.00061832038261) T_{atm,wb}^2 \\
&+ (0.000084967776296 T_{in,cw}^2 - 0.0067128829235 T_{in,cw} \\
&+ 0.23836348677) T_{atm,wb} - 0.006443915064 T_{in,cw}^2 \\
&+ 0.95482871943 T_{in,cw} - 1.1396350496\} \\
&\times \left[1 - \left\{1 - \left(-0.288961\left(\frac{R_{cw}}{104}\right)^2 + \frac{0.86331 R_{cw}}{104} + 0.4370549\right)\right\}\right] \\
&\times \frac{T_{in,cw} - T_{atm,wb}}{0.5 T_{in,cw} + 12}
\end{aligned}
\tag{2-47}
$$

where, $T_{atm,wb}$ is the outdoor wet bulb temperature [°C]. The cooling water temperature variation is determined by iterative calculation. The initial value of $T_{out,cw}$ from CT was set to 32 °C.

2.1.14   Pumps

In this research, the pumps for chilled/hot water, the circulating fluid of GSHP, and cooling water have the same characteristics. The initial values of the rated mass flow ($m_{rd,pump}$) [L/min] and rated pump pressure ($H_{rd,pump}$) [kPa] should be determined. The electricity consumption ($c_{E,pump}$) of the pump is determined as follows:

$$c_{E,Pump} = \frac{m_{pump} H_{pump}}{600 \mu_{pump}} \tag{2-48}$$

where, m_{pump} is the mass flow rate [L/min], and μ_{pump} the pump efficiency [-] calculated as follows:

$$\mu_{\text{pump}} = (-0.92922968675125 R_m^2 + 1.79498334402997 R_m \\ + 0.109364093104081)\mu_{\text{max,pump}} \tag{2-49}$$

$$\mu_{\text{max,pump}} = -8.58\left(\log_{10}\frac{m_{\text{rd,pump}}}{1000}\right)^2 + 17.48\log_{10}\frac{m_{\text{rd,pump}}}{1000} + 74.23 \tag{2-50}$$

where, R_m is the ratio of mass flow rate to rated value [-], and $\mu_{\text{max,pump}}$ the maximum pump efficiency determined using the rated mass flow rate. H_{pump} is determined as follows:

$$H_{\text{pump}} = H_{\text{rd,pump}}\left(\frac{\psi}{\psi_{\text{rd}}}\right)^2(-0.394658899805463 R_m^2 + 0.096329067908277 R_m \\ + 1.29350965543578) \tag{2-51}$$

$$\psi = \begin{cases} \psi_{\text{lb}} & \text{if } \psi_{\text{req}} \leq \psi_{\text{lb}} \\ \psi_{\text{ub}} & \text{if } \psi_{\text{req}} \geq \psi_{\text{ub}} \\ \psi_{\text{req}} & \text{otherwise} \end{cases} \tag{2-52}$$

$$\psi_{\text{req}} = \psi_{\text{rd}}\left\{\frac{\alpha_{\text{pump}}\left(\frac{m_{\text{pump}}}{60}\right)^2}{H_{\text{Rd,pump}}}\right\}^{0.5} \tag{2-53}$$

where, ψ and ψ_{rd} the pump frequency and rated pump frequency [Hz], respectively; ψ_{ub} and ψ_{lb} the upper and lower bound of the frequency which were set to 60 and 20 Hz, respectively; ψ_{req} the required frequency [Hz]; and α_{pump} the coefficient of the pump, which is determined as follows:

$$\alpha_{\text{pump}} = \frac{H_{\text{rd,pump}}}{\left(\frac{m_{\text{rd}}}{60}\right)^2} \tag{2-54}$$

2.2 Optimization methodology

2.2.1 Basic optimization strategy for energy systems

When the operation of energy systems is optimized, the method of formulating the actual phenomenon in the mathematical models is important. For example, some parameters, such as machine load rate and distribution rate of a splitter, can be decision variables; however, mass flow rate

should be the decision variable instead of machine load rate, and bulb opening rate should be used instead of distribution rate.

The appropriate order of optimization methods that should be considered is as follows:

1) Full-search algorithm
2) LP (linear programming)
3) DP (dynamic programming)
4) Metaheuristic optimization method

First, a full-search algorithm is the simplest method to solve optimization problems. In addition, this algorithm can yield a theoretical optimal solution for problems under various conditions, such as nonlinear, linear, continuous, and discrete. However, this algorithm has the largest computation costs of all the methods.

Second, LP is a mathematical programming method that can be applied to reduce computation costs using a linearization technique. As mentioned in Section 1.2.2, although the characteristics of heat source machines and the other equipment are nonlinear, many previous studies attempted to simplify the optimization problem, particularly by using linearization. Hence, linear programming might be useful in an academic paper, but it is not suitable for use in actual systems. In addition, continuous linear programming can solve a problem quickly, but a discrete condition makes the problem complex.

Third, DP is powerful algorithm to solve linear and nonlinear functions, and it can derive a theoretical optimal solution based on a mathematical theorem. Although this method is limited to use in discrete decision variable applications, it can reduce the computation costs drastically compared to a full-search algorithm. However, it should be considered that the computation costs of DP have an exponential dependence on the number of decision variables because DP should set a multi-dimensional matrix.

Finally, when an optimization problem is large and not easily solved using the aforementioned methods, alternative approximation methods should be applied. There are two common approximation methods: metaheuristic optimization methods and machine learning, where the latter involves reinforcement learning to determine a quasi-optimal result. The metaheuristic optimization method, which is simply called "metaheuristics," consists of numerous methods such as genetic algorithm (GA), particle swarm optimization (PSO), differential evolution (DE), cuckoo search (CS), and bat algorithm (BA).

2.2.2 Mixed-integer linear programming (MILP)

MILP consists of a linear objective function, linear constraints, and at least one integer variables. In fact, the integer variables make the optimization problem difficult. Hence, relaxation methods are often used in an attempt to reduce the number of the integer variables. Although continuous variables can be transformed to discrete variables using a rounding technique, it cannot always guarantee optimality of the solution. Therefore, numerous researches have proposed suitable methods for MILP. First, a transformation of integer variables to continuous variables must be conducted; this is called continuous relaxation. Following this, linear programming (e.g., the simplex method and interior point method) is conducted on the relaxation model to determine an optimal solution. If the optimal solution unexpectedly meets the integer constraints, it is an optimal solution of the original problem. However, in practice such cases are rare. Thus, it is necessary to formulate the continuous variables using a branch-and-bound method [148,149] which is known as the most useful and powerful method employing an MILP algorithm.

Although theoretically, MILP does not always obtain the global optimum, the technique is often applied to complex optimization problems as a consequence of improvements to the algorithm and the performance of the personal computer. Alternative methods that have also been used with MILP include presolving [150], cutting planes [151], and heuristic methods. Moreover, a combination algorithm using these above methods is applied in some solvers such as GAMS, CPLEX, and MATLAB.

2.2.3 Dynamic programming (DP)

DP was proposed by Bellman [152] in 1957. DP can be applied to almost all optimization problems, such as linear, nonlinear, continuous, and discrete conditions. DP is based on the "Principle of Optimality" which was also proposed by Bellman. Most scheduling problems that include energy system optimization or network modeling are based on the above principle, because it is composed of multi-stage decisions. DP has two algorithms: backward and forward algorithms. Fig. 2-8 shows both algorithms for optimization of a battery and thermal energy storage.

DP not only has the advantage of flexibility in applicable problems, but also has the ability to reduce computational complexity. When the full-search algorithm is applied to a problem with a number of decision variables (N_{dv}), number of time horizons (N_{th}), and number of discrete points (N_{ds}), the computational complexity can be expressed as $N_{\mathrm{ds}}^{N_{\mathrm{dv}}N_{\mathrm{th}}}$; it can also be expressed as $O(N_{\mathrm{ds}}^{N_{\mathrm{dv}}N_{\mathrm{th}}})$ in Landau notation.
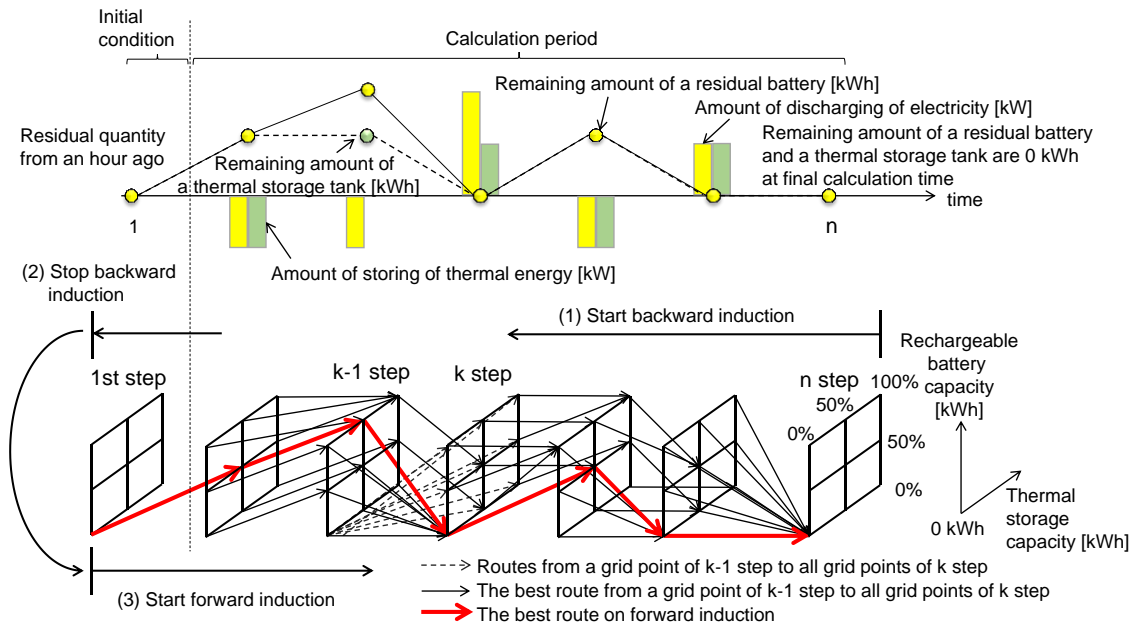
Fig. 2-8 | Conceptual diagram of DP algorithm [153]

However, the computational complexity of DP can be reduced by $O(N_{\text{ds}}^{2N_{\text{dv}}})$. Hence, the complexity of DP does not depend exponentially on the number of time horizons.

2.2.4 Genetic algorithm (GA)

The genetic algorithm (GA), developed by Holland et al. [154] in the 1960s was inspired by biological evolution based on Charles Darwin's theory of natural selection. The expression for individual modeling of GA is composed of two types: bit string and real-coded. The bit string GA is suitable for discrete optimization, whereas real-coded GA (RCGA) is suitable for continuous optimization.

The bit string GA uses the selection, crossover, and mutation method operators to determine the optimal solution. First, the algorithm conducts an initialization of the population, which is composed of individuals that assume the value of the decision variables. The individuals are scattered across the entire search space by using uniformly allocated random numbers.

Second, some individuals are selected as parent individuals to create new solutions called child individuals. This selection is performed using a selection method such as roulette-wheel selection, tournament selection, or elitist selection. The roulette-wheel selection method involves the calculation of the selected probability of each individual by using Eq. (2-55).

$$R_{\text{sl},i} = \frac{f_i}{\sum_{j=1}^{N_{\text{pop}}} f_j} \tag{2-55}$$

where $R_{\text{sl},i} \in [0,1]$ denotes the selected probability of the i-th individual, f_i the objective function value of the i-th individual, and N_{pop} the number of populations. The elitist selection method leads to the preferential selection of the individual with the preferred value. This selection method can always locate the optimum point near the current best individual, but this is likely to be trapped in a local optimum. Third, the crossover method uses the crossover probability (α_{cv}) and employs methods such as one-point or two-point crossover.

Finally, the mutation method is performed for all individuals with a mutation probability (α_{mt}) by employing methods such as bit string mutation, flip bit, and uniform. The crossover probability is usually high and lies in the range of 0.7–0.9, which is larger than the mutation probability, for which the range is 0.001–0.05. The advantage of the mutation method is that individuals can be retrieved easily from the local optimum.

The RCGA uses the same approach as the bit string GA when using the crossover method for selection. In particular, the selection procedure is referred to as the "generation alternation model," which is based on methods such as the minimal generation gap (MGG) [155] and the just generation gap (JGG) [156]. In the MGG method, parent individuals are selected randomly, after which child individuals are generated using the crossover method. Finally, the elitist method is used to replace the parent individuals with the top layer of individuals, which includes both parents and children. The advantage of the MGG method is its ability to obtain an optimal solution in the proximity of the preferred individuals; however, unfortunately the solution is often a local optimum. Considering this, JGG was developed to resolve this problem. In the JGG method, all parent individuals are replaced by child individuals with an objective value that is superior to those of the other children. This strategy maintains the diversity of the population. Although there are numerous crossover methods for use with the RCGA, the real-coded ensemble crossover (REX) [157] and adaptation of expansion rate REX (AREX) [156,157] were developed recently. AREX, which is an updated version of REX, adopts the Mahalanobis distance to handle the ill-scale problem efficiently.

The RCGA can be applied to continuous optimization problem with a high degree of accuracy, because of its powerful mathematical theory. However, it results in a long calculation time when the applied problem has a complicated objective function, such as an energy system, because of the high population and large number of generated child individuals.

2.2.5 Particle swarm optimization (PSO)

PSO was developed by Kennedy and Eberhart [158]. This method mimics the collective behavior of birds or fish. An individual uses three vectors when it moves to other positions: the current velocity vector (v_i^g), best position vector for all particles (x_{gb}), and past best position vector for itself ($x_{\text{pb},i}$). Each individual (x_i^g) moves iteratively as follows:

$$x_i^{g+1} = x_i^g + v_i^{g+1} \tag{2-56}$$

$$v_i^{g+1} = v_i^g + \alpha_{\text{PSO},1}\mathcal{U}\big(x_{\text{pb},i} - x_i^g\big) + \alpha_{\text{PSO},2}\mathcal{U}\big(x_{\text{gb}} - x_i^g\big) \tag{2-57}$$

$$v_i^{g+1} = wv_i^g + \alpha_{\text{PSO},1}\mathcal{U}\big(x_{\text{pb},i} - x_i^g\big) + \alpha_{\text{PSO},2}\mathcal{U}\big(x_{\text{gb}} - x_i^g\big) \tag{2-58}$$

$$v_i^{g+1} = \begin{cases} v_i^{g+1} \text{ if } v_i^{g+1} \leq v_{\text{max}} \\ v_{\text{max}} \text{ if } v_i^{g+1} > v_{\text{max}} \end{cases} \tag{2-59}$$

where w is an inertia weight factor to control the velocity and has the same meaning as the step length, $\alpha_{\text{PSO},1}$ and $\alpha_{\text{PSO},2}$ are acceleration constants, $\mathcal{U}$ a uniform random number [0, 1], and v_{max} the maximum velocity. Although the inertia weight factor w was not included when the method was first proposed by Kennedy, Shi and Eberhart [159] added it to the PSO method in 1998. Recently, a simplified version of the PSO was defined to include this factor, which is controlled by Eq. (2-63).

$$w = w_{\text{max}} - \frac{w_{\text{max}} - w_{\text{min}}}{N_g} g \tag{2-60}$$

Although PSO has the advantage of high calculation and convergence speeds, it has a tendency to become trapped in a local optimum in multi-modal functions, a disadvantage which became possible to avoid when Higashi [160] added a mutation method to PSO according to:

$$x_{i,j} = x_{i,j}\big(1 + \mathcal{N}(0,\sigma)\big), \qquad \sigma = 0.1\text{length}(n_j) \tag{2-61}$$

where, $x_{i,j}$ denotes the j-th vector component value of the i-th individual, and $\text{length}(n_j)$ denotes a range of j-th decision variables.

In addition, Stacey [161] proposed a modification to the velocity as follows:

$$v_i^g = \begin{cases} -\dfrac{v_{\max}}{2}\mathcal{U} & \text{if initialization}(g = 0) \\ v_{\max}\mathcal{U} & \text{if } v_i^g > v_{\max} \\ v_i^g & \text{otherwise} \end{cases} \tag{2-62}$$

where, $\mathcal{U} \in [0, 1]$ denotes a uniformly distributed random number. Miranda [162] proposed evolutionary PSO (EPSO), which is a hybrid PSO method with an evolutionary strategy. In EPSO, the inertia weight factor w_i^g and the best position vector of all particles x_{gb}^g are updated as follows:

$$w_i^{g+1} = w_i^g + \alpha_{\text{EPSO}}\mathcal{N}(0,1) \tag{2-63}$$

$$x_{\text{gb}}^{g+1} = x_{\text{gb}}^g + \alpha'_{\text{EPSO}}\mathcal{N}(0,1) \tag{2-64}$$

where, $\alpha_{\text{EPSO}} \in [0, 1]$ denotes a learning dispersion constant, which is determined at initial iteration by a uniformly distributed random number; and α'_{EPSO} denotes the noise dispersion parameter, which is a small value. To improve the ability of PSO, the author proposed mutation PSO (m-PSO) to optimize the operating schedule of a simple energy system [153]. m-PSO has a mutation operator to avoid trapping in a local optimum. The mutation operator is used at the final step of the procedure of the original PSO. When the mutation rate (α_{mt}) set to 0.9 is greater than a uniformly random number ($\mathcal{U}$), the position of the individual is changed randomly.

$$x_{i,j} = \begin{cases} \mathcal{U} & \text{if } \mathcal{U} \leq \alpha_{\text{mt}} \\ x_{i,j} & \text{otherwise} \end{cases} \tag{2-65}$$

Fig. 2-9 shows the comparison of original PSO, EPSO, and m-PSO in a simple energy system. m-PSO exhibits a better ability to determine a better solution than the other two methods.

2.2.6 Cuckoo search (CS)

CS was developed by Yang et al. [163] in 2009. They showed that CS is superior to GA and c-PSO, and Civicioglu et al. [164] showed that CS is superior to c-PSO and is as efficient as DE. The CS algorithm is based on the brood parasitism of a cuckoo. Initial individuals are selected randomly. Lévy flight is performed when generating a new individual in the next iteration. The best individual at each iteration carries over to the next iteration. Brood parasitic behavior is formulated in CS in terms of a single parameter, α_{CS}, representing the probability of eggs being discovered by the host bird. In general, α_{CS} is a large number, typically in the range of 0.80-0.90, to search a global optimum. Hence, CS has a good ability to search an optimal solution under not only a unimodal function, but also a multimodal function, although the conversion speed of CS is not as high as that of PSO and DE.
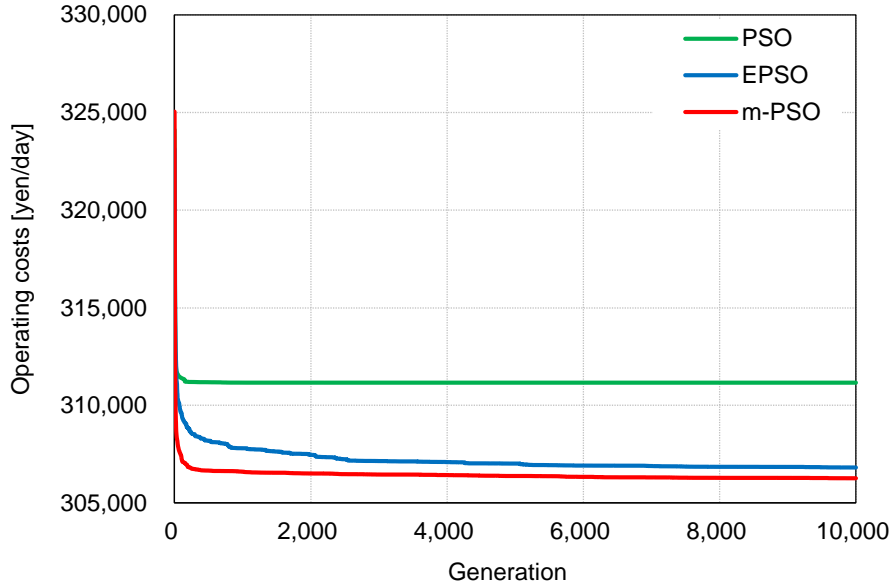
Fig. 2-9 | Comparison of three types of PSO [153]

2.2.7 Self-learning bat algorithm (SLBA)

Bahman et al. [101] developed SLBA, which combines BA [165] and the self-learning method [102], in 2010. BA imitates the gulping behavior of a bat literally. The difference between BA and SLBA is the method of calculating the velocity. In BA, only Eq. (32) is used to create a new individual, as follows:

$$\psi_i^{g+1} = \psi_{\min} + (\psi_{\max} - \psi_{\min})\mathcal{U} \tag{2-66}$$

$$v_i^{g+1} = v_i^g + \left(x_i^g - x_{\mathrm{gb}}^g\right)\psi_i^{g+1} \tag{2-67}$$

$$x_i^{g+1,\mathrm{new}} = x_i^g + v_i^{g+1} \tag{2-68}$$

where $\psi_{\max}$ and $\psi_{\min}$ are frequency of bat's echo set to two and zero, respectively. In contrast, four velocity-updating strategies are used in SLBA, as follows [101].

- Velocity updating strategy 1:

$$v_i^{g+1} = v_i^g + \left(0.3\psi_i^{g+1} + 0.4\right)\left(x_{\mathrm{gb}}^g - x_i^g\right) + (0.6\mathcal{U} + 0.4)(x_{\mathrm{gb}}^g - x_{\mathrm{gw}}^g) \tag{2-69}$$

- Velocity updating strategy 2:

$$v_i^{g+1} = v_i^g + \{x_{p1}^g + \mathcal{U}(x_{p2}^g - x_{p3}^g)\} \tag{2-70}$$

- Velocity updating strategy 3:

$$v_i^{g+1} = \mathcal{U}v_i^g + (0.3\mathcal{U} + 0.2)\psi_i^{g+1}(x_{gb}^g - x_i^g) \tag{2-71}$$

- Velocity updating strategy 4:

$$v_i^{g+1} = \mathcal{U}v_i^g + 0.5(0.3\mathcal{U} + 0.2)\psi_i^g(x_{gb}^g - \text{round}(1 + \mathcal{U})\overline{x^g}) \tag{2-72}$$

where, $\overline{x^g}$ is the mean value of all the individuals. The strategy to be used at each step is selected using a roulette wheel mechanism (RWM).

2.2.8 Differential evolution (DE)

DE was developed by Storn and Price [166] to solve global optimization problems, regardless of the search domain landscape, such as linear, nonlinear, convex, concave, discrete, and continuous models. The DE optimization procedure is as follows: 1) initialize individuals (N_{pop}) using a uniformly random number; 2) independently choose three individuals for each individual (x_{p1}, x_{p2}, x_{p3}); 3) apply the mutation method to generate donor individual x_i^{donor} using Eq. (7), in which α_{mt} denotes the mutation rate (=0.5); and 4) employ the crossover method to generate child individual x_i^{child} using Eq. (8). Here, $x_{i,k}$ indicates the k-th decision variable of individual i, and α_{cv} represents the crossover rate, which is set to decrease exponentially with an increase in the iteration number.

$$x_i^{\text{donor}} = x_{p1} + \alpha_{\text{mt}}(x_{p2} - x_{p3}) \tag{2-73}$$

$$x_{i,k}^{\text{child}} = \begin{cases} x_{i,k} & \text{if } \mathcal{U} \le \alpha_{\text{cv}} \\ x_{i,k}^{\text{donor}}, & \text{if } \mathcal{U} > \alpha_{\text{cv}} \end{cases} \tag{2-74}$$

2.2.9 Method of handling constraint conditions

A previous study [153] compared the six aforementioned methods, namely DP, GA, PSO, DE, CS, and SLBA. The paper showed that CS had the highest conversion ability, m-PSO had the fastest conversion speed, and the results of GA and SLBA were the worst.

Metaheuristic methods have an advantage in solving a complex nonlinear problem comparing to deterministic methods. However, the method of handling constraints is an issue because the general metaheuristic method was developed under no-constraint conditions. To solve many constraints, an epsilon constraint handling method was developed by Takahama [167]. In this method, constraint violation $\varphi(x_i)$ is applied to each individual using Eq. (2-75), in which $h_{k,1}(x_i)$ and $h_{k,2}(x_i)$ signify the inequality and equality constraints, respectively, and α_ε is a positive number set to 1.0. In addition, i-th individual x_i, which has objective function value and constraint violation (f_i, φ_i), is compared with x_i^{child}, which has objective function value and constraint violation (f_i^{new}, φ_i^{new}), using Eq. (10). Fig. 2-10 shows a conceptual image of the algorithm.

The better of the two individuals, x_i or x_i^{child}, is applied to the next iteration. It is important that the value of ε decreases exponentially as the number of iteration increases. When the value of ε is zero, the objective function values are compared regardless of the value of phi. This means a strict constraint optimization.

$$\varphi(x_i) = \sum_k \max\{0, h_{k,1}(x_i)\}^{\alpha_\varepsilon} + \sum_k |h_{k,2}(x_i)|^{\alpha_\varepsilon} \tag{2-75}$$

$$(f_i^{new}, \varphi_i^{new}) <_\varepsilon (f_i, \varphi_i) \Leftrightarrow \begin{cases} f_i^{new} < f_i, & \text{if } \varphi_i, \varphi_i^{new} \leq \varepsilon \\ f_i^{new} < f_i, & \text{if } \varphi_i = \varphi_i^{new} \\ \varphi_i^{new} < \varphi_i, & \text{otherwise} \end{cases} \tag{2-76}$$
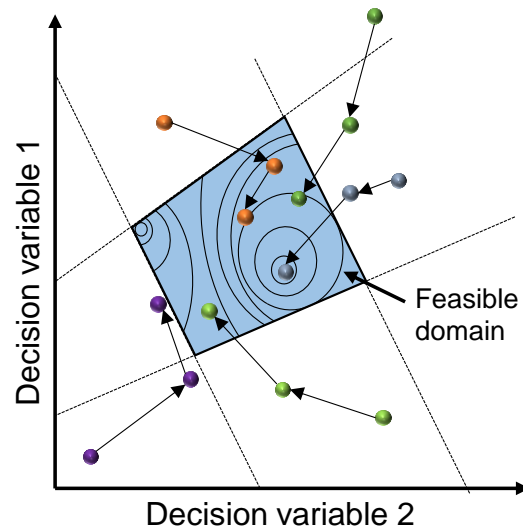
Fig. 2-10 | Algorithm of epsilon constraint handling method

2.2.10   *ε-constrained differential evolution (εDE)*

In fact, the ε-constrained method can be applied to alternative metaheuristics such as GA, PSO, and CS, but the ε-constrained DE method is the most suitable method. For example, PSO uses a continuous generation model to select survived individuals as the next generation. The continuous generation model means that all individuals, parent and children, are compared simultaneously and superior individuals are survived. However, this model causes a conversion problem in that all individuals trap in a local optimum and the algorithm cannot find a feasible solution. In the optimization method, CS has a high mutation rate α_{CS}. The mutation rate causes low conversion of minimizing the constraint violations. Finally, it results in no feasible solution to be found. Although GA has a low mutation rate, an original performance of GA to find a better solution is lower than that of alternative methods. Thus, εGA cannot be superior to εDE. The algorithm flow chart is shown in Fig. 2-11.
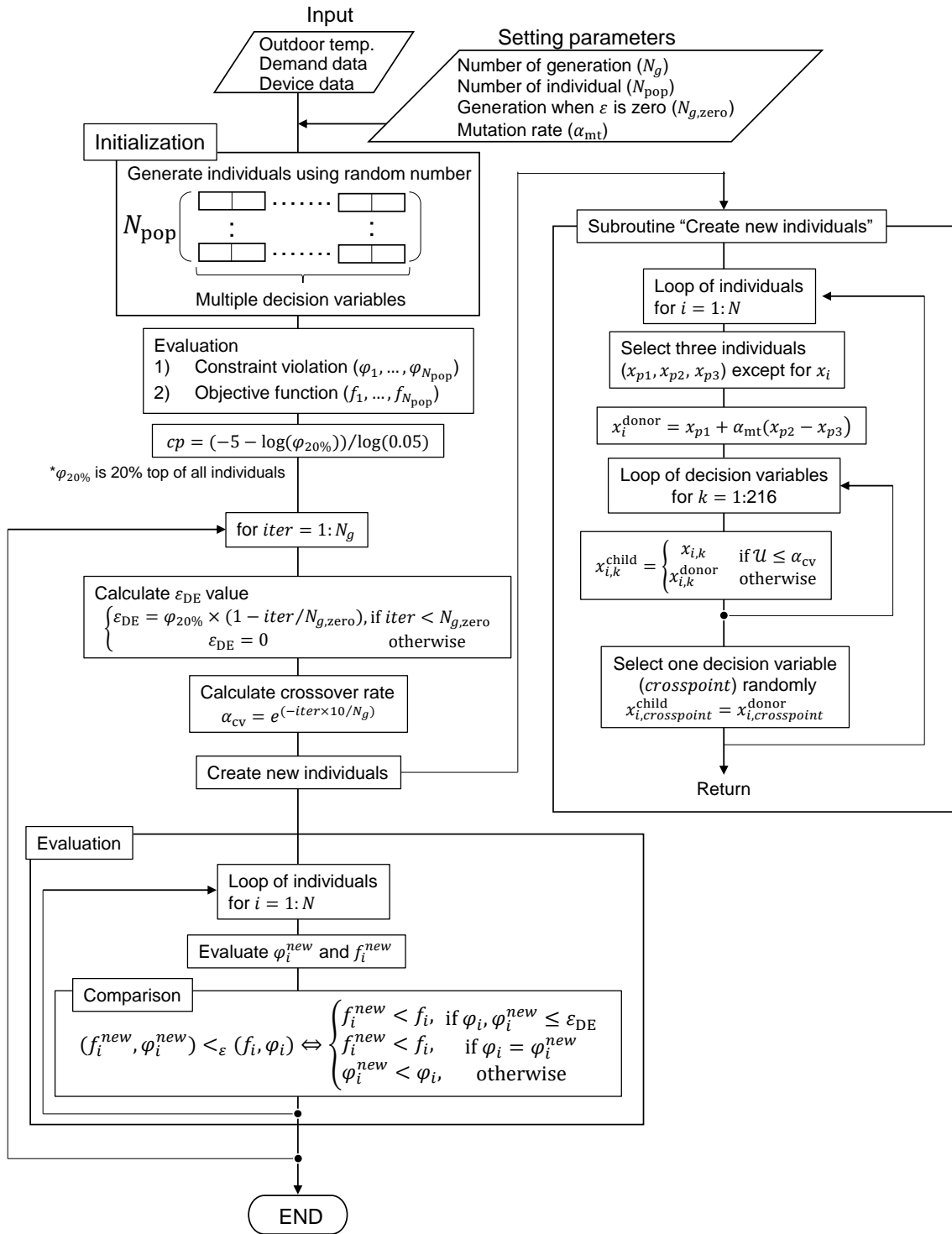
Fig. 2-11 | Flow chart of εDE algorithm

2.2.11   Q-learning

Q-learning [168] is a reinforcement learning technique that is increasingly popular for the optimization of energy system operations. Q-learning is a model-free method, which means that the method can be applied to any type of problem. Q-learning is mathematically based on the Bellman equation in the same manner as DP. DP uses a deterministic approach to solve a target problem and it reaches a theoretical optimal solution. However, Q-learning uses an approximate approach to find a better solution. Hence, Q-learning can be applied instead of the metaheuristics. In fact, Q-learning is a fundamental technique used in recent artificial intelligent technology. Therefore, Q-learning was adopted in Section 10 to optimize an operating schedule of a district energy system.

In this section, the theorem of Q-learning is described. First, Q-learning is used for a discrete problem. Q-learning collects reward information with a certain action. For example, we think when a refrigerator generated a cooling heat of 100 kW at a certain time step t and generated 200 kW at the next time step $t+1$. Both the thermal outputs are called "state". In addition, operating costs were 20,000 and 40,000 yen/h at time step t and $t+1$, respectively. An "action" is defined as the increase in thermal output from 100 to 200 kW. In addition, a "reward" is defined as total operating costs of 20,000 and 40,000 yen/h, respectively, in this case. Then, Q-learning stores the information in accordance with the action and reward into a Q-table as a Q-value.

The Q-value is updated as follows:

$$Q(S_t, A_t) \leftarrow Q(S_t, A_t) + \alpha_Q \left(r_{t+1} + \gamma \max_{a_{t+1}} Q(S_{t+1}, A_{t+1}) - Q(S_t, A_t) \right) \tag{2-77}$$

where, $Q(S_t, A_t)$ is the Q-value with the action (A_t) and the state (S_t); α_Q and γ are the learning rate and discount rate as hyperparameters of Q-learning, respectively; and r_{t+1} is the reward at time step $t+1$. This equation is based on the Bellman optimal equation. Q-learning uses iterative calculation to update the Q-values in the Q-table.

2.3   Conclusion

This chapter describes the basic theory for machine characteristics and optimization methods. In addition, εDE is a promising method which can be used to solve a constrained problem efficiently. In the following chapters, εDE is mainly used to optimize a complex energy system and the performance of εDE is validated in various energy systems through comparisons with alternative methods. Finally, a modified εDE to improve its stability is proposed in Chapter 6.

CHAPTER 3

Development and application of single- and multi-objective optimizations for complex energy systems

3.1 Introduction

This chapter describes how to optimize the operating schedule of a complex building energy system that especially comprises several storage equipment. In addition, an efficiently constrained multi-objective optimization method is proposed to minimize the operating costs and primary energy consumption simultaneously. The contents of this chapter is translated in English from my peer-reviewed article published in Journal of Environmental Engineering of Architectural Institute of Japan [169].

3.2 Calculation conditions

3.2.1 Description of energy system

Fig. 3-1 shows the configuration of the energy system. This system comprises electricity, space cooling, and domestic hot water supply systems. RB and two TES systems, i.e., TES for cooling TES_{cl} and that for domestic hot water TES_{hw}, were introduced as time-dependent equipment. The capacities of TES_{cl} and TES_{hw} were 10,000 and 1,200 kWh, respectively. These values were determined to be equal to 10% of the total cooling and hot water demand. Seven heat source machines were considered for this simulation: CR, AR, HRAR, two ASHPs (ASHP1 and ASHP2), CHP, and GB. The following four operating modes of TES and the other heat source machines were available at each time step: 1) only charging thermal energy from the heat source machines to TES, 2) only heat source machines supplying thermal energy to a secondary system, 3) only discharging thermal energy from TES to the secondary system, and 4) TES and the heat source machines supplying thermal energy. Above these were typical operating modes in an actual energy management.

The specification of the machines and devices is shown in Table 3-1. The inlet and outlet temperatures of the heat source machines were fixed, as shown in Fig. 3-1, to simplify the model. Chilled water and hot water could be varied with the machine's partial load rate. Further, the mass flow rate and temperature of cooling water were varied because these values played a significant role in the efficiency of CR and AR. In the case of an optimal combination of cooling water temperature and mass flow rate, the following procedure was used: 1) the mass flow rate of cooling water was fixed and the temperature was varied in accordance with the outdoor wet bulb temperature and machine operations; 2) when the difference of inlet and outlet temperatures of cooling water in terms of the refrigerator was less than 3 °C, the mass flow rate was decreased to maintain the difference to more than 3 °C. The calculation for variations in cooling water temperature was referred from the component described in Chapter 2.

In the electricity system, PV and RB were considered. The operation strategy of PV was as follows: 1) supplying electricity to RB, 2) supplying electricity to the secondary system, and 3) selling it to the grid. The operation strategy of RB was as follows: 1) supplying electricity to the secondary system and 2) selling it to the grid. Each operation could be chosen at each time step.

Conversion coefficients of primary energy consumption were set to 9.97 MJ/kWh for electricity and 45 MJ/m^3 for gas energy. The coefficients of CO_2 emissions of electricity and gas were set to 0.512 kg-CO_2/kWh and 2.29 kg-CO_2/m^3, respectively. Operating costs of electricity and gas were set to dynamic pricing and fixed to 87.2 yen/m^3.

The characteristics of all components that formed the energy system were referred from the machine models described in Chapter 2.1.
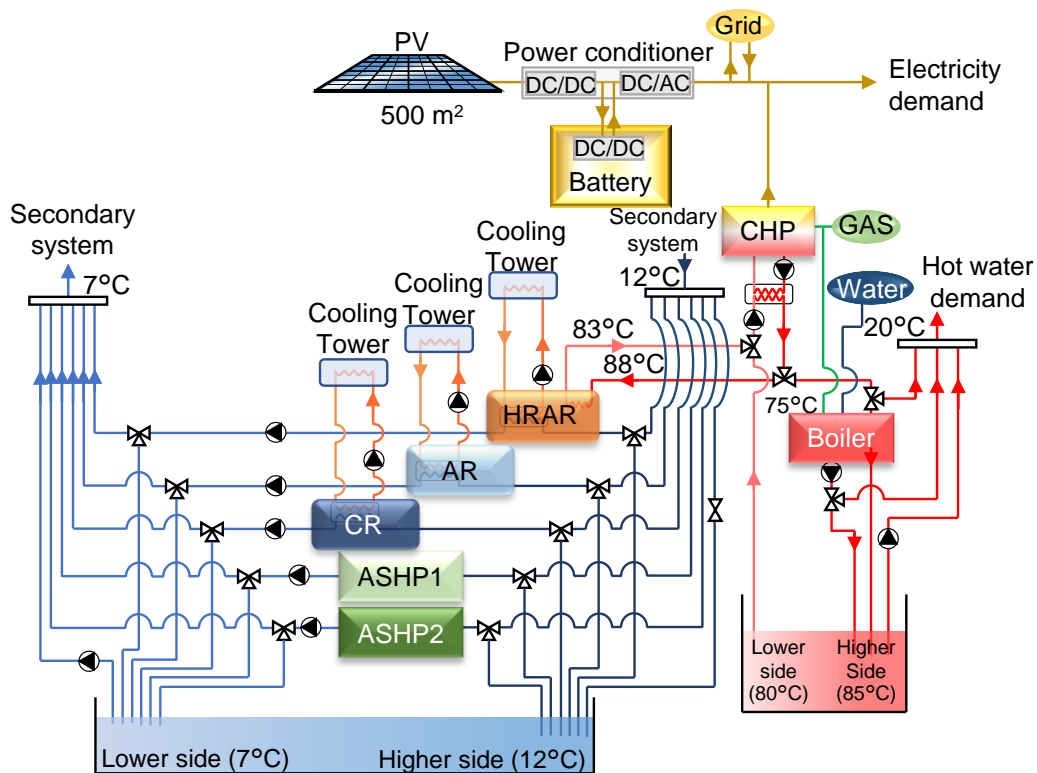
Fig. 3-1 | System configuration: a blue line shows cooling water pipe, a red line shows domestic hot water pipe, and a yellow line indicates electricity.

Table 3-1 | Rated specification of each machinery

Centrifugal refrigerator	Cooling capacity	2,500	kW
(CR)	Electricity consumption	500	kW
Absorption refrigerator	Cooling capacity	1,500	kW
(AR)	Gas consumption	86.8	m^3/h
	Electric consumption	15	kW
Heat recovered AR	Cooling capacity	1,000	kW
(HRAR)	Gas consumption	59.4	m^3/h
	Electric consumption	9.85	kW
	Amount of recovered heat	307	kW
Air-source heat pump 1	Cooling capacity	550	kW
(ASHP1)	Electric consumption	153.4	kW
Air-source heat pump 2	Cooling capacity	500	kW
(ASHP2)	Electric consumption	139.5	kW
Combined heat and	Power generation capacity	363	kW
power (CHP)	Amount of recovered heat	300	kW
	Gas consumption	71.3	m^3/h
Gas boiler (GB)	Heating capacity	750	kW
	Gas consumption	73	m^3/h
	Electric consumption	2.1	kW
Thermal energy storage	Capacity	10,000	kWh
for cooling (TES$_{cl}$)	Charging/discharging efficiency	100	%/cycle
	Self-heat loss rate	5	%/day
Thermal energy storage	Capacity	1,200	kWh
for how water (TES$_{hw}$)	Charging/discharging efficiency	100	%/cycle
	Self-heat loss rate	5	%/day
Rechargeable Battery	Capacity	500	kWh
(RB)	Maximum charge/discharge	100	kW
	Rated charging/discharging efficiency	81	%/cycle
	Self-discharge rate	0	%/day
Photovoltaic device	Area	1,000	m^2
(PV)	Conversion efficiency	13	%
	Conversion efficiency of power conditioner	97	%

3.2.2 Demand and price profiles

A typical hotel building with a total floor space of 20,000 m^2 is considered as a building model in this chapter because the hotel had enough domestic hot water demand. The calculation time horizon was set to 24 h and the time interval was set to 1 h. Demand curves were referred from CASCADE III, which was provided from the Society of Heating Air-Conditioning and Sanitary Engineers of Japan [170], as shown in Fig. 3-2. Outdoor conditions such as atmospheric temperature and solar radiation were referred from AMeDAS standard weather data in Tokyo (2005) provided by [171], as shown in Fig. 3-2(a). The variation in purchased electricity price is shown in Fig. 3-2(b). The dynamic electricity price with time was assumed, based on Ref. [153].

To obtain the price of electricity, the type of power plant, the number of each type of power plant, the composition rate of each power plant, and the power generation costs of each type of power plant were considered: nuclear power plant (composition rate 20.4%, high generation costs 11.33 yen/kWh, and low generation costs 10.1 yen/kWh), liquid natural gas fired power plant (30%, 15.29 yen/kWh,
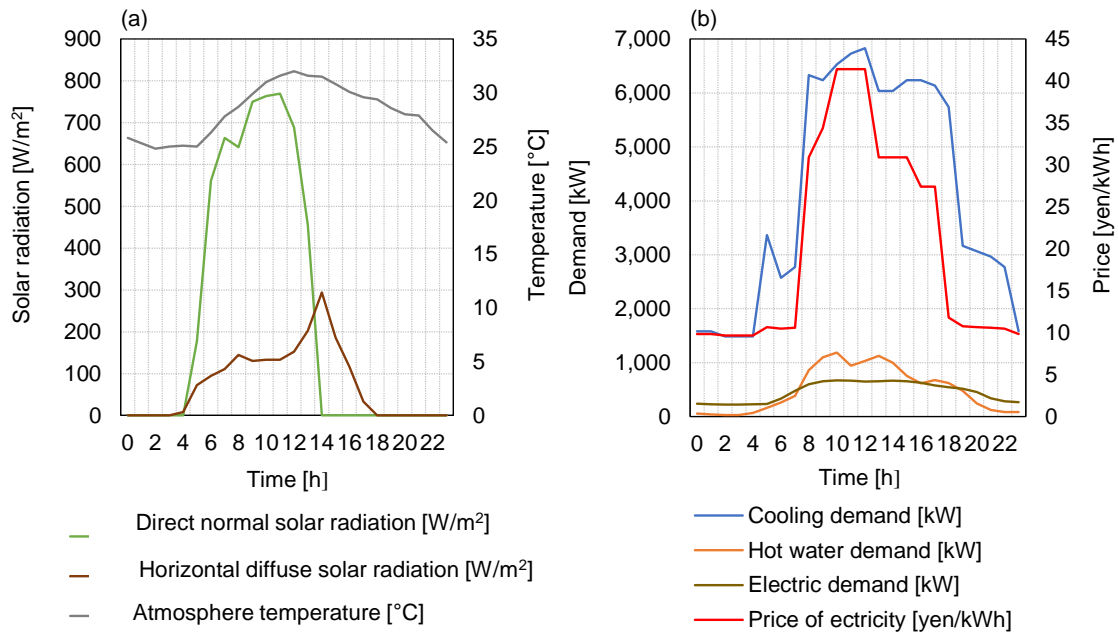
Fig. 3-2 | Outdoor and demand conditions: a) temperature and solar radiations, b) demands and price of purchased electricity

13.4 yen/kWh), coal fired power plant (26%, 14.19 yen/kWh, 12.3 yen/kWh), and hydroelectric power plant (23.6%, 12.1 yen/kWh, 11 yen/kWh). These values were taken from a Japanese government report [172]. The number of each type of plants was set to three. The dynamic price was determined using a merit ordering of each plant's generation cost. Thus, when the demand was high during day time, the price was also high. During night time, the price was low, which was a common price variation in the actual system. The same condition was used in the all later chapters.

3.3 Optimization method

3.3.1 Problem formulation

This chapter aims to minimize the daily operating costs, which are the total of electricity and gas prices, as a single objective optimization problem. It can be transformed as follows:

$$
\begin{aligned}
\text{minimize } f = \sum_t^{N_{\text{th}}} & p_{\text{E,pd}}^t \left(D_{\text{E}}^t + P_{\text{EGtoRB}}^t - P_{\text{RBto}D_{\text{E}}}^t - P_{\text{PVto}D_{\text{E}}}^t - P_{\text{CHPto}D_{\text{E}}}^t \right) \\
& - p_{\text{E,sd}}^t (P_{\text{RBtoEG}}^t + P_{\text{PVtoEG}}^t) \\
& + \sum_t^{N_{\text{th}}} p_{\text{E,pd}}^t \left(c_{\text{E,TES}_{\text{cl}}}^t + c_{\text{E,CR}}^t + c_{\text{E,AR}}^t + c_{\text{E,HRAR}}^t + c_{\text{E,ASHP1}}^t \right. \\
& \left. + c_{\text{E,ASHP2}}^t + c_{\text{E,CHP}}^t + c_{\text{E,GB}}^t \right) + \sum_t^{N_{\text{th}}} p_{\text{G,pd}}^t \left(c_{\text{G,AR}}^t + c_{\text{G,CHP}}^t + c_{\text{G,GB}}^t \right)
\end{aligned}
\tag{3-1}
$$

where P_{XtoY}^t indicates power and thermal output flows from a machine or device X to Y [kW]. $p_{\text{E,sd}}^t$, $p_{\text{E,pd}}^t$, and $p_{\text{G,sd}}^t$ indicate the price of selling electricity, the price of purchasing electricity, and the price of gas, respectively. Although Eq. (3-1) can be seen as a linear objective function, each term such as $c_{\text{E,TES}_{\text{cl}}}^t$ and $c_{\text{E,CR}}^t$ contains nonlinear and discontinuous characteristics, as shown in Chapter 2.1. In a multi-objective optimization problem that aims to minimize the operating costs and primary energy consumption, an objective function of the minimization of primary energy consumption can be expressed as follows:

$$
\begin{aligned}
\text{minimize } f = \sum_t^{N_{\text{th}}} & \alpha_{\text{E}} \left(D_{\text{E}}^t + P_{\text{EGtoRB}}^t - P_{\text{RBto}D_{\text{E}}}^t - P_{\text{PVto}D_{\text{E}}}^t - P_{\text{CHPto}D_{\text{E}}}^t \right) \\
& + \sum_t^{N_{\text{th}}} \alpha_{\text{E}} \left(c_{\text{E,TES}_{\text{cl}}}^t + c_{\text{E,CR}}^t + c_{\text{E,AR}}^t + c_{\text{E,HRAR}}^t + c_{\text{E,ASHP1}}^t + c_{\text{E,ASHP2}}^t \right. \\
& \left. + c_{\text{E,CHP}}^t + c_{\text{E,GB}}^t \right) + \sum_t^{N_{\text{th}}} \alpha_{\text{G}} \left(c_{\text{G,AR}}^t + c_{\text{G,CHP}}^t + c_{\text{G,GB}}^t \right)
\end{aligned}
\tag{3-2}
$$

where α_{E} and α_{G} indicate conversion coefficients of electricity (=9.97 MJ/kWh) and gas (=45 MJ/m³), respectively.

The following are the constraint conditions:

$$
P_{\text{EGtoRB}}^t \leq P_{\text{max,RB}}
\tag{3-3}
$$

$$P_{\text{RBtoEG}}^t \leq P_{\text{max,RB}} \tag{3-4}$$

$$P_{\text{RBto}D_{\text{E}}}^t \leq P_{\text{max,RB}} \tag{3-5}$$

$$\begin{cases} P_{\text{PVtoRB}}^t = 0 & \text{if discharging operation of RB} \\ P_{\text{PVtoRB}}^t \leq P_{\text{max,RB}} & \text{if charging operation of RB} \end{cases} \tag{3-6}$$

$$P_{\text{RBto}D_{\text{E}}}^t + P_{\text{PVto}D_{\text{E}}}^t + P_{\text{CHPto}D_{\text{E}}}^t \leq D_{\text{E}}^t \tag{3-7}$$

$$D_{\text{cl}}^t + P_{\text{TES}_{\text{cl}},\text{c}}^t - P_{\text{TES}_{\text{cl}},\text{d}}^t - P_{\text{AR}}^t - P_{\text{HRAR}}^t - P_{\text{ASHP1}}^t - P_{\text{ASHP2}}^t \leq P_{\text{rd,CR}} \tag{3-8}$$

$$D_{\text{hw}}^t + P_{\text{TES}_{\text{hw}},\text{c}}^t - P_{\text{TES}_{\text{hw}},\text{d}}^t - P_{\text{CHPto}D_{\text{hw}}}^t \leq P_{\text{rd,GB}} \tag{3-9}$$

Eqs. (3-3) to (3-5) indicate constraints on maximum charging and discharging capacities of RB. Eq. (3-6) is a constraint on charging operations from PV to RB. When RB was operated in the charging mode, PV could provide electricity to RB. On the other hand, PV could not provide it when RB was operated in the discharging mode, because an ordinal rechargeable battery cannot work in the charging and discharging modes simultaneously. Eq. (3-7) indicates a constraint on electricity supply balance of the secondary system. It shows that the total amount of electricity supplied from PV, RB, and CHP should be less than the electricity demand. This is because the selling electricity (e.g., surplus electricity) was defined as different decision variables to consider a different unit price of selling electricity of each source. Hence, the surplus electricity production from these three components had to be considered separately.

As decision variables, the following 14 types were considered: 1) the amount of stored electricity in RB, 2) the distribution rate of discharged electricity from RB to the electric grid, 3) the distribution rate of discharged electricity from RB to the electricity demand, 4) the distribution rate of discharged electricity from PV to the grid, 5) the distribution rate of discharged electricity from PV to RB, 6) the distribution rate of discharged electricity from PV to the electricity demand, 7) the amount of stored energy in TES_{cl}, 8) the amount of stored energy in TES_{hw}, 9) the load rate of AR, 10) the load rate of HRAR, 11) the load rate of ASHP1, 12) the load rate of ASHP2, 13) the load rate of CHP power generation, and 14) the distribution rate of waste heat from CHP to HRAR. The load rate of CR and GB could be determined using the left-hand sides of Eqs. (3-7) and (3-8). Therefore, the number of decision variable was 336 (=14 types $\times$ 24 h).

3.3.2 Parameters of εDE for single-objective function

εDE was used to optimize the above decision variables for single-objective optimization. The number of generations was set to 10,000 and the number of individuals was set to 100. The mutation rate was set to 0.5 and ε_{DE} was expected to be zero at half of the maximum generation.

3.3.3 Proposal of multi-objective εDE (εMODE)

In general, an original algorithm of metaheuristics was created for a single-objective optimization. Hence, it had to be extended to a multi-objective optimization method. There are many previous studies that proposed it, as mentioned Chapter 1.1. However, these methods did not consider complex constraint conditions with multi-objective optimization. Hence, a new and efficient multi-objective optimization method is proposed in this chapter.

The method was named εMODE, which comprises εDE and multi-objective techniques such as non-dominated sorting (NDS) and crowding distance algorithm (CDA). NDS and CDA were proposed in [173] with the genetic algorithm NSGA-II, which is a well-known multi-objective optimization method.

NDS was used to create a pareto front and CDA was used to avoid gathering individuals in a certain position, as shown in Fig. 3-3. In NDS, all individuals were categorized as F1, F2, and so on. F1–F5 in Fig. 3-3 indicate non-dominated ranks and F1 is the most superior group to create a pareto front. Hence, this algorithm aims at making individuals non-dominated.

In fact, a previous multi-objective optimization DE algorithm (MODEA) [174] used NDS and CDA with DE. However, MODEA could not handle many constraints and adopted a continuous generation model to select the survived individuals for the next generation. This continuous generation model is the biggest problem to be solved when MODEA is extended to εMODE. This is because the continuous generation model, as shown in Fig. 3-4(a), compares all individuals, parent and archive individuals, in terms of NDS ranks such as F1 and F2. Hence, how much the constraint violation is completely ignored. It causes a rapid unpredicted convergence and cannot find any feasible solution.

Hence, we proposed to use a discrete generation model, instead of the continuous generation model, to select individuals in the next generation, as shown in Fig. 3-4(b), when the individual is an infeasible solution. The comparison of NDS ranks was performed for feasible individual groups only.
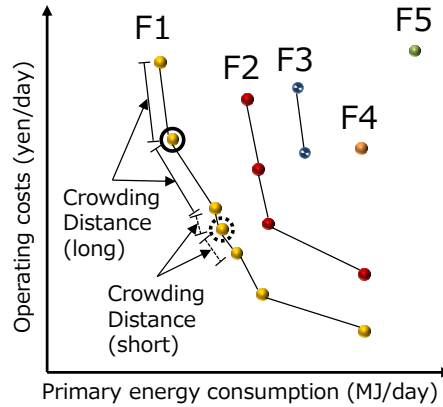
Fig. 3-3 | Conceptual diagram of NDS and CDA: F1–F5 indicates a domination level. The individuals in F1 level consist of a pareto front.
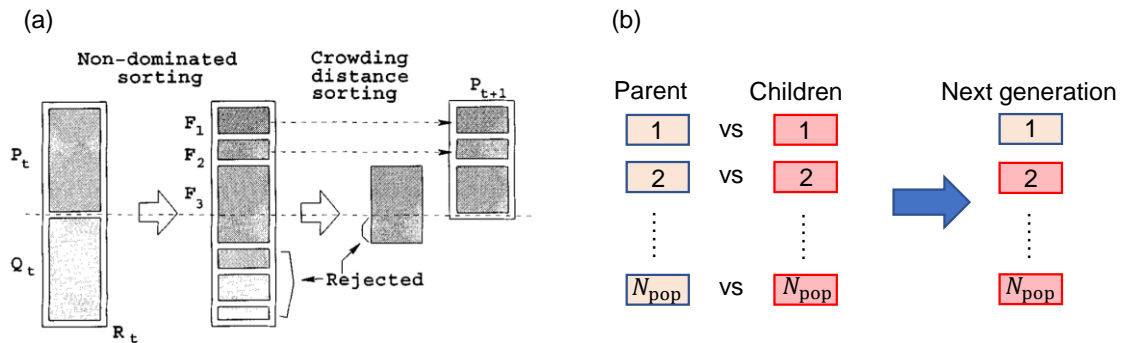
Fig. 3-4 | Conceptual diagram of continuous and discrete generation models: a) This graph shows a continuous generation model [173]. Pt and Qt indicate a parent individual group and an archive individual group, respectively. b) This graph shows a discrete generation model.

3.4 Result

3.4.1 Case setting and overview of results

The following three case studies were conducted:

1) Case 1 (an energy system without CHP)

An energy system in this case did not introduce CHP to clarify the effectiveness of the CHP system against the following two cases. However, the rated capacity of Table 3-1 was not enough to meet hot water demand, because CHP could not be introduced. Hence, the rated capacity of GB increased to 900 kW.

2) Case 2 (a predetermined scenario-based empirical operation)

This case was similar to that of an actual energy management because an ordinal building energy system did not have optimization software and an expert operator often determined an operating
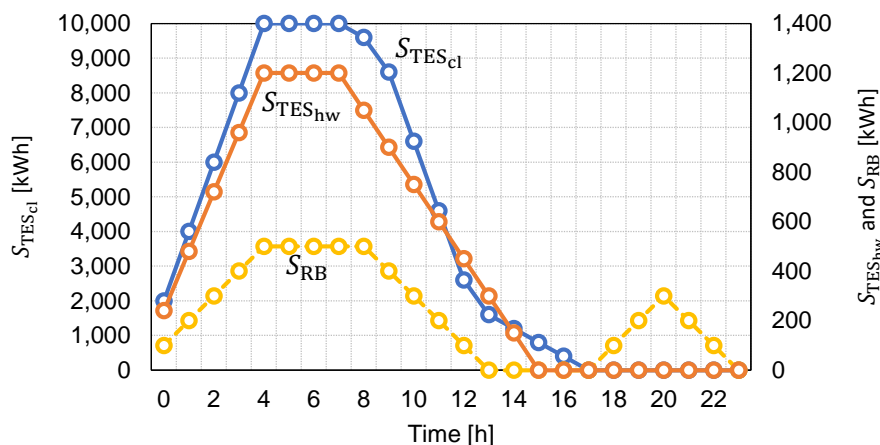
Fig. 3-5 | Operating schedule of the empirical case (Case 2): all storage devices charged thermal and electricity energy during early morning, 0 a.m. to 3 a.m., and discharged it during daytime.

schedule empirically for the next day.

The scenario used in this case is as follows:

i) Power generated from PV was sold to the grid.

ii) Discharged electricity from RB was supplied to the electricity demand during daytime because the peak demand occurred at that time. In addition, RB charged electricity and discharged it alternately during night time, especially 6 p.m. to 11 p.m., because this operation could earn maximum profits in this case. In addition, this was a fair condition when Case 2 was compared with Case 3, because Case 3 would find a solution similar to this operating pattern.

iii) The heat source machine, which had relatively high rated COP such as CR, worked in priority as compared to the other machines. Further, when the price of the purchased electricity was low, during 0 a.m. to 7 a.m. and 6 p.m. to 11 p.m., the electric heat machines such as CR, ASHP1, and ASHP2 were operated on priority. On the other hand, AR and HRAR were operated on priority when the price was high during 8 a.m. to 5 p.m.

iv) RB, TES_{cl}, and TES_{hw} charged energy from 0 a.m. to 4 a.m. when the price was the lowest. During daytime, the equipment discharged energy to meet demands. The charging and discharging operations are shown in Fig. 3-5.

3) Case 3 (optimization using εDE)

Table 3-2 | Results of single objective optimization

	Operating costs (yen/day)	Primary energy consumption (MJ/day)	CO_2 emissions (kg-CO_2/day)
Case 1	825,467	400,089	20,485
Case 2	765,444	393,073	20,099
Case 3	721,983	376,879	19,284

As shown in Table 3-2, the operating cost of Case 1 was 825,467 yen/day. In contrast, the costs of Case 2 and Case 3 could be reduced by 7.27% and 12.5% against Case 1, respectively. Hence, the effectiveness of CHP introduction was high. Additionally, Case 3 could the reduce operating costs by 5.7% against Case 2, the empirical operation. Therefore, the applied optimization method, εDE, was a powerful method to achieve cost reduction under dynamic pricing and a complex energy system.

3.4.2 Optimal operation of electricity system

This section focuses on an optimal operation of the electricity system. Fig. 3-6 shows the optimal operation given by εDE in Case 3. CHP worked at daytime to reduce the amount of purchased electricity from the grid. In contrast, CHP did not work at all from 0 a.m. to 6 a.m. and from 8 p.m. to 11 p.m. because the price of purchased electricity was lower than that at daytime.

As shown in Fig. 3-7(a), the power generation of PV was sold to the grid from 4 a.m. to 7 a.m. and from 4 p.m. to 5 p.m. because the price of selling electricity was higher than that of purchasing it. Electricity distribution from PV to RB could not be chosen because the charging and discharging efficiency of RB was 81%, and would cause electricity loss.

As shown in Fig. 3-7(b), RB charged electricity from the grid during night and the operation of selling electricity was conducted. This operation was a typical one. Hence, εDE could recognize the relationship between the two prices without any pre-provided information, and thus, could find the operating schedule properly.
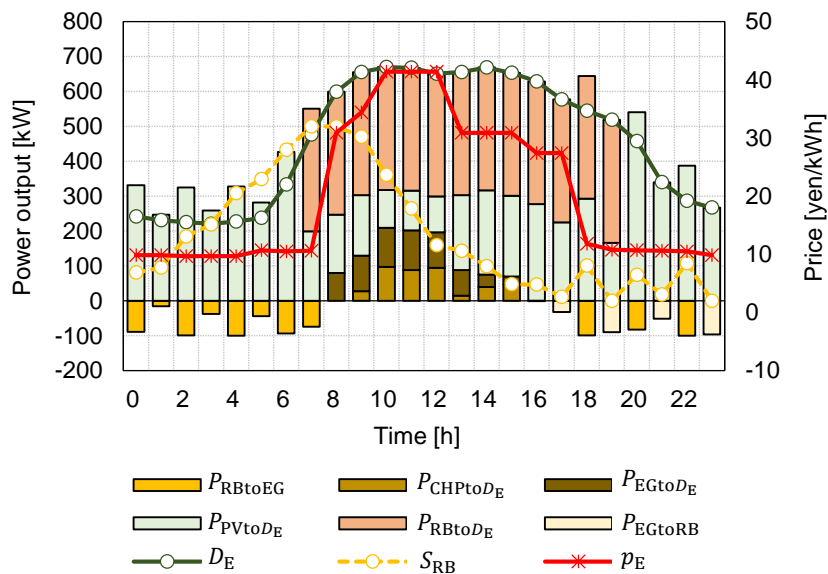
Fig. 3-6 | Optimal operation of electricity system in Case 3: P_{XtoY} indicates power output from source X to source Y. D_E indicates electricity demand, S_{RB} indicates electricity stored in rechargeable battery, and p_E indicates price of purchased electricity.
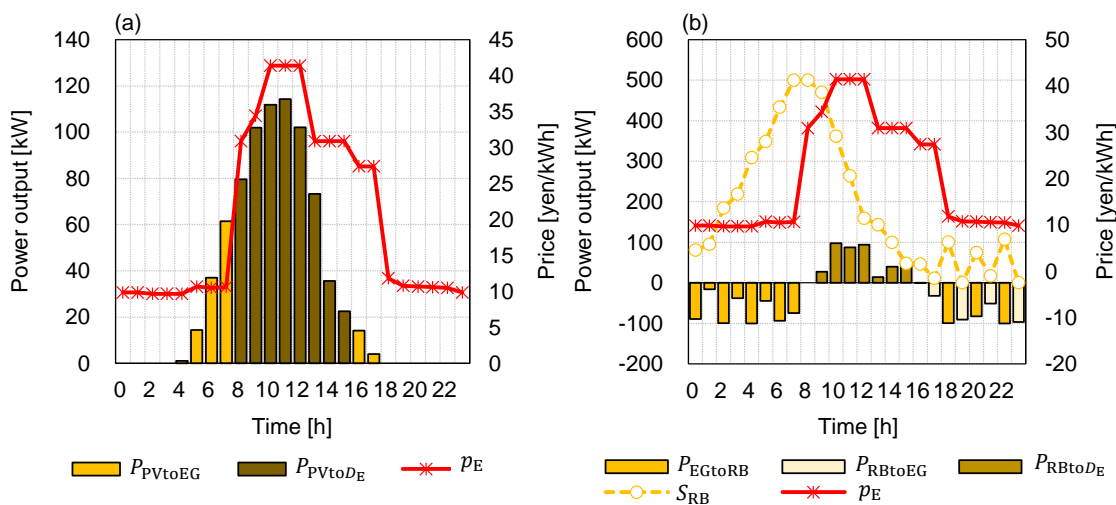
Fig. 3-7 | Optimal operation of PV and RB in Case 3: a) PV operation, b) RB operation

3.4.3 Optimal operation of cooling system

An optimal operation of TES did not depend on the variation in electricity prices, as compared to RB, because TES had a self-loss rate of only 2%, which was small as compared to that of RB. However, we cannot ignore the electricity consumption of pumps, especially in the discharging operation of TES. Hence, the same operating pattern as that of RB would be optimal in the cooling system. Fig. 3-8 shows an optimal operation of the cooling system given by εDE in Case 3.

Note that the charging operation of TES was conducted during night and early morning, 0 a.m. to 7 a.m., while the discharging operation was conducted at daytime. In addition, the electric machines, CR and ASHPs, were mainly operated from 0 a.m. to 7 a.m. In contrast, the gas-based machines, AR and HRAR, were operated during daytime. However, the total demand at daytime was greater than the total rated capacity of AR and HRAR. Hence, CR and TES_{cl} provided cooling heat to the secondary system to meet the demand. TES_{cl} discharged considerable cooling heat from 10 a.m. to 0 p.m. because the price of purchased electricity was the highest during the day. Hence, this operating schedule can be considered as an optimal one.

Fig. 3-9 shows the optimal load rates of ASHP1 and ASHP2. When the two heat pumps worked simultaneously, we found the load rates to be very similar. This operation can be thought of as an optimal one because the same load rate of the same characteristic machine was mathematically optimal in accordance with Lagrange's multiplier [175]. Hence, εDE could find a better solution in terms of mathematical fundamentals.
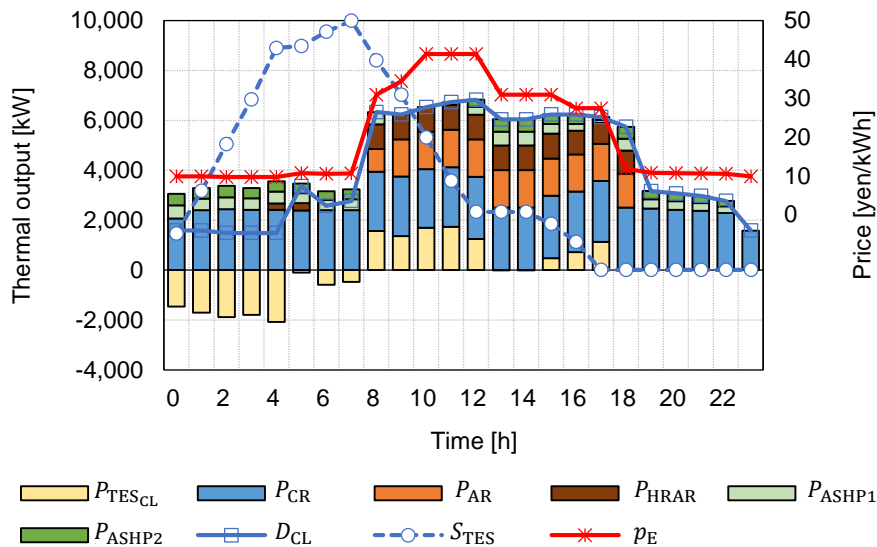
Fig. 3-8 | Optimal operation of HVAC system in Case 3
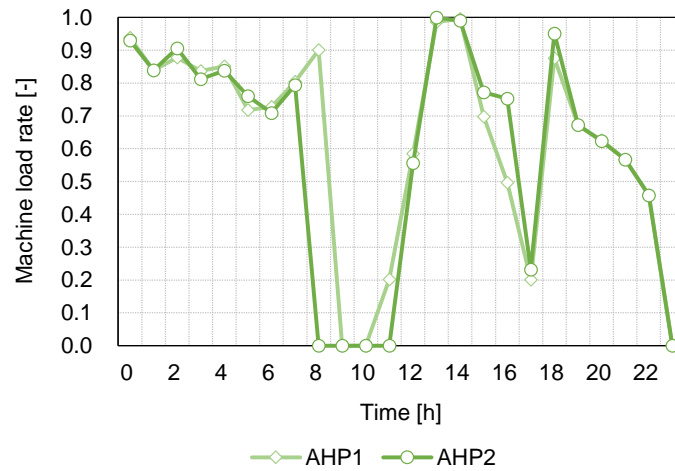
Fig. 3-9 | Optimal operation of ASHP1 and ASHP2 in Case 3 in terms of partial load rate.

3.4.4 Domestic hot water system

Fig. 3-10 shows an optimal operation of the domestic hot water supply system given by εDE in Case 3. In general, an optimal operation of GB and CHP does not depend on the variation in the price of electricity because these two machines are based on gas energy. However, we can find an operating schedule of TES_{hw} similar to the results of the electricity and cooling system. This is because pumps with GB and CHP consumed electricity, although the consumption was lower than that of the other heat source machines. Hence, it is clarified that εDE could recognize the small factor and properly optimize all machines under the nonlinear conditions.
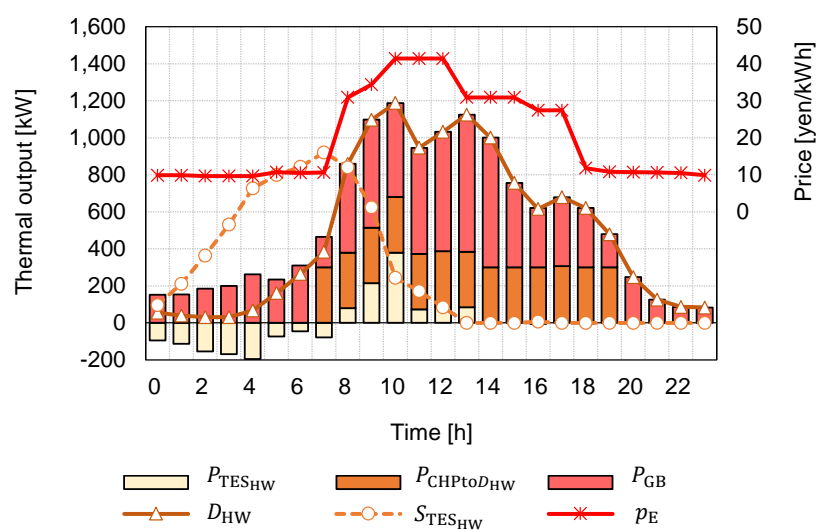
Fig. 3-10 | Optimal operation of domestic hot water system in Case 3.

3.5   Multi-objective optimization using εMODE

3.5.1 Analysis for searching performance of εMODE

In this section, the daily operating costs and primary energy consumption were set as dual objective functions. εMODE can find better solutions for these objective functions simultaneously. Parameters of εMODE are the same as those of single-objective εDE.

To evaluate the ability of εMODE, we focus on the following two factors:

1) Variation in $\varepsilon_{\mathrm{DE}}$ and φ, which is an εDE feature.
2) Variation in the number of individuals of the each NDS rank.

Fig. 3-11(a) shows the variations in the two objective functions, $\varepsilon_{\mathrm{DE}}$ and $\varphi_{\min}$. $f_{\min,\mathrm{oc}}$ indicates the minimum value of operating costs [yen/day] and $f_{\min,\mathrm{pe}}$ indicates the minimum value of primary energy consumption [MJ/day]. These two values decreased drastically during 0 to 500 of the rated number of the generation. After that, these values increased gradually during 500 to 1200 of the generation of $\varepsilon_{\mathrm{DE}}$, while φ decreased. The two objective function values decreased slightly during 1,500 to the last generation. This performance can be explained as follows.

First, there are many infeasible individuals during 0 to 500 generations. Although the minimum value of constraint violation ($\varphi_{\min}$) was not zero, the individuals were optimized in terms of minimizing the objective function values. The infeasible solutions might have an operating schedule in which the amount of charged energy is more than the rated capacity. Thus, the objective value increased as $\varphi_{\min}$ decreased, because the surplus charged energy could not be allowed.

Fig. 3-11(b) shows the variation in the number of individuals in terms of various categories. When all individuals were infeasible ($\varphi_{\min} > 0$), the individuals with φ greater than $\varepsilon_{\mathrm{DE}}$ increased up to approximately 100. After that, the number of individuals decreased slightly until a feasible number of individuals was found. Before the generation reached 4,000, a feasible individual was found and the number of individuals ($\varphi \geq \varepsilon_{\mathrm{DE}}$) rapidly decreased to approximately 10. In contrast, the number of feasible individuals drastically increased up to 190 including the parent and archive groups. After the first number of feasible individuals was found, the number became stable at 160. In terms of NDS ranks, the number of individuals at rank 1, which consisted of a pareto front, increased and was the largest compared to ranks 2 and 3. All parent individuals were in rank 1 because the number of individuals at rank 1 was more than 100. Hence, εMODE could find a feasible number of individuals efficiently and created the pareto front as shown in Fig. 3-12.
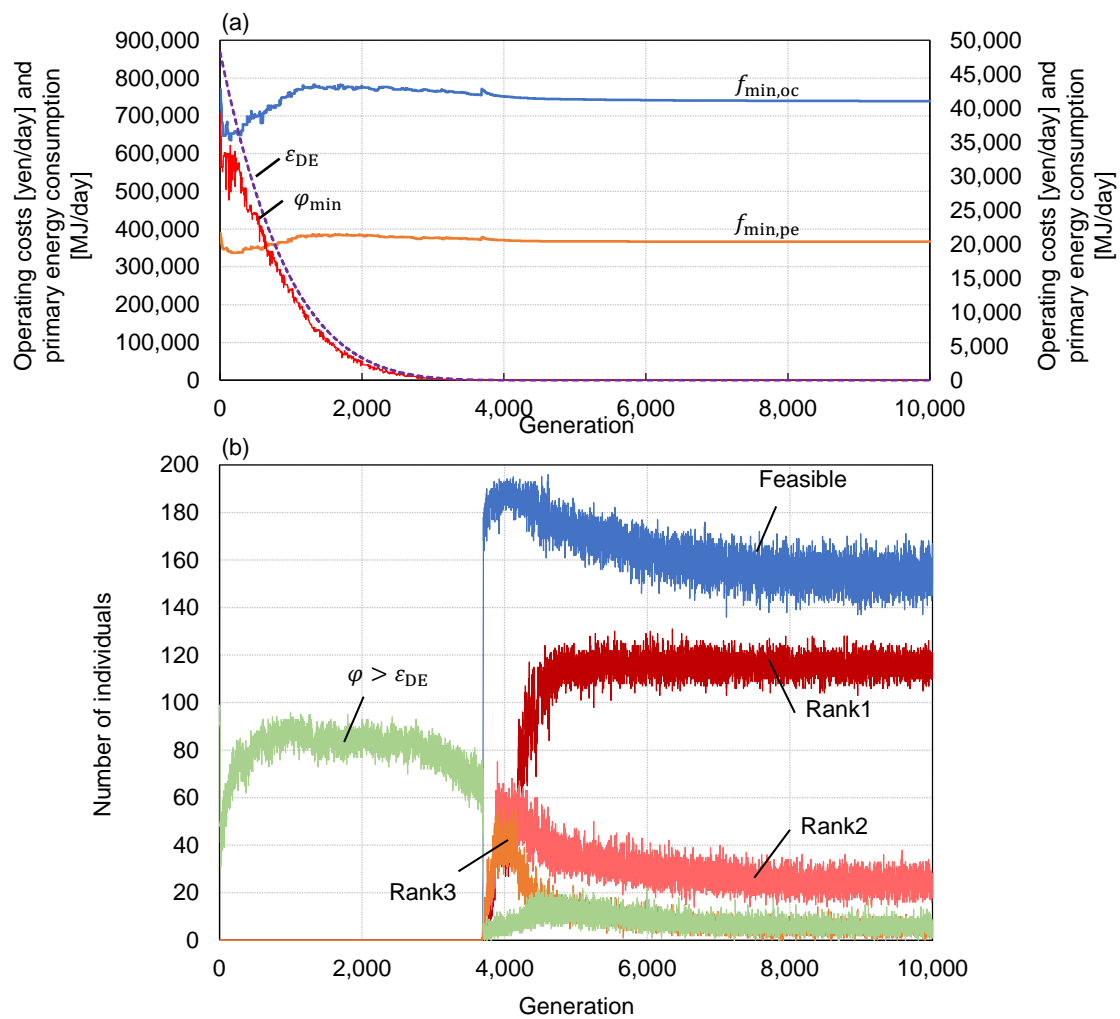
Fig. 3-11 | Performance of εDE.
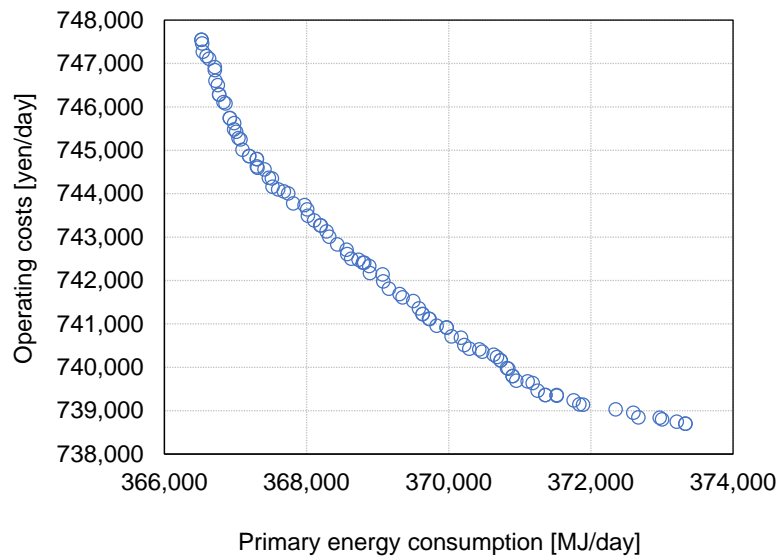
Fig. 3-12 | Pareto-optimal solutions.

3.5.2 Difference of optimal operations in terms of minimizing costs and primary energy consumption

Fig. 3-13(a) and (b) show the optimal operations of CHP to minimize the operating costs and primary energy consumption, respectively. To minimize the operating costs, the electric machines should be operated when the price of purchased electricity is low and the gas-based machines should be operated when the price is high. Fig. 3-13(a) shows the reasonable operation of CHP, while Fig. 3-13(b) shows that CHP was operated during not only the high-price time but also the low-price time, such as 2 a.m., 4 a.m., and 6 p.m. to 8 p.m. In addition, the waste heat of CHP was used for HRAR, which is different from the operation shown in Fig. 3-13(a). The reason for this can be found in the characteristics of GB and HRAR.

The gas consumption of GB at below 20% partial load rate is constant. Hence, the reduction of gas consumption will be zero when GB operates at 0–20% partial load rate. On the other hand, the waste heat utilization from CHP to HRAR ($P_{\text{CHPtoHRAR}}$ [kW]) can reduce 3.5 MJ/kW of energy consumption of HRAR. Hence, the waste heat was provided to HRAR instead of the domestic hot water demand.

In addition, CHP provided the waste heat to HRAR at 7 a.m. It can be thought that this operation maintains the partial load rate of GB at 20%. Fig. 3-14(b) shows the partial load rate of GB maintained at 20% during 0 a.m. to 7 a.m. In fact, GB generates hot water to meet the demand at that time and night, although the partial load rate of GB was lower than 20% because the demand was less than the

75
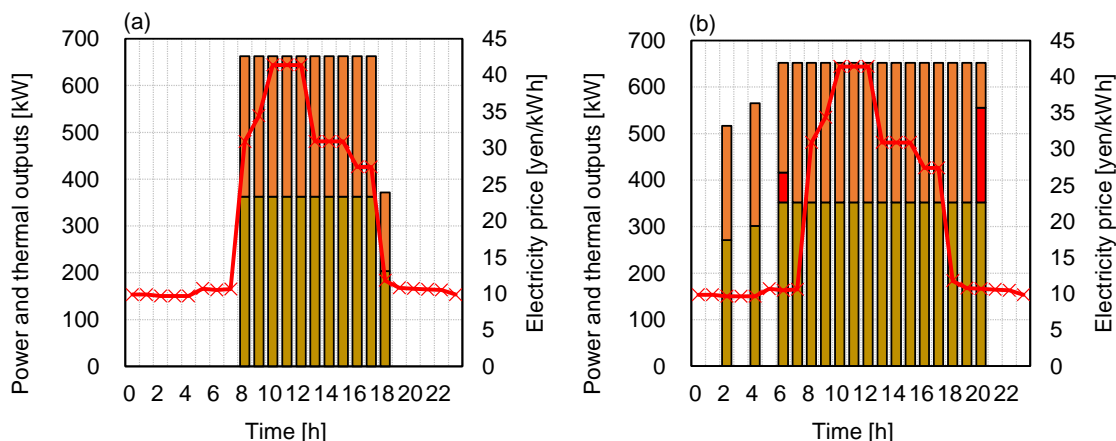
Fig. 3-13 | Optimal operation of CHP: a) the operation to minimize the operating costs, b) the operation to minimize the primary energy consumption.
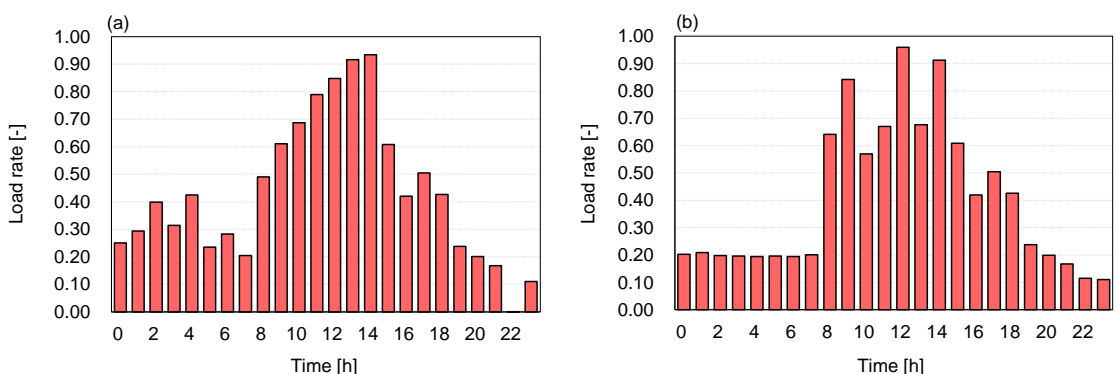
Fig. 3-14 | Optimal operation of GB: a) the operation to minimize the operating costs, b) the operation to minimize the primary energy consumption.

amount of thermal output of 20% partial operations. However, the partial load rate of GB was maintained at 20%. This is because the energy consumption will be reduced by 5.75 MJ/kW when GB's partial load rate increases beyond 20%. In contrast, the waste utilization from CHP to HRAR is 3.5 MJ/kW, as mentioned above. Therefore, it is the most suitable that the waste heat is provided to the hot water supply system instead of HRAR when GB operates at more than 20% partial load rate.

3.6   Conclusion

This chapter shows an efficient constrained optimization method, εDE, to optimize a single-objective optimization to minimize the operating costs of a complex energy system, which comprises electricity, cooling, and hot water supply systems. Although the system was difficult to be solved because of the several storage equipment, εDE could find a reasonable operating schedule of the components. The utilization of εDE could reduce the operating costs by 5.7% against an empirical and a typical operating schedule.

In addition, we proposed εMODE to minimize the operating costs and primary energy consumption simultaneously. εMODE consisted of εDE [167], MODEA [174], and a proposed revised technique, which is a discrete generation model. The generation model was used instead of previous models, such as a continuous generation model, to avoid trapping in a local optimum. As a result, εMODE could create a pareto front that consisted of many individuals and the given optimal operations were reasonable in terms of the machine characteristics.

Therefore, εDE has a high ability to find a quasi-optimal solution for the complex energy system in realistic computation time, and εMODE can be used to find a pareto front in two objective functions. In fact, εMODE algorithm can be quickly extended to three-objective optimization. Hence, εMODE has high adaptability to multi-objective optimization problems.

CHAPTER 4

Proposal of simple index for decision-making optimal operation of electricity system

4.1 Introduction

This chapter focused on electricity and space cooling systems which were consisted of renewable power generators, such as PV, and some storage devices such as TES and RB. As the installation of the PV systems has increased, business models for the sale of electricity generated from PVs have spread globally in recent years. In addition, RB have been gradually installed not only to manage the grid's voltage and frequency, but also to minimize operational costs [176,177]. To achieve the goals, it is important to evaluate the effect of the relationship between the prices of the purchased and the sold electricity, as well as the effect of energy system connections.

However, it is not enough to merely evaluate the difference in the dynamic pricing models. The difference between the purchase and sale prices needs to be considered. Therefore, we conducted a great deal of optimization of the energy system under the various prices to address the results quantitatively. Thus, we applied εDE to three energy systems that had different connections of PVs, RB and HVAC systems, and 126 cases with varying electricity purchase and sale prices were investigated. Moreover, we propose a simple index for decision-making optimal operations of electricity systems. The content of this chapter is referred to my peer-reviewed article published in Sustainable Cities and Society [178].

4.2 Calculation conditions

4.2.1 Description of energy system

The electricity system is consisted of EG, PV, RB, and electricity demand (D_E). The capacity and maximum amount of electric charge to or discharge from the battery is set to 500 kWh and 100 kW, respectively. The charging and discharging efficiency is set to 0.9, so one cycle efficiency is 81%.

The HVAC system is consisted of ASHP, TES, and cooling demand (D_{cl}). RB and EG supply electricity to equipment in HVAC system. The power output of the ASHP depends on the outdoor temperature, with a maximum of 1000 kW. The inlet and outlet water temperature of ASHP were fixed at 12 °C and 7 °C. The amount of chilled water changed to consider the operation at partial load rate.

TES has a capacity of 3,000 kWh. Its charging and discharging efficiency were set to 1.0. Further, the self-loss rate was fixed at 5% per day (0.2% per hour) and respective inlet and outlet water temperature were fixed at 12 °C and 7 °C. Pumps for ASHP and TES can vary the amount of chilled water according to the power output of the ASHP and the amount of charging and discharging thermal energy in TES. We established three energy systems connections to be used as case studies, as illustrated in Fig. 4-1.
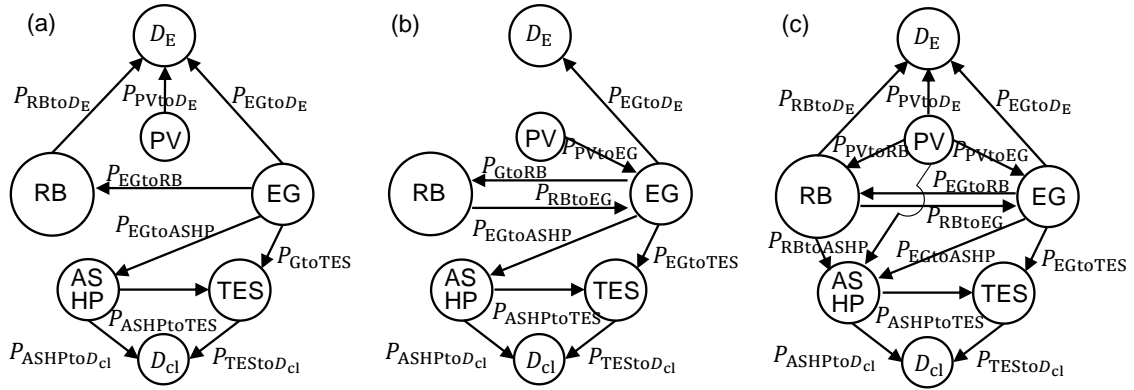
Fig. 4-1 | Three different types of energy system: (a) Case 1 (self-consumption model); (b) Case 2 (total amount purchased model); (c) Case 3 (full connectivity model).

In Case 1, PV power generation and discharged electricity from RB are provided to the electricity demand. The shortage in the provided electricity is compensated by EG. Case 1 indicates a self-consumption model. In Case 2, electricity from these sources is sold to EG. This process is called the full-amount purchase model because all electricity for electricity demand is purchased from EG, and all electricity generated from PV and RB is sold to EG. In Case 3, we established full connectivity as follows: 1) PV-generated power is distributed to the electricity demand, EG, RB, and ASHP. 2) Electricity discharged from RB is also distributed to the electricity demand, EG, and ASHP.

4.2.2 Demand and price profiles

An office building in Tokyo with a total floor area of 16,531.1 m^2 was considered. The load and electricity demand were determined by NewHASP/ACLD [179] and CASCADEIII [170], respectively. The analyzed time horizon and interval were set to 24 hours and 1 hour, respectively on 15th August. The price of purchased electricity in each interval varied according to the dynamic pricing. The price of sold electricity was set to be constant at 26 yen/kWh. These profiles were shown in Fig. 4-2. It is important that we investigate the difference between two optimal operating scenarios: firstly, when the price of purchased electricity is lower than that of sold electricity at 0 a.m. to 7 a.m. and 6 p.m. to 11 p.m.; and secondly, when the price of purchased electricity is higher than that of sold electricity during the day time. The reason for this is that PV generates electric power from 7 a.m. to 5 p.m., resulting in a difference in the purchase and sale price relationship in the two scenarios. We can therefore assume that there are different optimal PV operations for each scenario.
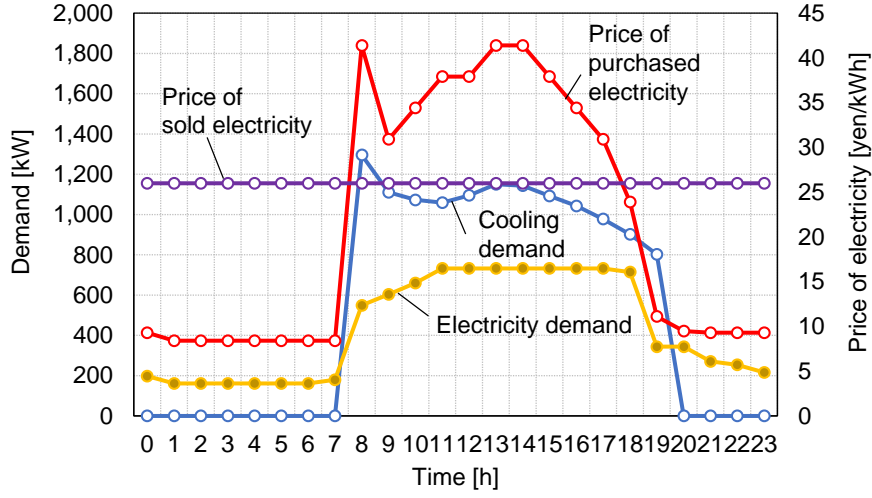
Fig. 4-2 | Demand and price of electricity

4.3 Optimization method

4.3.1 Problem formulation

The aim of the optimization is to minimize operating costs for a 24-hour period as follows:

$$\text{minimize } f = \sum_{t=1}^{N_{\text{th}}} \{p_{\text{E,pd}}^t \left(D_{\text{E}}^t - P_{\text{PVto}D_{\text{E}}}^t - P_{\text{RBto}D_{\text{E}}}^t + c_{\text{E,TES}}^t + c_{\text{E,ASHP}}^t \right)$$

$$- p_{\text{E,sd}}^t (P_{\text{RBtoEG}}^t + P_{\text{PVtoEG}}^t)\} \tag{4-1}$$

and is subject to

$$\begin{cases} 0 \leq \dfrac{C_{\text{RB}}(R_{\text{RB}}^t - R_{\text{RB}}^{t-1})}{\mu_{\text{RB}}} \leq P_{\text{max,RB,d}} & \text{if}(R_{\text{RB}}^t - R_{\text{RB}}^{t-1}) \geq 0 \\ 0 \leq C_{\text{RB}}(R_{\text{RB}}^t - R_{\text{RB}}^{t-1})\mu_{\text{RB}} \leq P_{\text{max,RB,d}} & \text{otherwise} \end{cases} \tag{4-2}$$

$$\begin{cases} P_{\text{PV}}^t \times R_{\text{PVtoRB}}^t \leq \dfrac{C_{\text{RB}}(R_{\text{RB}}^t - R_{\text{RB}}^{t-1})}{\mu_{\text{RB}}} \leq P_{\text{max,RB,c,d}} & \text{if}(R_{\text{RB}}^t - R_{\text{RB}}^{t-1}) \geq 0 \\ P_{\text{PV}}^t \times R_{\text{PVtoRB}}^t & \text{otherwise} \end{cases} \tag{4-3}$$

$$\begin{cases} D_{\text{E}}^t + C_{\text{RB}}(R_{\text{RB}}^t - R_{\text{RB}}^{t-1}) \geq P_{\text{PV}}^t \left(R_{\text{PVtoRB}}^t + R_{\text{PVto}D_{\text{E}}}^t\right) & \text{if}(R_{\text{RB}}^t - R_{\text{RB}}^{t-1}) \geq 0 \\ D_{\text{E}}^t \geq \left|C_{\text{B}}(R_{\text{RB}}^t - R_{\text{RB}}^{t-1})\right| \times R_{\text{RBto}D_{\text{E}}}^t & \text{otherwise} \end{cases} \tag{4-4}$$

$$0 \leq C_{\text{TES}} \left(R_{\text{TES}}^t - R_{\text{TES}}^{t-1}(1 - \tau_{\text{TES}})\right) \leq C_{\text{ASHP}}^t \tag{4-5}$$

$$R_{\text{PVtoEG}}^t = \frac{R_{\text{PVto}D_{\text{E}}}^t}{R_{\text{PVto}D_{\text{E}}}^t + R_{\text{PVtoEG}}^t + R_{\text{PVtoASHP}}^t + R_{\text{PVtoRB}}^t} \tag{4-6}$$

where t denotes the time interval [h], N_{th} represents the time horizon (= 24 h), $p_{\text{E,pd}}^t$ is the price of purchased electricity [yen/kWh], $p_{\text{E,sd}}^t$ indicates the price of sold electricity [yen/kWh], $XtoY^t$, as in RBtoEG, signifies the amount of electricity or cooling heat transferred from device X to device Y [kWh], and C_a represents the capacity of device a. Furthermore, $R_a^t \in [0,1]$ signifies the decision variables of device a, μ_{RB} indicates the battery's charging and discharging efficiency (= 0.9), $P_{\text{max,RB,c,d}}$ is the battery's maximum amount of charging and discharging electricity (=100 kW), D_{E}^t denotes electricity demand [kW], P_{PV}^t represents PV power generation [kW], τ_{TES} is the TES self-loss rate (= 0.05/day), and $R_{XtoY}^t \in [0,1]$ signifies the power distribution rate from device X to device Y. For example, R_{PVtoEG}^t is calculated using Eq. (4-6). Moreover, Eq. (4-2) refers to the constraints concerning the battery's maximum electrical charge and discharge, Eq. (4-3) represents the necessary constraints to balance the amount of energy required to charge the battery and the amount provided from the PV to the battery, Eq. (4-4) is the electricity demand energy balance, and Eq. (4-5) indicates the maximum TES charging and discharging thermal energy. There are 216 decision variables (9 types × 24 hours), and 144 constraints.

4.3.2 Parameters of εDE

The number of generation and individuals were set to 10,000 and 300, respectively. Also, the ε_{DE} were set to zero at 3,000 of the maximum generations.

4.4   Results and discussion

4.4.1 Case 1 (Demand connection)

The performance of the εDE is displayed in Fig. 4-3. Every individual in the first iteration is an infeasible solution. Thus, the minimum value of phi (green solid line) is greater than zero. The first feasible individual (purple solid line) is determined after 1,000 iterations because the minimum value of phi is zero. The number of feasible individuals drastically increases over the next 3,000 iterations.

Finally, the objective function value is 360,183 yen/day. Fig. 4-4(a) indicates that a similar phenomenon occurs with the HVAC system. The charging operation of the TES (negative values denoted by orange bars) occurs when the price of purchased electricity is low, and the discharging

operation (positive values) occurs when it is high. Fig. 4-5(a) shows that RB is charged (negative values depicted by gray bars) when the price of purchased electricity is low and RB is discharged (positive values) when the price is high. Thus, the amount of purchased electricity decreases during the day. All electricity produced from RB discharge and PV power generation is provided to the electricity demand (Fig. 4-5(a) and Fig. 4-6(a)). It can be seen that the operation of the PV and RB changes according to the relation of the purchase and selling prices of the electricity.
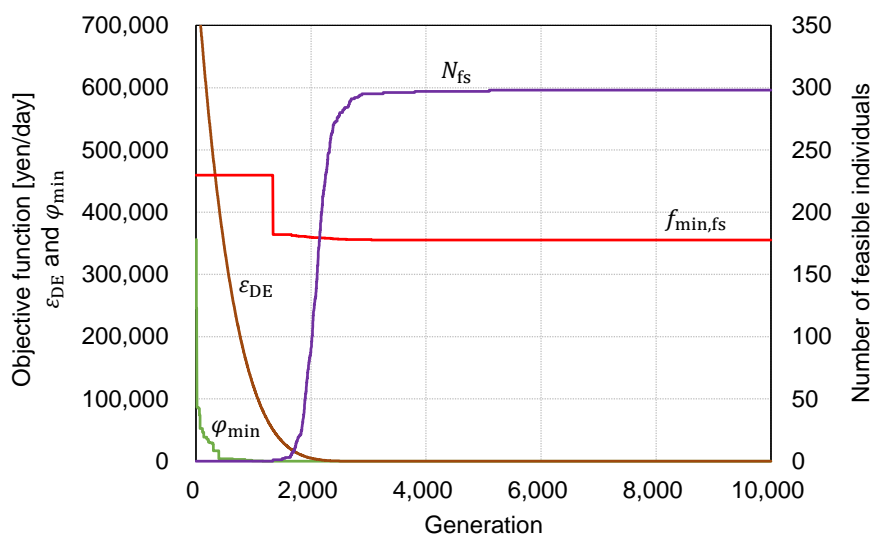
Fig. 4-3 | Performance of εDE in Case 1: N_{fs} denotes the number of feasible individuals, φ_{min} denotes the minimum value of constraint violations. $f_{min,fs}$ denotes the minimum objective function value of feasible individuals.
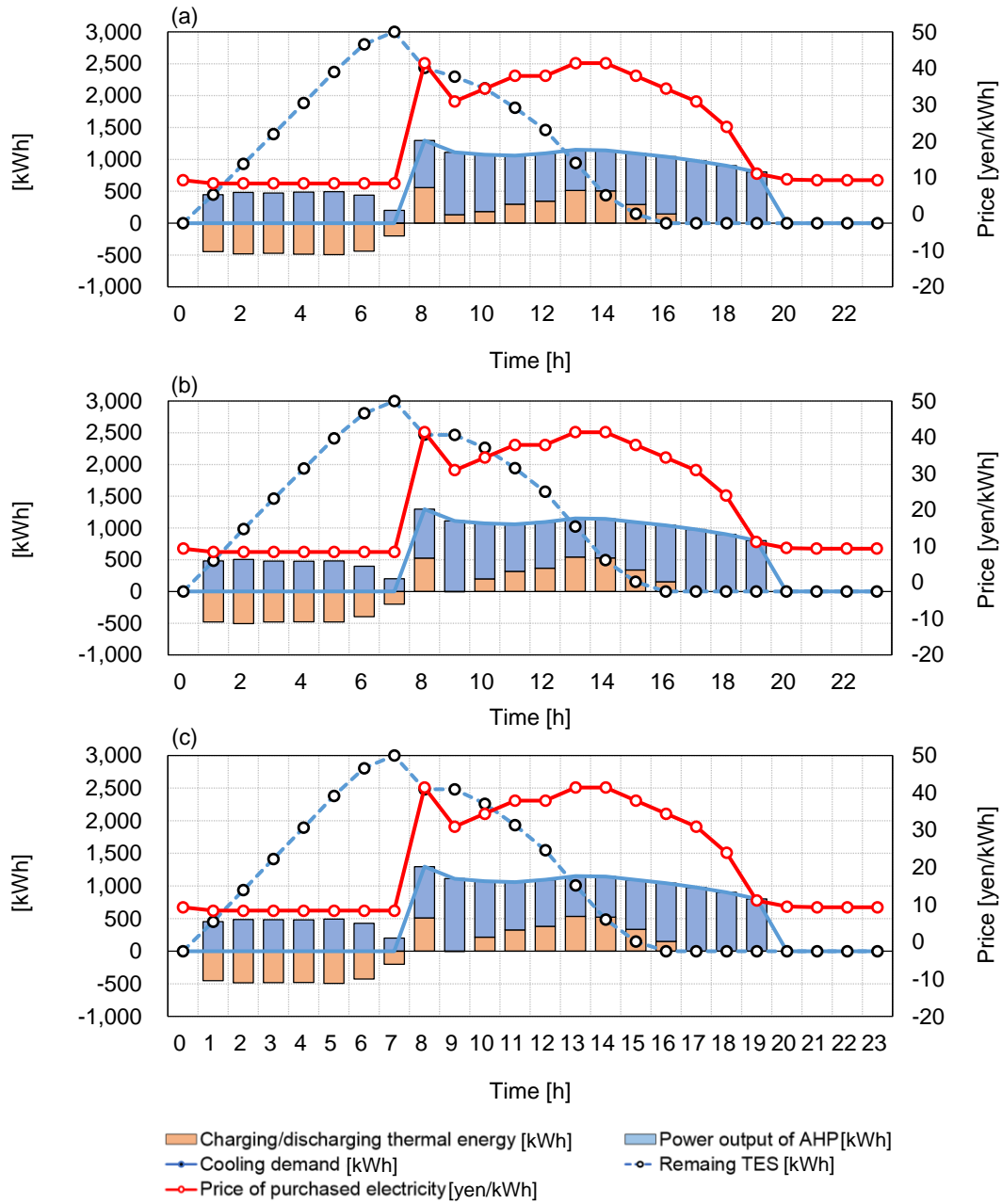
Fig. 4-4 | Optimal operating schedules of HVAC system: (a) Case 1, (b) Case 2, and (c) Case 3.
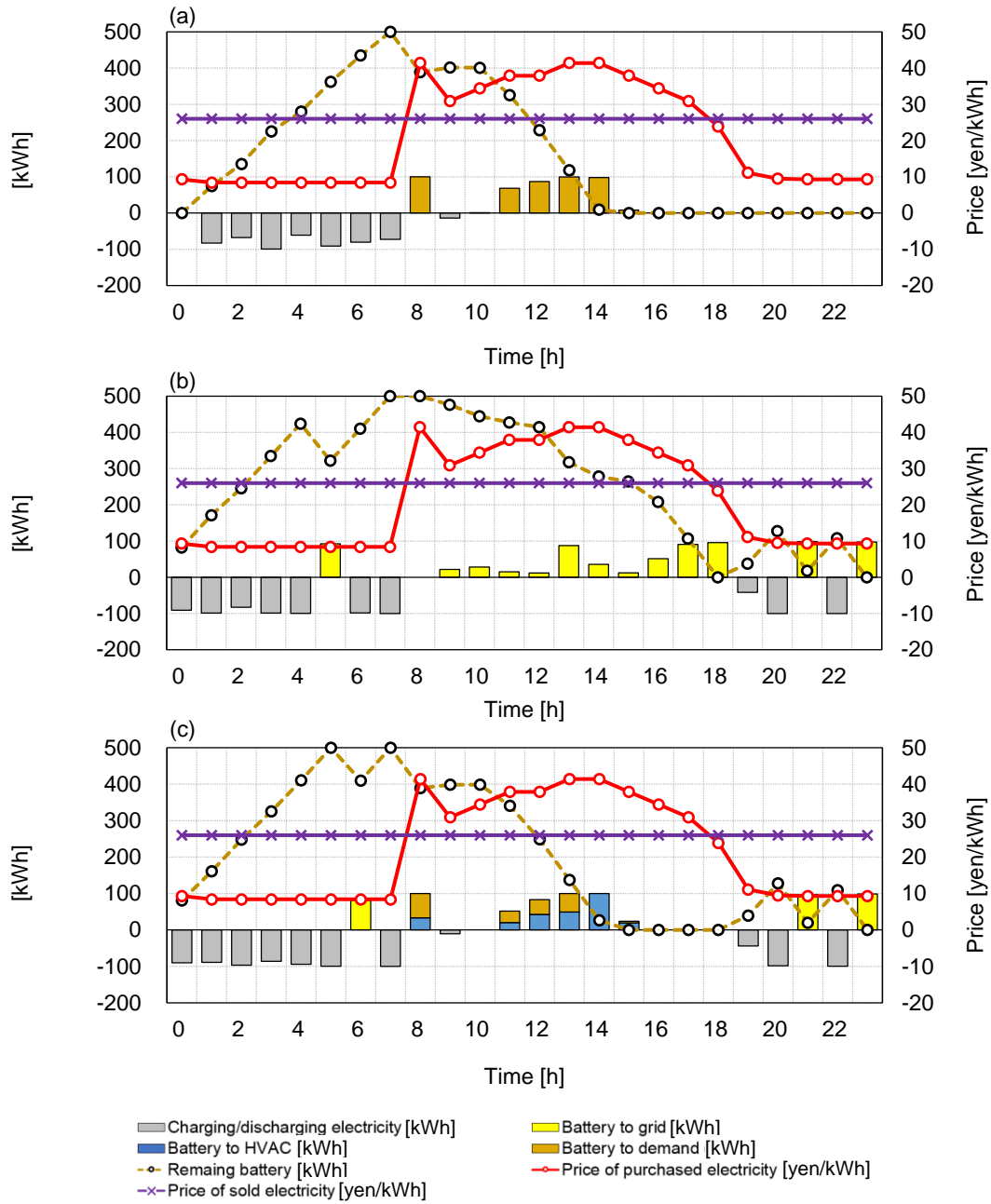
Fig. 4-5 | Optimal operating schedules of the rechargeable battery: (a) Case 1, (b) Case 2, and (c) Case 3.
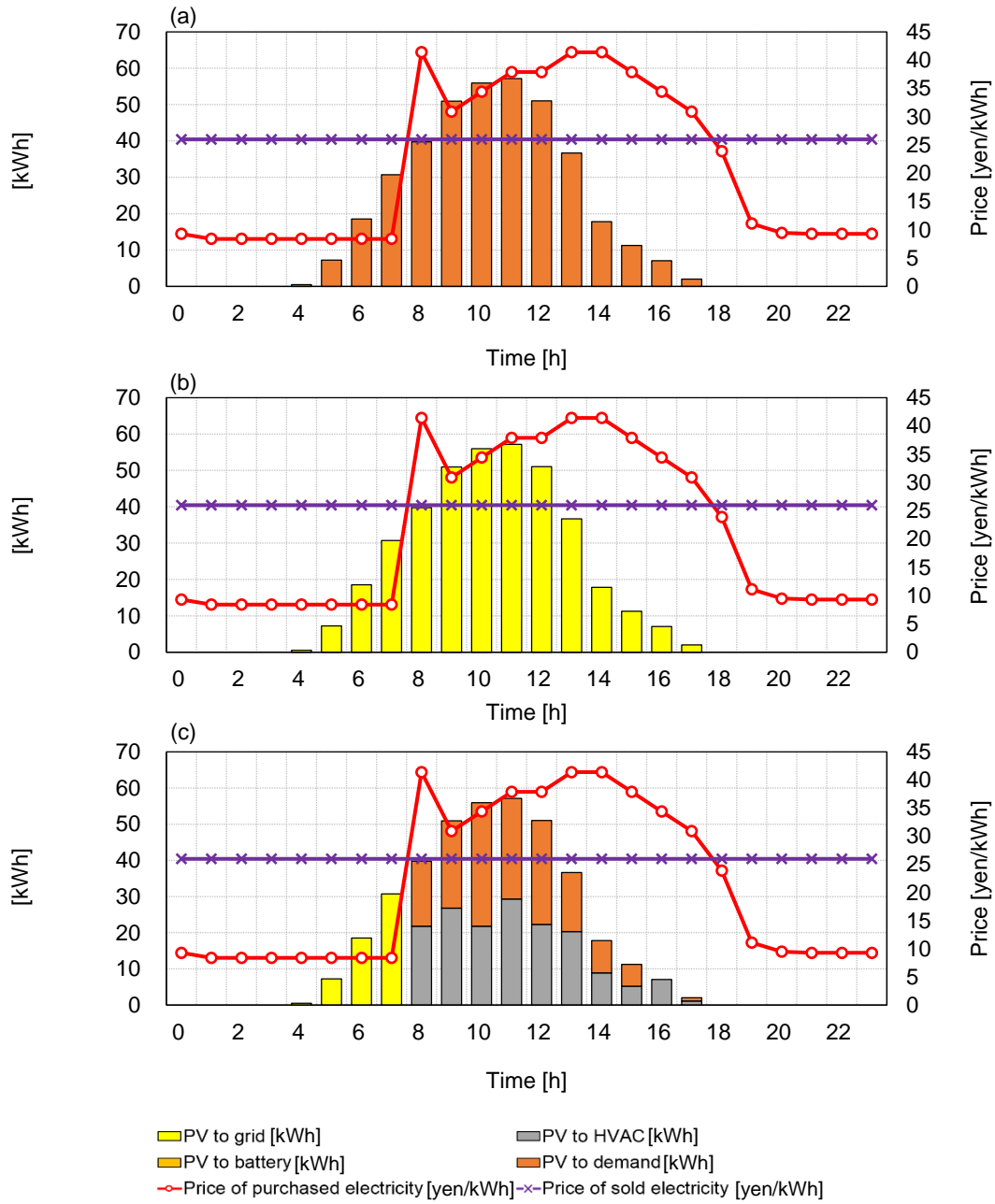
Fig. 4-6 | Optimal power distributions of PV: (a) Case 1, (b) Case 2, and (c) Case 3.

4.4.2 Case 2 (Grid connection)

In Case 2, the objective function value is 365,137 yen/day, which exceeds that of Case 1 (360,183 yen/day). This is because, in Case 2, all electricity produced from RB and PV system is sold to EG as shown in Fig. 4-5(b) and Fig. 4-6(b). We represent the price of purchased electricity using a red line in Fig. 4-4, Fig. 4-5, and Fig. 4-6. This price varies from 8.9 yen/kWh to 41.2 yen/kWh. On the other hand, the price of sold electricity is set to 26 yen/kWh for each time interval. Thus, during the day, electricity provided by RB and PV system should be provided to the electricity system or HVAC system, because the purchase price of electricity is less than the sale price during the night, and greater during the day. Therefore, the result for Case 2 is more than that for Case 1.

4.4.3 Case 3 (Full connection)

The objective function value is 355,258 yen/day, a decrease of 1.4 and 2.7 % from Cases 1 and 2, respectively. The optimal RB operation is shown in Fig. 4-5(c). Electricity is discharged to EG (RBtoEG) at night. Full charging operations are conducted at 8 p.m. and 10 p.m., and full discharging operations are conducted at 9 p.m. and 11 p.m. to gain income from selling electricity. On the other hand, electricity is discharged to electric demand (RBtoD_E) and HVAC devices (RBtoASHP) during the daytime hours. The optimal operation for the distribution of PV power generation is displayed in Fig. 4-6(c).

These results let us determine an operation strategy for the PV system that is similar to that for RB. Distribution from the PV system to RB was not examined because RB efficiency is less than 1.0. The total amounts of electricity discharged from RB and PV power generation during the day are 500 and 329.7 kWh, respectively, and are provided not to EG, but to the electricity demand and HVAC system. Although 216 decision variables were used under the nonlinear condition, we were able to obtain the optimal solution within a short time period (16 minutes). All optimizations were performed using MATLAB R2015a, with the following computer specifications: Windows 8.1 Pro (64bit), 3.40GHz Core i7-4700 CPU, and 32GB RAM.

4.5 Verification of relation between price of purchased and sold electricity

4.5.1 Case study

In Section 4.4, we quantified the dependency of the operating costs on the energy system connection. Results indicate a notable difference between Case 1 (360,183yen/day) and Case 2

(365,137yen/day), which had an additional dependency on the price of purchased and sold electricity. Recently, some countries have implemented a feed-in-tariff to promote the installation of renewable resources such as PV, wind power, and geothermal energy. However, the results of Section 4.4 showed that Case 2, which was modeled as a total amount of purchased system, a typical feed-in-tariff model, depended on both the price of purchased and sold electricity. Thus, the total amount of the purchased system is not suitable for increased installation of renewable resources in the future because the price of feed-in-tariff has gradually decreased. In this situation, we need to optimize the operation or power distribution of each device. Thus, we should determine if it is best to sell the electricity to the power grid, to consume it directly, or to adopt both of these operations. Therefore, we conducted a parametric study on the effect of both prices on the operating costs, and propose a simple index "Area rate of prices (ARP)" to easily determine the quasi-optimal operating schedule over 24 hours.

For the parametric study, the price of sold electricity decreased from 35 to 15 yen/kWh to uncover the influence of the relationship between the electricity purchase and sale price. We examined 42 cases, evenly divided between Case 2 and Case 3, and evaluated the results from two perspectives: 1) the change of the objective function value in terms of electricity sale price, and 2) the reduction rates of the objective function value in two cases based on ARP. In this research, we propose an ARP defined as follows:

$$
\text{ARP} = \frac{\sum_{h=1}^{N_{\text{th,pd}}} (p_{\text{E,pd}}^{h} - p_{\text{E,sd}}^{h})}{\sum_{j=1}^{N_{\text{th,sd}}} (p_{\text{E,sd}}^{j} - p_{\text{E,pd}}^{j})}
\tag{4-11}
$$

where, $N_{\text{th,pd}}$ [h] indicates the length of the time intervals when the price of purchased electricity is higher than that of sold in a 24-hour period. The numerator of Eq. (4-11) is shown as area (a) in Fig. 4-7. $N_{\text{th,sd}}$ [h] indicates the length of the time intervals when the price of purchased electricity is lower than that of sold. The denominator of Eq. (4-11) is shown as area (b) in Fig. 4-7. Thus, we can assume from the results of Case 2 in Section 4.4 that the operating costs gradually become bigger as the ARP value increases. The reason for this is that the increasing ARP value indicates that the price of sold electricity is becoming low. On the other hand, the operating costs of Case 3 increase more slowly than that of Case 2 as the price of sold electricity decreases. This is because the PV and RB systems can distribute power not only to the power grid but also to electricity demand and the HVAC system, including AHP and TES. Further analysis involved conducting the optimization for Case 2 and 3 to evaluate the relation between prices of purchased and sold electricity quantitatively.

However, it is difficult to clarify the relation of both prices with only one demand curve, even if we conduct 42 cases with varying price values. Therefore, we conducted further parametric study by applying a further two types of demand curves. Thus, we finally calculated 126 cases under three

different types of demand curves as shown in Fig. 4-8. The "Original" curve represents the cooling and electricity demand curve in previous section. "Rand01" and "Rand02" indicate new demand curves. These are created using Eq. 4-12.

$$D_{cl}^{t,\text{new}} = D_{cl}^t + 0.1 \times D_{cl}^t \times \mathcal{N}(ave, \sigma) \tag{4-12}$$

where, $D_{cl}^{t,\text{new}}$ indicates a new value of cooling demand at t time interval [kW]. D_{cl}^t indicates an original value of cooling demand [kW]. $\mathcal{N}(ave, \sigma)$ is a random number with normal distribution with a mean of ave and a standard deviation of σ, to 0 and 0.5, respectively.

Fig. 4-9 shows the price of the purchased electricity for three cases using the dynamic pricing model. The price curves of "Rand01" and "Rand02" were obtained using the same calculation method used for the "Original" case. The original case (blue solid line) represents an ordinary day with a typical pricing structure. The "Rand01" price varies sharply due to the peak demand at 8 a.m., while "Rand02" has three peak prices at 8 a.m., 11 a.m. and 1 p.m. Therefore, these cases represent a number of assumed cases in one year.
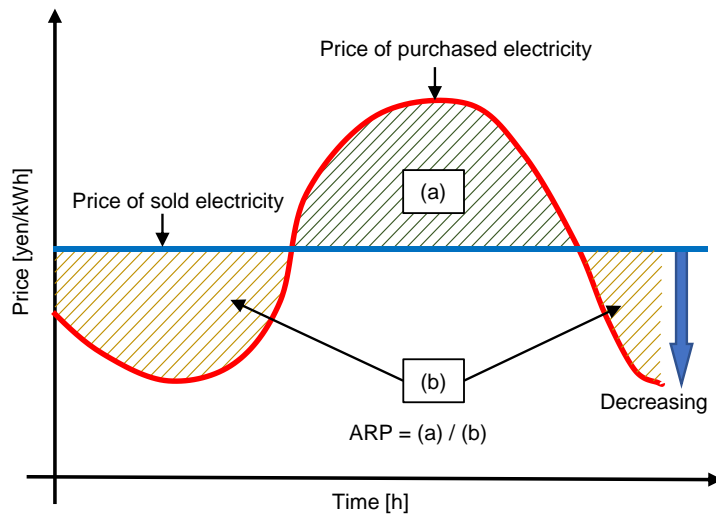
Fig. 4-7 | Conceptual diagram of definition of ARP.
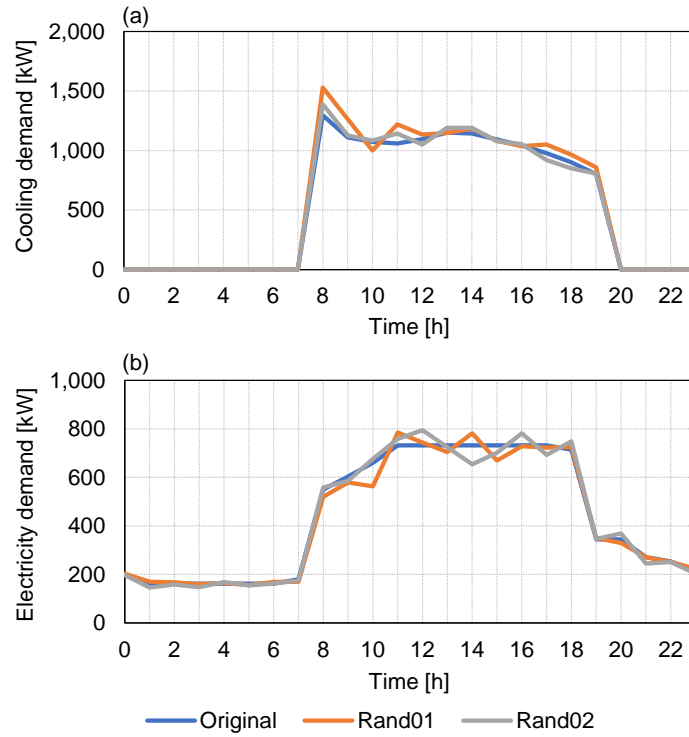
Fig. 4-8 | Three types of demand curve: (a) cooling demand, (b) electricity demand.
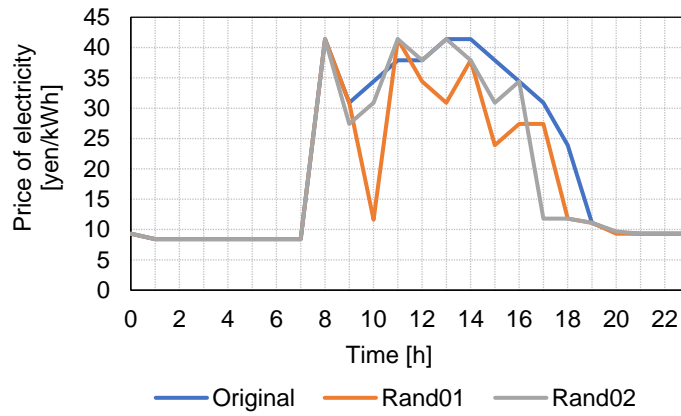
Fig. 4-9 | Three types of purchased electricity price.

4.5.2 Results of original data

In Fig. 4-10, the vertical and horizontal axes indicate operating costs and the price of sold electricity, respectively. In Case 2, the operating costs increased linearly from 355,048 to 377,691 yen/day (6.4%) as the sale price of electricity decreased from 35 to 15 yen/kWh. The reason was that the total income obtained selling electricity to the grid decreased with the decreasing sale price. On the other hand, the operating costs in Case 3, increased by less than 1.5%, from 353,700 to 359,088 yen/day. However, there was greater dispersion amongst the Case 3 results, as shown in Fig. 4-10. Finally, the difference in the operational costs of Cases 2 and 3 was 5.2% when the price of the sold electricity was 15 yen/kWh. In addition, although the price of sold electricity drastically decreased, the operating costs in Case 3 are lower than that of Case 1 (360,183 yen/day).

In Fig. 4-11, the vertical and horizontal axes indicate operating costs and the value of ARP, respectively. The blue and red markers represent the Case 2 and Case 3 results, respectively, with each set comprising 21 data points. The green markers represent the reduction rate of Case 3 against Case 2. The area of the purchased electricity price increases as the value of ARP increases. Case 2 showed a logarithmic increase, in contrast to the linear shape shown in Fig. 4-10. This is attributed to the nonlinear configurations of both the purchased and sold electricity. In the ARP range of zero to one, the operating costs increased sharply. An ARP value of one indicates that both areas of the two prices are equal. Thus, the power selling income of Case 2 decreases as the value of ARP increases.

In Case 3, the rate of increase was lower than that of Case 2, even when the price of sold electricity was low. The reason for this is that the Case 3 energy system can distribute electric power not only to EG, but also to the HVAC and TES systems. It can be assumed that the operating costs of Case 3 will finally increase up to the optimal solution of Case 1 when the price of sold electricity is low. The reduction rates were 3.5 and 5.0% at ARP values of 1 and 3, respectively. Moreover, when the ARP value is less than 0.2, the operating costs of Case 2 are lower than those of Case 1, which is a self-consumption model. When the ARP value was the smallest (= 0.078), the operating costs of Case 2 were lower than those of Case 1 by 1.45%. On the other hand, at ARP values greater than 0.2, this result was reversed. When the ARP value was the highest (=2.90), the operating costs of Case 1 were lower than those of Case 2 by 4.64%.
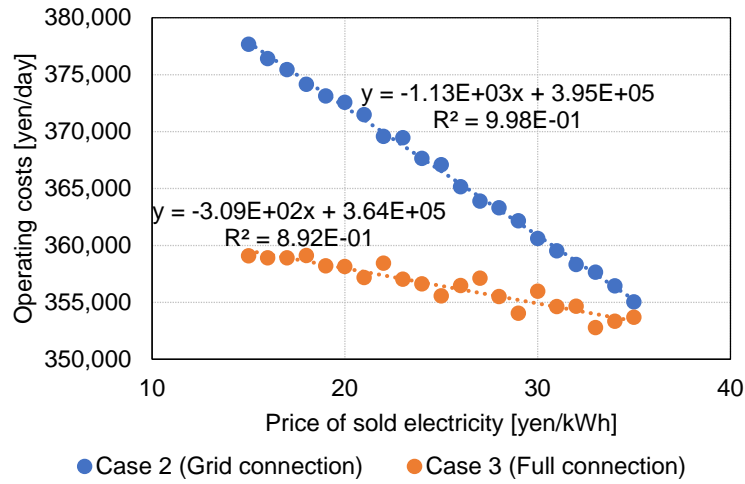
Fig. 4-10 | Results of each price of sold electricity.
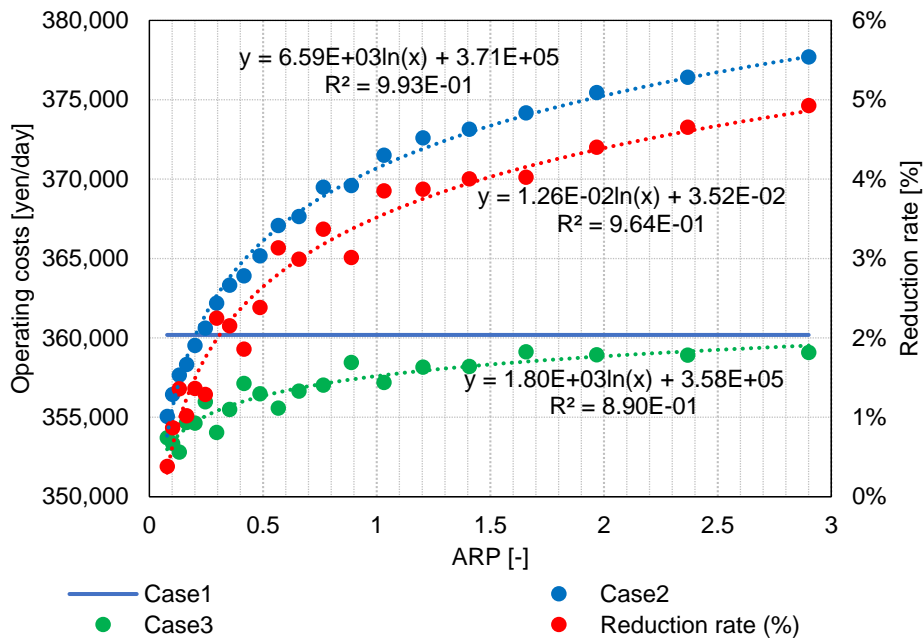
Fig. 4-11 | Comparison of results in terms of ARP (Original).

4.5.3 Results of various types of demand curve

The results of Case 2 and Case 3 for demand curves "Rand01" and "Rand02" are shown in Fig. 4-12 and Fig. 4-13, respectively. Each result showed that the increase in operating costs of Case 2 was faster than that of Case 3, as per the results of the original case. However, the reduction rates of "Rand01" and "Rand02" increase faster than that of the original case. In terms of comparison between Case 1 (blue solid line) and Case 2, the results of "Rand01" and "Rand02" showed that the operating costs of Case 2 were lower than that of Case 1 when the ARP value was less than 0.2. In "Rand01," when the ARP value was the smallest (= 0.037), the operating costs of Case 2 were lower than those of Case 1 by 1.7%. In "Rand02," at the smallest value of ARP (= 0.062), those of Case 2 were lower than those of Case 1 by 2.6%

On the other hand, when the ARP value was greater than 0.2, Case 1 showed better results than Case 2, as per the original case. Thus, the priority of each operation strategy is the same for various types of demand curve. Therefore, the operators of an energy system in a certain building can easily determine the operating schedule simply by calculating the ARP value if they do not have the time or equipment to obtain the optimal solution. Moreover, in terms of comparison between Case 1 and Case 3, the Case 3 results did not exceed the optimal result of Case 1. For example, in "Rand01", the optimal solution of Case 1 is 295,070 yen/day and that of Case 3, when the price of sold electricity is the lowest (ARP of 1.89), is 293,791 yen/day. In "Rand02", the former is 320,450 yen/day and the latter is 319,269 yen/day. Although it was necessary to conduct detailed calculations for Case 3 due to the large number of distribution routes, εDE was able to obtain the optimal solution in all 126 cases. Therefore, this optimization method can be applied to complex nonlinear problem such as practical energy systems.
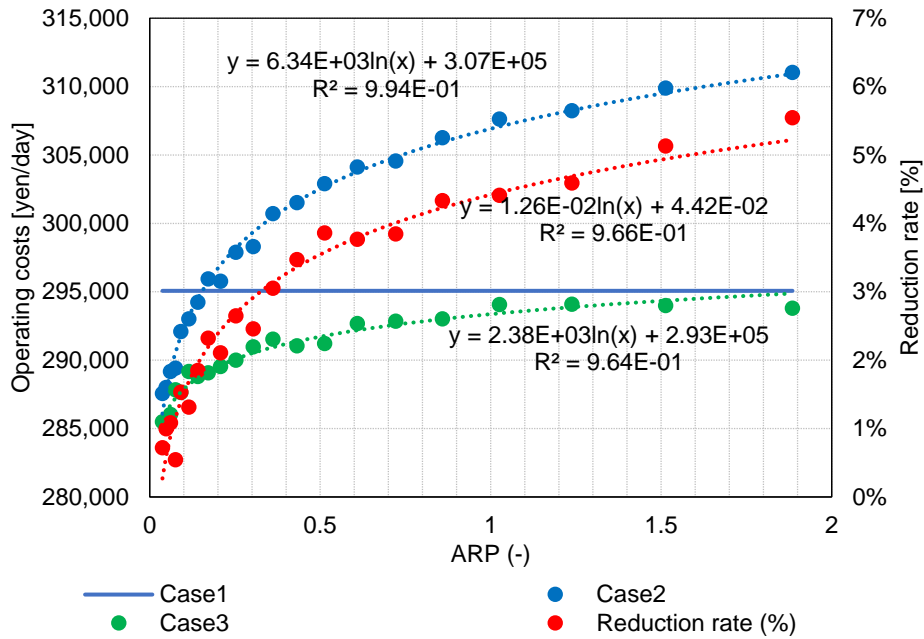
Fig. 4-12 | Comparison of results in terms of ARP (Rand01).
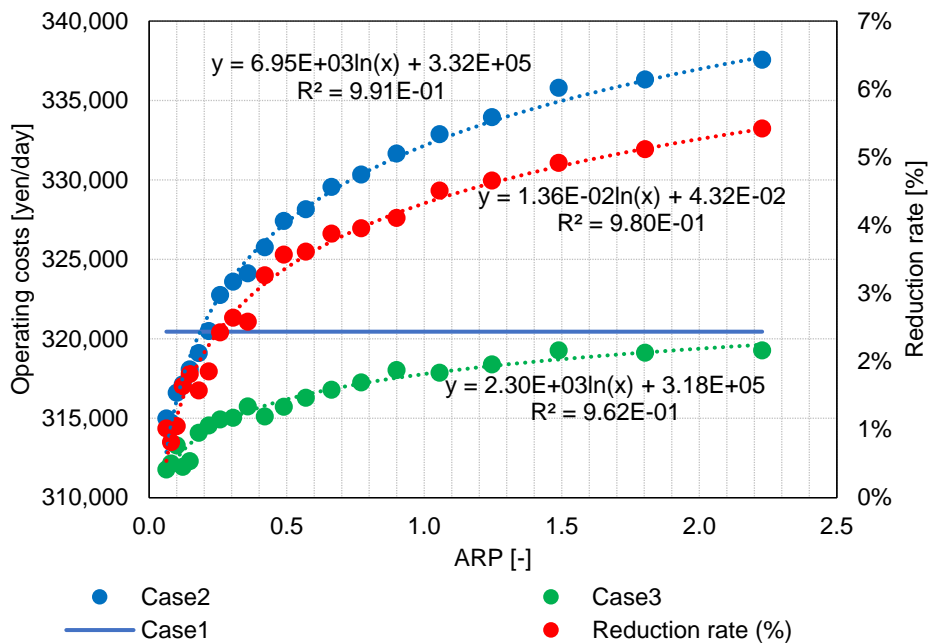
Fig. 4-13 | Comparison of results in terms of ARP (Rand02).

4.6   Conclusion

In this chapter, we optimized energy systems that include RB and TES systems. Moreover, we clarified the effect of energy system connections and of the price of purchased and sold electricity. Firstly, we demonstrated the ability of the εDE to efficiently determine an optimal solution under the nonlinear condition, and we detailed its performance. Secondly, we confirmed that the total amount of a purchased system does not always minimize the operating cost and that it depends on the relation between the prices of purchased and sold electricity.

In addition, we proposed a simple index "ARP" as a value of comparison between the prices of purchased and sold electricity in order to validate the relation between the two prices. We compared the results of Case 1 (self-consumption model) and Case 2 (total amount of a purchased model) The results showed that Case 2 was superior to Case 1 up to an ARP value of 0.2. On the other hand, Case 1 was superior to Case 2 when the value of ARP was greater than 0.2. Additionally, we conducted the same simulation under two different demand profiles: Rand01 and Rand02 in order to confirm the results. Finally, 126 cases were tested and the priority of operating strategies of Case 1 and Case 2 changed at an ARP value 0.2. Thus, we can conclude that the ARP method is a suitable method for easily determining the most efficient operating strategy.

Therefore, we can conduct the optimization on everyday practical situations because εDE requires low computational cost. Even if the operators cannot conduct the optimization in practical energy management, they can easily determine the operation strategy by calculation of the ARP value. Therefore, the εDE and ARP methods have substantial advantages for energy system optimization.

CHAPTER 5

Proposal of re-optimization framework for uncertainty of demand and PV power generation

5.1　Introduction

This chapter describes an efficient recalculation strategy for handling uncertainty. Although there are some real-time optimization methods for short time horizons mentioned in Section 1.2.3, they are not capable of recalculating operating schedules which includes long time-dependent equipment such as TES and RB. When the operating schedule of the time-dependent equipment is revised, it has to be significantly considered to avoid energy shortage or excessive amount of heat. Thus, an efficient recalculation strategy for handling uncertainty and detailed calculations is needed to maintain the optimal energy balance.

A simple and effective method to recalculate operating schedules of all time steps at every time interval is called the "all-time steps recalculation strategy" (AtsR) in this thesis. The AtsR can be thought of as an ideal optimization strategy, but it requires large amounts of computation time. Thus, it cannot be easily applied to actual energy management systems, which require quick recalculations of the operating schedules when unpredicted demand changes occur. In this chapter, we propose a new recalculation strategy that is called the "two-time steps recalculation strategy" (TtsR). The TtsR aims to recalculate operating schedules in two-time steps, namely, when the changes occur and while fixing the results for the amounts of remaining battery power and TES effects; these later issues are treated as constraints. We compared TtsR and AtsR procedures and results to clarify the effectiveness of the new TtsR. The contents of this chapter is referred to my peer-reviewed article published in Energy and Buildings [180].

5.2　Calculation conditions

5.2.1 Description of energy system

We considered an energy system consisting of RB, PV device, power conditioner, two centrifugal refrigerators (CR1 and CR2), three air-source heat pumps (ASHP1, ASHP2, and ASHP3), and TES for cooling; a schematic of the system is shown in Fig. 5-1. Further data for each component are shown in Table 5-1.

The PV device and RB were key components of the electricity system. The area of the PV panels and conversion rate were set to 1,000 m^2 and 13%, respectively. Power from the PV devices was distributed to RB, to equipment with an electricity demand, and to EG simultaneously at each time step. The capacity and maximum amount of charging or discharging of RB were set to 1,500 kWh and 300 kW, respectively. RB was charged with electricity from the PV device or EG, and it discharged power to meet the electricity demand or to EG as well.

The capacity of the TES was 10,000 kWh, which met approximately 15% of the total amount of cooling demand for the day. The charging or discharging efficiency was 100%, and the self-heat loss rate was set to 0.2%/h. Heat source equipment consisted of the five aforementioned devices. The rated capacities of CR1 and CR2 were set to 2,000 kW and 1,500 kW, respectively; those of ASHP1, ASHP2, and ASHP3 were set to 1,200 kW, 1,000 kW, and 600 kW, respectively. To simplify the problem, the inlet and outlet temperatures of chilled water for each heat source were fixed to 7 ℃ and 12 ℃, respectively. In reality, the temperature of chilled water varies in accordance with the power output of the heat source machine in partial load operations. In calculations for the cooling tower, when the difference between the inlet and outlet cooling water temperatures was larger than 3 ℃, the amount of cooling water was set to the rated amount and water temperatures varied according to variations in the CR's power output. In contrast, when the difference was less than 3 ℃, the amount of cooling water was reduced to keep the difference at 3 ℃. The cooling water temperature was allowed to be influenced by outdoor conditions and heat source power outputs.
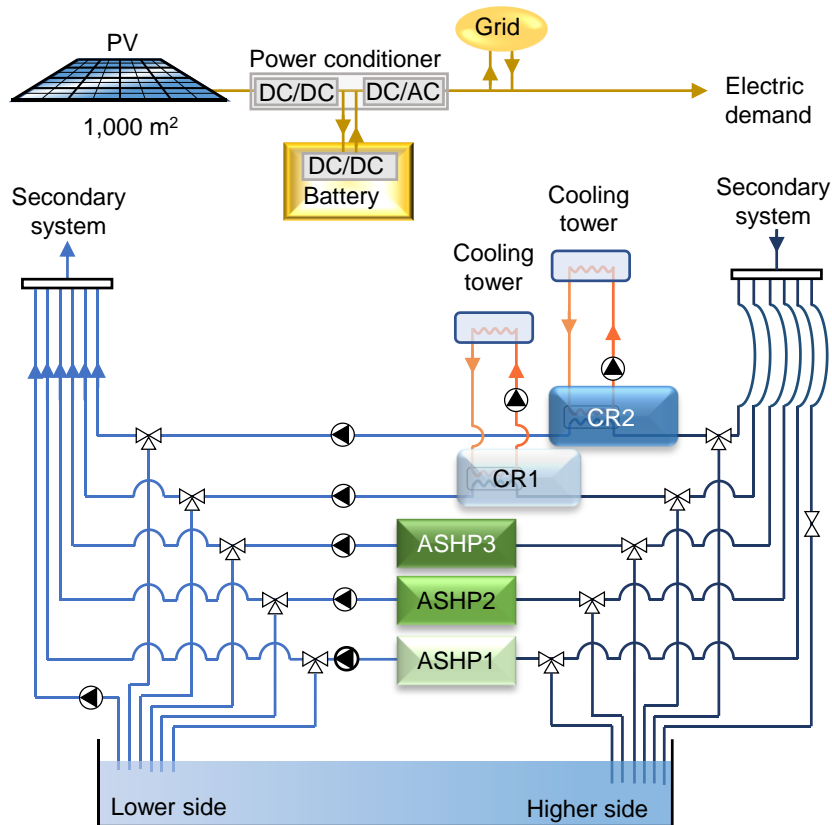
Fig. 5-1 | Schematic of the energy system.

Table 5-1 | Rated specifications of system components.

PV	Area	1000	m²
	Conversion efficiency	13	%
	Power conditioner efficiency	97	%
Battery	Capacity	1500	kWh
	Maximum charging/discharging	300	kW
	Self-discharge rate	0	%
	Efficiency	72	%/cycle
TES	Capacity	10,000	kWh
	Maximum charging/discharging	3000	kW
	Self-heat loss rate	0.2	%/h
	Efficiency	100	%/cycle
CR1–2	Capacity	2000;1500	kW
	COP based on primary energy	2.04	
ASHP1–3	Capacity	1200; 1000; 600	kW
	COP based on primary energy	1.30	

5.2.2 Demand profile and electricity price

An office building in Tokyo with a total floor space of 20,000 m² is considered. The time horizon and sampling interval were set to 24 h and 1 h, respectively. Electricity demand was determined by using CASCADE III [170]. The analyzed day represented a typical day in August. The price of purchased electricity in each time interval was set to vary with the total hourly predicted electricity consumption. Electricity and cooling demands, and the sold and purchased price of electricity, are shown in Fig. 5-2. In this chapter, these demand curves were set as predicted demands. When we considered unpredicted changes in the demand and solar radiation, we applied uniformly distributed random numbers to these demands to create new values for them.
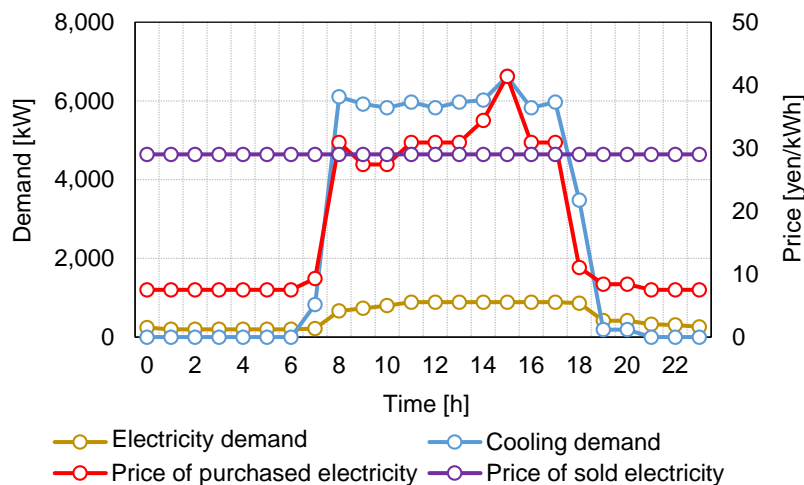
Fig. 5-2 | Electricity and cooling demands, and electricity prices.

5.3   Optimization method

5.3.1 Problem formulation

In this chapter, the aim of the optimization was to minimize the operating costs for a 24-h operation period, and this was accomplished with the following equations:

$$
\text{minimize } f = \sum_{t=1}^{N_{\text{th}}} \{ p_{E,pd}^t \left(D_E^t - P_{PVtoD_E}^t - P_{RBtoD_E}^t + c_{E,TES}^t + c_{E,ASHP1}^t + c_{E,ASHP2}^t \right.
$$
$$
\left. + c_{E,ASHP3}^t + c_{E,CR1}^t + c_{E,CR2}^t \right) - p_{E,sd}^t \left(P_{RBtoEG}^t + P_{PVtoEG}^t \right) \}
\tag{5-1}
$$

and subject to

$$
\begin{cases}
0 \leq \dfrac{C_{RB}(R_{RB}^t - R_{RB}^{t-1})}{\mu_{RB}} \leq P_{\text{max,RB,d}} & \text{if}(R_{RB}^t - R_{RB}^{t-1}) \geq 0 \\
0 \leq C_{RB}(R_{RB}^t - R_{RB}^{t-1})\mu_{RB} \leq P_{\text{max,RB,d}} & \text{otherwise}
\end{cases}
\tag{5-2}
$$

$$
\begin{cases}
P_{PV}^t \times R_{PVtoRB}^t \leq \dfrac{C_{RB}(R_{RB}^t - R_{RB}^{t-1})}{\mu_{RB}} \leq P_{\text{max,RB,c,d}} & \text{if}(R_{RB}^t - R_{RB}^{t-1}) \geq 0 \\
P_{PV}^t \times R_{PVtoRB}^t & \text{otherwise}
\end{cases}
\tag{5-3}
$$

$$
\begin{cases}
D_E^t + C_B(R_{RB}^t - R_{RB}^{t-1}) \geq P_{PV}^t \left(R_{PVtoRB}^t + R_{PVtoD_E}^t \right) & \text{if}(R_{RB}^t - R_{RB}^{t-1}) \geq 0 \\
D_E^t \geq \left| C_B(R_{RB}^t - R_{RB}^{t-1}) \right| \times R_{BtoD_E}^t & \text{otherwise}
\end{cases}
\tag{5-4}
$$

$$
0 \leq C_{TES}\left(R_{TES}^t - R_{TES}^{t-1}(1 - \tau_{TES}) \right) \leq C_{CR1}^t + C_{CR2}^t + C_{ASHP1}^t + C_{ASHP2}^t + C_{ASHP3}^t
\tag{5-5}
$$

$$
D_{cl}^t + P_{TES,c}^t - \left(P_{TES,d}^t + P_{CR2}^t + P_{ASHP1}^t + P_{ASHP2}^t + P_{ASHP3}^t \right) \leq C_{CR1}
\tag{5-6}
$$

Others include

$$
R_{PVtoEG}^t = \frac{R_{PVtoD_E}^t}{R_{PVtoD_E}^t + R_{PVtoEG}^t + R_{PVtoRB}^t}
\tag{5-7}
$$

where t denotes the time step [h], N_{th} represents the time horizon [24 h], $p_{E,pd}^t$ is the price of purchased electricity (yen/kWh), $p_{E,sd}^t$ indicates the price of sold electricity [yen/kWh], P_{XtoY}^t is the power generation and thermal output [kW] from device X to device Y. C_a represents the capacity of device a. Furthermore, $R_a^t \in [0,1]$ signifies the decision variables of device a, μ_{RB} indicates the RB's charging and discharging efficiency (= 0.9), $P_{\text{max,RB,c,d}}$ is the RB's maximum amount of charging and discharging electricity (= 300 kW), D_E^t and D_{cl}^t denote the electric and cooling demand

[kW], respectively. τ_{TES} is the TES self-loss rate (= 0.02/h). R_{PVtoEG}^{t} was calculated by using Eq. (5-7). In Eq. (5-6), $P_{\text{TES,c}}^{t}$ and $P_{\text{TES,d}}^{t}$ indicate the amount of charging or discharging energy of the TES. This value can be obtained by the difference between the amount of remaining battery power at t and $t-1$ time steps. Moreover, Eq. (5-2) refers to the constraints concerning the RB's maximum amount of charging and discharging electricity, Eq. (5-3) represents the constraints needed to balance the amount of energy required to charge RB and the amount provided from the PV device to RB, Eq. (5-4) is the energy balance of the electricity demand, and Eq. (5-5) indicates the maximum amount of TES storing and releasing thermal energy. In this study, the number of decision variables was 240 (10 types $\times$ 24 hours), and the number of constraints was 168.

5.3.2 Decision variables

The decision variables consisted of the following 10 factors: 1) rate of remaining battery, 2) distribution rate of RBtoEG, 3) distribution rate of PVtoEG, 4) distribution rate of PVtoRB, 5) distribution rate of PVtoD_{E}, 6) rate of remaining TES, 7) machine load rate of CR2, 8) machine load rate of ASHP1, 9) machine load rate of ASHP2, and 10) machine load rate of ASHP3. The first variable indicates the remaining energy within RB, and the second variable was used to determine the power output of RBtoEG and RBtoD_{E}. The third to fifth variables were used to determine the power output of each of the PV routes with Eq. (5-7). The sixth variable indicates the remaining TES power [kWh]. The seventh to tenth variables represent the partial load rate of the four pieces of heat source equipment; note that CR1 was excluded here. The power output of CR1 was determined by using the left-hand side of Eq. (5-6).

5.3.3 Parameter of εDE

The number of individuals and generations were set to 100 and 5,000, respectively. The mutation rate and the crossover rate were set to 0.5 and 0.9, respectively.

5.4   Proposal of a new methodology for assessing the uncertainty of renewable energy sources and demand changes

5.4.1 All time steps recalculation strategy (AtsR)

Unpredicted changes in power generation from PV devices can occur when outdoor conditions change; moreover, unpredicted changes in the electricity or cooling demand can be caused by changes in occupant behaviors. When those changes occur, a rescheduling of operations is needed to minimize the operating costs. To minimize the objective function value, the best strategy is to recalculate for all time steps under the changed conditions, as shown in Fig. 5-3. The horizontal axis indicates the recalculated time horizon, and the vertical axis indicates the time of recalculation. For example, three-time intervals (9, 10, 11 p.m.) were recalculated at 9 p.m. Generally, long computation times are required to optimize a complex nonlinear problem with mathematical techniques. However, εDE can be used to obtain the quasi-optimal solution stochastically over short computation times. Thus, εDE was applied to the AtsR strategy.

5.4.2 Two time steps recalculation strategy (TtsR)

AtsR yields an accurate quasi-optimal solution because this strategy recalculates at every time step. However, this requires long computation times, especially for former calculation times that are associated with long time horizon recalculations. Thus, this technique is not always practical to use with actual systems. Here, we propose a new recalculation strategy, that is, TtsR. We recalculated the operating schedules to match the energy balance during two hours for the current time interval (t) and the next time interval ($t + 1$) as shown in Fig. 5-4.
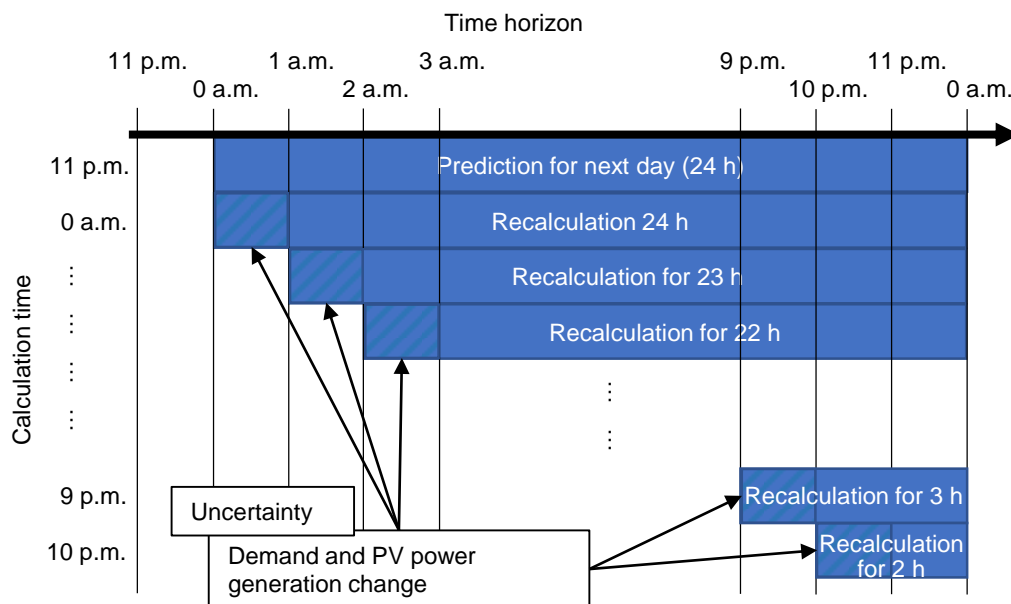
Fig. 5-3 | Recalculation concept of AtsR.
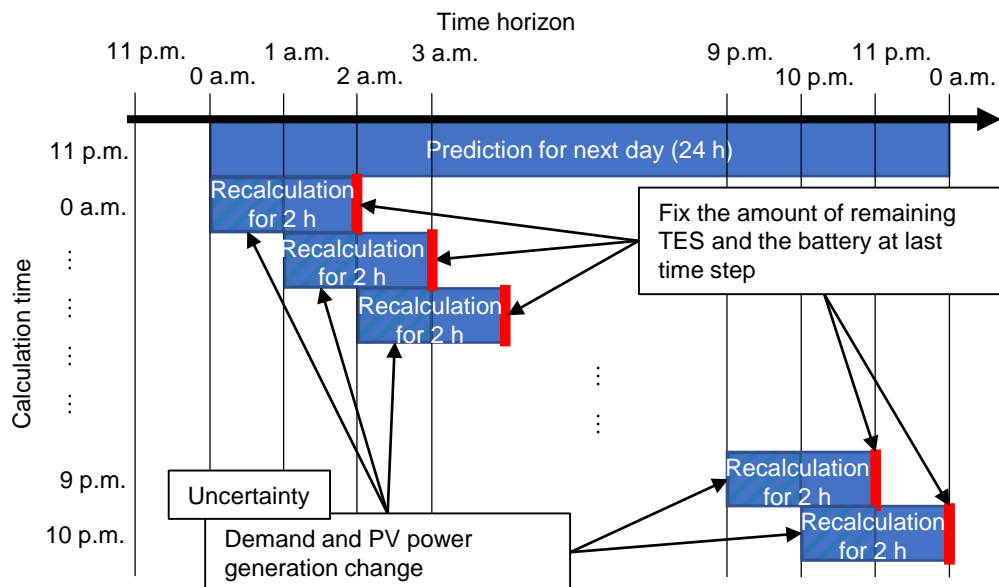
Fig. 5-4 | Recalculation concept of TtsR.

Fig. 5-5 shows a flow chart of the TtsR algorithm. In the prediction phase, we obtained each type of demand and outdoor condition as shown in Fig. 5-2 by using thermal load calculations and weather forecast data. Secondly, the amount of power generation from the PV device was calculated by using solar radiation data. Then, εDE was used to optimize the operating schedules of each decision variable in a manner that minimized the total operating costs for 24 hours. Next, initialization and time step updates were conducted. In modeling the uncertainty, i.e., changes in the cooling demand, electricity demand, and power generation by the PV device, values were changed by using uniformly distributed numbers. In the TtsR algorithm, the new amounts of stored energy within RB and TES power at $t+1$ time step ($S_{RB}^{t+1,new}$ and $S_{TES}^{t+1,new}$) were fixed to the same value as those obtained during the prediction phase ($S_{RB}^{t+1,new}$ and $S_{TES}^{t+1,new}$), i.e., these values were used as constraints. Finally, the operating schedules for the two-time steps (t and $t+1$) were optimized by using εDE.

AtsR and TtsR are not optimization methods, but rather frameworks that enable problem formulation for the recalculation. Thus, these methods should work with various optimization method such as linear programming, mixed integer linear programming, genetic algorithm, and steepest decent method. In this study, we adopted εDE because the optimization problem contained nonlinear and iterative configuration, and many constraints.

In Fig. 5-6, the left-hand side shows the optimal operating schedule obtained during the prediction phase, while the right-hand side shows the unpredicted demand changes and the results of recalculations. When the current time step was 1 p.m., the demand at 2 p.m. increased. Then, we conducted optimization for two-time intervals (e.g., 2 p.m. and 3 p.m.). The power output of the TES and CR1 increased to meet the demand. However, this operational change caused the remaining TES (kWh) to decrease. Thus, in the next time step (3 p.m.), power output of TES decreased and CR1 increased in comparison with the predicted values to match the TES remaining at 3 p.m. to the previous value obtained in the predictions. This procedure could rebalance the energy system while avoiding large-scale recalculations and thereby achieved reduced computation costs.

TtsR and AtsR can be used efficiently when the energy system includes devices that have time-dependent characteristics, such as storage equipment and AR. This is because the stored energy in such equipment affects the subsequent time step, furthermore, an AR cannot rapidly start and stop generating heat, and it is sufficient to conduct a given optimization method at each time step when we do not consider the storage system. Moreover, another advantages of TtsR and AtsR strategies is that they do not require the number of heat sources and storage units to be specified.
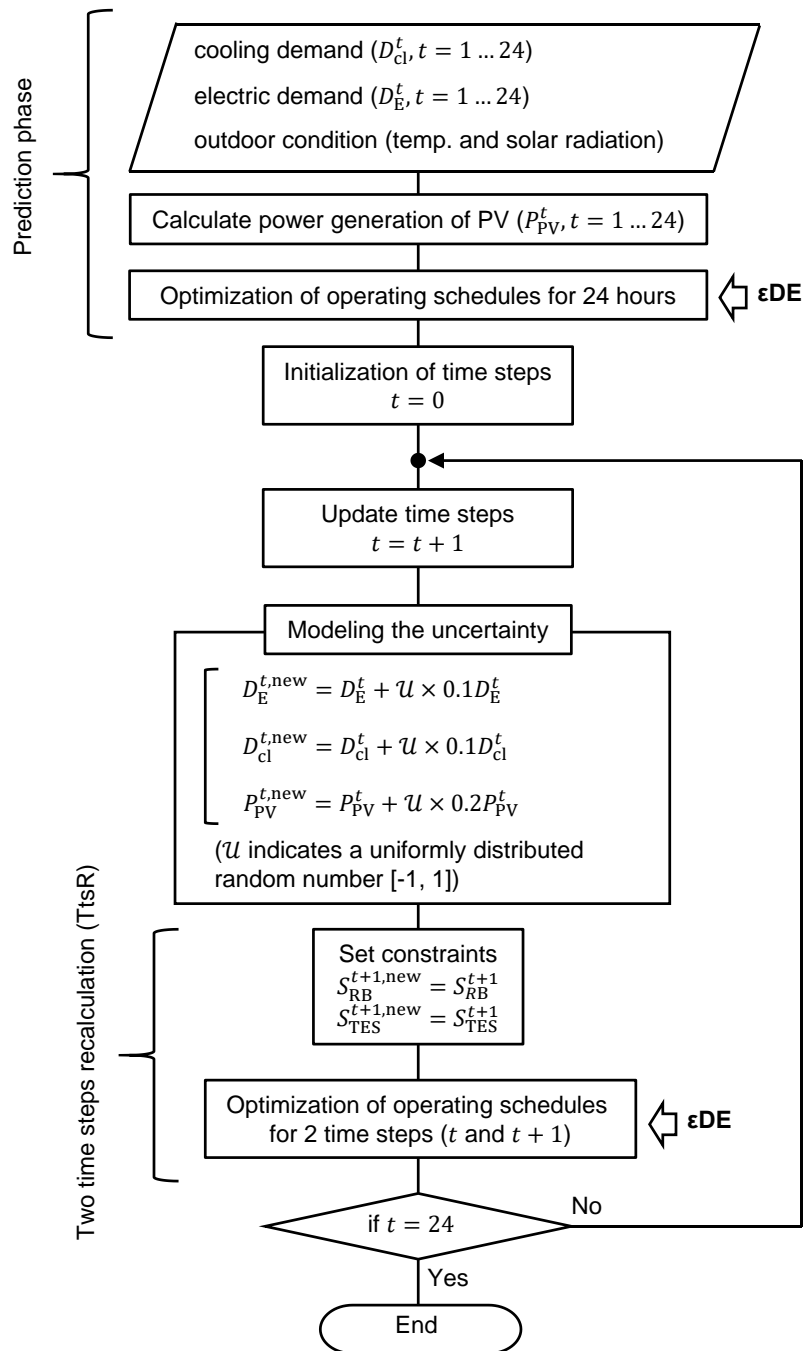
Fig. 5-5 | Flow chart for the TtsR algorithm.
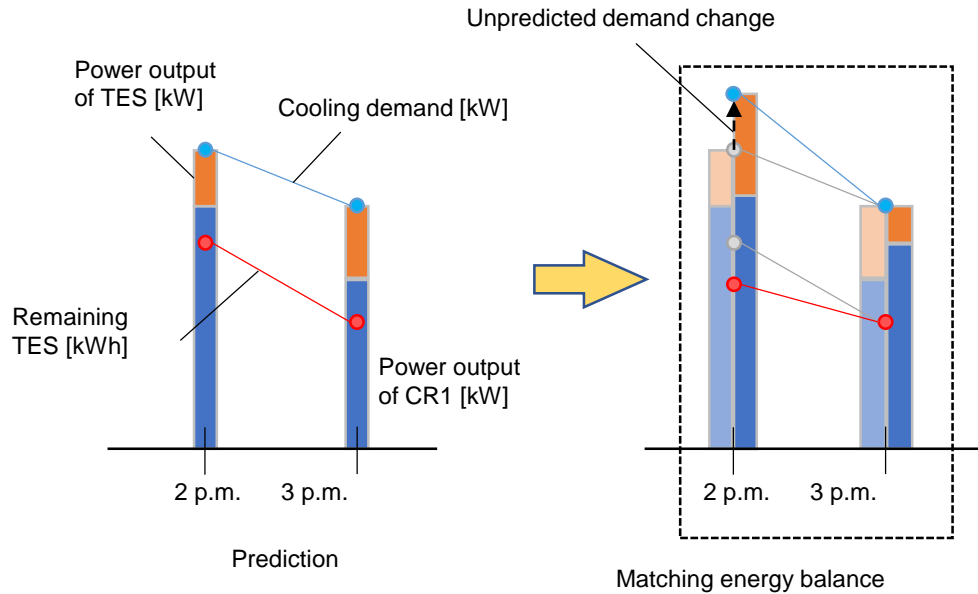
Fig. 5-6 | Conceptual diagram of the recalculation process under unpredicted demand change.

5.5 Results and discussion

5.5.1 Case study

We conducted three case studies to clarify the accuracy and effectiveness of the proposed TtsR. Case 1 (prediction) determined the quasi-optimal operating schedule under predicted conditions, the so-called "perfect prediction." In Case 2 (uncertainty of PV), the power generation from the PV device was changed by a uniform random number in the range of the upper and lower 20%, as shown in Fig. 5-7. In this figure, the blue bars (predicted PV) indicate the amount of power generated from the PV device during the prediction, and the red bars (changed PV) indicate the amount of power generated after modeling the uncertainty. The power level increased by 19.2% at 1 p.m. and decreased by 12–14% at 9 a.m., 10 a.m., and 2 p.m. in Case 1. In the results for the uncertainty modeling, the total amount of power generation increased from 773.4 kWh/day (predicted PV) to 781.2 kWh/day (changed PV). Two cases were considered, namely, Case 2-1 (AtsR) and Case 2-2 (TtsR).

In Case 3 (uncertainty of demand), we used a model that accounted for the uncertainty of demand resulting from changes in occupant behaviors. In this scenario, three specific cases were considered: Case 3-1 (AtsR), Case 3-2 (TtsR), and Case 3-3 (Emp). Case 3-3 represented an empirical operation model for comparison with Case 3-1 and Case 3-2. The empirical model considered as follows: 1) when cooling demand exceeded the prediction, a heat source machine with the most efficient COP rating (CR in this chapter) generated heat to meet the additional demand, 2) when the demand
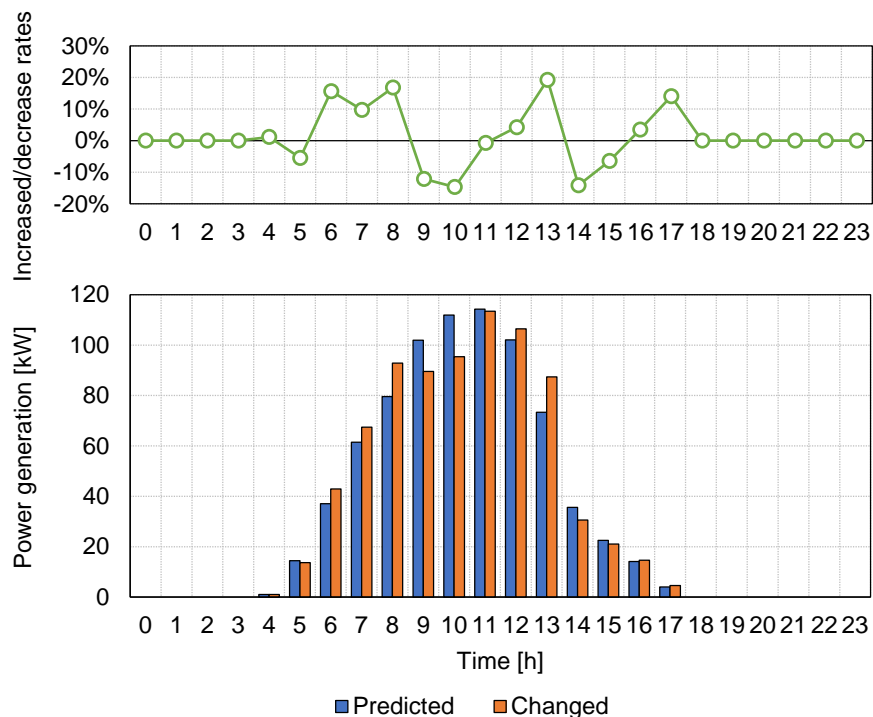
Fig. 5-7 | PV power generation variation.

exceeded the total capacity of all machines, the TES discharged heat to meet this demand, 3) when the demand decreased, AHP3 that had the smallest capacity reduced generating heat to meet the demand. The demand changes were modeled by using a uniform random number in the range of the upper and lower 10%. Electricity demand and cooling demand changed as shown in Fig. 5-8 and Fig. 5-9, respectively. The results show that the total amount of electric demand increased from 12,614 kWh/day to 12,794 kWh/day, while the cooling demand increased from 64,715 kWh/day to 67,736 kWh/day.

Finally, we considered the uncertainty of both factors (i.e., power generation fluctuations and changes in demand) in Case 4 (uncertainty of both types). Case 4-1 (AtsR) and Case 4-2 (TtsR) were evaluated. The modeling results of Case 4 represent the combined results of Case 2 and Case 3.
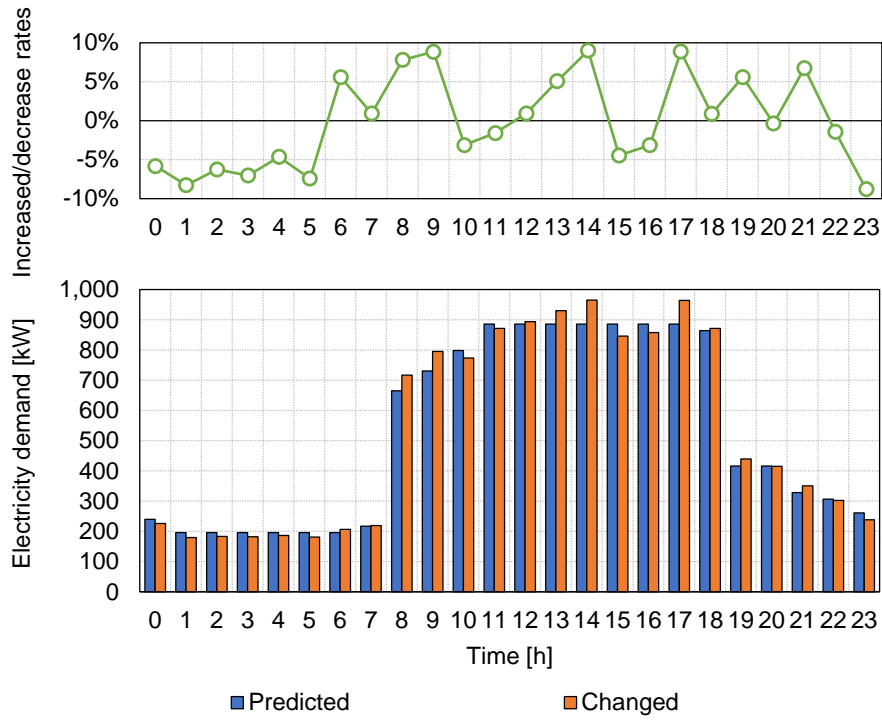
Fig. 5-8 | Electricity demand (ED) variation.
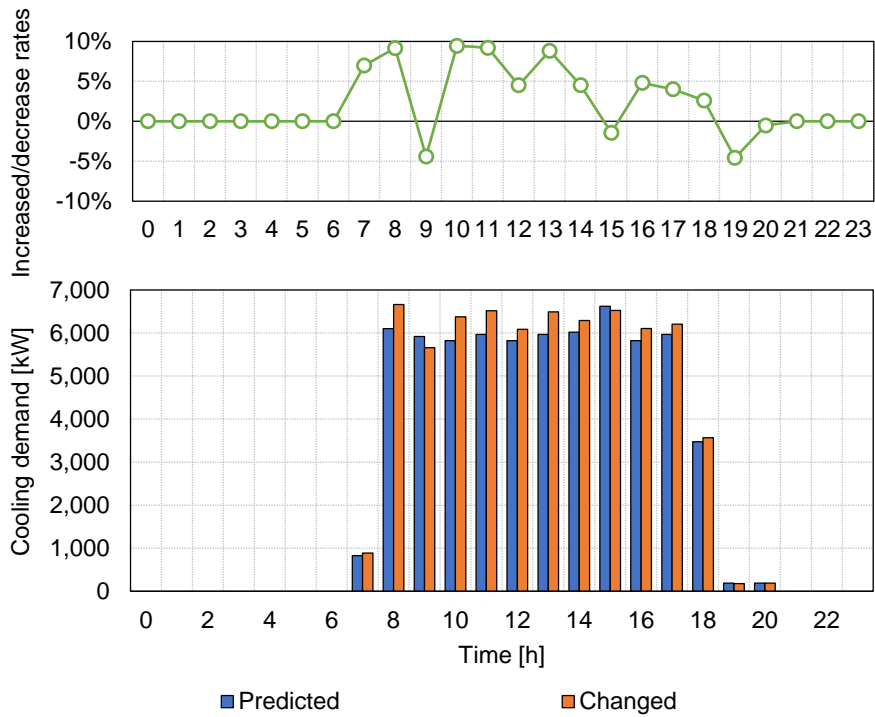
Fig. 5-9 | Cooling demand (CD) variation.

5.5.2 Result of Case 1 (predictions)

Fig. 5-10 shows the quasi-optimal operation of the electricity system. When the price of purchased electricity was lower than that sold (0–7, 9, 10 a.m. and 6–11 p.m.), the system could obtain income by charging electricity and immediately selling it to EG. However, in the early morning hours, charging and storage operations (green bars) were mainly conducted because the electricity was needed to reduce the operating costs during the daytime. Although discharging operations were conducted at 2 a.m., this was not a problem because RB was already charged to the full amount of electricity by 7 a.m. before the start of the business day. In daytime, electricity from RB (yellow bars) and PV device (pink bars) was supplied to meet the electricity demand of the building. At night (8–11 p.m.), charging and discharging operations were conducted frequently to obtain income because no constraints for the number of charging or discharging events were used in this chapter.

Fig. 5-11 shows the quasi-optimal operation of the HVAC system. The TES charged the full amount of thermal energy before the start of the business day. When the charging operation was conducted, CR1 (light blue bars) mainly generated cooling heat because CR1 was highly efficient. In the daytime, the five heat source machines generated cooling heat because the amount of cooling demand was larger than the total rated capacities. We were able to obtain the quasi-optimal solution within a short time period (390 s). All optimizations were performed by using MATLAB R2015a software with the following computer specifications: Windows 8.1 Pro (64 bits), 3.40 GHz Core i7-4700 CPU, and 32 GB RAM.
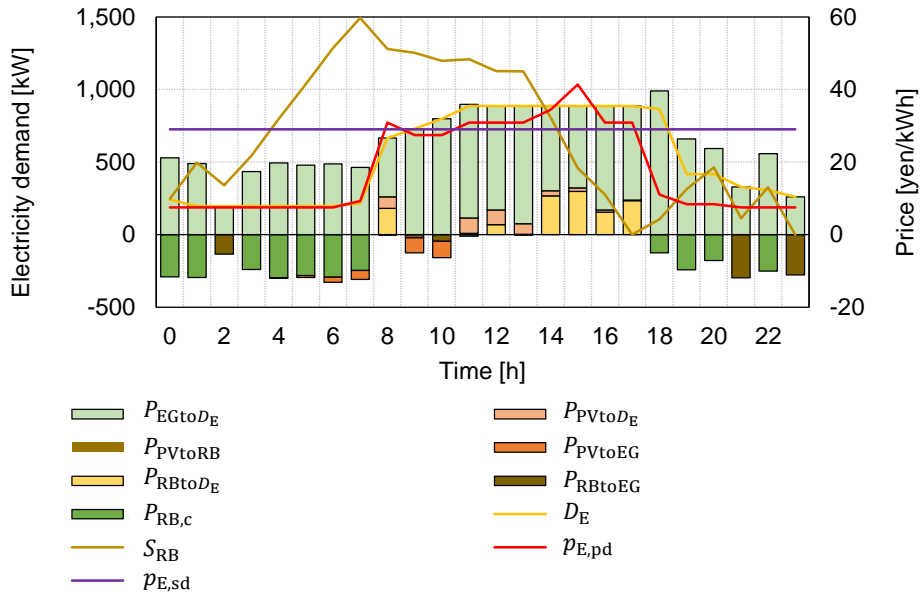
Fig. 5-10 | Quasi-optimal operation of the electric system in predictions.
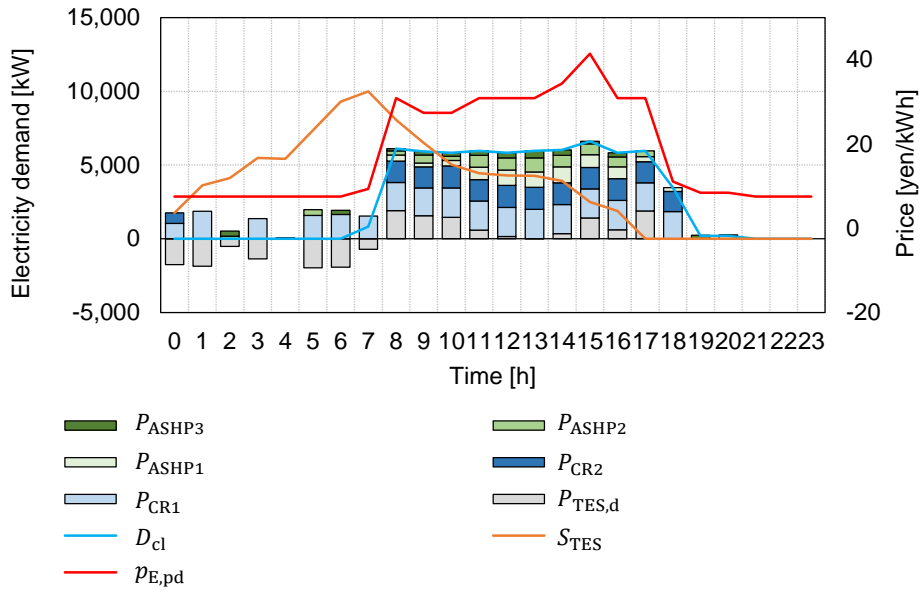
Fig. 5-11 | Quasi-optimal operation of the HVAC system.

5.5.3 Result of Case 2 (uncertainty of PV power)

The results for the operating costs and computation times per time step for Case 2-1 and Case 2-2 are shown in Fig. 5-12. The computation times for Case 2-1 (blue line) decreased gradually from 382 s at 0 a.m. to 14 s at 11 p.m. In contrast, the computation times for Case 2-2 (red line) stayed at approximately 40–50 s during all time intervals. The total computation times for Case 2-1 and Case 2-2 were 4,608 s and 1,290 s, respectively. Thus, TtsR reduced the computation time by 73% compared to AtsR. The operating costs of Case 2-1 and Case 2-2 were 604,633 yen/d and 608,304 yen/d, respectively. Hence, no major differences in operating costs were detected (i.e., the cost increase was less than 0.61%).
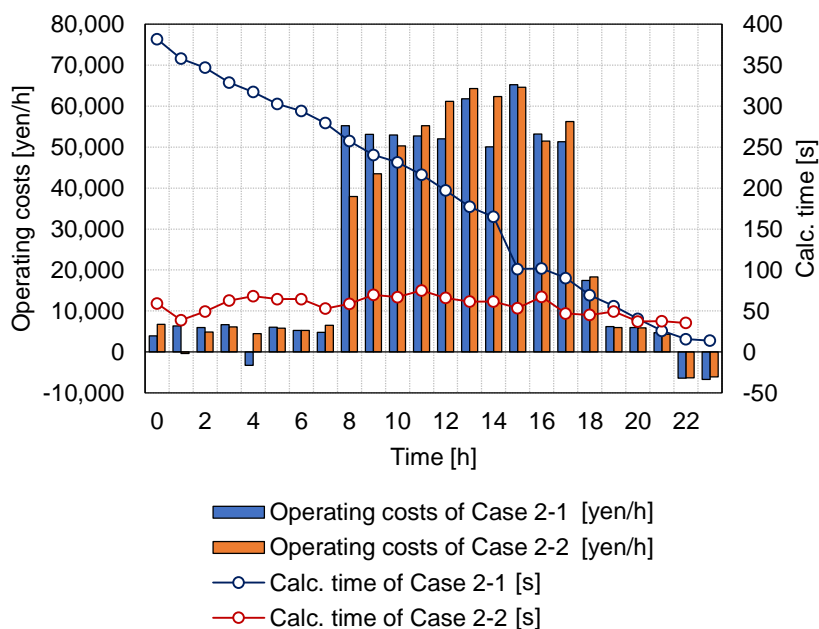
Fig. 5-12 | Comparison of the results for Case 2-1 and Case 2-2.

5.5.4 Result of Case 3 (uncertainty of demand)

Fig. 5-13 shows the results for Case 3-1, Case 3-2, and Case 3-3 under the uncertainty of demand changes. Similar to Case 2, the computation time of Case 3-1 decreased gradually and that of Case 3-2 stayed at 40–50 s during each time step. Here, TtsR reduced the computation time by 73% compared to AtsR. The computation time for Case 3-3 was very short, because it only involved the empirical operational scenario rather than an optimization procedure.
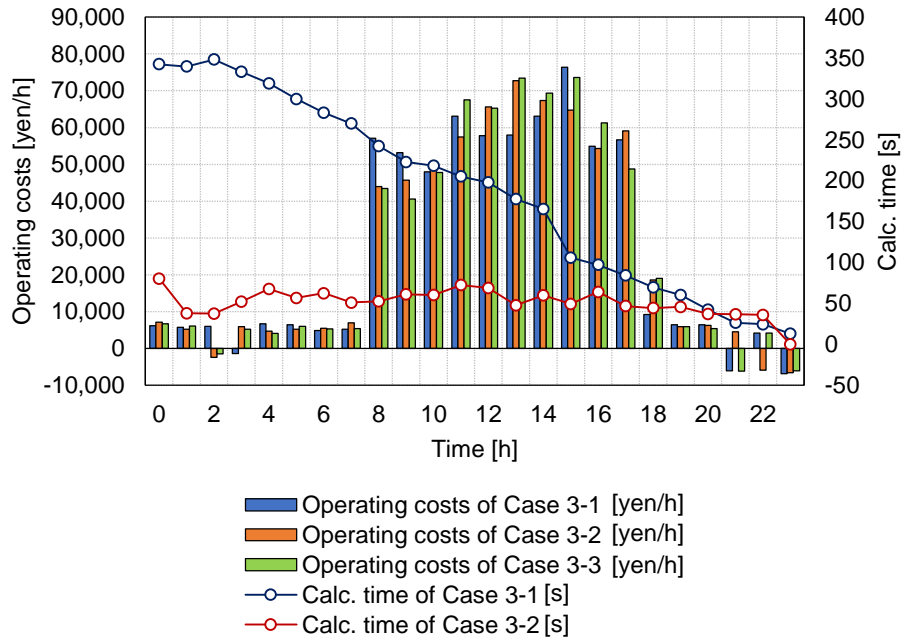
Fig. 5-13 | Comparison of the results for three cases.

The total operating costs for Case 3-1, Case 3-2, and Case 3-3 were 640,985 yen/day, 641,129 yen/day, and 650,249 yen/day, respectively; no major differences in operating costs were detected between Case 3-1 and Case 3-2 (i.e., the cost increase was less than 0.02%). However, there was a substantial difference between the proposed method (Case 3-1 and Case 3-2) and Case 3-3. Therefore, AtsR and TtsR were superior to an empirical operation and TtsR provided an advantage over AtsR in terms of reduced computation time. Therefore, TtsR dealt effectively with the uncertainty of demand changes.

Focusing on Case 3-1 and Case 3-2, in terms of the differences in operations of the TES (Fig. 5-14), the results for Case 3-2 (green line) were similar to those of Case 1 (blue line) because the algorithm for TtsR had constraints related to the amount of remaining TES as did Case 1. The results for Case 3-1 (red line) were, however, different from the other results because AtsR could freely calculate the operating schedules regardless of the results of Case 1. At 9 a.m., the amount of remaining TES in Case 3-1 did not change compared to 8 a.m. The reason for this was that the charging/discharging operations were not conducted because the cooling demand decreased compared to the predicted demand, and the demand at 10 a.m. increased compared to the predictions as shown in Fig. 5-9. Thus, the discharging operation was conducted not at 9 a.m., but at 10 a.m. Next, the reduction rates of remaining TES for Case 3-1 and 3-2 were slower than that of Case 1 from 8 a.m. to 1 p.m. because the thermal energy from TES was used to supply the demand, and the amount of cooling demand increased at those time steps.
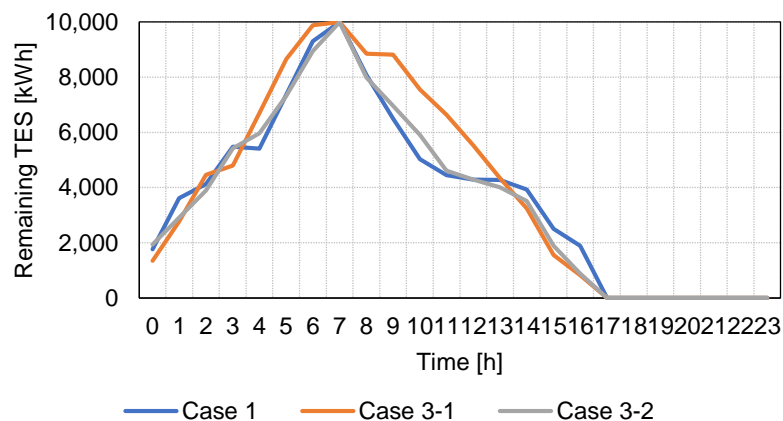
Fig. 5-14 | Variations in the amount of remaining TES [kWh].
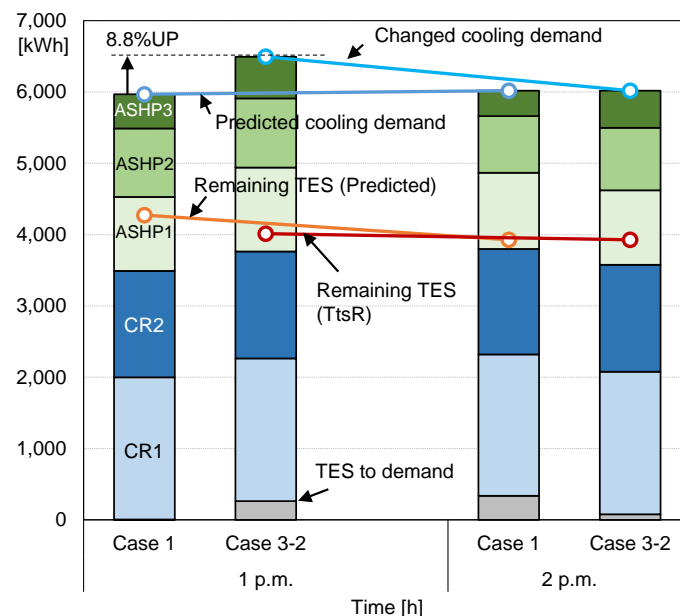
Fig. 5-15 | Comparison of each solution for Case 1 and Case 3-2.

The quasi-optimal operations at 1 p.m. for Case 3-1 and Case 3-2 are shown in Fig. 5-15. Here, it was supposed that the cooling demand increased unexpectedly by 8.8% compared to the predicted amount. Although the amount of discharging thermal energy from TES to the demand was zero in Case 1, TES discharged thermal energy (263 kWh) to the cooling demand in Case 3-2. The reason for this was that the total capacity of each piece of machinery was lower than the increased demand (6500 kWh). However, the amount of discharging thermal energy of TES was lower than the original amount

of that at 2 p.m. to maintain the amount of remaining TES at the end of the 2 p.m. interval. To meet the demand, ASHP2 and ASHP3 generated more cooling heat than in Case 1.

5.5.5 *Result of Case 4 (uncertainty of both types)*

Finally, the results for Case 4-1 and Case 4-2, which considered both types of uncertainty, are shown in Fig. 5-16. The trend of each result was similar to the results of Case 2 and Case 3. The total operating costs for Case 4-1 and Case 4-2 were 636,536 yen/day and 641,087 yen/day, respectively, and no major differences in operating costs were detected (i.e., the cost increase was less than 0.7%). The computation times of Case 4-1 and Case 4-2 were 4,521 s and 1,234 s, respectively. Thus, TtsR reduced the computation time by 73%. In general, we found that TtsR performed well in dealing with common types of uncertainty while maintaining the computational accuracy for actual building scenarios.
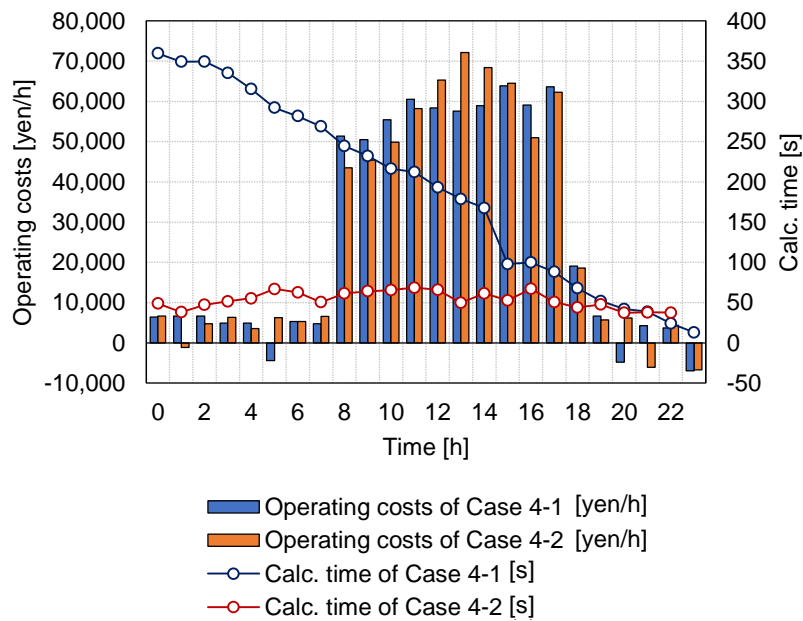
Fig. 5-16 | Comparison of Case 4-1 and Case 4-2.

5.6   Conclusion

In this chapter, we proposed a new strategy, TtsR, for recalculating the operating schedules of energy management systems to optimize energy production and minimize costs during periods of uncertainty caused by changes in renewable energy sources and changes in demand initiated by alterations in occupant behavior. These unpredicted changes are often encountered during the operation of actual energy systems. In TtsR, the operating schedules of two-time steps were optimized while fixing the amount of remaining battery power and TES at the second-time step. We compared TtsR with AtsR, which optimized the operating schedules of all-time steps and was a more time consuming but highly accurate procedure. Comparisons of the two calculation strategies showed that TtsR could obtain the quasi-optimal solution in 73% shorter computation times than AtsR while maintaining good accuracy. Therefore, TtsR should be a valuable technique to use for dealing with uncertainty when optimizing energy systems in actual buildings.

CHAPTER 6

Proposal of improved and robust εDE method and application to multiple ground source heat pump system

6.1 Introduction

This chapter describes optimal operations of GSHP for cooling and hot water demands. Although a ground source heat pump (GSHP) has recently emerged as a promising heat source/sink for reducing energy consumption and carbon dioxide emissions [181,182] and many studies have been conducted with the aim of investigating and evaluating GSHP [183–188], when and how much heat should be generated from GSHP considering ground temperature variation has not been studied thus far. Pardo et al. [189] optimized an energy system component that included GSHP and TES throughout a long-term calculation. Cui et al. [43] and Sayyadi et al. [117] adopted a multi-objective evolutionary algorithm to find a pareto-front curve in terms of two objective functions: thermodynamic and economic. They set a fixed temperature difference between inlet and outlet temperatures of ground fluid loop and thus, dynamic variation of a GSHP performance corresponds to the inlet fluid temperature of heat pump was not considered. However, previous studies have not optimized the operating schedule. Instead of optimizing the operation, previous studies have only compared some operating scenarios to reduce the computation costs, because the calculation of ground temperature variation under multiple boreholes involves complicated calculations and high computation costs.

In terms of optimizing the operating schedule, although Edwards and Finn [35] proposed a decision-making strategy for optimal mass flow rates considering the partial load rate and ground temperature, they did not consider the thermal history of the ground temperature in determining the operation time of GSHP. Zeng [98] optimized the capacity and load rate of GSHP as constant values for a year under the condition of two energy systems that included GSHP. However, they did not discuss how they considered the change in ground temperature and the resulting COP changes of GSHP. Owing to a lack of information, their results cannot be evaluated in terms of realistic GSHP operation, and their work did not achieve optimal operation.

When conducting an optimization that determines when and how much heat should be generated by GSHP, it needs to compare infinite combinations of heat source operations as in the case of previous optimization studies that have not considered GSHP. Comparing infinite operation schedules is impractical; moreover, linear programming, which is often used in many studies, cannot be adopted for this problem because GSHP has highly nonlinear characteristics and the ground temperature calculation requires nonlinear and discrete iterative calculations. Although DP used in many studies can handle the characteristics, DP is not suitable to solve this problem because it requires numerous combinations of each discrete decision variable, which involves high computation costs.

Owing to the above-mentioned factors, optimization problems that involve GSHP operation cannot be solved easily, and sometimes, unrealistic assumptions are made in GSHP operation. For example,

GSHP is often assumed to be able to continuously generate the rated output corresponding to a dynamic load variation without performance degradation caused by thermal build-up or depletion in the ground. To reflect the actual behavior of GSHP in the optimization, the ground thermal history (i.e., past heat exchange rate between GSHP and ground) should be considered as an optimization of a system including a thermal storage tank whose thermal behavior is similar to that of the ground.

In this chapter, an efficient optimization method that can be applied to a problem that involves a nonlinear physical phenomenon is needed. The proposed optimization method is called epsilon-constrained differential evolution with random jumping (εDE-RJ). It is an improved method based on εDE to be more stable for searching solutions. Using the proposed method, the optimal operation of a hybrid GSHP system is determined considering the dynamic variation in the ground temperature and machine performance. The system assumed in this study consists of ASHP, four GSHPs, and GB. The contents of this chapter is referred to my peer-reviewed article published in Applied Energy [190].

6.2   Calculation conditions

6.2.1 Description of energy systems

A simple energy system consisting of an ASHP, four GSHPs, and a GB was considered, as shown in Fig. 6-1. The ASHP and three GSHPs (denoted by $GSHP_{cl}1$–3) handled the cooling load, while one GSHP (denoted by $GSHP_{ht}$) and the GB handled the hot water demand. The inlet and outlet temperatures of chilled water were fixed at 6 °C and 11 °C, respectively. The temperature of publicly supplied water was assumed to be constant at 25.2 °C [191], and when this water passed through the heat exchanger (outlet temperature), its temperature was increased by 60 °C. To consider the approach temperature of 1°C, the GB and $GSHP_{ht}$ generated hot water at 61 °C and the returning water temperature was fixed at 26.2 °C. Thirty vertical closed-loop borehole heat exchangers (BHEs) were installed; 20 BHEs were connected to $GSHP_{cl}$ and the remaining 10 BHEs were connected to $GSHP_{ht}$. The distance between the BHEs was set to 5.0 m in accordance with [188]. The specifications of the system components are listed in Table 6-1. The values of the rated capacity and electricity consumption of GSHP were calculated under the condition that the entering fluid temperatures were 25°C and 10°C for cooling ($GSHP_{cl}$) and heating ($GSHP_{ht}$), respectively.

The characteristics of each component including the pumps were modeled according to the nonlinear configuration described in Section 2.1. To carry out the partial load operation, the pump could vary the flow rate from 20% to 100% with a resolution of 5%. The maximum heat generation and COP of the GSHPs were affected by the ground water temperature, as shown in Fig. 2-6. Although
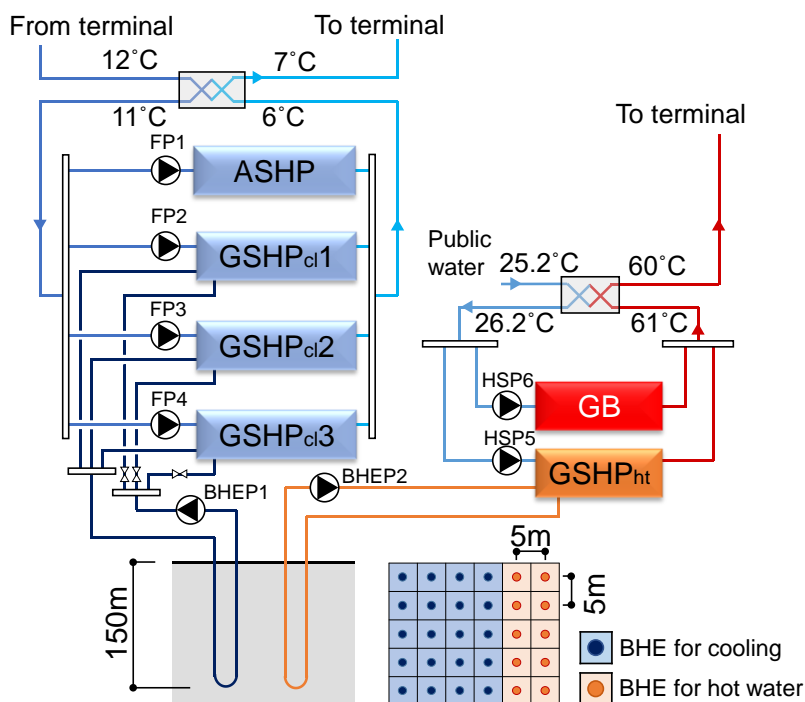
Fig. 6-1 | System configuration.

Table 6-1 | Rated specification of system components (as given in [144])

ASHP	Cooling capacity	180	kW
	Electricity consumption	49.1	kW
GSHP$_{cl}$1, 2, 3	Cooling capacity	53	kW
	Electricity consumption	10.8	kW
	Mass flow rate of BHE loop	183	L/min
GSHP$_{ht}$	Heating capacity	61	kW
	Electricity consumption	15.2	kW
	Mass flow rate of BHE loop	133	L/min
GB	Heating capacity	46	kW
	Gas consumption	4.5	m^3

GSHP$_{cl}$ had relatively high efficiency when the inlet fluid temperature was in the range of 2 °C–12 °C, the COP decreased drastically as the temperature increased. GSHP$_{ht}$ was not efficient compared to GSHP$_{cl}$ because the hot water supply temperature from GSHP$_{ht}$ was set to 61 °C. The pumps for the heat sources (FP1–6) had a constant rated pressure of 100 kPa. The pressure was changed under a partial load condition by the inverter control. In the case of the pumps for the borehole heat exchanger (BHEP), the rated electricity consumption of BHEP1 and BHEP2 was 3.7kW and 2.2kW, respectively. These values were determined on the basis of catalogs published by pump manufacturers [192,193].

When one GSHP generated heat at the rated load rate, the flow rate of the ground loop was 183

L/min. The flow rate was zero when the operation of GSHP was halted. Therefore, the water flow rate changed in a discrete manner. When the number of operating $GSHP_{cl}$ was changed from 0 to 3, the flow rate changed in a discrete manner, i.e., 0, 183, 366, and 549 L/min. The electricity consumption of the pumps also changed in a discrete manner, i.e., 0, 1.25, 2.50, and 3.75 kW. The electricity consumption of BHEP2 was zero or 2.2 kW depending on whether $GSHP_{ht}$ was off or on.

6.2.2 Modeling of borefield

In this chapter, the outlet fluid temperature of the borefield (i.e., inlet temperature of GSHP) comprising 30 BHEs was calculated using the infinite line source (ILS) model [194,195]. This is an analytical solution derived from the one-dimensional thermal diffusion equation; thus, only heat conduction is considered. The ground is assumed to be an infinite, homogeneous, and isotropic medium. Using the ILS solution, the transient ground temperature changes with reference to a constant step pulse released from the infinite line source/sink is calculated. The inlet and outlet fluid temperatures can be respectively expressed in time-discretized form as follows.

$$T_{in}^t = T_b^t + R_{BHE}^t s_b + \frac{P_{BHE}^t}{2\kappa m_{cirw}} \tag{6-1}$$

$$T_{out}^t = T_b^t + R_{BHE}^t s_b - \frac{P_{BHE}^t}{2\kappa m_{cirw}} \tag{6-2}$$

where m_{cirw} is the flow rate of the circulating fluid, κ is the volumetric thermal capacity of the fluid, and $P_{BHE}^t = R_{BHE}^t L_{BHE}$ is the heat exchange rate between the BHE and the GSHP. s_b denotes thermal resistance of the soil. In the cooling and heating operations, P_{BHE} is calculated as follows:

Cooling operation

$$P_{BHE}^t = P_{GSHP_{cl}}^t + \frac{P_{GSHP_{cl}}^t}{COP_{cl}^t} \tag{6-3}$$

Heating operation

$$P_{BHE}^t = P_{GSHP_{ht}}^t - \frac{P_{GSHP_{ht}}^t}{COP_{ht}^t} \tag{6-4}$$

Note that the heat rate P_{BHE}^t is positive when the heat pump injects the heat to the ground (cooling mode) and negative when heat is extracted from the ground (heating mode). In addition, note that the BHE's outlet temperature T_{out} is equal to the GSHP's inlet temperature T_{in}. The BHE geometry and parameters used for the GSHP calculation are listed in Table 6-2.

Table 6-2 | Parameters of the borehole heat exchanger (BHE) setup and soil.

Borehole heat exchanger	Borehole depth	150	m
	Borehole diameter	100	mm
U-tube: High-density polyethylene	Outer diameter	34	mm
	Inner diameter	27	mm
	Shank spacing	44	mm
	Thermal conductivity	0.38	W/(m·K)
Heat carrier fluid: Water	Thermal conductivity	0.6	W/(m·K)
	Density	1,000	kg/m^3
	Specific thermal capacity	4,200	J/(kg·K)
Ground	Thermal conductivity	2.0	W/(m·K)
	Volumetric heat capacity	2.5	MJ/m^{3}K
Grout	Thermal conductivity	2.0	W/(m K)

6.2.3 Demand and electricity price profiles

A virtual hotel building in Tokyo with a total floor space of 1,000 m^2 was considered. Cooling and hot water loads for 24 h were calculated at time steps of 1 h. Although the hotel had cooling, heating, electricity, and hot water demands, we only focused on summer days and the corresponding cooling and hot water demands. The demand and price profiles are shown in Fig. 6-2. Demand curves are taken from [196]
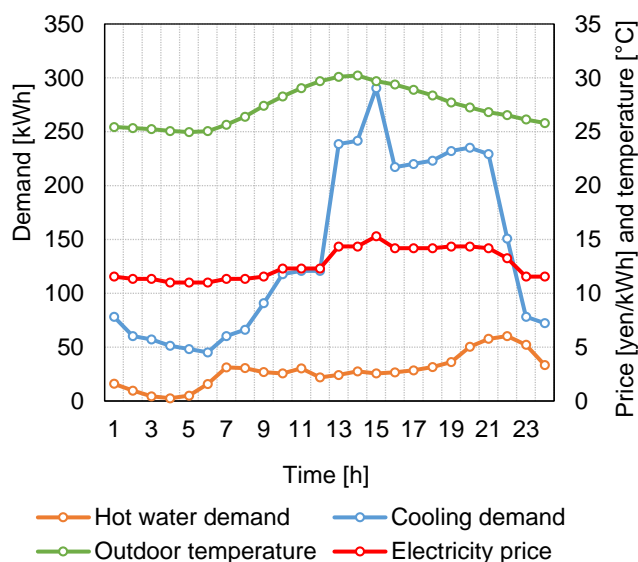
Fig. 6-2 | Demand and price profiles

6.3   Optimization method

6.3.1 Problem formulation

In this study, the aim was to minimize the operating cost of the system as follows:

$$\text{minimize } f = \sum_{t=1}^{24} \left(p_E^t \left\{ \sum_{i=1}^{6} (c_{E,i}^t) + c_{E,\text{BHEP}}^t \right\} + p_G^t c_{G,\text{GB}}^t \right) \tag{6-5}$$

where t is the time step, p_E represents the electricity price [yen/kWh], i is the machine number (1: ASHP, 2: GSHP$_{cl}$1, 3: GSHP$_{cl}$2, 4: GSHP$_{cl}$3, 5: GSHP$_{ht}$, 6: GB), $c_{E,i}$ represents the electricity consumption of machine i, which includes the electricity used by FP [kWh], $c_{E,\text{BHEP}}$ represents the electricity consumption of BHEP1 and BHEP2 [kWh], p_G represents the gas price [yen/m³], which is constant at 82.7 yen/m³, and $c_{G,\text{GB}}$ represents the gas consumption of GB [m³].

The decision variables are described in . The following constraints were set: 1) upper and lower bounds of circulating fluid temperature of GSHP outlet and 2) maximum thermal output (i.e., rated capacity) of system components. The upper and lower bounds of the GSHP's outlet temperature were set to 40 °C and 2 °C for GSHP$_{cl}$ and GSHP$_{ht}$, respectively (i.e., cooling and hot water demands, respectively). This restriction prevents system failure due to extremely high inlet temperature or freezing. Although the outlet temperature set point, 2 °C, has a risk of freezing in some extremely cold areas, the ambient temperature in many parts of Japan rarely drops below zero. Furthermore, the heat generation of ASHP and GB was restricted to be less than the rated capacity of each machine because these values are determined by the difference between the demand and the generated heat of the GSHPs. This restriction was applied because, when the determined power output of GSHP is significantly small and the remaining demand is thus larger than the rated capacity of ASHP and GB, there is a possibility that ASHP and GB will generate a larger amount of heat than their rated capacity. To prevent this undesirable situation, when the determined output of GSHP is extremely small, and the remaining demand is larger than the rated capacity of ASHP and GB, the GSHP is forced to generate more heat such that the remaining demand can be handled by ASHP and GB.

6.3.2 Drawback of epsilon-constrained differential evolution (εDE) algorithm

To handle the nonlinear characteristics of GSHP, we propose an efficient algorithm instead of using linear programming or dynamic programming, which are not suitable for solving the problem. Although εDE can handle the configuration without any simplifications, εDE has a critical drawback

in searching for a solution, which is based on the original DE algorithm. When a certain variable value is the same for all individuals (which has a low probability), the individuals cannot move to any other places because

$$x^*{}^g_{\text{p1},j} = x^g_{\text{p2},j} + \alpha_{\text{DE}}\left(x^g_{\text{p3},j} - x^g_{\text{p4},j}\right)$$

(6-6)

where α_{DE} indicates the mutation rate (=0.5); $x^g_{\text{p1}-4,j}$ is a temporary value of the j-th variable of individual (p1– p4) at generation g.

6.3.3 Proposal of an improved algorithm (εDE-RJ)

To avoid being trapped in a local optimum, an improved algorithm is proposed, namely εDE with random jumping (εDE-RJ). The random jumping strategy is inspired to the mutation method of GAs. Although m-PSO has already been developed from the same point of view in [153], εDE is more suitable for solving a constrained problem. When $x^g_{\text{p3},j}$ is equal to $x^g_{\text{p4},j}$, the following equation is applied:

$$x^{g+1}_{\text{p1},j} = \begin{cases} x^g_{\text{p2},j} + \alpha_{\text{DE}}(x^g_{\text{p3},j} - x^g_{\text{p4},j}) \text{ when } \left|x^g_{\text{p3},j} - x^g_{\text{p4},j}\right| > 1.0 \times 10^{-3} \\ x^g_{\text{p2},j} + \mathcal{U} \qquad \text{when } \left|x^g_{\text{p3},j} - x^g_{\text{p4},j}\right| \leq 1.0 \times 10^{-3} \end{cases}$$

(6-7)

where $\mathcal{U}$ is a uniformly distributed random number within the range [0,1].

Although this method is simple, it shows robust searching performance. The accuracy of εDE-RJ is almost the same as that of εDE [197] mentioned above because the possibility that would require use of the RJ method is low. An algorithm flowchart is shown in Fig. 6-3.
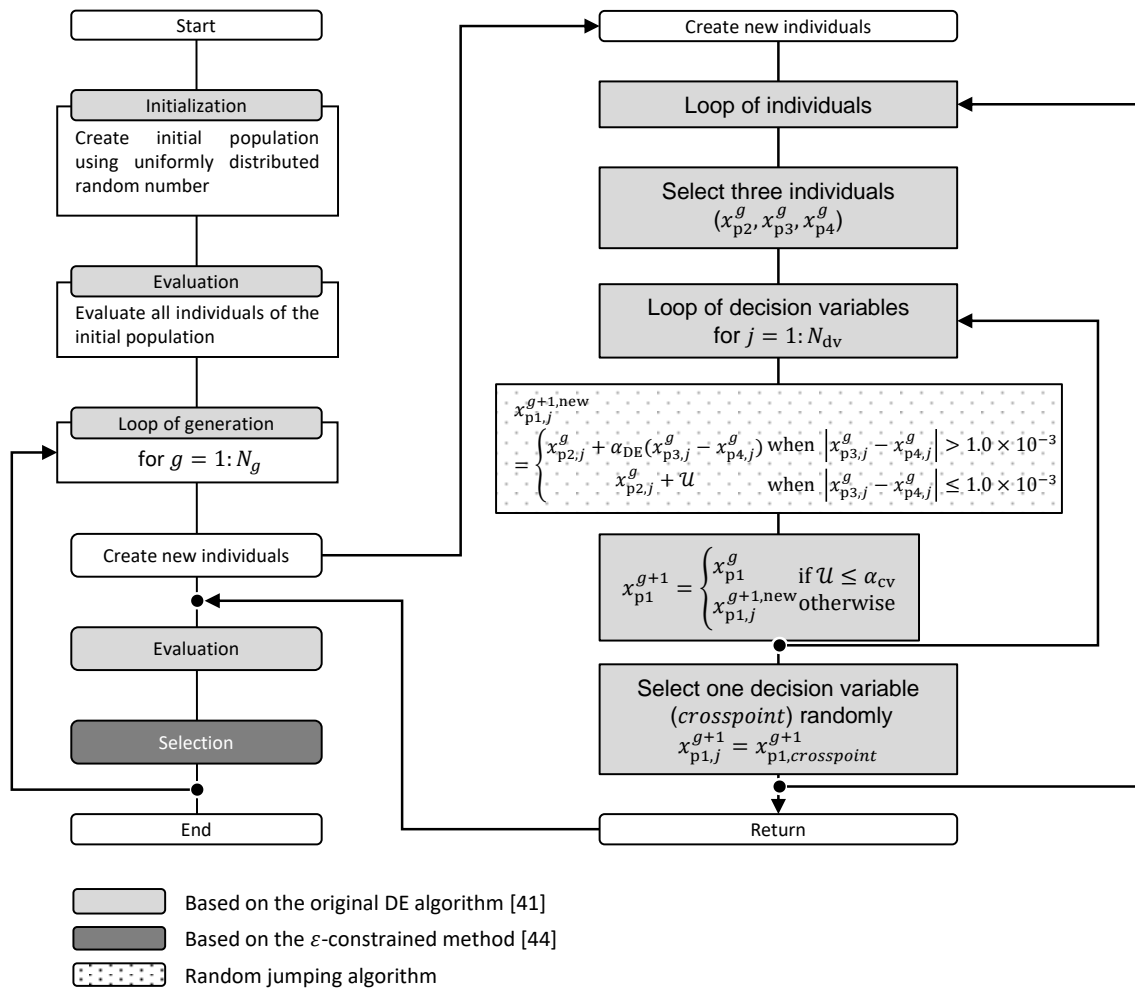
Fig. 6-3 | Flow chart of εDE-RJ algorithm (N_g: number of generations, N_{dv}: number of decision variables, α_{cv}: crossover rate, $\mathcal{U}$: uniformly distributed random number).

6.3.4 Optimization condition

Two stopping criteria were set as follows: 1) the search reaches the predefined number of generations, and 2) the objective function value does not change. The first one is a well-known criterion in the field of optimization. However, there is a possibility that the objective function value will not change when the individuals find the best solution. Thus, to reduce the computation costs, the search was terminated the search when the value did not change by more than 10% of the rated number of generations. The computer used for all simulations had the following specifications: Windows 10 64-bit, 3.40 GHz Core i7-6700 CPU, and 16 GB RAM. All the simulations were performed using MATLAB R2016a and Parallel Computing Toolbox with four CPU cores. The population size and maximum number of generations were set to 20 and 500 in all the optimizations.

6.3.5 Details of case studies and decision variables

To confirm the effectiveness of the proposed optimization method, two case studies were set up: Case 1 and Case 2. In Case 1, the calculation period was 24 h. In terms of operation, Case 1-1 set the GSHPs' operation as the first priority; thus, $GSHP_{cl}$ and $GSHP_{ht}$ first generated heat. Subsequently, if the total demand could not be handled by the GSHPs, the ASHP and GB handled the remaining demand. This operation strategy was considered as an empirical operation. In Case 1-2, εDE-RJ determined the start and stop times of operation. During the time interval, $GSHP_{cl}$ and $GSHP_{ht}$ had the first priority in the operation, as with Case 1-1. Thus, there were four decision variables for one day: the start and stop times of $GSHP_{cl}$ and $GSHP_{ht}$. In Case 1-3, εDE-RJ determined the amount of heat generations of all the machines at each time step. Therefore, Case 1-3 had 96 decision variables (24 h × 4 machines). Case 2 had a calculation period of 7 days. However, the operation schedule of 168 h was not optimized at once. The optimization was conducted at intervals of 24 h; first, the optimal operation schedule of the first 24 h was set, and then, the optimization of the next 24 h (i.e., 25–48 h) was conducted with the ground condition including the 24 heat pulses of the first day. Similarly, the operation schedule for the third day was determined with the past 48 h of thermal history.

When the optimal heat generation of $GSHP_{cl}1$–3 was determined, the heat generation ratio was optimized, defined as the ratio of the heat output to the total maximum capacity, and based on this ratio, the number of $GSHP_{cl}$ in operation was determined. For example, when the ratio was 0.8 and the total maximum capacity was 159 kW (= 53 kW × 3), the total heat generation of $GSHP_{cl}1$–3 was 127.2 kW and the load rate of each GSHP was 80%. When the ratio was 0.4, the total heat generation was 64 kW and $GSHP_{cl}1$ and $GSHP_{cl}2$ generated 32 kW at a load rate of 60%; $GSHP_{cl}3$ did not operate.

Furthermore, in Cases 1-1, 1-2, 2-1, and 2-2, when the outlet fluid temperature of GSHP$_{ht}$ was lower than 2 °C and that of GSHP$_{cl}$ was greater than 40°C, the heat generation was reduced by 50% to keep the fluid temperature within the upper and lower bounds.

To confirm the differences in the results in terms of the calculation period, six cases were considered because the performance of GSHP systems depends on the thermal history (i.e., heat demand of past time steps).

6.4   Results

6.4.1 Comparison of Cases 1-1, 1-2, and 1-3 (one-day optimization) for cooling

The obtained optimal operations of Cases 1-1, 1-2, and 1-3 are shown in Fig. 6-4. The heat exchange rate of the BHE and the COP variations of each component are shown in Fig. 6-5 and Fig. 6-6, respectively.

In Case 1-1, GSHP$_{cl}$ showed more efficient operation than ASHP during 1 a.m. to 2 p.m., as shown in Fig. 6-6 (a). However, the COP of GSHP$_{cl}$ became lower than that of ASHP after 3 p.m., because GSHP$_{cl}$ continuously operated from the start time of operation. Although the COP of ASHP was low during 1 p.m. to 3 p.m., because of the high outdoor temperature, the COP of ASHP gradually increased as the outdoor temperature decreased with time, as shown in Fig. 6-2.

In Case 1-2, the optimal results showed that GSHP$_{cl}$ started to operate from 1 p.m. and stopped at 9 p.m. Meanwhile, ASHP continuously operated during the day (Fig. 6-4 (b) and Fig. 6-5 (b)). The COPs of ASHP were around 1.8 and 1.6 during night time and day time, respectively (Fig. 6-5 (b)). In accordance with the result of Case 1-1, GSHP$_{cl}$ showed better performance than ASHP from 1 a.m. to 3 p.m. In contrast to the result of Case 1-1, GSHP$_{cl}$ did not operate before 1 p.m., when the peak demand and price occur, to keep the ground temperature at an initial value 16 °C (Fig. 6-4 (b) and Fig. 6-5 (b)). In addition, GSHP$_{cl}$ stopped working after 9 p.m. because the outlet fluid temperature of BHE increased by 32.9 °C and the COP of ASHP increased; thus, ASHP showed better performance than GSHP as the outdoor temperature decreased. The COP of GSHP$_{cl}$ was lower than that of ASHP from 6 p.m. to 9 p.m. because εDE-RJ determined only the start and stop time in Case 1-2.

In Case 1-3, where εDE-RJ determined the optimal operation in each time step, a clear difference was found in the results compared to the other two cases in terms of the operation schedule and resulting COP variations (Fig. 6-4 (c), and Fig. 6-5 (c)). GSHP$_{cl}$ always showed better performance than ASHP because GSHP$_{cl}$ operated intermittently to avoid thermal build-up and maintain a good operating condition. In addition, unlike Cases 1-1 and 1-2, which operated under a load rate of 100%

during the peak load period, GSHP$_{cl}$ worked under various load rates to achieve high performance and low operation cost when the electricity price was high. The total operating costs for the cooling system are summarized in Table 6-3. The operating cost of Case 1-1 was 10,280 yen/day and that of Case 1-2 was 9,738 yen/day, representing a reduction of 5.27%. The operating cost of Case 1-3 was 9,346 yen/day, representing a reduction of 9.09% compared to Case 1-1.

6.4.2 Comparison of Cases 1-1, 1-2, and 1-3 (one-day optimization) for heating

In all the cases, GSHP$_{ht}$ continuously operated for 24 h and GB only operated during 9–10 p.m. to meet the peak hot water demand. Although the ground temperature gradually decreased, the performance degradation was very small, which shows the COP of GSHP$_{ht}$ with respect to the inlet fluid temperature. There was a moderate variation in the COP of GSHP$_{ht}$ because the hot water outlet temperature was set to a high value of 61 °C. Thus, the results showed that the continuous operation of GSHP$_{ht}$ is an optimal solution. On the other hand, the operating cost in Case 1-3 was 4,027 yen/day, representing a reduction of 1.08% compared to Cases 1-1 and 1-2, owing to the difference in the partial load operation of GSHP$_{ht}$ and GB at 9 and 10 p.m. (Fig. 6-5). This difference is small. However, when long-term optimization beyond 24 h is conducted, this difference would be much larger because the performance of GSHP$_{ht}$ would be degraded compared to its initial condition. If the optimization for this hybrid GSHP system is conducted without considering the thermal history of the ground, such a difference would not be observed in the results. Therefore, to achieve optimal operation of the complex system, it is important to not operate GSHP as the first priority based on the empirical conception, but to find an optimal combination of the thermal outputs from the different components.

6.4.3 Comparison of Cases 2-1, 2-2, and 2-3 (one-day iterative optimization for 7 days) for cooling

As described previously, Case 2-1 operates the GSHPs at the rated capacity and the remaining demand is handled by the other components. In Cases 2-2 and 2-3, which correspond to Cases 1-2 and 1-3, the optimization was conducted for a period of 24 h and thus iteratively conducted for 7 days. The duration of 7 days was chosen to confirm the mid-term effects that are important for the GSHP operation. Fig. 6-7 shows the operating schedules of each case. Fig. 6-8 shows the variations in the ground temperature and heat exchange rate of the BHE, while Fig. 6-9 shows the COP variations of the GSHPs.

In Case 2-1, although $GSHP_{cl}$ generated heat constantly for 7 days, the outlet fluid temperature never reached the upper bound of 40 °C (Fig. 6-8(a)). However, the COP of $GSHP_{cl}$ decreased gradually, and it can clearly be seen that the COP of $GSHP_{cl}$ was always lower than that of ASHP from the fourth day of operation. Although the temperature was recovered during night time owing to a low heat exchange rate, the continuous operation caused thermal build-up in the ground and degraded the performance. Therefore, the operation of GSHP was more expensive than that of ASHP (an empirical operation could not keep maintain the COP).

In Case 2-2, GSHP operated during the peak time period as in Case 1-2. The ground temperature was significantly recovered during night time because GSHP did not operate; thus, $GSHP_{cl}$ could achieve higher COP than ASHP during the peak time of 1–3 p.m. The total operating cost of cooling for 7 days was 68,740 yen, and it was reduced by 12.54% compared to Case 2-1 (Table 6-3).

In Case 2-3, $GSHP_{cl}$ worked intermittently and generated heat under partial load conditions to keep the COP of $GSHP_{cl}$ higher than that of ASHP over 7 days. The total reduction rate was 16.35% compared to Case 2-1.

Table 6-3 | Results of all cases.

	Calc. period	Operating costs (yen)		
		Cooling system	Hot water system	Total
Case 1-1	1 day	10,280	4,071	14,351
Case 1-2	1 day	9,738	4,071	13,809
Case 1-3	1 day	9,346	4,027	13,373
Case 2-1	7 days	78,596	29,500	108,096
Case 2-2	7 days	68,740	29,162	97,902
Case 2-3	7 days	65,748	28,851	94,599

6.4.4 Comparison of Cases 2-1, 2-2, and 2-3 (one-day iterative optimization for 7 days) for heating

In Cases 2-1 and 2-2, during the peak time period (8–11 p.m.) after the fourth day, $GSHP_{ht}$ reduced its output in some time steps to prevent the outlet fluid temperature of GSHP from falling below 2 °C. However, there was a difference between the two cases on the seventh day. In Case 2-2, $GSHP_{ht}$ stopped operation from 1 a.m. to 4 a.m. for recovery of the ground temperature under very low partial load; then, the peak load was handled fully during night time, which is an effective operation strategy to reduce the operation costs. In Case 2-3, partial load operation was mainly conducted during peak time to keep the temperature higher than 2 °C while maintaining high COP of $GSHP_{ht}$ (Fig. 6-7). The operating costs of Cases 2-2 and 2-3 were reduced by 1.15% and 2.20% compared to Case 2-1, respectively. As mentioned in Section 7.4.2, the optimal combination of $GSHP_{ht}$ and AB significantly reduces the operating costs.
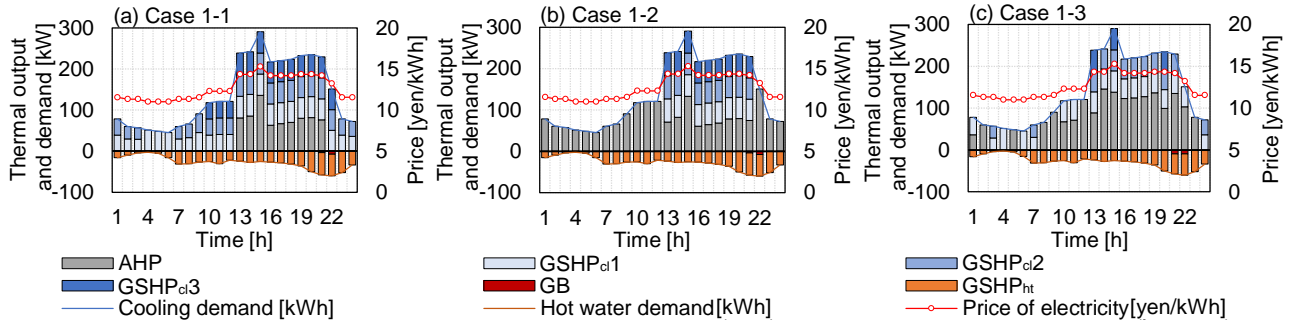
Fig. 6-4 | Operating schedule in each case study
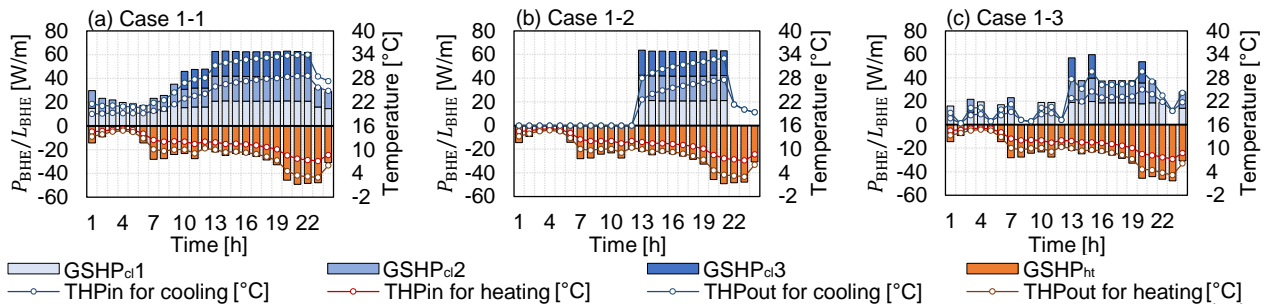
Fig. 6-5 | Variations in ground temperature and heat injection
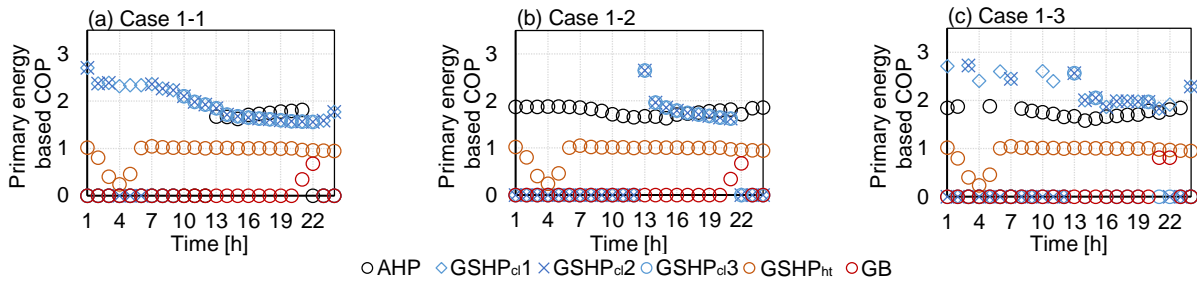
Fig. 6-6 | Primary energy-based COP variation in each case study (conversion rates are 9.97 MJ/kWh and 45 MJ/m³ for electricity
and natural gas, respectively)

131
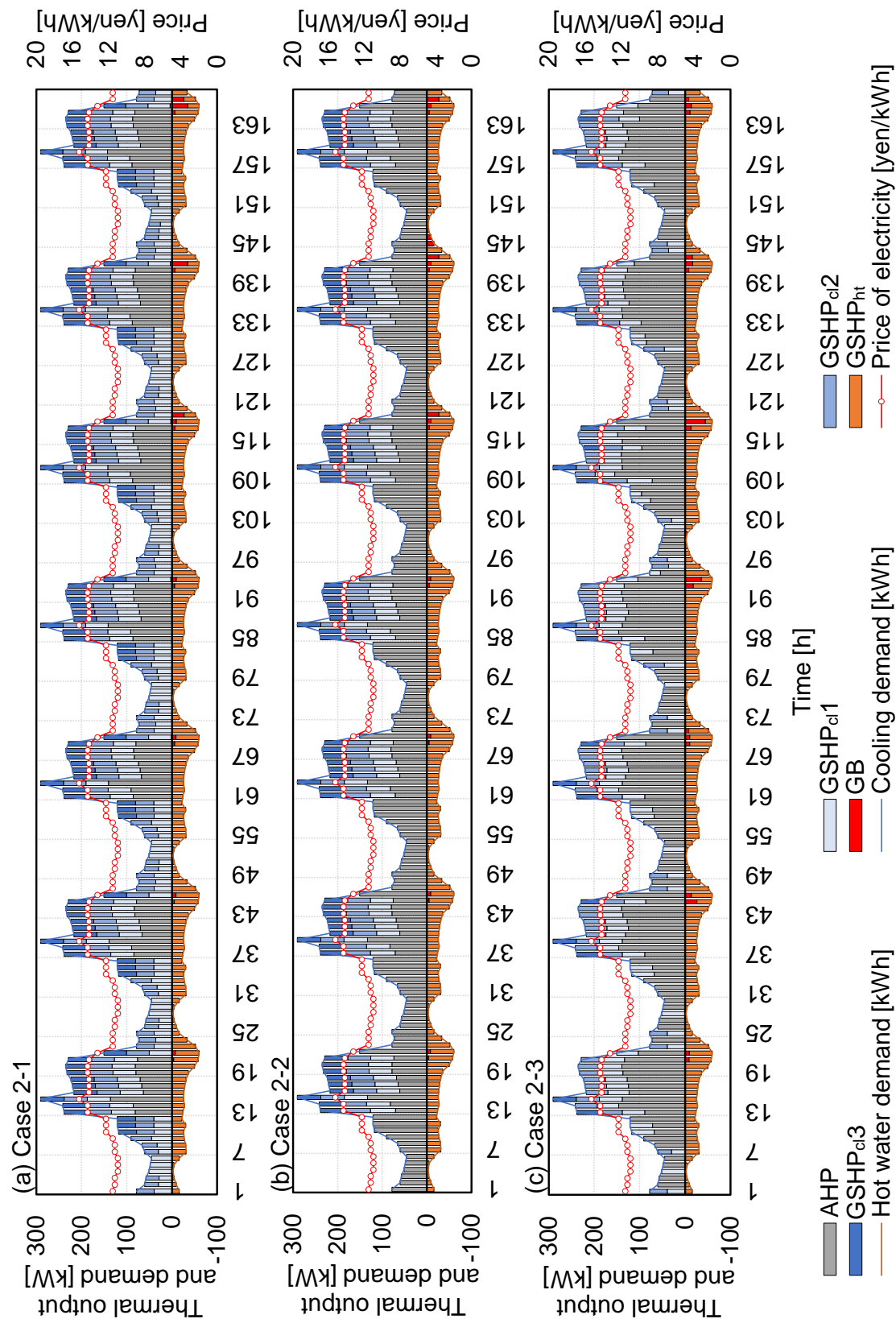
Fig. 6-7 | Operating schedule in each case study
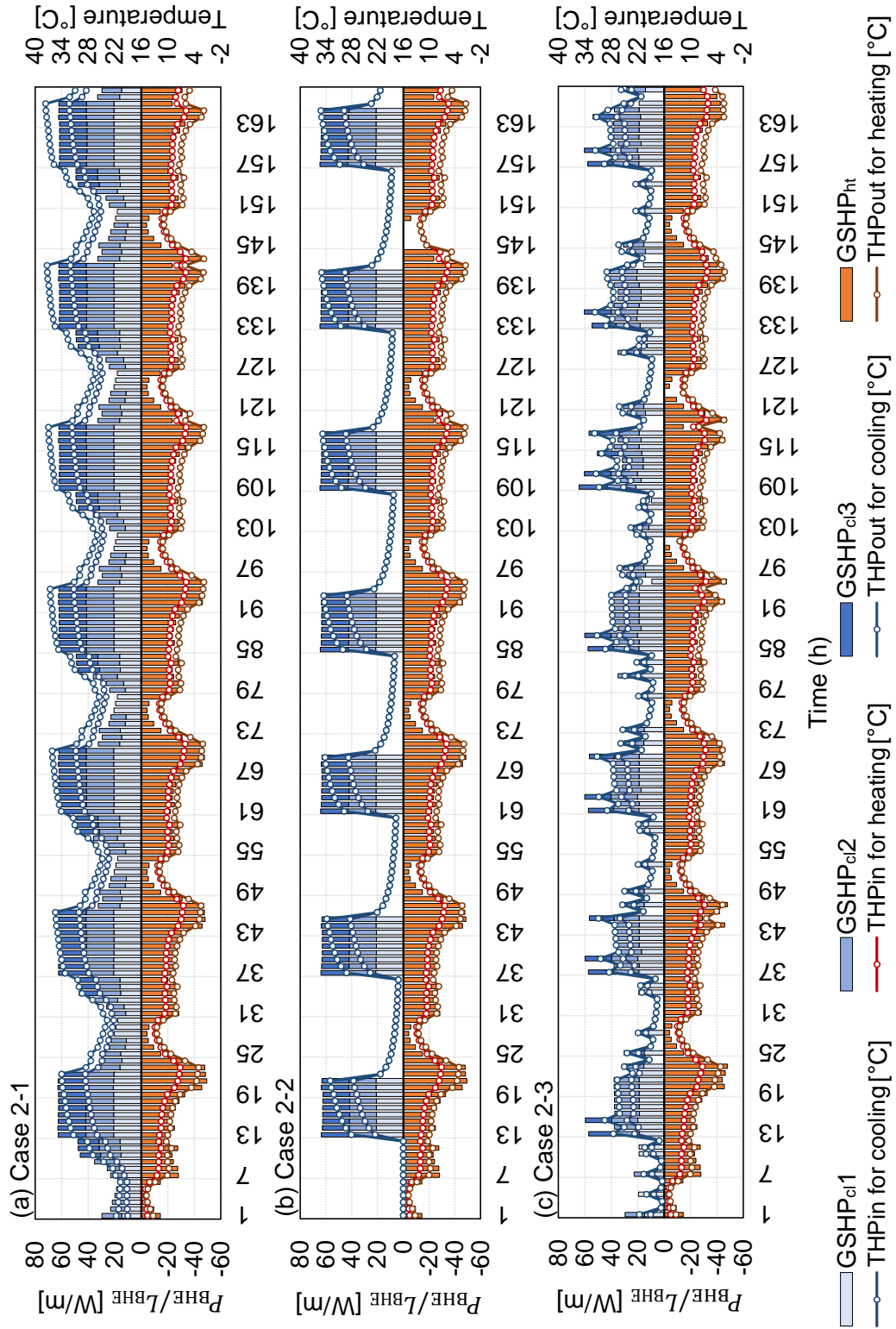
Fig. 6-8 | Variations in ground temperature and heat injection
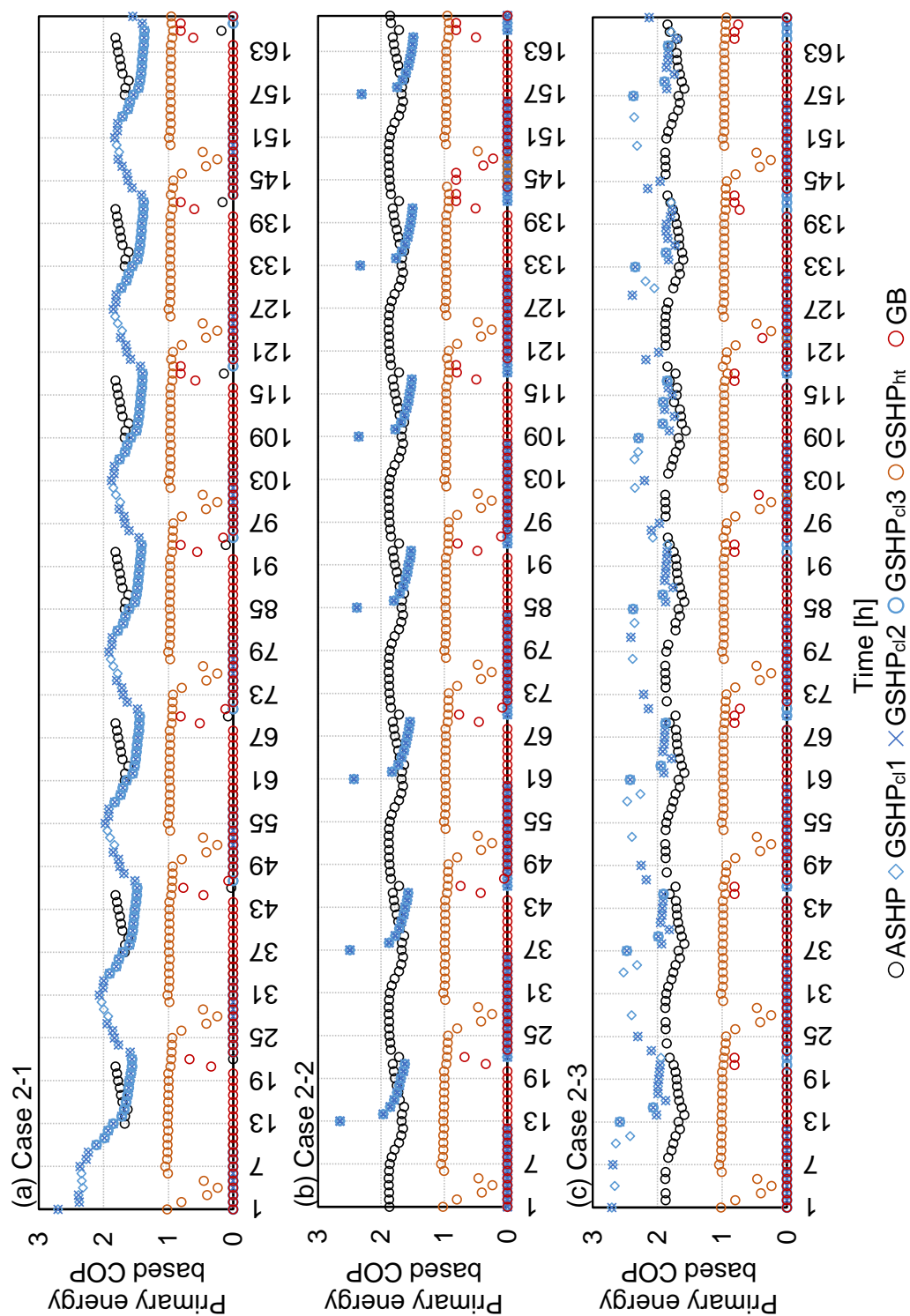
Fig. 6-9 | Primary energy-based COP variation over 7 days in each case study (conversion rates are 9.97 MJ/kWh, 45 MJ/m^3 for electricity and natural gas, respectively)

6.5   *Discussion*

In this chapter, the operating optimizations of a hybrid GSHP system under various scenarios were conducted using the proposed εDE-RJ method. Although the problem includes the computation of the ground loop's fluid temperature, which has nonlinear characteristics and requires iterative calculation, an optimal solution could be obtained without applying any relaxations, such as linearization or approximation. This is an important advantage of the proposed optimization algorithm over some previously used methods, such as linear programming and the Newton method, which requires a convex condition.

Owing to the advantage of the proposed optimization method, the optimal operation point of the system under different scenarios was found. Compare to the operating costs of Cases 1-1 and 2-1, where the GSHPs had higher priority in operation and were thus operated continuously, the other cases showed better results because Cases 1-2 and 2-2 operated intermittently and Cases 1-3 and 2-3 found the optimal combination of outputs from each heat source in every time step.

From the comparison between Cases 1-2 and 1-3 (Fig. 6-4 (b, c), Fig. 6-5 (b, c), and Fig. 6-6 (b, c)), and Cases 2-2 and 2-3 (Fig. 6-7 (b, c), Fig. 6-8 (b, c), and Fig. 6-9 (b, c)), it was confirmed that the intermittent operation of GSHP is the key factor in achieving good performance and minimizing the operating costs, because in contrast to ASHP and other renewable heat sources, the thermal history exchanged between the ground and the GSHP has a long-lasting effect due to the large thermal capacity of the ground.

When only on the comparison between Cases 2-2 and 2-3 is considered, Case 2-3 clearly showed a solution superior to Case 2-2 in terms of minimizing the operating costs. However, it would be difficult to realize the result of Case 2-3 in practical operations because it requires frequent on–off operations with various partial load conditions. In such situations, the result of Case 2-2 is suitable for actual operation, and this simple optimization could reduce the operation cost by 5.27%–12.54% compared to the empirical operation.

Moreover, from the viewpoint of computation costs, Cases 1-2 and 1-3 required only 3.6 min and 15.6 min, respectively. Although $20^{24\times4} \times 20^{24} \times 20^{24}$ (24 h of four GSHPs, ASHP, and GB) combinations should be considered when resorting to a full searching method (note that 20 represents a discrete value of heat generation with a resolution of 5% of rated capacity), εDE-RJ requires only 10,000 (= 20 individuals $\times$ 500 iterations) combinations. Thus, the proposed εDE-RJ method can be used for day-ahead optimization in practical situations.

6.6 Conclusion

In this chapter, an optimization method for the operating schedules of a composite energy system including GSHP was proposed. The method, namely εDE-RJ, can efficiently solve highly nonlinear configurations and iterative calculations to calculate the ground temperature. In addition, it can be used in practical situations owing to its adaptability as well as its potential to reduce computation costs. The contributions of this study can be summarized as follows.

- The simplified optimization strategy that determined only the start and stop times of the GSHP operation could reduce the operating costs compared to the empirical operation for a single day and 7 days by 3.78% and 9.59%, respectively.

- The detailed optimization strategy that determined the load rates of all the components in each time step could reduce the operating costs compared to the empirical operation for a single day and 7 days by 6.81% and 12.56%, respectively.

- When the mid-term optimization (7 days) was conducted, the performance of $GSHP_{ht}$ was gradually degraded compared to its initial condition because of the thermal depletion of the ground. Therefore, to achieve an optimal operation of the complex system, it is important to not operate GSHP as the first priority, but to find an optimal combination of the thermal outputs from the different components.

- εDE-RJ could solve a complex optimization problem while maintaining high computation accuracy. In addition, this method could account for the realistic behavior of the ground. Thus, the proposed method can be widely used in both theoretical and practical studies when users want to obtain an optimal operation schedule.

In future work, it remains to address how this method can be applied to a much longer period such as for an analysis of the life-cycle impact of GSHP, thermal interaction among BHEs, and optimal GSHP design. The proposed algorithm requires high computation costs because it uses iterative calculations to find a quasi-optimal solution and obtain the fluid temperature for the ground loop corresponds to the load assigned. Hence, consideration of a reduction in computation costs to carry out a long-term simulation for multiple years is highly required.

CHAPTER 7

Development of hybrid method of εDE-RJ with artificial neural network for temperature-dependent energy systems

7.1   Introduction

This chapter describes the utilization of εDE-RJ to optimize the operating schedule of a heat recovered absorption refrigerator (HRAR), GSHP for cooling and heating, a solar collector (SC), a stratified thermal energy storage (TES) system, and a combined heat and power (CHP) system. In particular, the temperature variation should be considered because it affects the machine efficiency of the SC and the GSHP. However, a physical model, such as the ILS used in Chapter 6, suffered from long computation times to calculate this variation. It showed that the number of generations and the individual population of εDE-RJ should be small, compared to when an energy system that did not include GSHP was optimized. Hence, the artificial neural network (ANN) model was used in this chapter to reduce this computation cost.

7.2   Calculation conditions

7.2.1 Description of an energy system

Fig. 7-1 shows a configuration of an energy system that consists of both a cooling system and domestic hot water supply system. The CHP system could supply waste heat to both systems. The TES was connected to the hot water system, the waste heat circulation of the CHP system, and the SC system.

The waste heat from the CHP system was provided through heat exchanger No.1 (HEX1), with a rated area of 28.4 m^2. The area was determined with the rated mass flow rate of the waste heat circulation of CHP (61.1 L/min) and an overall heat transfer coefficient of the HEX. The coefficient was fixed at 1,500 W/(m^2·K) [198], as follows:

$$A_{\text{HEX}} = \frac{4186 R_{\text{m}} \Delta T}{60 \times 1500} \tag{7-1}$$

where A_{HEX} indicates the area of the HEX [m^2], R_{m} denotes the rated mass flow rate of waste heat circulation of CHP [L/min]. ΔT denotes the temperature difference of inlet and outlet water, which was fixed at 10 °C.

The exchanged heat through HEX1 was separated into HEX2 and HEX3 using a splitter and mixture No.1 (SM1). The areas of HEX2 and HEX3 were 82.1 m^2 and 27.9 m^2, respectively. The area of HEX2 depended on the rated mass flow rate of Pump 3 which was 176.5 L/min. The area of HEX3 depended on the rated mass flow rate of Pump 5 (60 L/min) which was used to charge the thermal energy to TES.

The thermal output of the SC depended on solar radiation (the input data) and the mass flow rate of Pump 4. The rated value of the area of the SC and the mass flow rate were 100 m^2 and 57.3 L/min, respectively. Hot water from the SC was delivered through HEX3 to exchange heat with the TES.

The TES charged the thermal energy through HEX 3 and HEX 4. In general, the outlet temperature of the hot water from the SC was approximately 30 °C to 70 °C. In contrast, the outlet temperature of the waste water from the CHP unit was approximately 80 °C to 95 °C. Hence, HEX4 was set later than HEX3 to raise the temperature of the circulating fluid efficiently. The volume of TES was 43 m^3. Discharged heat was provided to the hot water supply system through HEX5 which had an area of 27.9 m^2. This area was dependent on the rated mass flow rate of Pump 6.

In the hot water supply system, a ground source heat pump for hearing (GSHP$_{ht}$) could provide hot water to a secondary system through HEX 6 which had an area of 60.3 m^2. In addition, the discharged heat directly supplied HEX6 through SM4. The distribution rule of SM4 was as follows:

1) When the supply temperature through SM4 was greater than 65 °C, the hot water was supplied to HEX6 directly through Pump 8.

2) When the temperature was less than 65 °C, the hot water was heated to 65 °C with GSHP$_{ht}$. Subsequently, it was supplied to HEX6.

Because of the abovementioned distribution rule, a decision variable was not needed to operate SM4. The public water temperature was fixed at 25.5 °C, in accordance with [191].

In the cooling system, the GSHP for cooling (GSHP$_{cl}$) and the HRAR could supply cooling heat to the secondary system through HEX7. This had the largest area of 302.2 m^2, as the cooling demand was greater than the hot water demand. Pump 9, with the HRAR, and Pump 10, with the GSHP$_{cl}$, had a rated mass flow rate of 1146.7 L/min and 153 L/min, respectively, because the rated cooling capacity of the GSHP was smaller than that of the HRAR.

It was noted that the cooling system and the domestic hot water system were connected through both the GSHP$_{cl}$ and the GSHP$_{ht}$ with a ground heat exchanger (BHE). The length of the BHE for cooling and heating were set to 150 m with circulating pumps with 183 L/min of the rated mass flow rate. There were eight BHEs for cooling and eight BHEs for heating. The distance between the BHEs was 5 m, to reduce each other's effect, in accordance with [188].

The specification of each machine is shown in Table 7-1.
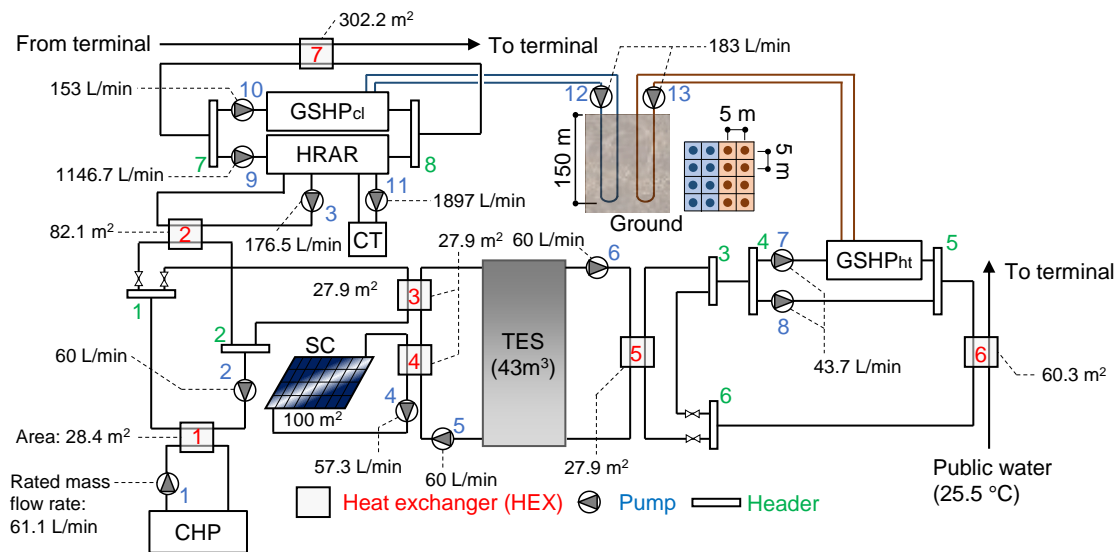
Fig. 7-1 | Configuration of the energy system: red colored numbers indicate heat exchangers, blue colored numbers indicate pumps, and green colored numbers indicate splitters and mixtures.

Table 7-1 | Specifications of each machine.

Combined heat and power (CHP)	Rated power generation	50	kW
	Rated waste heat utilization	42.6	kW
	Rated mass flow rate of circulating water	61.1	L/min
Heat recovered absorption refrigerator (HRAR)	Rated cooling capacity	400	kW
	Rated heating capacity	398.7	kW
	Rated electricity consumption for cooling and heating	7.2	kW
	Rated gas consumption for cooling	23.8	m³/h
	Rated gas consumption for heating	36.5	m³/h
Ground source heat pump (GSHP)	Rated cooling capacity	53	kW
	Rated heating capacity	61	kW
	Rated electricity consumption for cooling	10.8	kW
	Rated electricity consumption for heating	15.2	kW
	Rated mass flow rate of circulating water	133	L/min
Solar collector (SC)	Panel area	100	m²
	Rated mass flow rate	57.3	L/min

7.2.2 Demand and outdoor conditions

A hotel was used for this simulation because it had a large enough supply of domestic hot water. Demand curves at each time step were referred to as per [170]. The weather data was referred to as per [171]. The price of the purchased electricity was referred to a dynamic pricing system: the price was high at the peak period and the price was low at the off-peak period. Fig. 7-2 shows the temperature of the atmosphere (T_{atm}) [°C], cooling demand (D_{cl}) [kW], domestic hot water demand (D_{hw}) [kW], and total solar radiation (I_{total}) [kW/m²].
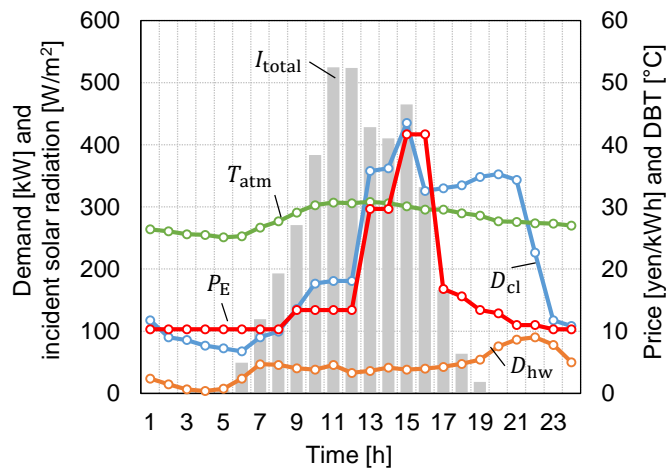
Fig. 7-2 | Demand and price profiles

7.2.3 Artificial neural network for BHE modeling

In Chapter 6.1, one issue using the numerical BHE model, such as the infinite line source model (ILS), was that it took long computation times to calculate a variation of the circulating fluid. Although ILS was the lowest computation cost model, εDE-RJ had only 1000 generations and took 56 min on an ordinal computer. Hence, longer computation costs are imposed to optimize a more complex system.

To reduce computation costs of the BHE model, an artificial neural network (ANN) was used in this chapter. When the BHE model is used, the outlet fluid temperature from BHE is the most important value. The ANN was used to predict the outlet temperature with a shorter computation time compared to the ILS model.

The ILS model could calculate the variation of circulating fluid temperature using the initial values of ground temperature, thermal history of the injection heat to the BHE, and the elapsed time. Although

the ILS had a lower computation complexity compared to an FEM model, the complexity can be expressed as $O(t \times N_{\text{BHE}}^2)$. This exponentially depends on the number of introduced BHEs.

However, the computation costs of the ANN do not depend on the number of BHEs or time horizons. The following three factors were used as input data into the ANN:

1) Injected heat at the previous time step (P_{BHE}^{t-1} [kW])

2) Injected heat at the current time step (P_{BHE}^{t} [kW])

3) Outlet temperature of the circulating fluid from the BHE to the GSHP at the previous time step ($T_{\text{out,BHE}}^{t-1}$)

The output value, which was the same as the predicted value of the ANN, was the outlet temperature at the current time step ($T_{\text{out,BHE}}^{t}$).

In fact, there are two GSHPs for cooling and heating in this system. There is the possibility that an operation GSHP$_{\text{cl}}$ affects the temperature variation of the GSHP$_{\text{ht}}$. Hence, the ANN had the above input and output data for both the cooling and heating. Therefore, the number of input and output data were six and two, respectively.

A structure of the ANN was shown in Fig. 7-3. It is most important to collect the learning data to improve the prediction accuracy of the ANN. Thus, εDE-RJ was used to create the learning data. Firstly, εDE-RJ optimized an optimization problem at 20 individuals and 50 generations. Although this was a very small problem compared to that of which we want to solve, there are 24,000 samples for the training ANN. To avoid over-fitting, 80% of 24,000 samples were used to train ANN and 20% of all samples were used to validate whether the ANN trapped in the over-fitting model or not.
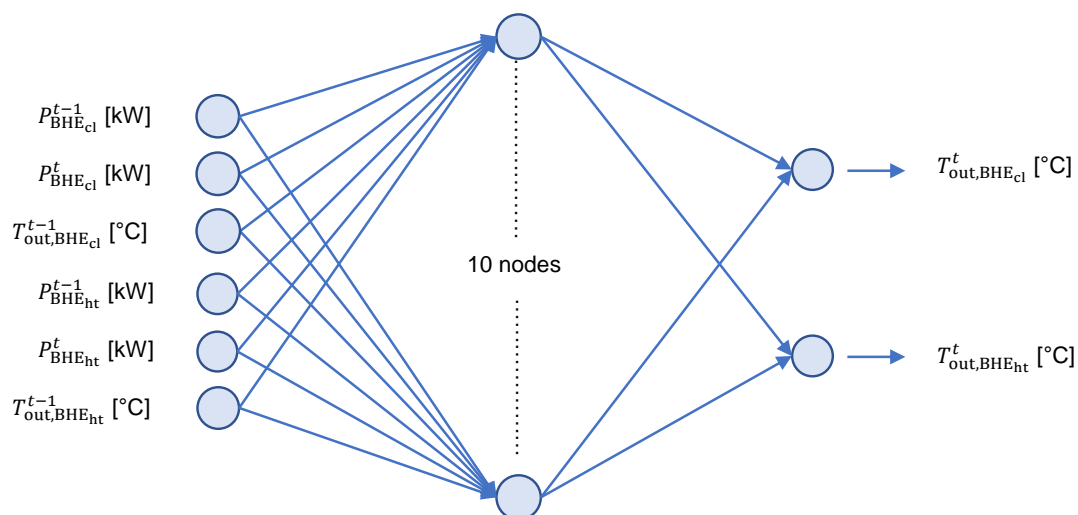
Fig. 7-3 | A structure of ANN$_{\text{BHE}}$

7.2.4 Artificial neural network for TES modeling

The stratified water thermal energy storage is one aspect where we can reduce the computation cost, as well. The stratified model depends on the number of nodes and the resolution of the time steps. As mentioned in Section 2.1.12, we used the 4th Runge–Kutta method to solve the differential equation of temperature variation. Although it is a linear equation, the computation cost was relatively high, used with an iterative optimization method such as metaheuristics. Hence, the ANN was also used to predict the internal temperature of the TES, instead of using the physical model.

In a structure of the ANN, some of the following variables were set as input data:

1) Water temperature at each node (1–20).

2) Mass flow rate of Pumps 5 and 6.

3) Inlet temperature of charging and discharging fluid ($T_{out,ls,HEX3}^{t-1}$: outlet temperature of low temperature circulation side of HEX3, $T_{out,hs,HEX5}^{t-1}$: outlet temperature of high temperature circulation side of HEX5).

The output variable was the water temperature of each node (1–20). In general, the number of nodes at a hidden layer is more than the output layer. Hence, 30 nodes were used and the number of hidden layers was set to three, as shown in Fig. 7-4.
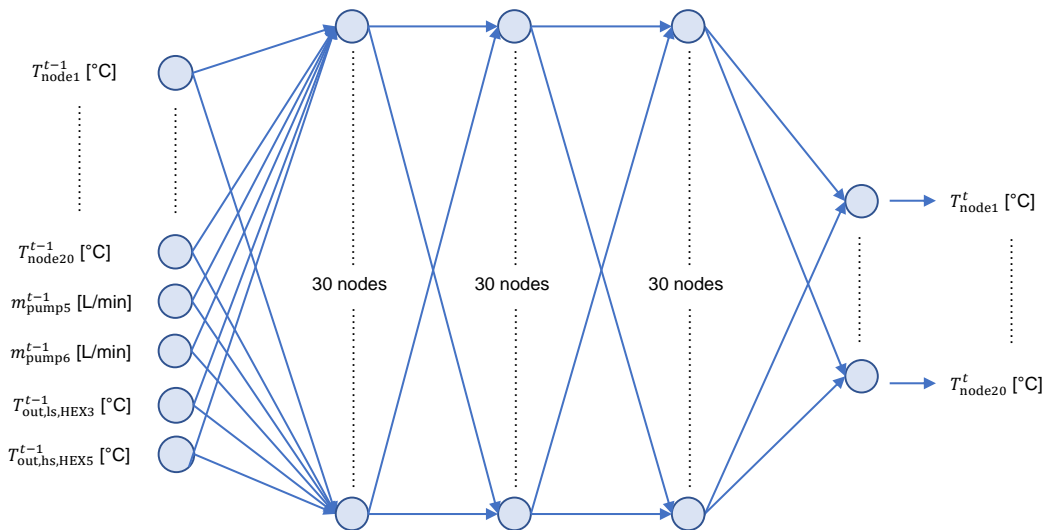
Fig. 7-4 | A structure of ANN$_{\text{TES}}$

7.3 Optimization method

7.3.1 Problem formulation

The objective function is as follows:

$$\text{minimize } f = \sum_{t}^{N_{\text{th}}} \left\{ p_E^t \left(\sum_{k=1}^{13} c_{E,\text{pump},k}^t + \sum_{k=1}^{2} c_{E,\text{GSHP},k}^t + c_{E,\text{HRAR}}^t \right) \right.$$
$$\left. + p_G^t \left(c_{G,\text{CHP}}^t + c_{G,\text{HRAR}}^t \right) \right\} \tag{7-2}$$

where t denotes the time step (=1 [h]), N_{th} denotes the time horizon (=24 [h]), and p_E^t and p_G^t denote the price of electricity and gas, respectively. The gas price was fixed at 87.2 yen/m³. $E_{\text{pump},k}^t$ denotes the electricity consumption of the k th pump [kW], $c_{E,\text{GSHP},k}^t$ denotes the electricity consumption of the GSHP (k =1: GSHP$_{\text{cl}}$, k =2: GSHP$_{\text{ht}}$), $c_{E,\text{HRAR}}^t$ denotes the electricity consumption of the HRAR and its cooling tower [kW]. $c_{G,\text{CHP}}^t$ and $c_{G,\text{HRAR}}^t$ were the gas consumption of the CHP unit and the HRAR [m³/h], respectively.

The decision variables were as follows:

1) Mass flow rate of the pumps except for Pumps 8, 12, and 13.

2) Power generation ratio of the CHP unit

3) Distribution rate of SM1

4) Distribution rate of SM6

The number of decision variables were 288 (=12 types × 24 hours). All decision variables were normalized 0 to 1 with a 5% resolution because an actual operation system could not continuously set the parameters.

Some constraints were set as follows:

1) The circulating water temperature should be less than 100 °C.

2) The above temperature should be greater than 3 °C.

3) The outlet temperature from both the GSHP$_{\text{cl}}$ and the GSHP$_{\text{ht}}$ should be less than 40 °C.

4) The above temperature should be less than 3 °C.

5) The supply water temperature through HEX6 should be greater than 60 °C because the required water temperature of the secondary system was set to 60 °C.

6) The supply water temperature through HEX7 should be less than 7 °C because the space cooling secondary system required 7 °C cooling water.

The total number of constraints were 192. If the full-search algorithm was conducted, the computational complexity was 20^{288}. This complexity was not realistic for an ordinal computer. Hence, εDE-RJ was used to find an optimal or quasi-optimal solution with the iterative calculation.

7.3.2 Parameters of εDE-RJ

The number of the individual population was 40. The number of generations was 2,000. The mutation rate was set to 0.5 and the ε_{DE} should be zero at 70% of the number of generations.

7.4   Results and discussions

7.4.1 Optimal operation of the domestic hot water supply system

Fig. 7-5 shows the optimal operation of the domestic hot water supply system. $P_{GSHP_{ht}}$ denotes the thermal output of GSHPh [kW], P_{TES} denotes the thermal output from TES through pump 8 directly, and $T_{HEX6toD_{hw}}$ denotes public water temperature from HEX6 to the secondary system after rising at HEX6. $T_{SM5toHEX6}$ denotes the hot water inlet temperature of HEX6 from SM5. m_{pw} denotes mass flow rate of the public water [L/min] and m_{HEX6} denotes mass flow rate through HEX6 [L/min]. p_{E} denotes the price of purchased electricity [yen/kWh].

As shown in Fig. 7-5, $T_{HEX6toD_{hw}}$ was always greater than 60 °C. Thus, the supply water temperature constraint was met completely. Although $T_{out,hs,HEX6}$ was not controlled as a decision variable, $T_{out,hs,HEX6}$ was always greater than 40 °C. Hence, the hot water stored thermal energy, based on the public water inlet temperature of HEX6, was 25.5 °C. This result shows that the thermal energy is stored not only in the TES but also inside of pipes.

In terms of the heat source machine operation, the discharged energy from TES was provided through Pump 8 to HEX6 when the price of purchased electricity was high, especially between 2 p.m. and 4 p.m. During these time intervals, HRAR did not work at all.

Therefore, it is concluded that εDE-RJ could optimize the hot water system considering the price variation while maintaining the constraints.
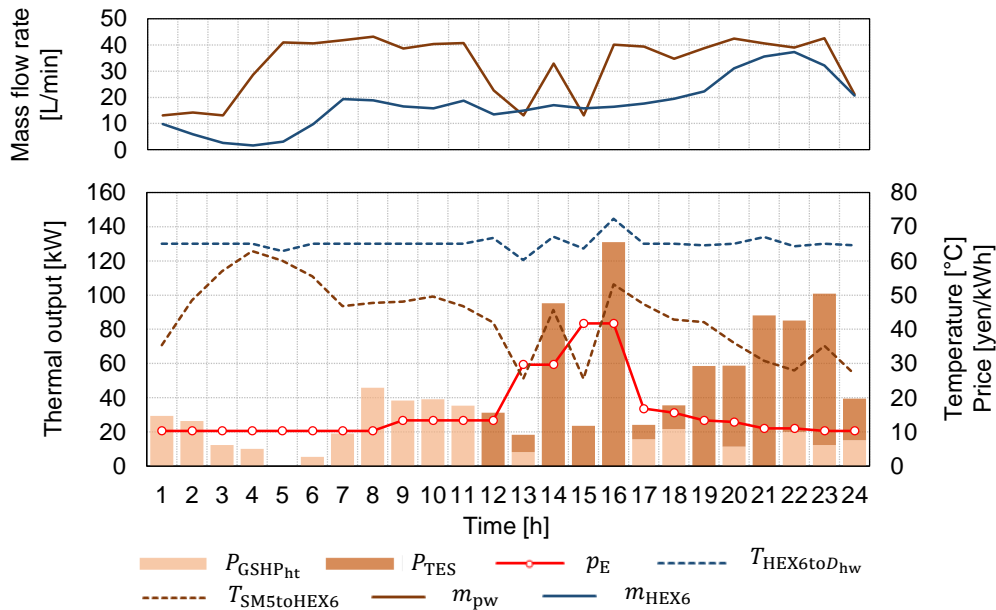
Fig. 7-5 | Optimization results of the domestic hot water

7.4.2 Optimal operation of the cooling system

Fig. 7-6 shows the result of the cooling system operation. m_{hs} and m_{ls} denote the mass flow rates of both the temperature high side circulation and the low side circulation [L/min], respectively. $T_{in,hs,HEX7}$ and $T_{out,hs,HEX7}$ denote the inlet and outlet temperatures of the temperature high side circulation, respectively. $T_{in,ls,HEX7}$ and $T_{out,ls,HEX7}$ denote the inlet and outlet temperature of temperature low side circulation, respectively. P_{HRAR} and P_{GSHPc} denote the thermal output of the HRAR and the GSHPc [kW], respectively. Fig. 7-7 displays the conceptual image explaining the above variables. $T_{in,ls,HEX7}$ was always 6 °C because the outlet temperature of chilled water from the heat source machines was fixed at 6 °C. In addition, $T_{out,hs,HEX7}$ was always less than 7 °C. This shows that the temperature constraint was completely met. During 1 p.m. to 10 p.m., $T_{out,hs,HEX7}$ was approximately 7 °C because the cooling demand at that time was higher than the other time steps. Hence, this operation could reduce the thermal output of the heat source machines to minimize primary energy consumption as well as minimizing operating costs while maintaining $T_{out,hs,HEX7}$ at less than 7 °C.
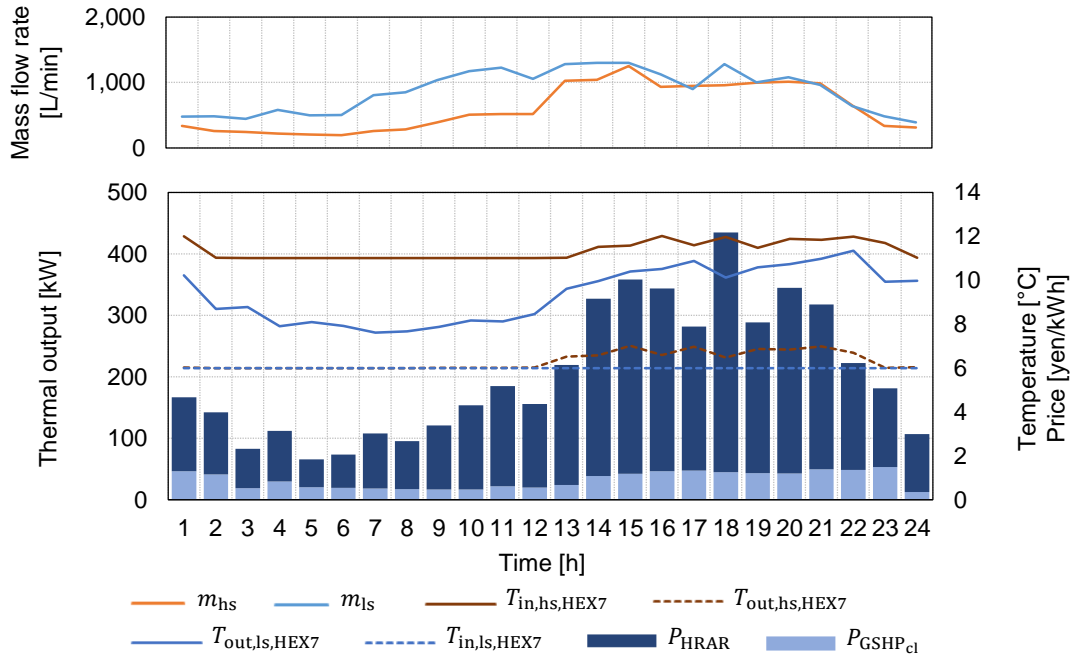
Fig. 7-6 | Optimization result of the cooling system
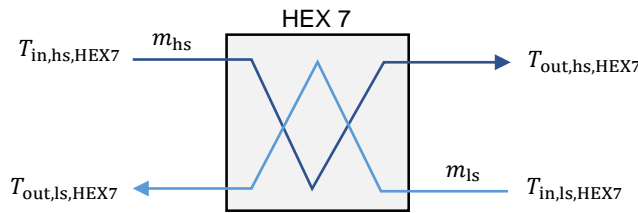
Fig. 7-7 | Conceptual diagram of variables

7.4.3 Validation of the ANN models for computation costs reduction and prediction accuracy

Due to the utilization of the ANN, the total computation cost could be reduced by 95.7% from 132 s of the ILS model to 5.62 s of the ANN model per generation. The calculation was conducted on an ordinal PC with CPU Core i7-6700 (3.40 GHz) and RAM 16 GB using MATLAB R2016a with Parallel Computing Toolbox and Neural Network Toolbox.

In ANN_{GSHP}, the computation cost was reduced by 76% from 0.97 s to 0.23 s per generation. The accuracy of the results were 0.04 °C and 0.10 °C for the GSHPc and GSHPh, respectively. As shown in Fig. 7-8, the temperature variations of the GSHPc (Fig. 7-8(a)) and the GSHPh (Fig. 7-8(b)) were predicted properly.
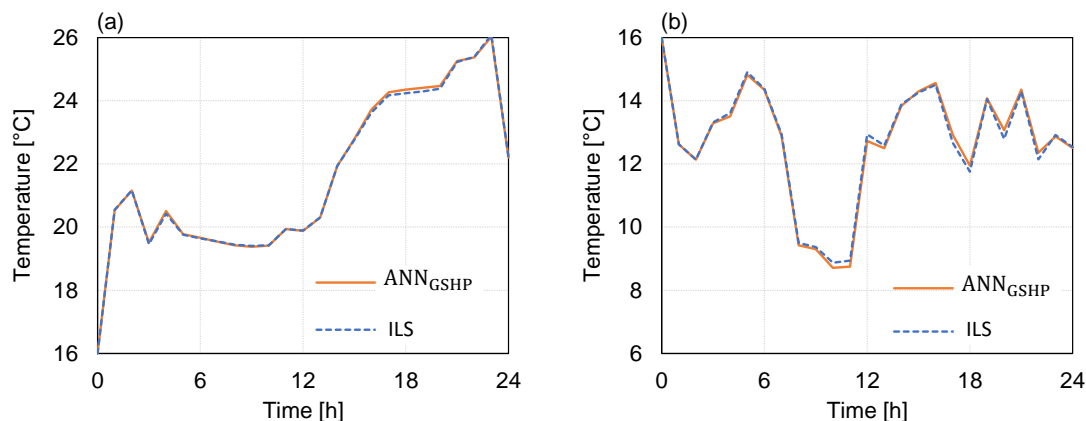
Fig. 7-8 | Prediction result of the ANN$_{BHE}$: a) variations of circulating water temperature of the GSHP$_{cl}$. An orange colored line denotes the result of the ANN$_{BHE}$ and a blue colored line denotes the result of the ILS. b) variations of the circulating water temperature of the GSHP$_{ht}$. The orange and blue lines denote the same as a).

Fig. 7-9 and Fig. 7-10 show the predicted results of the 20 layers. Fig. 7-9(a) to (j) describe the temperature variation of the 1st to the 10th layers. Fig. 7-10(a) to (j) describe the temperature variation of the 11th to the 20th layers.

Although the temperature variation of the top layer (layer 1) was the most intense, the tolerance between the target value and the predicted value was small. A mean value of the tolerance of the first layer was 0.67 °C. In general, the top layer has the hottest water in terms of hot water storage. Hence, it is important that the predicted accuracy of the top layer is high.

In contrast, layers 4 and 5, as shown in Fig. 7-9(d) and (e), respectively, had relatively large differences between the target and predicted values. The reason is that the return water temperature from HEX5 was around 40 to 60 °C at the time steps. It makes the layer 4 and 5 inlet layers of the return water at the time. Hence, the temperature variation is higher than the other layers, and the ANN could not predict the exact temperatures. Further, the prediction tolerance had increased gradually from noon to the end of the day, as the cooling and hot water demand increased(shown in Fig. 7-11). In particular, the upper layer's accuracy was decreased. This is due to the temperature variation through HEX5 and HEX6 being high and affecting the prediction accuracy. However, the tolerance affected only 0.02% of the daily operating costs. Hence, the advantage of a reduction in computation time of the ANN is greater than the tolerance of predicted values in this case.

Finally, we should focus on the lower layers, such as layers 16 to 20. Basically, the temperature variation of these layers was not high compared to the other upper layers, because the initial temperatures of the TES were set to 30 °C, and the charging water temperature through HEX3 and the

return water temperature through HEX5 was often more than 35 °C. Hence, the lower layers could not be inlet layers at 24 hours, which stabilizes the temperature. As shown in Fig. 7-10(j), the predicted variations of the ANN decreased compared to the target variation, especially at 10 p.m. and 11 p.m. This is because a prediction for stable values is a problem for ANN. Although the prediction accuracy from 1 a.m. to 6 p.m. was relatively high compared to the other upper layer, the accuracy at the last three-time steps were not precise.

In an actual system, the inlet layer and outlet layer are often fixed, e.g. as the top or bottom layer, in terms of construction adaptability or maintenance feasibility. Hence, the ANN structure in this chapter should be modified to predict the temperature variation at only reasonable and suitable layers. In the next chapter, revised input and output data of ANN are discussed through a district energy optimization.

7.5 *Conclusion*

This chapter investigates a method to optimize the operating schedule of multiple renewable heat sources, while reducing the computation costs. A key factor in this is that the energy system consists of some mechanisms that were highly affected by the temperature variation of the circulating fluid. Hence, we must think about the variation without fixing the temperature or the temperature difference between the inlet and outlet of the heat exchangers. However, naturally, the simulation that considered temperature variation incurred high computation costs. Therefore, the artificial neural network model was used to reduce the costs instead of using physical models.

Although the ANN incurred training computation costs, it could quickly calculate or predict the temperature variation. This makes the solution of the optimization problem simple, using an iterative optimization algorithm. Finally, the ANN models could reduce computation costs by 95% against the physical model. Due to this advantage of the ANN, εDE-RJ could find a quasi-optimal solution in a realistic computation time on an ordinal computer.

In fact, there are some additional modification methods for the ANN model to correctly predict the temperature variation of the TES. They will be proposed in the next chapters, 8 and 9, through a district energy optimization problem.
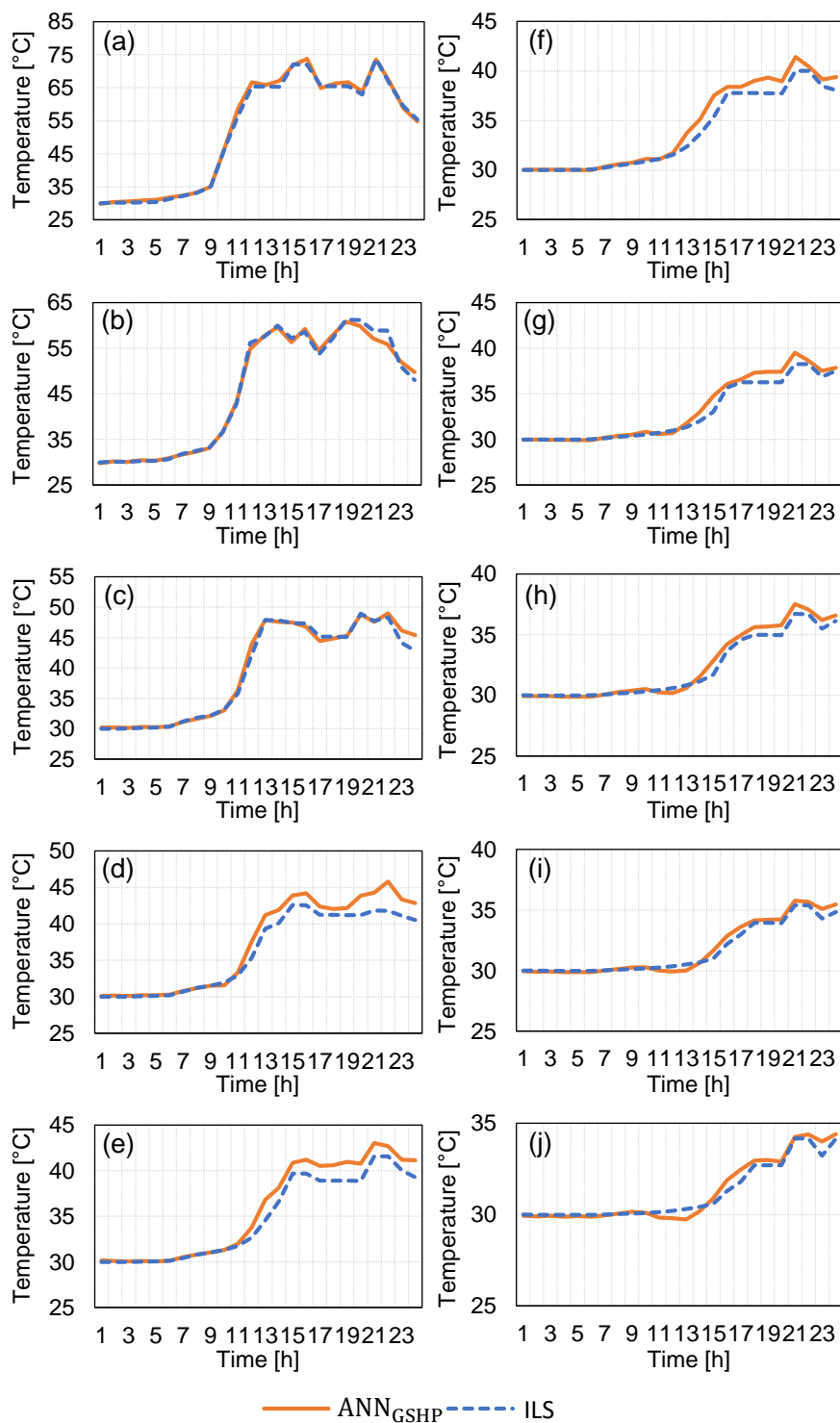
Fig. 7-9 | Predicted results of ANN_TES at the 1st note (a) to the 10th (j) note from the top layer.
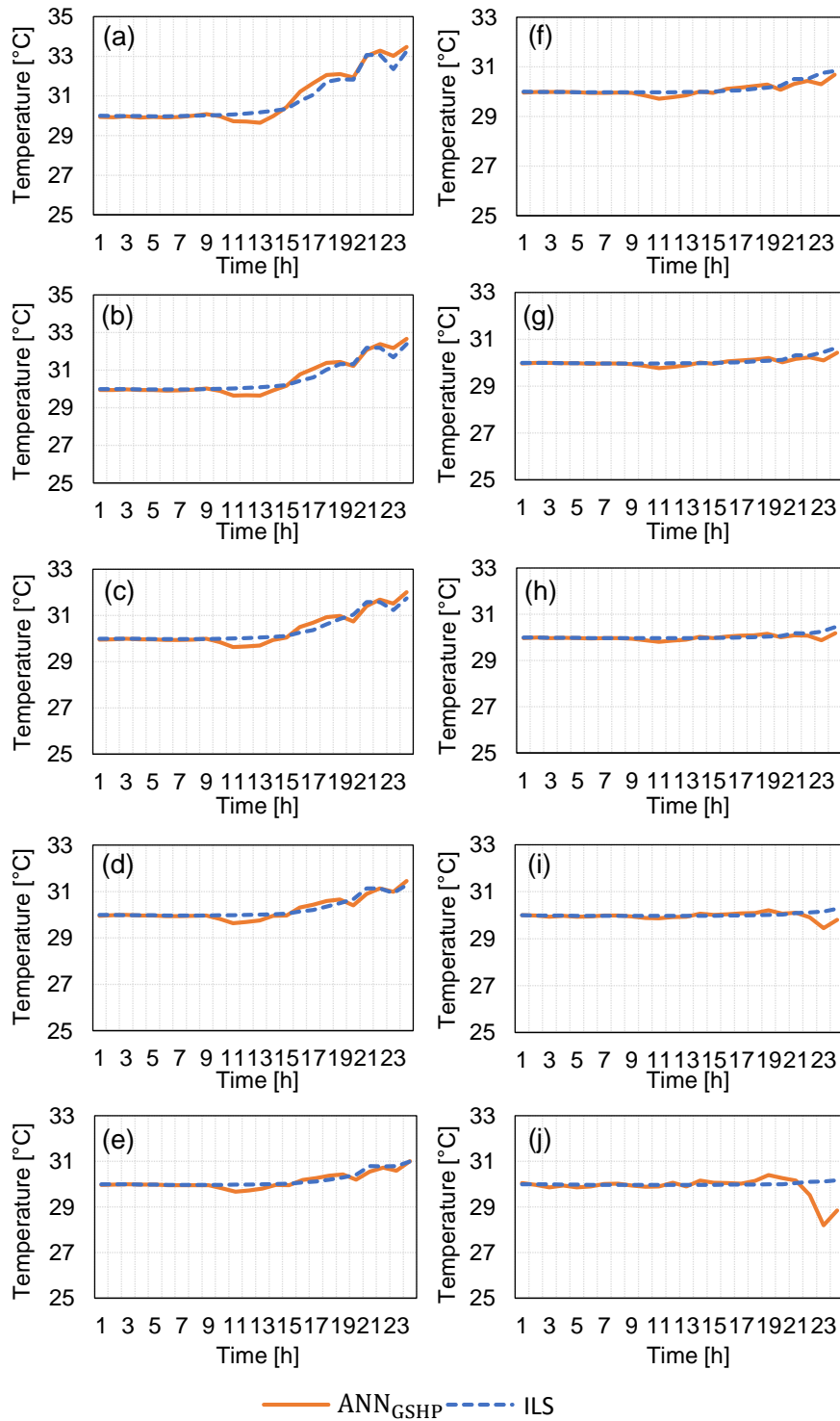
Fig. 7-10 | Predicted results of ANN$_{TES}$ at the 11th note (a) to the 20th note (j) which is the bottom layer.
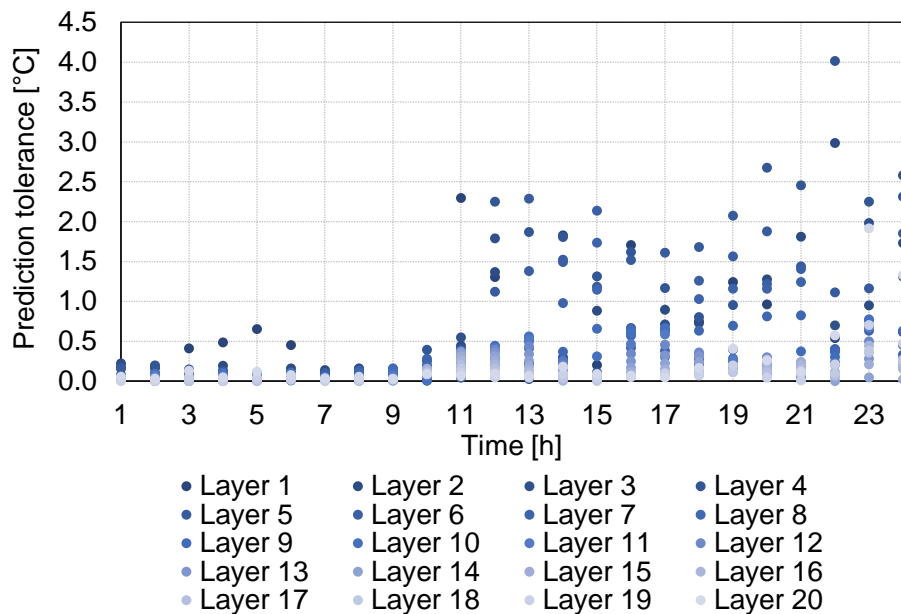
Fig. 7-11 | Predicted tolerance of each time step: layer 1 is the top layer and layer 20 is the bottom layer.

CHAPTER 8

The hybrid method of εDE-RJ with artificial neural network for optimizing a district cooling system

8.1   Introduction

District energy systems for cooling and heating have become increasingly popular to improve energy efficiency [199]. District heating and cooling systems (DHCs) have long histories compared to other district energy systems, such as the micro-distributed energy system [200,201] and heat sharing network [202]. Within these systems, many issues should be considered, such as peak-shifting, peak-cutting, resilience of the system, demand response, and dynamic pricing.

Properly controlling machines can be challenging in the context of district and building energy management. Generally, the operating schedule has depended on the operator, based on empirical observations rather than mathematical principles. However, as energy systems become more complex, empirical operation becomes more challenging. To address these issues, many studies have been performed, as presented in Section 1.2. These prior works have described limited case studies, simple linearized models, or continuous decision variables.

Therefore, in this chapter, the hybrid method proposed in Chapter 7.1 is applied to optimization problems, such as daily operation of a DHC system. The contents of this chapter is translated in English from my peer-reviewed article published in the transactions of the Society of Heating, Air-Conditioning and Sanitary Engineers of Japan [203].

8.2   Calculation conditions

8.2.1 Description of the target district and energy system

The target virtual district is comprised of six buildings, two office buildings, two commercial buildings, a hospital, and a hotel. The total floor areas of each building are as follows: office building 1 is 10,000 m², office building 2 is 15,000 m², commercial building 1 is 8,000 m², commercial building 2 is 12,000 m², the hospital is 20,000 m², and the hotel is 20,000 m².

The DHC plant was placed at the same location as office building 1. The plant has multiple heat source machines, which generate cooling and heating for the buildings through a district pipe network, consisting of a central pipe (Pipe 7 in Fig. 8-1) and six branch pipes (Pipe 1 to Pipe 6). The cooling and heating are distributed through Pipes 2–6 after Pipe 1, as shown in Fig. 8-1. The distance between each building is fixed at 50 m and the pipes are set at right angles within the district.

Fig. 8-2 shows the system configuration of the district plant. There are nine heat source machines, three centrifugal refrigerators (CR1, CR2, and CR3), two air-source heat pumps (ASHP1 and ASHP2), two gas heat pumps (GHP1 and GHP2), and two absorption refrigerators (AR1 and AR2). Thermal energy storage (TES), e.g., stratified water tank, is also included. Each heat source machines has an

associated pump. The refrigerators (CR1–CR3 and AR1–AR2) have associated cooling towers and cooling water pumps. The number of cooling towers was determined as follows. First, the rated mass flow rate of one cooling tower was fixed to 2,000 L/min. Second, the number of cooling towers was determined to meet the rated mass flow rate of the refrigerator. For example, when the rated mass flow rate of cooling water from CR1 is 8,600 L/min, five cooling towers are required.

The component specifications are described in Table 8-1.
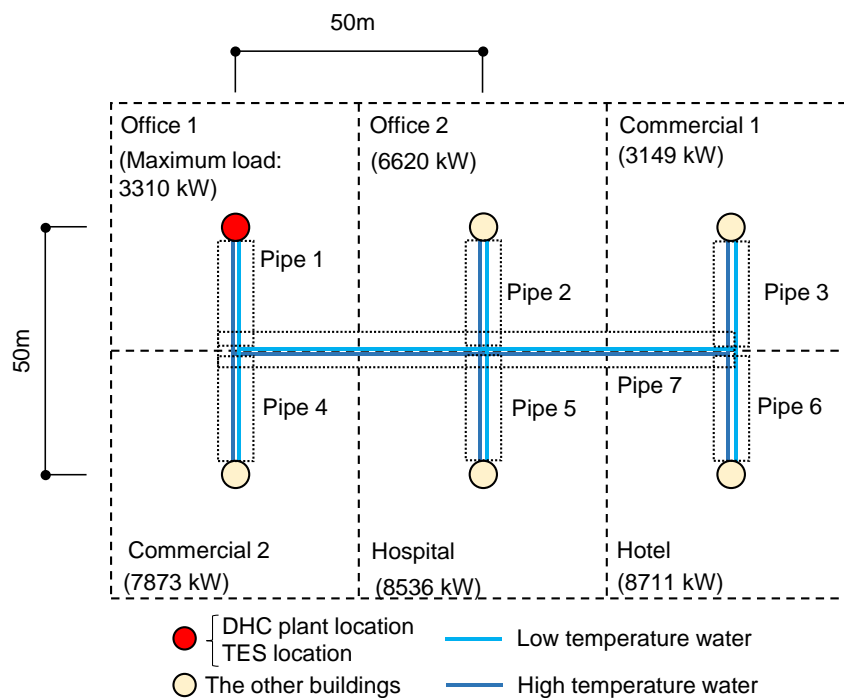
Fig. 8-1 | Building and plant locations.
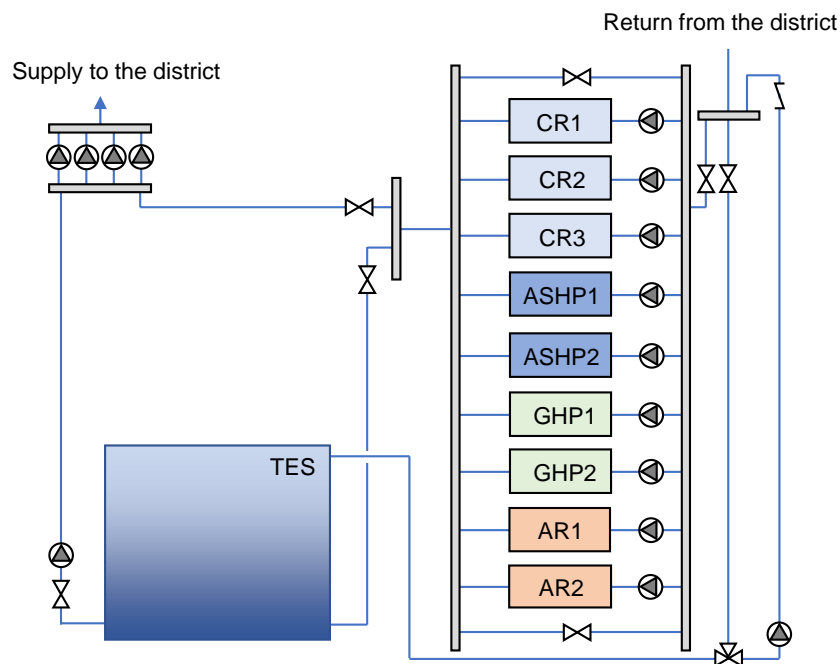
Fig. 8-2 | System configuration of the plant.

Table 8-1 | Specifications for each component.

Thermal energy storage (TES)	Rated capacity*	50,000	kWh
	Maximum mass flow rate of charging and discharging fluid	38,364	L/min
Centrifugal refrigerator (CR1; CR2; CR3)	Rated cooling capacity	5,000; 3,400; 3,000	kW
	Rated COP	5.8	
	Rated mass flow rate of cooling water	16,950; 11,526; 10,170	L/min
Absorption refrigerator (AR1; AR2)	Rated cooling capacity	2,000; 1,500	kW
	Rated gas consumption	118.6; 88.95	m³/h
	Rated electricity consumption	17.2; 12.9	kW
	Rated mass flow rate of cooling water	9229.8; 6922.4	L/min
Air-source heat pump (ASHP1; ASHP2)	Rated cooling capacity	2,000; 1,500	kW
	Rated COP	3.59	
Gas heat pump (GHP1; GHP2)	Rated cooling capacity	1,600; 1,200	kW
	Rated gas consumption	114.08; 85.56	m³/h
	Rated electricity consumption	43.36; 32.52	kW

* Note that the TES rated capacity was calculated using a 10 °C temperature difference between the top and bottom nodes.

8.2.2 Pressure drop between the central and branch pipes

In accordance with [204,205], heat loss from each central and branch pipe was calculated using the Darcy-Weisbach Equation as follows:

$$\Delta\tau_{\text{pressuredrop}} = \frac{0.0055\left\{1 + \left(20000\frac{\alpha_{\text{pipe}}}{2r} + \frac{10^6}{\text{Re}}\right)^{1/3}\right\}}{2r} \times \frac{\rho v^2}{2} \tag{8-1}$$

where, $\Delta\tau_{\text{pressuredrop}}$ is the pressure drop per meter [Pa/m], ρ is water density (1,000 kg/m³), r is the pipe radius, v is fluid velocity (2.0 m/s), and α_{pipe} is the pipe wall equivalent roughness (2 × 10⁻⁴). The radius of each pipe is determined using the maximum mass flow rate and the temperature difference between the inlet and outlet of each pipe. First, the maximum cooling demand of each building ($D_{\text{max,cl},i}$) is determined using Eq. (8-2). Subsequently, the maximum demand and temperature difference ($T_{\text{in}} - T_{\text{out}}$) are used to determine the maximum mass flow rate for each pipe as follows:

$$D_{\text{max,cl},i} = \max\left(D_{\text{cl},i}^1, \dots, D_{\text{cl},i}^{24}\right) \tag{8-2}$$

$$m_i = \frac{D_{\text{max,cl},i}}{4186 \times (T_{\text{in}} - T_{\text{out}})} \tag{8-3}$$

where, i denotes the building number.

Finally, the pipe radii are determined using m_i and velocity (v). The temperature difference depends on the set point of the outlet temperature of the heat source machines and the return temperature set point from the secondary system. Hence, the pipes radii varied in accordance with the set points in each case study.

$\Delta\tau_{\text{pressuredrop}}$ can be calculated using the previously defined parameters. After $\Delta\tau_{\text{pressuredrop}}$ is calculated for each pipe, $\Delta\tau_{\text{pressuredrop}}$ is multiplied by two to determine the total distance of the supplying and returning pipes. In addition, the doubled $\Delta\tau_{\text{pressuredrop}}$ is then multiplied by 1.5 to account for a local pressure drop and 50 kPa is added to address the heat exchanger pressure drop between the branch pipes and buildings. Finally, the final $\Delta\tau_{\text{pressuredrop}}$ is used to determine the rated pump pressure for four parallel pumps. Although there were some optimization problems, e.g., pump allocation, the four pumps are fixed as parallel in this study.

8.2.3 Heat loss between the central and branch pipes

The pipe material is 20 mm thick stainless steel, which has a heat transfer coefficient of 20 W/(m·K). In addition, the pipe was wrapped with 40 mm thick insulation material, which has a heat transfer coefficient of 0.021 W/(m·K). Heat loss, or heat gain during cooling, is determined as follows:

$$\Delta \tau_{\text{heatloss}} = \frac{2\pi L(T_{\text{sr}} - T_{\text{cw}})}{\sum_{i=1}^{2} \frac{1}{\lambda_i} \ln \frac{r_{i+1}}{r_i}} \tag{8-4}$$

where L is the pipe lengths [m], T_{sr} is the temperature of the surrounding environment [°C], T_{cw} is the chilled water temperature in the pipes [°C], r_i is radius [m] (r_1 is the radius of the stainless pipe and r_2 is the total radius of the stainless pipe and insulation material). T_{sr} is fixed at 20 °C because the DHC pipes are located underground, where the temperature is relatively stable compared to atmosphere temperature.

The heat loss can be considered as additional heat demand for the DHC plant. Here, the additional heat demands are: 0 kW for office building 1 because the plant is located onsite, 2.37 kW for office building 2, 3.25 kW for commercial building 1, 1.41 kW for commercial building 2, 2.44 kW for the hospital, and 3.36 kW for the hotel. These values are small compared to the net demand of each buildings because of the insulation material. For example, without insulation, the additional heat demand of the hotel would be 123 kW. Hence, the insulation material results in a significant reduction in heat loss.

8.2.4 Demand and price profiles

The calculation time horizon and time interval are set to 24 hours and 1 hour, respectively. Demand profiles were referenced from [170] and atmosphere temperature was referenced from [171]. Although the office buildings and commercial buildings have no cooling demands around midnight (12 a.m. to 3 a.m.), early morning (4 a.m. to 7 a.m.), and late evening (10 p.m. to 11 p.m.), the hospital and hotel have cooling demands for the full 24 hours. In addition, the hotel demand curve is clearly different from the other demand curves. For example, the cooling demand before noon is low, but the demand after 7 p.m. is clearly higher than the other building demands.
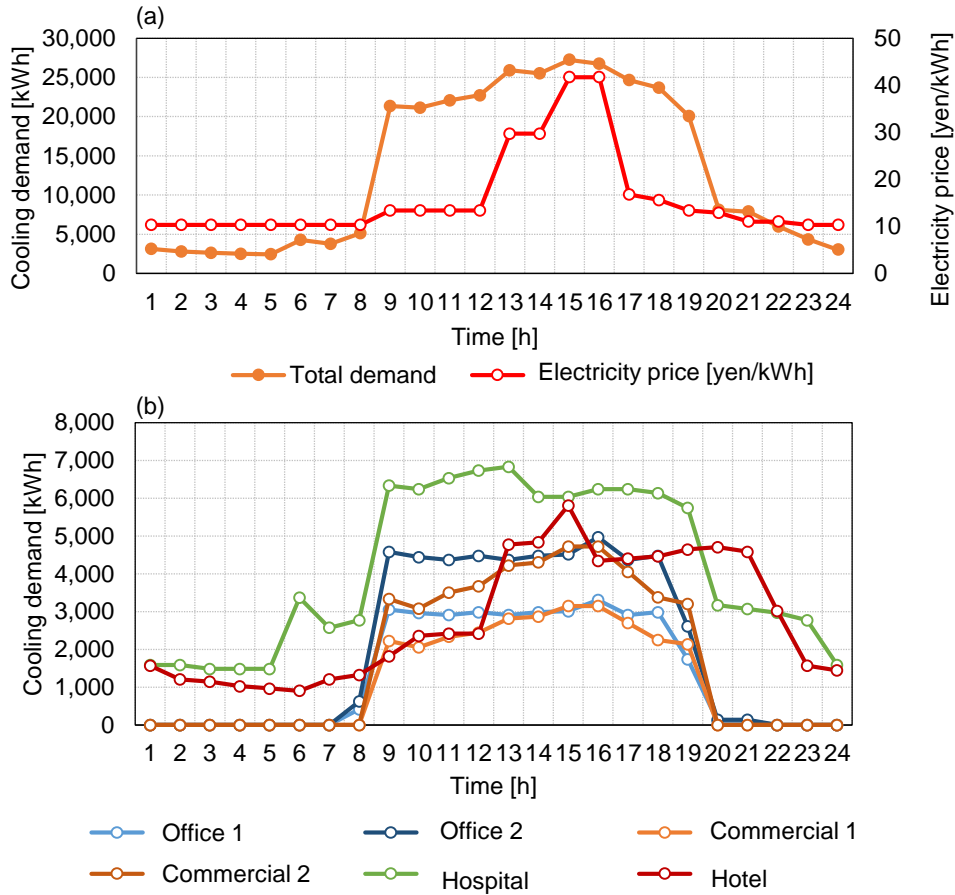
Fig. 8-3 | Demand and electricity price profiles: a) the total cooling demand for the district and price variation for purchased electricity and b) cooling demand for each building.

8.2.5 Regression models to predict inside TES temperature

The stratified TES was based on [147] and the number of nodes was set to 20. An inlet node for charging operation and an outlet node for discharging operation are fixed to a bottom node. An outlet node for charging operation and an inlet node for discharging operation are fixed to a top node.

Here, only the bottom temperature was required to determine when to cease discharging the TES because the bottom temperature is generally considered the TES outlet temperature. The outlet temperature must be less than a certain temperature (e.g. a set point temperature) required by the secondary system. An upper set point of chilled water temperature of the secondary system is usually 6 °C or 7 °C in actual energy systems. Hence, optimal operation should control the bottom temperature to less than the set point temperature.

The rated capacity of the TES is determined as follows:

1) The initial temperature of all nodes is set to the return temperature from the secondary system, e.g., 11 °C. Hence, the initial remaining thermal energy in the TES is zero.

2) An upper bound for the outlet chilled water temperature from the TES is set to 6 °C. Hence, the difference between 6 °C and 11 °C results in unavailable remaining energy in the TES. In practice, this is termed the dead water region.

3) The amount of daily heat shortage is 37,000 kWh in this district because the total cooling capacity from all heat sources is 20,500 kW. Thus, the TES should have a rated capacity more than the shortage, while considering the dead water region. In this study, the dead water region for the charging mode is set to 3%.

4) The available capacity is 37,000 kWh and the theoretical capacity is 38,144 kWh. The TES volume is determined using the theoretical capacity and a temperature difference of 5 °C.

The final volume is 8,416 m^3, 23.7 × 23.7 m in length and width and 15 m tall.

To reduce computational cost when using the physical model described in Chapter 2, some approximation methods are utilized. First, some data were input:

Input data 1: the maximum stored heat in the TES for a day ($S_{\text{max,TES}}$).

Input data 2: the remaining heat from 3 p.m. to 7 p.m. ($S_{\text{TES}}^{15}, \dots, S_{\text{TES}}^{19}$).

Input data 3: the bottom temperature from 3 p.m. to 7 p.m. ($T_{\text{bottom}}^{15}, \dots, T_{\text{bottom}}^{19}$).

Second, four methods are used as regression models: 1) a multiple linear regression model (MLR), 2) a coefficient assimilation using m-PSO, 3) utilizing the curve fitting toolbox in MATLAB (CF), and 4) an artificial neural network (ANN).

To generate a training dataset, 2,000 available operating schedules are created using random numbers, as shown in Fig. 8-4.

Then, 10,000 combinations of $S_{\text{max,TES}}$, S_{TES}^t, and T_{bottom}^t are exploited from the 2,000 operating schedules. To train the models, 80% of the 10,000 combination dataset are used, and the remaining 20% are used to evaluate the models, as shown in Fig. 8-5. In the m-PSO and CF regression models, the following quadratic equation is considered:

$$T_{\text{bottom,TES}}^t = \alpha_{1,\text{TES}} S_{\text{max,TES}}^2 + \alpha_{2,\text{TES}} S_{\text{max,TES}} + \alpha_{3,\text{TES}} (S_{\text{TES}}^t)^2 + \alpha_{4,\text{TES}} S_{\text{TES}}^t + \alpha_{5,\text{TES}} \tag{8-5}$$

Where the m-PSO and CF models optimize the coefficients ($\alpha_{1-5,\text{TES}}$) to minimize the sum of the squared errors of the prediction. Fig. 8-5 shows the results from the four regression models. Although the coefficients of determination (R^2) for each regression model are greater than 90%, the ANN clearly produces the best results. In addition, the online learning in the ANN model does not need batch
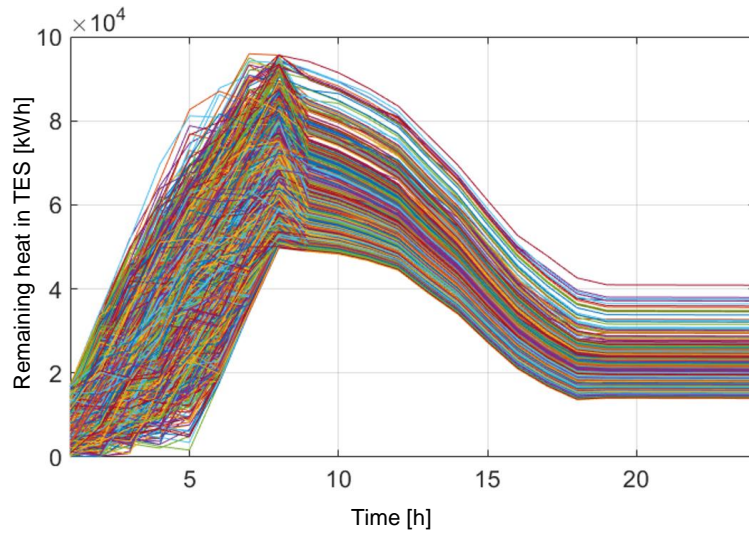
Fig. 8-4 | 2,000 operating patterns created using random numbers.
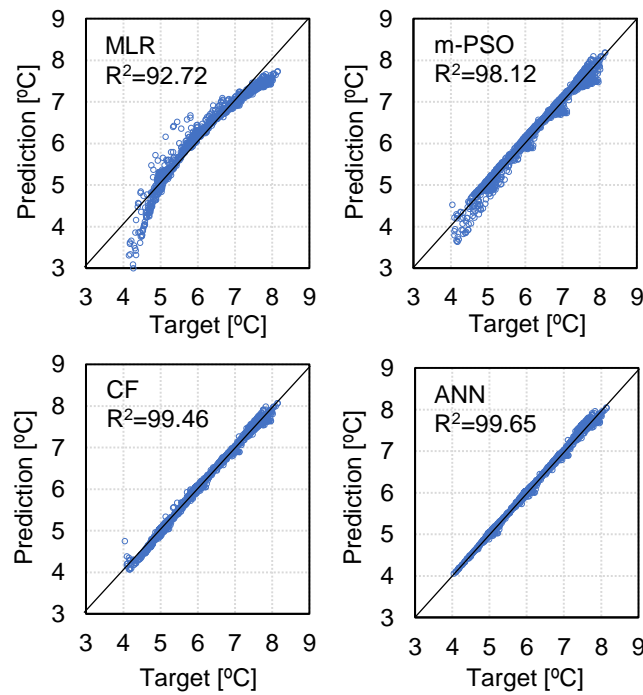
Fig. 8-5 | Prediction results from each regression model.

learning, which always has high computational costs, whereas the other three methods require this batch learning strategy. Therefore, the ANN model is superior to the other three methods in terms of prediction accuracy and training computational costs.

8.3   Optimization method

8.3.1 Problem formulation

The objective function minimizes the daily operating costs of the district as follows:

$$\text{minimize } f = \sum_{t=1}^{24} \left(p_E^t \sum_{i=1}^{9} c_{E,i}^t + p_G \sum_{j=1}^{4} c_{G,j}^t \right) \tag{8-4}$$

where, p_E^t and p_G are the prices of electricity [yen/kWh] and gas [yen/m³], respectively. Here, p_G is fixed at 87.2 yen/m³. $c_{E,i}^t$ and $c_{G,j}^t$ are electricity [kW] and gas [m³/h] consumption at time step t, respectively. i and j denote the number of machines that consume electricity and gas, respectively. $c_{E,i}^t$ incorporated the electricity consumption of the machine, cooling tower fan, and pumps for cooling and chilled water. The constraints are as follows:

$$\sum_{m=1}^{9} P_m^t \geq D_{cl}^t \tag{8-5}$$

$$\max\{T_{bottom}^{15}, \dots, T_{bottom}^{24}\} \leq 6.0 \tag{8-6}$$

Eq. (8-5) shows the heat balance between the total thermal output of the heat source machines and total cooling demand of the buildings, including the additional heat. T_{bottom}^{15-24} indicates the bottom temperature of the TES. In addition, CR and AR should continue working at least two or three consecutive hours, respectively, in accordance with actual machine conditions.

There is a total of 216 decision variables (8 machines × 24 hours) in accordance with the problem formulation shown in Eq. (8-4). If the full-search algorithm is used, the available combinations of decision variables would be $51^{8 \times 24}$, i.e., 51 operating load rates with 2% resolution, 8 machines, and 24 hours. However, the metaheuristics method does not always try the maximum number of combinations due to the stochastic searching algorithm.

This optimization problem has the following features.

1) Dependence of the decision variables

As mentioned in Chapter 1, the dependence of the decision variables creates challenges. In this chapter, the time dependence of the TES, CR, and AR machines are the dependence of the decision variables. The dynamic programming method (DP) has been often applied to this type of the problem. However, the DP's computational complexity depends on the number of decision variables, as indicated in Chapters 1 and 2. For the DP to be used, the complexity would be 1.51×10^{25} ($= 24 \times 21^{9 \times 2}$); therefore,

it is unrealistic to use DP in this problem.

2) Discrete decision variables

All decision variables are formulated as discrete variables. Hence, a typical linear programming method was not applied because the method only handles continuous problems. Although mixed integer linear programming (MILP) could be applied, there are 9792 decision variables, 51 operating load rates with 2% resolution × 8 machines × 24 hours. Hence, the using MILP is unrealistic due to the total number of decision variables and nonlinearity of machine characteristics.

1. Adaptability for utilizing complex regression models

To reduce computational cost, ANN is a complex mathematical model that has been utilized in this chapter. ANN could not be absolutely adopted if MILP was also used. Hence, an optimization method with high adaptability is strongly needed.

8.3.2 Parameters of the εDE-RJ

The εDE-RJ can manage all of the described features. The numbers of generations and individuals are set to 4,000 and 40 in this chapter. The ε_{DE} value should be zero at 70% of the maximum generation.

8.4   Results and discussions

8.4.1 Setting case studies

Four case studies are conducted. In Case 1, an empirical operating schedule is considered with a fixed temperature difference of 10 °C and chilled water outlet temperature of the machines fixed at 4 °C. In Case 2, the εDE-RJ optimizes an operating schedule with the same temperature difference and the same outlet temperature as Case 1. In Case 3, the εDE-RJ is conducted with a 15 °C temperature difference and 3 °C outlet temperature. This case considers the largest temperature difference to maximize TES capacity. In Case 4, εDE-RJ is conducted with the same conditions as Case 2 with the addition of a peak-cutting constraint. The results from all cases are shown in Table 8-2.

Table 8-2 | Results from the four conducted case studies

	Operating costs [yen/day]	Peak electricity consumption [kW]
Case 1	1,312,985	3,145
Case 2	1,172,943	3,088
Case 3	1,235,722	3,158
Case 4	1,223,094	2,562

8.4.2 Case 1

A scenario based operation of Case 1 is as follows:

1. Machine priority: when the electricity price is low between 1 a.m. and 12 p.m. and 5 p.m. to 12 a.m., the electric based machines are operated in priority. In particular, CR, which has the highest rated COP is top priority. When prices are high, from 1 p.m. to 4 p.m., the gas based machines, such as AR and GHP, are operated in priority. If the total capacity of the gas based machines does not meet the district cooling demand, CR also contributes.

2. TES operation: TES charges cooling heat by 8 a.m. and discharges it when prices are high, as shown in Fig. 8-6(a). In Case 1, the primary energy based COPs for CR, AR, ASHP, and GHP are approximately 1.0 to 2.0, 1.2, 1.5 to 1.7, and 1.0 to 1.2, respectively, as shown in Fig. 8-7(a). The daily operating costs are 1,312,985 yen/day and the peak electricity demand is 3,145 kW.
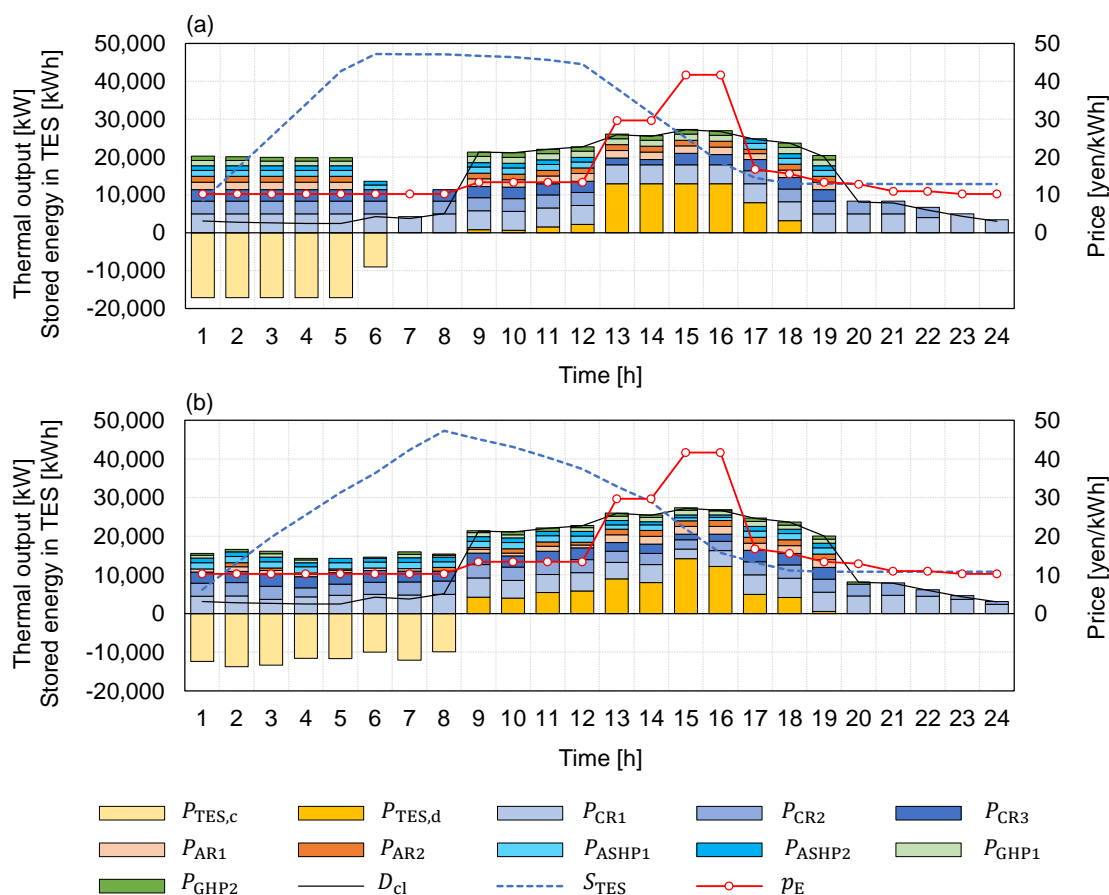
Fig. 8-6 | Operating schedules: a) Case 1 (empirical operation) and b) Case 2 (εDE-RJ)
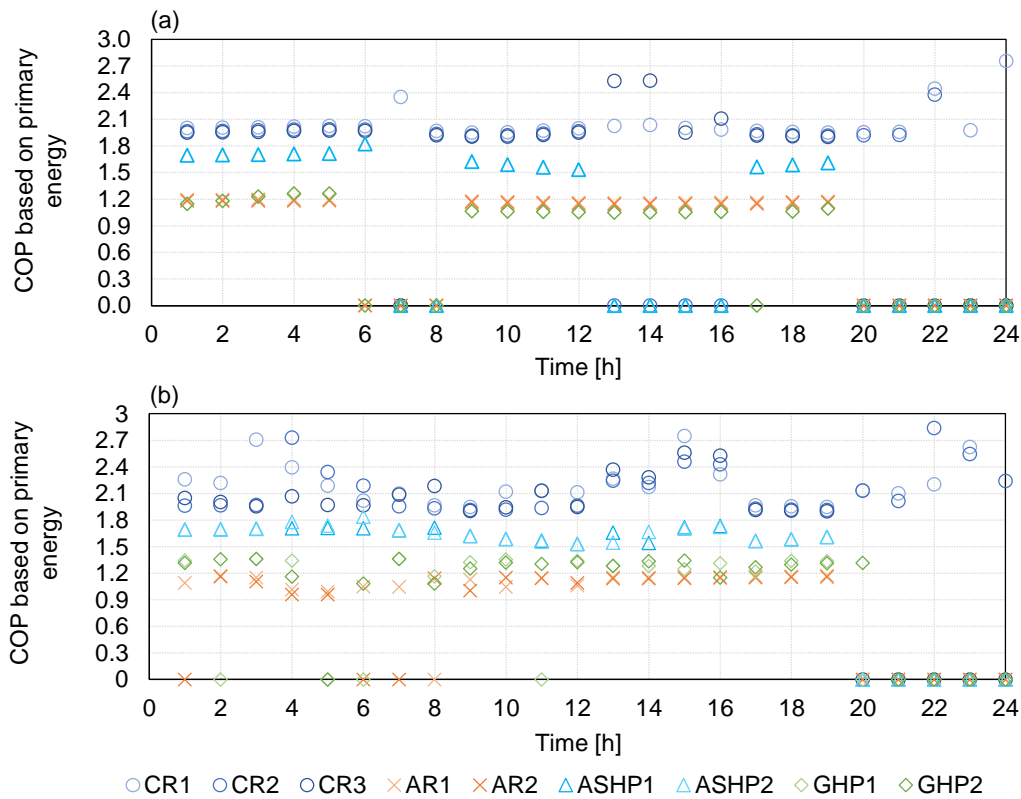
Fig. 8-7 | Hourly variation in COP for each heat source machine: a) Case 1 (empirical operation) and b) Case 2 (εDE-RJ)

8.4.3 Case 2

Fig. 8-6(b) shows the results from optimizing using the hybrid εDE-RJ - ANN method in Case 2. Although the multiple heat source machines generate cooling heat and charge the TES from 1 a.m. to 8 a.m., the operating load rates are not at the rated value. Because of the partial load operation, the COP from each machine is improved comparing to the result from Case 1, as shown in Fig. 8-6(a). The CR COPs are improved, from 2.0 to 2.1–2.7, due to the nonlinearity characteristics of CR. In addition, the GHP COP is especially improved, from 1.0 in Case 1 to 1.3 in Case 2.

Focusing on the optimal operation of TES, the TES discharges continuously from 9 a.m. to 6 p.m. In particular, the amount of discharged energy between 3 p.m. and 4 p.m. is greater than in the result from Case 1, and the discharged energy from 1 p.m. and 2 p.m. is less than in the result from Case 1.

The daily operating cost is 1,172,943 yen/day and peak electricity consumption is 3,088 kW, which is a 10.67% cost reduction compared to Case 1. Although peak electricity consumption is not included in the optimization problem, there is a 1.8% reduction compared to Case 1.

Fig. 8-8 and Fig. 8-9 show the temperature profiles inside the TES and the temperature variation of the bottom node of the TES, respectively. Here, the profile is unaffected by any disturbances because the simulation only depends on the physical model. The vertical axis indicates the node number and the horizontal axis indicates the temperature of stored water. The nonlinear lines indicate the time steps: the deepest color is the first time-step and the lightest color line is the last time-step. When the charging operation ceases, the temperatures of 9th to 20th node are 4 °C, while the 1st to 8th node are not 4 °C, e.g., the top node is 6.3 °C at 8 a.m. This observation indicates the presence of a dead water area. Furthermore, at the end of the discharging operation, such as at 24th time step, stored energy remains.

As shown in Fig. 8-9, the bottom temperature does not exceed 6 °C, which indicates that the constraint condition is completely satisfied while optimizing the operating schedule. At the end of the discharging operation, such as at 7 p.m., the temperature predicted with ANN is 5.88 °C, whereas the physical model result is 5.95 °C, with the same operating schedule as Case 2. Hence, ANN can be utilized for energy management because the prediction tolerance is only 0.07 °C.

The computational time is 615 s using MATLAB with the Parallel computing toolbox running on a Core i7-6700 (3.4 GHz) CPU with 16 GB of RAM. In comparison, the computation time is 7200 s when the physical model is used instead of ANN.
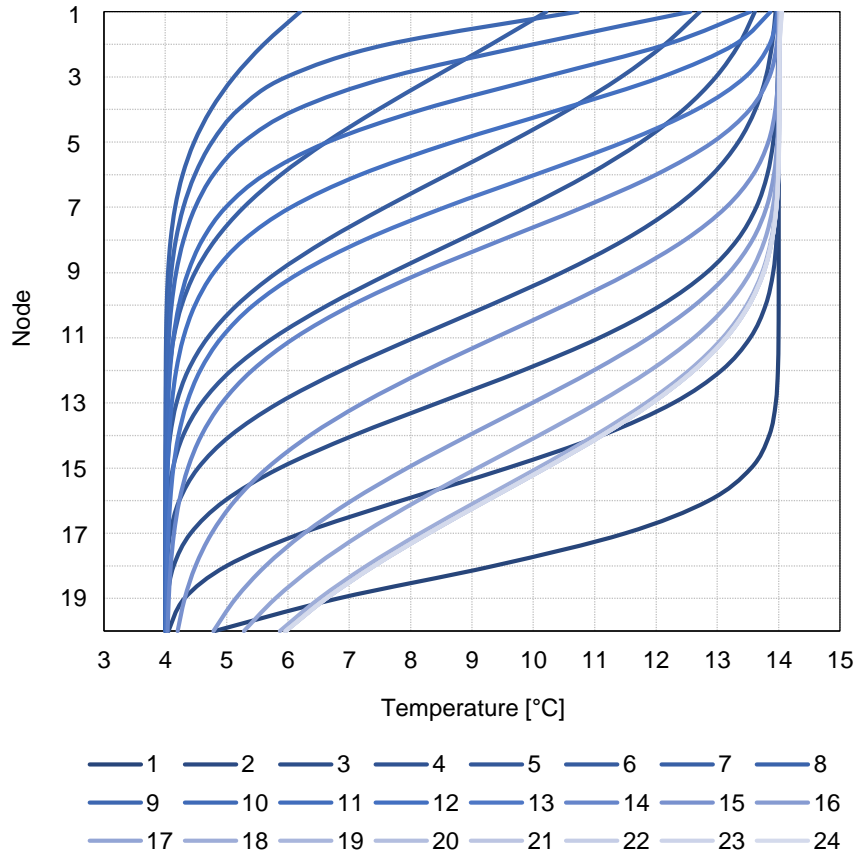
Fig. 8-8 | Temperature profiles inside the TES; colors vary from darker to lighter as time progresses from early time steps to the last time step.
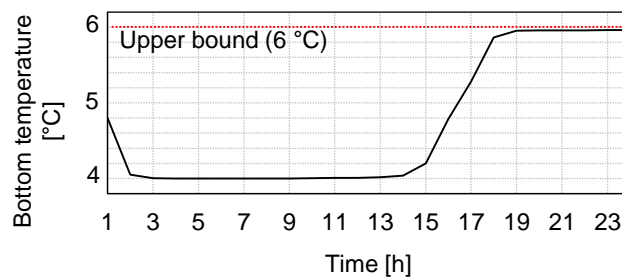
Fig. 8-9 | Temperature variation of the bottom node of the TES

8.4.4 Case 3

The temperature difference between the supply and returning fluid is set to the largest, 15 °C, in Case 3. The supply temperature is set to 3 °C. The daily operating cost is 1,235,722 yen/day, which is a 5.88% reduction compared to Case 1, but a 5.08% increase compared to Case 2. This difference is due to the large temperature difference, which requires more energy and causes a reduction in efficiency for each machine to generate cooling heat.

8.4.5 Case 4

This case requires cost optimization while reducing the peak electricity consumption more than 15% against Case 2. Significantly, the peak demand is directly associated with the base charge for electricity in Japan.

As shown in Table 8-2, the daily operating costs in Case 4 are 1,223,094 yen/day and the peak demand is 2,562 kW, a 17% reduction compared to Case 2. The multi-objective optimization proposed in Chapter 3 can be applied to this problem to minimize the operating costs and peak demand simultaneously. However, the peak demand should considered as a constraint instead of the objective function in the context of optimization stability and computation speed.

8.5   Conclusion

This chapter conducted an optimization of daily operating schedules for multiple heat source machines to minimize operating costs. The district energy system contains complex machines, such as time dependent equipment and thermal energy storage. The optimization method incorporated the εDE-RJ, a type of metaheuristic method, and ANN, a machine learning method. The εDE-RJ was used to identify a quasi-optimal solution and ANN was used to predict the bottom temperature of the TES while reducing computational cost.

The optimal operation identified using the εDE-RJ can reduce operating costs by more than 10% compare to empirical operation. The prediction tolerance of ANN was less than 0.1 °C. Hence, the accuracy of ANN is appropriate for use in an actual management system. The computational costs from using εDE-RJ with ANN showed a drastic reduction, more than 90%, compared to the physical model used.

Although ANN has many advantages, the ANN model is a complex mathematical model. Hence, common optimization methods, such as linear programming and quadratic optimization methods cannot integrate ANN. In contrast, εDE-RJ implement ANN easily, with superior optimization results

to the empirical operation and physical model, as described above. Therefore, εDE-RJ with ANN has the notable ability to optimize both building and district energy systems.

CHAPTER 9

District heat sharing energy optimization using the hybrid method of εDE-RJ with artificial neural network

9.1   Introduction

Although the district heating and cooling system (DHC) is one of the most common district energy systems, others, such as distributed energy or heat charging network systems, have received attention for reducing primary energy consumption and operating costs. The heat sharing network system is particularly promising due to its flexibility and resilience [10].

However, it is difficult to optimize an operating schedule for the district heat sharing network system as it consists of many components, such as heat source machines and pumps with nonlinear characteristics, as shown in Section 2.1. Hence, a hybrid εDE-RJ and ANN optimization method was applied to address the optimization problem. εDE-RJ was used to determine a quasi-optimal combination of thermal outputs from each heat source machine. ANN was used to predict variation in the bottom temperature of thermal energy storage (TES) to reduce the computation costs for calculation using a physical model, such as the ILS model. In addition, the Q-learning method [168,206], which has increasingly been used in recent years in building energy optimization studies [207–209], was used to compare the suitability of the hybrid and Q-learning methods for addressing this problem.

This chapter, therefore, describes a method for optimizing a complex district energy system using εDE-RJ and assesses the advantages of εDE-RJ against Q-learning.

9.2   Calculation conditions

9.2.1 Description of the energy system and demand conditions

Fig. 9-1 presents the configuration of the virtual district heat sharing network used for this simulation. The district consisted of the same six buildings as those presented in the previous chapter, including two office buildings, two commercial buildings, the hospital, and the hotel. The purchase price of electricity and the cooling demands of each building were also the same as those in the previous chapter, as shown in Fig. 9-2.

The energy system had two central circulation pipes for low and high-temperature fluids. Heat exchangers were used to provide and receive thermal energy between the buildings and the central pipes. In the basic operation strategy, all of the heat generated at a certain building was used in the building itself. Surplus heat should be provided to the other buildings through the pipes to meet demand. In contrast, heat shortage at a certain building should be met by receiving heat through the pipes from the heat exchangers.

TES acted as a compensation tank, not for a specific building, but the whole district. For example, TES received heat from the central pipe when the total heat generation was greater than the total cooling demand. In contrast, TES discharged heat to buildings experiencing energy shortage through the central pipe when the total heat generated was less than the total cooling demand. Heat loss, also indicated by heat gain in the cooling system, was not considered in this chapter as loss minimal, as shown in the previous chapter.

The temperature difference between the inlet and outlet fluids transferred through the heat exchangers was fixed to 10 °C. Hence, the frequency of the central pumps (CP9–CP22 as shown in Fig. 9-1) could be controlled to achieve the desired amount of heat exchange determined by the optimization method.

The mass flow rate of CP9–CP22 was determined using the maximum cooling demand of each building. The rated pump pressure of these pumps was set to 250 kPa. The central pipes (CP1–CP8) were installed in the central circulating pipes. The rated pump pressure and the mass flow rate of these pumps were set to 500 kPa and 47,190 L/min, respectively.
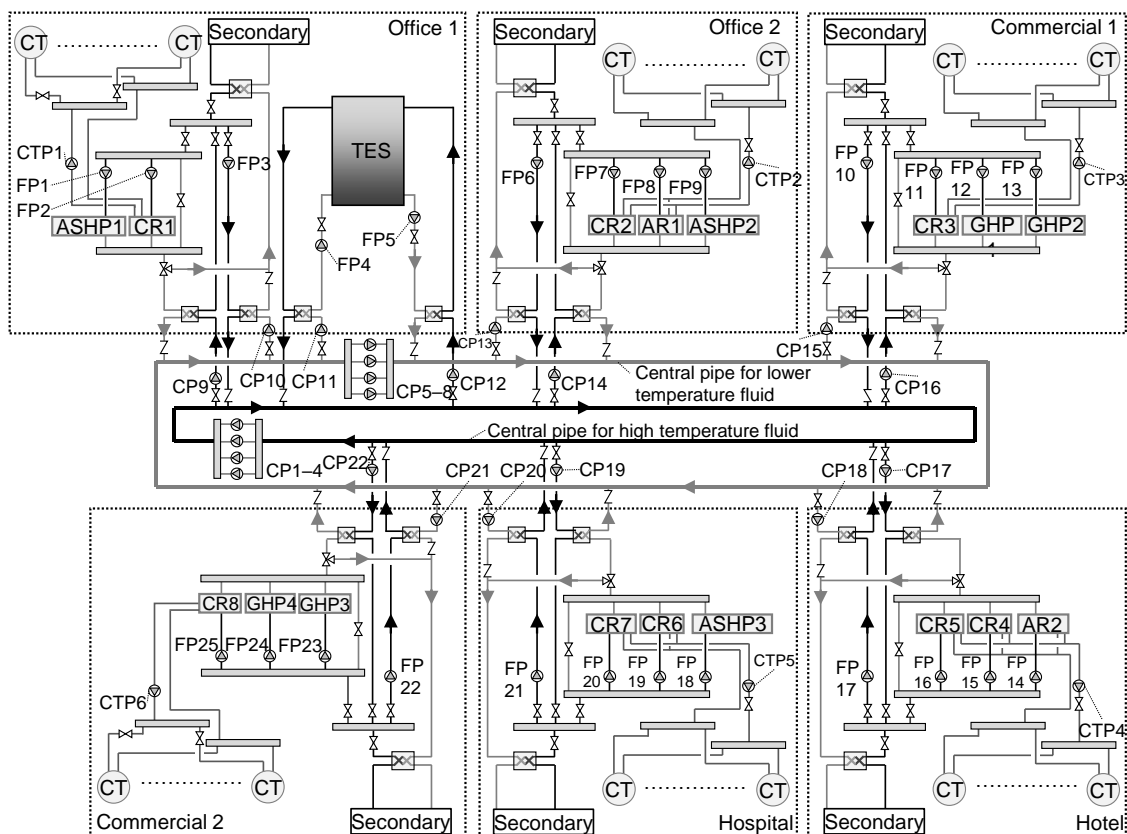
Fig. 9-1 | Configuration of the district heat sharing network energy system.

173
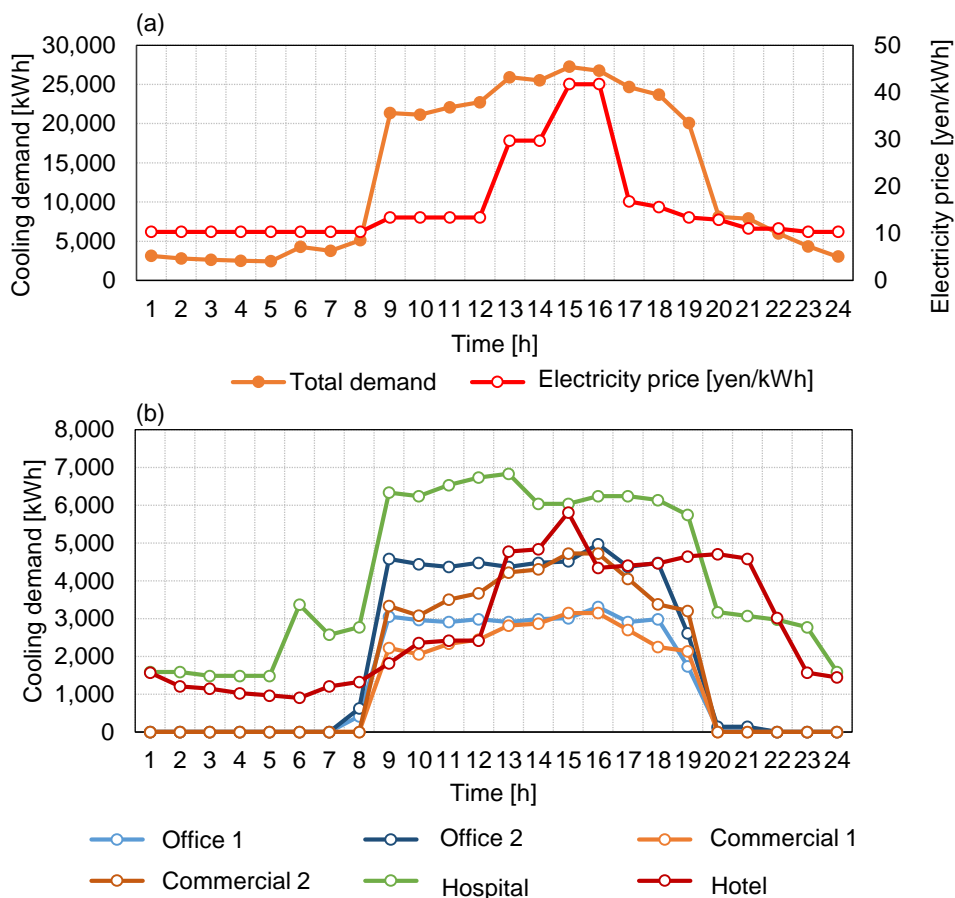
Fig. 9-2 | Demand and price profiles (the same as Fig. 8-3).

The first pumps for the heat source machines (FP1–FP25, as shown in Fig. 9-1) had a rated pump pressure of 150 kPa, and the cooling water pumps (CTP1-CTP6, as shown in Fig. 9-1) had a rated pump pressure of 300 kPa.

Table 9-1 shows the specifications of each heat source machine. In accordance with actual heat source machines, the rated capacities of CR and AR were relatively large, compared to those of other machines. The total capacity of all heat source machines was set to be a magnitude of 1.5 times the total demand of the district. Hence, all machines could meet the demand without TES, but the optimization method should be used to minimize operating costs with electricity price variation. The characteristics of each component were obtained from [144], as shown in Chapter 2.

Table 9-1 | Specification of heat source machines.

Thermal energy storage (TES)	Rated capacity	6,000	m^3
Centrifugal refrigerator (CR1–CR8)	Rated cooling capacity	CR1: 2,300, CR2: 2,000, CR3: 1,500, CR4: 2,200, CR5: 2,200, CR6: 3,000, CR7: 3,000, CR8: 2,500	kW
	Rated COP*	2.18	-
Absorption refrigerator (AR1, AR2)	Rated cooling capacity	AR1: 2,000, AR2: 1,700	kW
	Rated COP	1.32	-
Air-source heat pump (ASHP1– ASHP3)	Rated cooling capacity	ASHP1: 1,180, ASHP2: 1,200 ASHP3: 1,170	kW
	Rated COP	1.47	-
Gas heat pump (GHP1–GHP4)	Rated cooling capacity	GHP1: 900, GHP2: 900 GHP3: 1,230, GHP4: 1,230	kW
	Rated COP	1.09	-

*Note that the rated COP was based on primary energy.

9.2.2 Optimization strategy for the cooling tower system

In this chapter, an integrated multiple cooling tower system was considered, which shared a cooling water system with multiple heat source machines. For example, CR2 and AR1 shared one cooling water system and multiple cooling towers in office 2.

To optimize the cooling water system, decision variables were set for the mass flow rate of cooling water [L/min] and the number of activated cooling towers. The mass flow rate was set as discrete variables of 0%, or 50–100% (rated mass flow rate), which were optimized by a full-search algorithm as the computation complexity was low.

9.2.3 Improved prediction model for the bottom temperature using artificial neural network

An artificial neural network (ANN) was utilized to predict the bottom temperature of thermal energy storage, which was the same as the ANN discussed in the previous chapter. Although the former ANN model had high prediction accuracy, its use was limited by a unimodal TES operation. The unimodal operation means that charging was only conducted before business hours began, and discharging was only conducted during the daytime. However, there was a possibility that charging would be conducted during daytime in an actual energy system.

Hence, an improved ANN model was created, as follows. A multimodal TES operation, as shown in Fig. 9-3, was considered for creating the training dataset. For example, the bottom temperature (T_{bottom}) at the current time step, vortex C_2, was predicted using the maximum stored heat (A_1) and
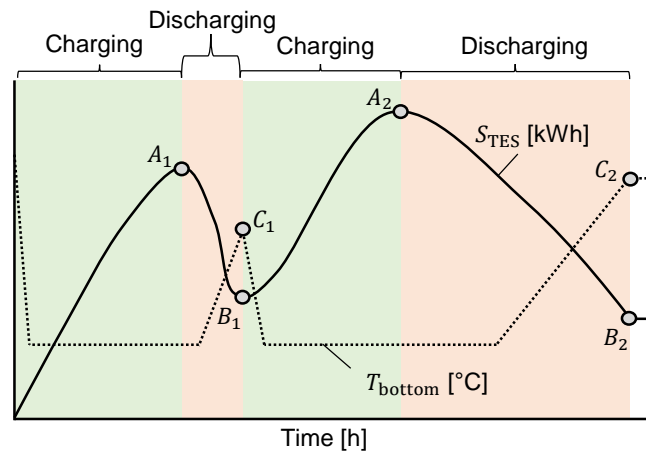
Fig. 9-3 | Conceptual diagram of the creation of the training dataset: S_{TES} denotes the energy stored in thermal energy storage. T_{bottom} denotes the bottom temperature of thermal energy storage.
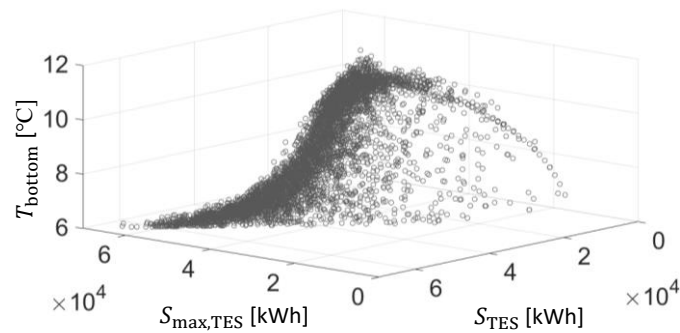
Fig. 9-4 | Relationship between the input and output dataset.

the stored heat at the current time step (B_1). Although the bottom temperature increased before vortex C_1 while the stored energy decreased from A_1 to B_1, only the temperature at C_1 was required to suitably control TES as this temperature (C_1) was the highest. The TES charging operation was again conducted from the end of first discharging period. The stored energy increased from B_1 to A_2, and finally, when the stored energy decreased to B_2, the bottom temperature of C_2 should be predicted to end the discharging operation.

Therefore, the input dataset consisted of the maximum energy [kWh] stored before the current time step and the current stored energy [kWh]. The output data was the bottom temperature when the discharging operation ended. A nonlinear relationship between input and output data is shown in Fig. 9-4.

The ANN structure is shown in Fig. 9-5. The ANN consisted of an input layer, three hidden layers, and an output layer. The number of nodes in each hidden layer was set to 10. The model using the three hidden layers model was superior to a simple layer model, and the use of 10 nodes in this case was also superior to using other numbers, such as 20 or 30. The computational costs of the ANN generally depended on the numbers of layers and nodes. Hence, the ANN adopted three hidden layers with 10 nodes for computation accuracy and speed, although such a structure could be extended with more layers and nodes.
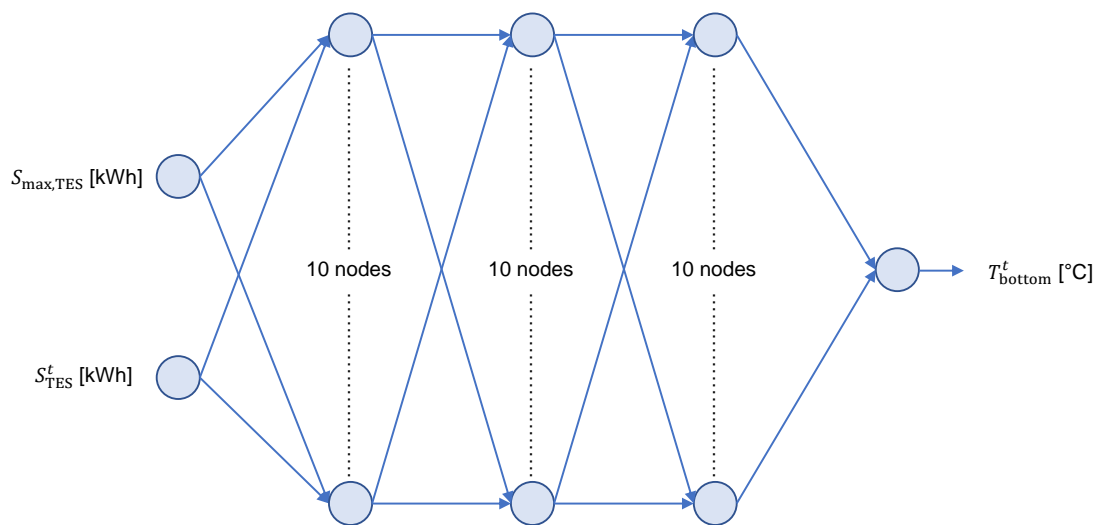
Fig. 9-5 | ANN structure diagram

9.3   Optimization method

9.3.1 Problem formulation

The objective of this chapter is to minimize operating costs, as follows:

$$
\text{minimize } f = \sum_{t=1}^{24} \left(p_E^t \right.
$$
$$
\times \left(\sum_{i1=1}^{17} c_{E,\text{Machine},i1}^t + \sum_{i2}^{6} \left(\sum_{i3}^{N_{CT,i2}} c_{E,CT,i3,i2}^t + c_{E,CTP,i2}^t \right) \right)
$$
$$
\left. + p_G \sum_{i4=1}^{4} c_{G,\text{Machine},i4}^t \right)
\tag{9-1}
$$

where p_E^t and p_G denote the price of electricity [yen/kWh] and gas [yen/m³]. $C_{E,\text{Machine},i1}^t$ and $C_{G,\text{Machine},i4}^t$ denote the electricity and gas consumption of the heat source machine, respectively. $N_{CT,i2}$ denotes the number of cooling towers at the $i2$-th building. $N_{CT,i2}$ depended on the total mass flow rate of the heat source machines at a certain building. $C_{E,CT,i3,i2}^t$ and $C_{E,CTP,i2}^t$ denote the electricity consumption of the cooling towers and cooling water pumps, respectively.

The decision variables were the loading rates of all heat source machines, producing 408 decision variables in total (17 machines × 24 hours). There were three constraints: 1) the upper bound of the TES' capacity, 2) the upper bound of the bottom temperature (7 °C) at the end of the discharging operation, and 3) minimum consecutive operating time steps of CR (2 hours) and AR (3 hours).

When the full-search algorithm was used for this problem, the total computational complexity was $21^{17×24} = 21^{408}$, which is difficult to calculate on an ordinal computer. Dynamic programming (DP) could then be used in this problem, but this produced a complexity of $21^{17×2}×24 = 24×21^{34}$. Although the complexity of DP was significantly lower than that of the full-search algorithm, conducting it was still difficult. Therefore, the hybrid optimization method was applied.

9.3.2 Parameters of εDE-RJ with ANN

The number of generations and individuals were 4,000 and 40, respectively. At 70% of the maximum possible generation, ε_{DE} should be zero. The total complexity of this method was, therefore, 160,000 (40 individuals × 4,000 generations).

9.3.3 Q-learning

Q-learning is one of the free model algorithms which are the same as metaheuristic optimization methods. The Q-learning algorithm was based on the Bellman's principle of optimality to approximately solve a problem. Hence, Q-learning is similar to DP as DP deterministically solves a problem based on the same principle. Fig. 9-6 shows the DP and Q-learning algorithms. Firstly, DP calculated all of the available combinations of thermal outputs between two-time steps, such as the current time step (t) and the previous time step ($t-1$). Following this, the most optimal combination was saved, and the other combination results were ignored due to "principle of optimality". Therefore, the computation complexity of DP exponentially depended on the number of machines.

Q-learning, however, did not exponentially depend on the number of machines; instead, it linearly depended on the number of time steps and machines, and the resolution of discrete variables.
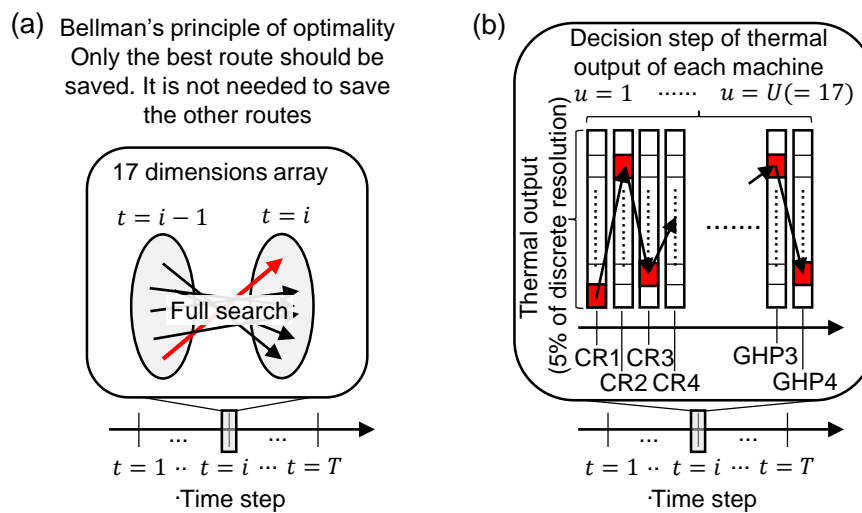
Fig. 9-6 | Conceptual diagram of the DP and Q-learning algorithms: a) DP algorithm based on the Bellman's principle of optimality, b) proposed formulation of the Q-learning problem, consisting of hierarchal searching steps, such as the time and decision steps of the thermal output of each machine.

In this case, the total number of combinations was 8,568 (21 discrete points of each machine × 17
machines × 24 time steps). In particular, a learning step (N_l) could be defined as 17 machines × 24
time steps (408). As shown in Fig. 9-6(b), Q-learning iteratively searches an optimal route of machine
load rates. The following two criteria were considered for stopping Q-learning searching: a) criteria I:
480 s, referred to as the computation time using εDE-RJ, which will be discussed later; and b) criteria
II: the number of episodes set to 160,000, which was the same as the number of generations in εDE-
RJ. The ε-greedy method [168] was also utilized to select the next action.

Fig. 9-7 presents an example of the Q-learning code, written in MATLAB. First, a Q-table, which
was used to save information about rewards, states, and actions, should be initialized. Generally, there
are two initialization approaches: zero and random. In this research, the Q-table elements should be
zero.

Second, parameter ε_Q was initialized to one. During the searching solution, ε_Q generally linearly
and exponentially decreased. Two ε_Q variations were tested in this research; the first was with ε_Q
fixed to 0.8, and the second was with ε_Q fixed to 1.0 during 0%–25% of the numbers of episodes.
During 25%-75% of the episodes, ε_Q decreased linearly. Finally, ε_Q was fixed to 0.1 during 75%–
100% of the episodes.

Third, the episode and learning step loops were started. In the learning step loop, the next action
should be determined using the ε-greedy method. Following that, constraint violation, defined as
εDE-RJ, was calculated. Then, a reward was calculated using an operating schedule determined by Q-
learning. The daily operating costs could not be known during the learning steps due to the time
dependence of machines including TES, CR, and AR. Hence, the reward (R_l) was zero when the
learning step was not the final step. When the learning step was the final step (N_l), the reward could
be calculated as shown in Fig. 9-7.

Finally, the value of the Q-table (Q-value) was updated using the following equation:

$$Q(S_l, A_l) = Q(S_l, A_l) + \alpha_Q \left(R_l + \gamma \max_{a_{l+1}} Q(S_{l+1}, a_{l+1}) - Q(S_l, A_l) \right) \tag{9-2}$$

where $Q(S_l, A_l)$ denotes the Q-value at state (S_l) and action (A_l). α_Q and γ were the parameters of
Q-learning that were tested as case studies. R_l was the reward at learning step (l).

```
Initialization of Q-table to zero
Initialization of ε_Q (ε_Q = 1)
for g = 1: N_episode
   Update ε_Q
   for l = 1: N_l *Update of learning step
      Set a variable, k, randomly
       Select actions (A_l) using ε-greedy method
```

$$\begin{cases} A_l = \underset{a_l}{\operatorname{argmax}} \, Q(S_l, a_l) & \text{if } k > \varepsilon_Q \\ A_l = k & \text{else} \end{cases}$$

```
    Update state of next learning step: S_{l+1} = S_l + A_l
    if l = N_l
       Calculate a constraint violation (φ_m)
    end
    Calculate a reward (R_l)
```

$$\begin{cases} R_l = 0 & \text{if } l < N_l \\ R_l = \dfrac{10^{10}}{\text{daily operating cost}} & \text{if } l = N_l \text{ and } \varphi_m = 0 \\ R_l = -\varphi_m & \text{if } l = N_l \text{ and } \varphi_m > 0 \end{cases}$$

```
    Update Q-table(Q(S_l, a_l)) as follows:
```

$$Q(S_l, A_l) = Q(S_l, A_l) + \alpha \left(R_l + \gamma \max_{a_{l+1}} Q(S_{l+1}, a_{l+1}) - Q(S_l, A_l) \right)$$

```
   end
end
```

Fig. 9-7 | Example Q-learning code written in MATLAB

9.4   Results and discussions

9.4.1 Searching performance of εDE-RJ

Table 9-2 shows the results of all cases. Case 1 presented the case of εDE-RJ, the results of which differed due to the randomness of εDE-RJ. Some statistical values, such as the mean and standard deviation (SD), were used to evaluate the method. The mean of the results generates by εDE-RJ was 1,408,726 yen/day, and the SD was 8,221. The minimum operating cost was 1,394,063 yen/day. The computation time using the same computer as that used in Chapter 8.1 was 480 s. The searching performance of the minimum operating cost case is shown in Fig. 9-8(a). $\varphi_{\min}$ denotes the minimum constraint violation value at every time step. $f_{\min,\text{all}}$ denotes the minimum operating costs of all individuals, including the feasible and infeasible individuals. $f_{\min,\text{fb}}$ denotes the minimum operating costs of the individual that had the minimum constraint violation. Therefore, $f_{\min,\text{fb}}$ was always greater than $f_{\min,\text{all}}$. N_{fb} indicated the number of feasible individuals. The upper bound of N_{fb} was 40, as the number of individuals was set to 40.

Table 9-2 | Results of all cases.

|	Method	$(\alpha_Q, \varepsilon_Q)$	Stopping criteria	Mean (SD)
Case 1	εDE-RJ	-	4,000 generation	1,408,726 (8,221)
Case 2-1	Q-learning	(0.01,0.8)	480 s	Feasible solutions were not found
Case 2-2	Q-learning	(0.01, decrease)	480 s	1,736,584 (9,760)
Case 2-3	Q-learning	(0.90,0.8)	480 s	Feasible solutions were not found
Case 2-4	Q-learning	(0.90, decrease)	480 s	1,736,775 (5,811)
Case 3-1	Q-learning	(0.01, 0.8)	160,000 episode	Feasible solutions were not found
Case 3-2	Q-learning	(0.01, decrease)	160,000 episode	1,724,174 (13,011)
Case 3-3	Q-learning	(0.90, 0.8)	160,000 episode	Feasible solutions were not found
Case 3-4	Q-learning	(0.90, decrease)	160,000 episode	1,724,131 (9,974)
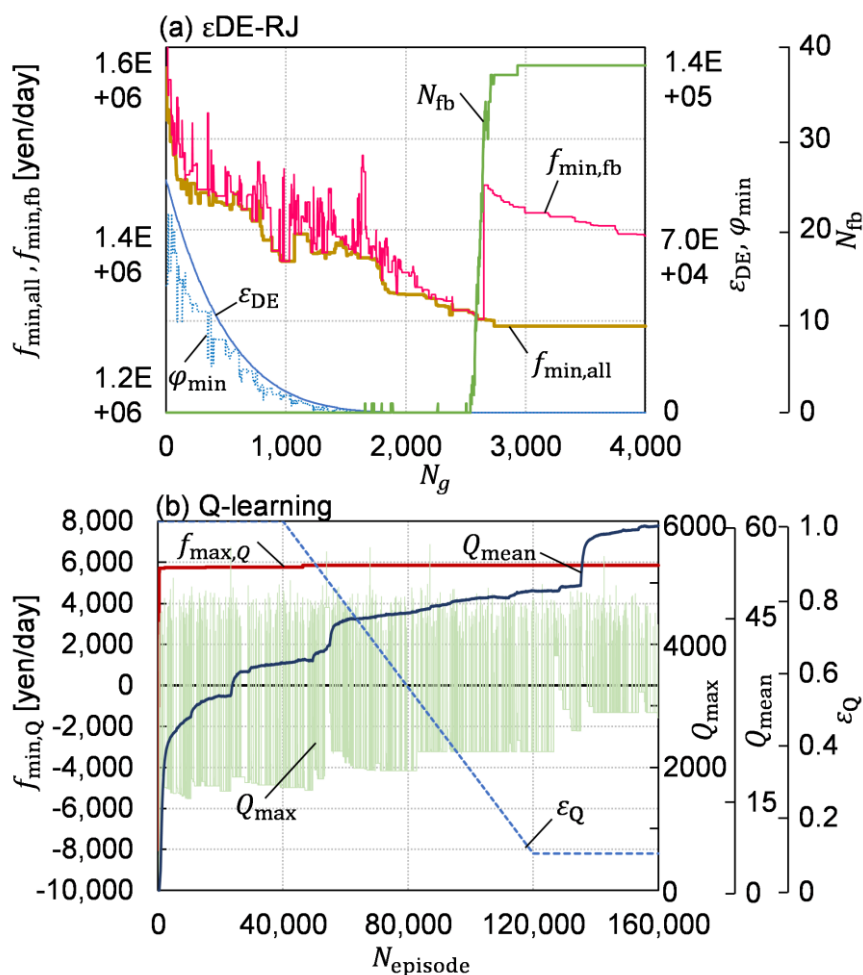
Fig. 9-8 | Searching performance: a) εDE-RJ, b) Q-learning.

All individuals were infeasible during the early generation steps because $\varphi_{\min}$ was greater than zero. As the generation step increased, $\varphi_{\min}$ and ε_{DE} gradually decreased. Then, some feasible individuals occurred at approximately 1,600 generation steps. When $\varphi_{\min}$ was greater than zero, $\varphi_{\min}$, $f_{\min,all}$, and $f_{\min,fb}$ decreased immediately due to the εDE-RJ searching algorithm. Hence, εDE-RJ could efficiently optimize constraint violation and objective functions, compared to other methods that first aimed to minimize constraint violation, and then minimize the objective function.

9.4.2 Searching performance of Q-learning

Table 9-2 shows the results of Q-learning. There were eight case studies covering different parameter values and stopping criterion. When the α_Q parameter was small, trapping in a local optimum can easily be avoided, but convergence of the results tends to be slower. In contrast, when the α_Q parameter was large, it would trap in a local optimum, but convergence of the results was quicker.

Fig. 9-8(b) shows the searching performance of Q-learning. In the cases where ε_Q was fixed to 0.8, no feasible solutions were not found. In contrast, feasible solutions were found in all cases with varying ε_Q. Therefore, a value of 0.8 for the ε_Q parameter was too low to identify a feasible solution to this problem, which had a long learning step ($N_l = 408$), and ε_Q should be 1.0 during the early episodes.

In terms of stopping criterion, although the computational complexity of Case 3-1 to 3-4 increased by a magnitude of seven times of that in Cases 2-1 to 2-4, there was a difference of only 0.7% between the results. In terms of parameter α_Q, the SD of the cases where α_Q was 0.90 was smaller than that of the cases where α_Q was 0.01. Thus, Case 3-4 was the most stable and could obtain the minimum result.

Fig. 9-8(b) shows the minimum result of Case 3-4, in which the operating cost was 1,707,947 yen/day. $f_{\max,Q}$ indicates the maximum value of the objective function of Q-learning. $Q_{\max}$ and Q_{mean} are the maximum and mean values of the Q-table, respectively. The Q-table was suitably updated because Q_{mean} increased gradually, however, $Q_{\max}$ was not suitably optimized because its value oscillated.

Q-learning could not fully optimize the problem due to the large number of learning steps. In previous studies, there were only four or five learning [209,210]. The computation time in Case 3-1 to Case 3-4 was 5,900 s when the computation complexity was the same as that for εDE-RJ. Therefore, Q-learning was not suitable for application to the complex energy system.

9.4.3 Comparison of operating schedules between εDE-RJ and Q-learning

Fig. 9-9 shows the operating schedules produced by εDE-RJ and Q-learning. Fig. 9-9(b) contains the result of εDE-RJ. TES discharged a larger amount of heat to the district at 3 p.m. and 4 p.m. when the electricity price was high compared to the other time steps. In contrast, in the result produced by Q-learning, TES did not discharge heat at these time steps, as shown in Fig. 9-9(c). The Q-learning result allowed TES to discharge heat at 9 a.m., when the price of electricity was low. Hence, the result from εDE-RJ was superior to that from Q-learning.

The machine efficiency of εDE-RJ was superior to that of Q-learning. Fig. 9-10 shows the frequency and distribution of system coefficient of performance (SCOP) based on the primary energy at each time step. SCOP included the electricity consumption of machines, pumps, and cooling tower fans, and the gas consumption of machines. In the result of εDE-RJ, SCOP $\in$ [1.4,1.7] accounted for 96% of all operations. In contrast, SCOP $\in$ [1.3,1.5] accounted for 75% of all operations in the Q-learning result. The operation given by εDE-RJ was, therefore, more efficient than that given by Q-learning.
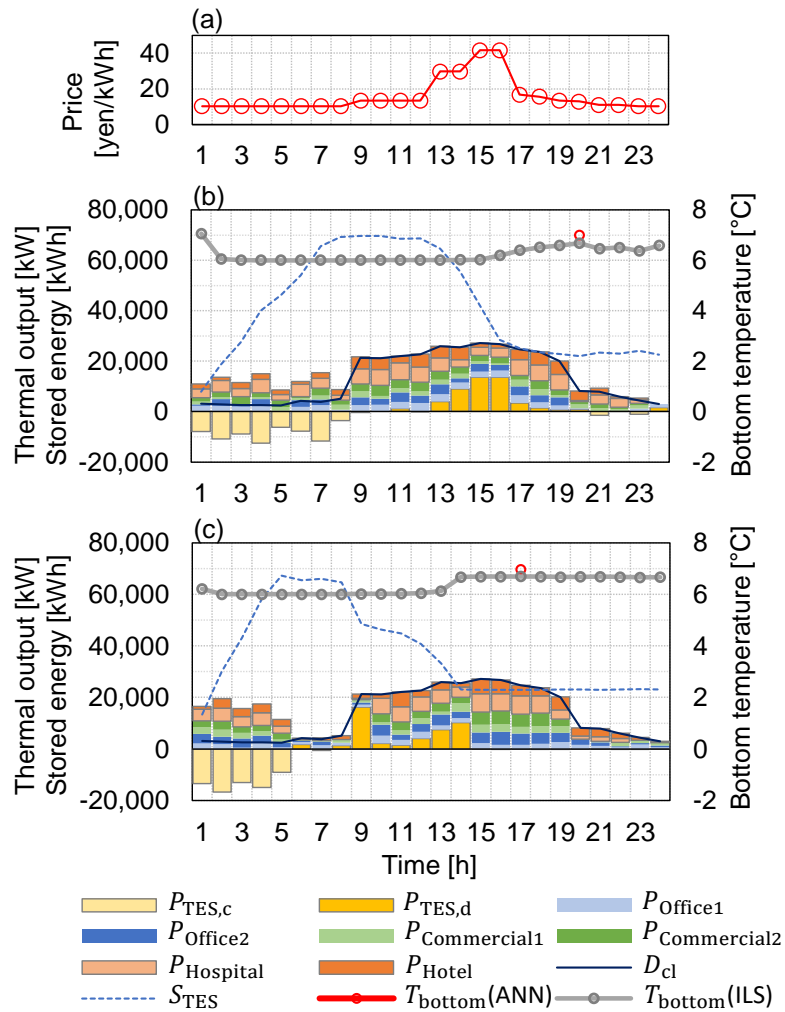
Fig. 9-9 | Operating schedules given by two optimization methods: a) variation of electricity price, b) εDE-RJ, c) Q-learning.
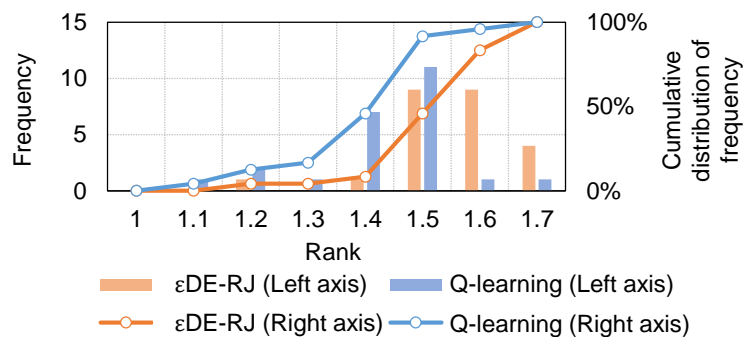
Fig. 9-10 | Cumulative distribution of the frequency of system COP.

9.4.4 Analysis of heat balance of districts

Table 9-3 shows the heat balance of each building in the solution given by εDE-RJ. "Received" refers to the amount of heat received from the district, and "provided" refers to the amount of heat provided from a building to the district.

Commercial building 2 provided the greatest amount of heat to the district because the building had two gas heat pumps (GHP) with a relatively large cooling capacity. The GHPs were used to generate heat instead of electric-based machines when the electricity price was high. CR8 generated heat with highly efficient COP during the morning and night. Hence, the other buildings provided the largest total amount of heat. Although the hospital and hotel had efficient CRs, these buildings also received heat from other efficient CRs during the night. Therefore, the total amount of provided and received energy was balanced.

Table 9-3 | Heat balance of each building.

	Office 1	Office 2	Commercial 1	Commercial 2	Hospital	Hotel
Received	3.7	16.4	10.4	11.4	17.4	14.7
Provided	17.6	12.4	13.4	21.9	16.0	15.5

9.4.5 Prediction accuracy of ANN

$T_{\text{bottom}}(\text{ANN})$ and $T_{\text{bottom}}(\text{ILS})$ in Fig. 9-9 indicate the bottom temperature of TES in the ANN and ILS, respectively. To obtain $T_{\text{bottom}}(\text{ILS})$, a daily simulation was conducted using the operating schedule produced by εDE-RJ and the ILS model.

In Fig. 9-9(b), ANN predicted a bottom temperature of 6.99 °C at 8 p.m. In contrast, the ILS model provided a temperature of 6.68 °C at that time. Hence, the prediction tolerance was 0.30 °C. In Fig. 9-9(c), ANN predicted a bottom temperature of 6.97 °C at 5 p.m. In contrast, the ILS model provided a temperature of 6.69 °C at that time. Hence, the prediction tolerance was 0.28 °C.

Both εDE-RJ and Q-learning could suitably generate a TES operating schedule, because both predicted temperatures (6.99 °C and 6.97 °C) were close to upper bound (7 °C). In addition, ANN can be used in an actual energy management system as it has high prediction accuracy.

9.5   Conclusion

This chapter discusses the application of the proposed hybrid method, consisting of εDE-RJ and ANN, to a complex district energy system, such as a heat sharing network. To evaluate the feasibility and accuracy of the hybrid method, Q-learning, which has increasingly been used in building energy optimization studies, was compared.

εDE-RJ had clear advantages for quickly identifying a quasi-optimal operating schedule compared to Q-learning. The objective function and daily operating costs of εDE-RJ with ANN could be reduced by 18.3% from those of Q-learning. The computation times of εDE-RJ with ANN and Q-learning were 480 s and 5,900 s, respectively. Moreover, ANN could suitably predict a TES bottom temperature with a tolerance of less than 0.3 °C.

CHAPTER 10

Conclusions and future studies

10.1 Conclusions

This thesis focused on developing efficient and flexible optimization methods for building and district energy operations. A detailed discussion and conclusions are given in Chapter 3–9; the main results of this thesis are summarized and highlighted as follows.

Chapter 3.1 considered the issue of how to determine the operating schedules for a building energy system that consisted of three parts: electricity, cooling, and hot water supply systems. This system had 336 decision variables and both nonlinear and discontinuous conditions. Although a linearization technique has been typically adopted in previous studies when a complex energy system was optimized, a flexible optimization method—ε-constrained differential evolution (εDE) algorithm— was applied in this study. This algorithm had advantages as it solved almost all constrained objective functions. As a result, εDE could find a quasi-optimal operation for the three systems at once, which reduced daily operating costs by 5.7% when compared with an empirical operation. Moreover, an efficient multi-objective optimization method— ε-constrained multi-objective differential evolution (εMODE)—was proposed to minimize the daily operating costs and primary energy consumption. In previous studies, εDE was proposed as a solution for constrained problems, while the MODE algorithm (MODEA) was proposed as a solution for multi-objective problems. However, a method for solving a constrained multi-objective optimization problem had not been proposed previously because it was difficult to determine a method that could minimize both constraint violations and objective functions at the same time. A new approach, εMODE, was therefore proposed by integrating the εDE algorithm and MODEA. In addition, the new algorithm was revised to find a feasible solution allowing comparison with the original MODEA. As a result, εMODE could find a pareto-front for the two objective minimizations.

In Chapter 4.1, a novel simple index was proposed to determine an optimal operating strategy for electricity systems, such as photovoltaic (PV) devices connected to a rechargeable battery (RB). For an ordinary residential building with PV and RB, once the feed-in-tariff period has expired, the occupants should identify the self-consumption or total amount purchased operations that are most suitable to change so as to minimize their daily operating cost. Although εDE can be applied to determine the optimal operation in practical computation time, it is not always user-friendly for non-expert users, particularly typical ordinary building occupants. In this situation, an index—an area ratio of prices (ARP)—was used to determine the most suitable operation, without requiring any optimization calculations. Although ARP was tested under various demand curves and price profiles

of purchased electricity, it showed the same threshold value. Therefore, it would be sufficient to use ARP once a day to provide optimal control.

In Chapter 5.1, a new recalculation strategy—two-time steps recalculation (TtsR)—for real-time controls was proposed. This strategy can be used for energy systems, including time-dependence equipment such as RB and thermal energy storage (TES), as a model predictive control methodology. It can be used with other optimization methods, such as mathematical programming and metaheuristic optimization methods, and can handle uncertainty of demand and PV power generation. Although all-time steps recalculation (AtsR), which is a typical model predictive control methodology, can derive the most optimal operating schedules, it also has high computational costs because the operating schedules for all time steps are updated at each step. In contrast, TtsR reduced the computational cost by 73% against AtsR, while the daily operating cost of TtsR only increased by 0.61% compared with AtsR. Therefore, TtsR provided a flexible recalculation framework and low computational costs for updating operating schedules while meeting demands.

In Chapter 6.1, a new stable optimization method— εDE with random jumping (εDE-RJ)—was proposed. This method inspired a mutation method of genetic algorithm. This is because the original εDE algorithm had a fundamental drawback as it was unable to drop in a local optimum. Hence, the mutation method was added to the original εDE to avoid trapping a local optimum. The new εDE-RJ method was applied to a complex building energy optimization, which included time-dependent heat sources, including a ground source heat pump (GSHP) system. Although previous studies applied various simplification methods for GSHP models to reduce computational costs, εDE-RJ could optimize the system without need for any simplifications. As a result, weekly operating costs were reduced by 16.35% using εDE-RJ when compared with empirical operation of the GSHP system.

In Chapter 7.1, a hybrid method of εDE-RJ and an artificial neural network (ANN) was proposed to optimize a building energy system that consisted of several time-dependent devices, including a GSHP and a solar collector. The ANN was used as a borehole exchanger (BHE) model with the GSHP, which reduced computational costs by 95% when compared with the physical model used in Chapter 6. The number of optimization iterations could then be increased due to the reduction in computational costs for the BHE and GSHP calculation. In addition, due to the lower computational costs, detailed temperature variations, which affected the efficiency of the GSHP and solar collector, could be calculated for each iteration to provide a quasi-optimal solution.

Chapter 8.1 and Chapter 9.1 focused on district energy optimizations and so differed from the previous chapters, which dealt with building energy optimizations. Although the district energy system contained multiple heat source machines, making it more difficult to identify an appropriate optimization method, εDE-RJ with ANN could be readily applied to this more complex optimization. This approach resulted in a reduction in daily operating cost of more than 10% compared with an empirical operation. The computational time was only 480 s on an ordinary personal computer. Hence, this method could be used in daily optimization procedures for actual energy systems. In addition, εDE-RJ was compared to Q-learning, which is a well-known reinforcement learning technique that has been used in many recent studies into energy system optimization. As a result, the daily operating cost using εDE-RJ was reduced by 18.3% compared with Q-learning, while the computational cost of εDE-RJ was only 480 s, compared with 5,900 s for Q-learning.

It is therefore concluded that εDE-RJ had an advantage over other optimization methods for finding quasi-optimal solutions, in terms of practical computational time on an ordinary computer; this advantage applied to complex energy systems that consist of nonlinear, discrete, and nondifferentiable configurations, and time-dependence machines.

10.2 *Recommendations for future studies*

This thesis focused on simulation-based building and district energy optimizations. The use of εDE-RJ and TtsR provided advantages over other methods, as summarized in the previous section. Recommendations for further studies are as follows:

1) ANN modeling for actual equipment

While ANN was used to create models of BHE and TES using data obtained from physical models, actual measurement data should be used to train ANN so as to produce an extended ANN for use in actual energy systems. As described in a previous co-authored conference paper [211], actual measured data has previously been used to train ANN; however, a wider range of situations should be studied to further demonstrate the flexibility of the ANN model and reduction in computational costs.

2) Application of εDE-RJ and TtsR to actual energy management

All cases investigated in this thesis considered realistic conditions associated with energy systems, such as nonlinear characteristics of heat source machines, discrete set points of partial load rates, mass flow rates, and the number of available machines. However, it is strongly recommended that the

methods described are assessed in real-world situations rather than for empirical operations, as well as for other optimization technologies as described in [212–220].

3) Annual and life cycle simulation for planning optimizations

This thesis aimed to optimize only the operating schedules for building and district energy systems. However, energy system planning optimization is also important due to the numerous combinations of machine types, capacity, and system configurations that could be applied. Approximation methods such as εDE-RJ would provide a suitable approach for this. However, such a study would need to consider a longer time horizon, such as annual or multiple year periods. The study could validate the εDE-RJ approach for use in system planning optimization and should also consider how to integrate two-stage optimizations for both system planning and operation.

REFERENCES

[1]   Kaizuka I. Residential PV Market in Japan. Int. Energy Agency Photovolt. Power Syst. Program., RTS Corporation; 2014.

[2]   The Ministry of Economy Trade and Industry. Japan's Energy Plan 2015. http://www.enecho.meti.go.jp/en/category/brochures/pdf/energy_plan_2015.pdf.

[3]   The Ministry of Economy Trade and Industry. Roadmap of utilization strategy of hydro-energy and fuel cell revised edition (in Japanese). 2016.

[4]   International Energy Agency (IEA). CHP/DHC Country Scorecard : Japan. 2008.

[5]   Pales AF. The IEA CHP and DHC Collaborative. Int Energy Agency Insights Ser 2013 2013.

[6]   Aganda AA, Coney JER, Sheppard CGW. Airflow maldistribution and the performance of a packaged air conditioning unit evaporator. Appl Therm Eng 2000;20:515–28. doi:10.1016/S1359-4311(99)00038-1.

[7]   Daikin AC. Packaged HVAC Systems n.d. http://www.daikinac.com/content/light-commercial.

[8]   Sustainable Dwelling. A Brief History of Heating and Cooling America's Homes n.d. https://sunhomedesign.wordpress.com/2007/10/26/a-brief-history-of-heating-and-cooling-americas-homes/.

[9]   U.S. Department of Energy. The Smart Grid: An Introduction. 2010. doi:10.1016/B978-1-59749-570-7.00011-X.

[10]   ICAX (International Heat Transfer). Heat Sharing Networks n.d. http://www.icax.co.uk/Heat_Sharing.html.

[11]   California Independent System Operator. What the duck curve tells us about managing a green grid. vol. Fact Sheet. 2016. doi:CommPR/HS/10.2013.

[12]   New Energy and Industrial Technology Development Organization (NEDO). Renewables and Clean Energy for Industries – Japanese Case for Variable Renewable Energy Highly Penetrated Energy System and for Replacement of Fossil-fuel Fired Boilers-. 2016.

[13]   Nord Pool. Official website of Nord Pool 2017. http://www.nordpoolspot.com/.

[14]   PJM. Official website of PJM 2017. http://www.pjm.com/.

[15]   Imaizumi D. Why is demand response needed and what is its effect? (in Japanese). J Infrastruct Invest 2012.

[16]   Mitsubishi Electric Corporation. Business Overview and Environmental Issues for Which Risks and Opportunities Have Been Recognized and Evaluated n.d. http://www.mitsubishielectric.com/company/environment/business/information/index_print.html.

REFERENCES

[17] Xu X, Huang G, Liu H, Chen L, Liu Q. The study of the dynamic load forecasting model about air-conditioning system based on the terminal user load. Energy Build 2015;94:263–8. doi:10.1016/j.enbuild.2015.01.018.

[18] Kiefer J. Sequential Minimax Search for a Maximum. Proc Am Math Soc 1953;4:502. doi:10.2307/2032161.

[19] Laouafi A, Mordjaoui M, Haddad S, Boukelia TE, Ganouche A. Online electricity demand forecasting based on an effective forecast combination methodology. Electr Power Syst Res 2017;148:35–47. doi:10.1016/j.epsr.2017.03.016.

[20] Laouafi A, Mordjaoui M, Laouafi F, Boukelia TE. Daily peak electricity demand forecasting based on an adaptive hybrid two-stage methodology. Int J Electr Power Energy Syst 2016;77:136–44. doi:10.1016/j.ijepes.2015.11.046.

[21] Liu Y, Wang W, Ghadimi N. Electricity Load Forecasting by an Improved Forecast Engine for Building Level Consumers. Energy 2017;139:18–30. doi:10.1016/j.energy.2017.07.150.

[22] Lahouar A, Ben Hadj Slama J. Day-ahead load forecast using random forest and expert input selection. Energy Convers Manag 2015;103:1040–51. doi:10.1016/j.enconman.2015.07.041.

[23] Abedinia O, Amjady N, Shafie-Khah M, Catalão JPS. Electricity price forecast using Combinatorial Neural Network trained by a new stochastic search method. Energy Convers Manag 2015;105:642–54. doi:10.1016/j.enconman.2015.08.025.

[24] Lusis P, Khalilpour KR, Andrew L, Liebman A. Short-term residential load forecasting: Impact of calendar effects and forecast granularity. Appl Energy 2017;205:654–69. doi:10.1016/j.apenergy.2017.07.114.

[25] Mocanu E, Nguyen PH, Kling WL, Gibescu M. Unsupervised energy prediction in a Smart Grid context using reinforcement cross-building transfer learning. Energy Build 2016;116:646–55. doi:10.1016/j.enbuild.2016.01.030.

[26] Javed F, Arshad N, Wallin F, Vassileva I, Dahlquist E. Forecasting for demand response in smart grids: An analysis on use of anthropologic and structural data and short term multiple loads forecasting. Appl Energy 2012;96:150–60. doi:10.1016/j.apenergy.2012.02.027.

[27] Ertugrul ÖF. Forecasting electricity load by a novel recurrent extreme learning machines approach. Int J Electr Power Energy Syst 2016;78:429–35. doi:10.1016/j.ijepes.2015.12.006.

[28] Short M, Crosbie T, Dawood M, Dawood N. Load forecasting and dispatch optimisation for decentralised co-generation plant with dual energy storage. Appl Energy 2017;186:304–20. doi:10.1016/j.apenergy.2016.04.052.

[29] Rasmussen LB, Bacher P, Madsen H, Nielsen HA, Heerup C, Green T. Load forecasting of supermarket refrigeration. Appl Energy 2016;163:32–40. doi:10.1016/j.apenergy.2015.10.046.

196

[30]   Kaur A, Nonnenmacher L, Coimbra CFM. Net load forecasting for high renewable energy penetration grids. Energy 2016;114:1073–84. doi:10.1016/j.energy.2016.08.067.

[31]   Dahl M, Brun A, Andresen GB. Using ensemble weather predictions in district heating operation and load forecasting. Appl Energy 2017;193:455–65. doi:10.1016/j.apenergy.2017.02.066.

[32]   Ma W, Fang S, Liu G, Zhou R. Modeling of district load forecasting for distributed energy system. Appl Energy 2017;204:181–205. doi:10.1016/j.apenergy.2017.07.009.

[33]   Perez KX, Baldea M, Edgar TF. Integrated HVAC management and optimal scheduling of smart appliances for community peak load reduction. Energy Build 2016. doi:10.1016/j.enbuild.2016.04.003.

[34]   Turner WJN, Staino A, Basu B. Residential HVAC fault detection using a system identification approach. Energy Build 2017;151:1–17. doi:10.1016/j.enbuild.2017.06.008.

[35]   Edwards KC, Finn DP. Generalised water flow rate control strategy for optimal part load operation of ground source heat pump systems. Appl Energy 2015;150:50–60. doi:10.1016/j.apenergy.2015.03.134.

[36]   Dufo-López R. Optimisation of size and control of grid-connected storage under real time electricity pricing conditions. Appl Energy 2015;140:395–408. doi:10.1016/j.apenergy.2014.12.012.

[37]   de Oliveira V, Jäschke J, Skogestad S. Optimal operation of energy storage in buildings: Use of the hot water system. J Energy Storage 2016;5:102–12. doi:10.1016/j.est.2015.11.009.

[38]   Rahiminejad A, Vahidi B, Hejazi MA, Shahrooyan S. Optimal scheduling of dispatchable distributed generation in smart environment with the aim of energy loss minimization. Energy 2016;116:190–201. doi:10.1016/j.energy.2016.09.111.

[39]   Oh SD, Kim KY, Oh SB, Kwak HY. Optimal operation of a 1-kW PEMFC-based CHP system for residential applications. Appl Energy 2012;95:93–101. doi:10.1016/j.apenergy.2012.02.019.

[40]   Jing ZX, Jiang XS, Wu QH, Tang WH, Hua B. Modelling and optimal operation of a small-scale integrated energy based district heating and cooling system. Energy 2014;73:399–415. doi:10.1016/j.energy.2014.06.030.

[41]   Calvillo CF, Sánchez-Miralles A, Villar J, Martín F. Optimal planning and operation of aggregated distributed energy resources with market participation. Appl Energy 2016;182:340–57. doi:10.1016/j.apenergy.2016.08.117.

[42]   Fang F, Wang QH, Shi Y. A novel optimal operational strategy for the CCHP system based on two operating modes. IEEE Trans Power Syst 2012;27:1032–41. doi:10.1109/TPWRS.2011.2175490.

[43]   Cui W, Zhou S, Liu X. Optimization of design and operation parameters for hybrid ground-source

heat pump assisted with cooling tower. Energy Build 2015;99:253–62. doi:10.1016/j.enbuild.2015.04.034.

[44] Hu B, Li Y, Mu B, Wang S, Seem JE, Cao F. Extremum seeking control for efficient operation of hybrid ground source heat pump system. Renew Energy 2016;86:332–46. doi:10.1016/j.renene.2015.07.092.

[45] Li M, Mu H, Li N, Ma B. Optimal design and operation strategy for integrated evaluation of CCHP (combined cooling heating and power) system. Energy 2016;99:202–20. doi:10.1016/j.energy.2016.01.060.

[46] Liu M, Shi Y, Fang F. A new operation strategy for CCHP systems with hybrid chillers. Appl Energy 2012;95:164–73. doi:10.1016/j.apenergy.2012.02.035.

[47] Ondeck AD, Edgar TF, Baldea M. Optimal operation of a residential district-level combined photovoltaic/natural gas power and cooling system. Appl Energy 2015;156:593–606. doi:10.1016/j.apenergy.2015.06.045.

[48] Thangavelu SR, Myat A, Khambadkone A. Energy optimization methodology of multi-chiller plant in commercial buildings. Energy 2017;123:64–76. doi:10.1016/j.energy.2017.01.116.

[49] Roldán-Blay C, Escrivá-Escrivá G, Roldán-Porta C, Álvarez-Bel C. An optimisation algorithm for distributed energy resources management in micro-scale energy hubs. Energy 2017;132:126–35. doi:10.1016/j.energy.2017.05.038.

[50] Tavakoli SD, Mahdavyfakhr M, Hamzeh M, Sheshyekani K, Afjei E. A unified control strategy for power sharing and voltage balancing in bipolar DC microgrids. Sustain Energy, Grids Networks 2017;11:58–68. doi:10.1016/j.segan.2017.07.004.

[51] Hein P, Kolditz O, Görke UJ, Bucher A, Shao H. A numerical study on the sustainability and efficiency of borehole heat exchanger coupled ground source heat pump systems. Appl Therm Eng 2016;100:421–33. doi:10.1016/j.applthermaleng.2016.02.039.

[52] Wakui T, Sawada K, Kawayoshi H, Yokoyama R, Iitaka H, Aki H. Optimal operations management of residential energy supply networks with power and heat interchanges. Energy Build 2017;151:167–86. doi:10.1016/j.enbuild.2017.06.041.

[53] Wakui T, Yokoyama R. Optimal sizing of residential gas engine cogeneration system for power interchange operation from energy-saving viewpoint. Energy 2011;36:3816–24. doi:10.1016/j.energy.2010.09.025.

[54] Lindberg KB, Doorman G, Fischer D, Korpås M, Ånestad A, Sartori I. Methodology for optimal energy system design of Zero Energy Buildings using mixed-integer linear programming. Energy Build 2016;127:194–205. doi:10.1016/j.enbuild.2016.05.039.

[55] Siemer L, Schöpfer F, Kleinhans D. Cost-optimal operation of energy storage units: Benefits of a

problem-specific approach. J Energy Storage 2016;6:11–21. doi:10.1016/j.est.2016.01.005.

[56] Beck T, Kondziella H, Huard G, Bruckner T. Optimal operation, configuration and sizing of generation and storage technologies for residential heat pump systems in the spotlight of self-consumption of photovoltaic electricity. Appl Energy 2017;188:604–19. doi:10.1016/j.apenergy.2016.12.041.

[57] Ashouri A, Fux SS, Benz MJ, Guzzella L. Optimal design and operation of building services using mixed-integer linear programming techniques. Energy 2013;59:365–76. doi:10.1016/j.energy.2013.06.053.

[58] Marzband M, Alavi H, Ghazimirsaeid SS, Uppal H, Fernando T. Optimal energy management system based on stochastic approach for a home Microgrid with integrated responsive load demand and energy storage. Sustain Cities Soc 2017;28:256–64. doi:10.1016/j.scs.2016.09.017.

[59] Zare Oskouei M, Sadeghi Yazdankhah A. Scenario-based stochastic optimal operation of wind, photovoltaic, pump-storage hybrid system in frequency- based pricing. Energy Convers Manag 2015;105:1105–14. doi:10.1016/j.enconman.2015.08.062.

[60] Ameri M, Besharati Z. Optimal design and operation of district heating and cooling networks with CCHP systems in a residential complex. Energy Build 2016;110:135–48. doi:10.1016/j.enbuild.2015.10.050.

[61] Pazouki S, Haghifam MR. Optimal planning and scheduling of energy hub in presence of wind, storage and demand response under uncertainty. Int J Electr Power Energy Syst 2016;80:219–39. doi:10.1016/j.ijepes.2016.01.044.

[62] Majidi M, Nojavan S, Zare K. Optimal stochastic short-term thermal and electrical operation of fuel cell/photovoltaic/battery/grid hybrid energy system in the presence of demand response program. Energy Convers Manag 2017;144:132–42. doi:10.1016/j.enconman.2017.04.051.

[63] Gu W, Lu S, Wu Z, Zhang X, Zhou J, Zhao B, et al. Residential CCHP microgrid with load aggregator: Operation mode, pricing strategy, and optimal dispatch. Appl Energy 2017;205:173–86. doi:10.1016/j.apenergy.2017.07.045.

[64] Kim Y, Norford LK. Optimal use of thermal energy storage resources in commercial buildings through price-based demand response considering distribution network operation. Appl Energy 2017;193:308–24. doi:10.1016/j.apenergy.2017.02.046.

[65] Stadler P, Ashouri A, Maréchal F. Model-based optimization of distributed and renewable energy systems in buildings. Energy Build 2016. doi:10.1016/j.enbuild.2016.03.051.

[66] Fujimoto T, Yamaguchi Y, Shimoda Y. Energy management for voltage control in a net-zero energy house community considering appliance operation constraints and variety of households. Energy Build 2017;147:188–99. doi:10.1016/j.enbuild.2017.05.009.

REFERENCES

[67]   IBM. IBM ILOG CPLEX Optimization Studio n.d. https://www.ibm.com/us-en/marketplace/ibm-ilog-cplex.

[68]   GAMS. GAMS Solvers n.d. https://www.gams.com/optimization-solvers/.

[69]   Gu W, Wang J, Lu S, Luo Z, Wu C. Optimal operation for integrated energy system considering thermal inertia of district heating network and buildings. Appl Energy 2017;199:234–46. doi:10.1016/j.apenergy.2017.05.004.

[70]   Sichilalu SM, Xia X. Optimal power dispatch of a grid tied-battery-photovoltaic system supplying heat pump water heaters. Energy Convers Manag 2015;102:81–91. doi:10.1016/j.enconman.2015.03.087.

[71]   Nwulu NI, Xia X. Optimal dispatch for a microgrid incorporating renewables and demand response. Renew Energy 2017;101:16–28. doi:10.1016/j.renene.2016.08.026.

[72]   Behzadi Forough A, Roshandel R. Multi objective receding horizon optimization for optimal scheduling of hybrid renewable energy system. Energy Build 2017;150:583–97. doi:10.1016/j.enbuild.2017.06.031.

[73]   Wamalwa F, Sichilalu S, Xia X. Optimal control of conventional hydropower plant retrofitted with a cascaded pumpback system powered by an on-site hydrokinetic system. Energy Convers Manag 2017;132:438–51. doi:10.1016/j.enconman.2016.11.049.

[74]   Tveit TM, Savola T, Gebremedhin A, Fogelholm CJ. Multi-period MINLP model for optimising operation and structural changes to CHP plants in district heating networks with long-term thermal storage. Energy Convers Manag 2009;50:639–47. doi:10.1016/j.enconman.2008.10.010.

[75]   Luo N, Hong T, Li H, Jia R, Weng W. Data analytics and optimization of an ice-based energy storage system for commercial buildings. Appl Energy 2017;204:459–75. doi:10.1016/j.apenergy.2017.07.048.

[76]   Farrokhifar M. Optimal operation of energy storage devices with RESs to improve efficiency of distribution grids; technical and economical assessment. Int J Electr Power Energy Syst 2016;74:153–61. doi:10.1016/j.ijepes.2015.07.029.

[77]   Ranaweera I, Midtgård O-M. Optimization of operational cost for a grid-supporting PV system with battery storage. Renew Energy 2016;88:262–72. doi:10.1016/j.renene.2015.11.044.

[78]   Wegmann R, Döge V, Becker J, Sauer DU. Optimized operation of hybrid battery systems for electric vehicles using deterministic and stochastic dynamic programming. J Energy Storage 2017;14:22–38. doi:10.1016/j.est.2017.09.008.

[79]   Facci AL, Andreassi L, Ubertini S. Optimization of CHCP (combined heat power and cooling) systems operation strategy using dynamic programming. Energy 2014;66:387–400. doi:10.1016/j.energy.2013.12.069.

[80]   Chen H-J, Wang DWP, Chen S-L. Optimization of an ice-storage air conditioning system using dynamic programming method. Appl Therm Eng 2005;25:461–72. doi:10.1016/j.applthermaleng.2003.12.006.

[81]   Keefe MPO, Markel T. Dynamic Programming Applied to Investigate Energy Management Strategies for a Plug-in HEV. Present 22nd Int Batter Hybrid Fuel Cell Electr Veh Symp Exhib 2006.

[82]   Chen S-Y, Hung Y-H, Wu C-H, Huang S-T. Optimal energy management of a hybrid electric powertrain system using improved particle swarm optimization. Appl Energy 2015;160:132–45. doi:10.1016/j.apenergy.2015.09.047.

[83]   Tsukada T, Tamura T, Kitagawa S, Fukuyama Y. Optimal operational planning for cogeneration system using particle swarm optimization. Proc. 2003 IEEE Swarm Intell. Symp. SIS'03 (Cat. No.03EX706), IEEE; 2003, p. 138–43. doi:10.1109/SIS.2003.1202259.

[84]   Elsied M, Oukaour A, Gualous H, Lo Brutto OA. Optimal economic and environment operation of micro-grid power systems. Energy Convers Manag 2016;122:182–94. doi:10.1016/j.enconman.2016.05.074.

[85]   Tang J, Wang D, Wang X, Jia H, Wang C, Huang R, et al. Study on day-ahead optimal economic operation of active distribution networks based on Kriging model assisted particle swarm optimization with constraint handling techniques. Appl Energy 2017;204:143–62. doi:10.1016/j.apenergy.2017.06.053.

[86]   Hosseinnezhad V, Rafiee M, Ahmadian M, Siano P. Optimal day-ahead operational planning of microgrids. Energy Convers Manag 2016;126:142–57. doi:10.1016/j.enconman.2016.07.076.

[87]   Kitamura S, Mori K, Shindo S, Izui Y. Modified multiobjective particle swarm optimization method and its application to energy management system for factories. Electr Eng Japan 2006;156:33–42. doi:10.1002/eej.20269.

[88]   Bhattacharyya B, Raj S. PSO based bio inspired algorithms for reactive power planning. Int J Electr Power Energy Syst 2016;74:396–402. doi:10.1016/j.ijepes.2015.07.037.

[89]   Kerdphol T, Qudaih Y, Mitani Y. Optimum battery energy storage system using PSO considering dynamic demand response for microgrids. Int J Electr Power Energy Syst 2016. doi:10.1016/j.ijepes.2016.03.064.

[90]   Ardakani   a. J, Ardakani FF, Hosseinian SH. A novel approach for optimal chiller loading using particle swarm optimization. Energy Build 2008;40:2177–87. doi:10.1016/j.enbuild.2008.06.010.

[91]   Haddadian H, Noroozian R. Optimal operation of active distribution systems based on microgrid structure. Renew Energy 2017;104:197–210. doi:10.1016/j.renene.2016.12.018.

[92]   Foroutan VB, Moradi MH, Abedini M. Optimal operation of autonomous microgrid including

wind turbines. Renew Energy 2016. doi:10.1016/j.renene.2016.07.008.

[93] Jin X, Mu Y, Jia H, Wu J, Xu X, Yu X. Optimal day-ahead scheduling of integrated urban energy systems. Appl Energy 2016;180:1–13. doi:10.1016/j.apenergy.2016.07.071.

[94] Rouholamini M, Mohammadian M. Heuristic-based power management of a grid-connected hybrid energy system combined with hydrogen storage. Renew Energy 2016. doi:10.1016/j.renene.2016.04.085.

[95] González A, Riba J-R, Rius A. Combined heat and power design based on environmental and cost criteria. Energy 2016;116:922–32. doi:10.1016/j.energy.2016.10.025.

[96] Pu L, Qi D, Xu L, Li Y. Optimization on the performance of ground heat exchangers for GSHP using Kriging model based on MOGA. Appl Therm Eng 2017;118:480–9. doi:10.1016/j.applthermaleng.2017.02.114.

[97] Huang W, Lam H. Using genetic algorithms to optimize controller parameters for HVAC systems. Energy Build 1997;26:277–82.

[98] Zeng R, Li H, Liu L, Zhang X, Zhang G. A novel method based on multi-population genetic algorithm for CCHP–GSHP coupling system optimization. Energy Convers Manag 2015;105:1138–48. doi:10.1016/j.enconman.2015.08.057.

[99] Wieczorek M, Lewandowski M. A mathematical representation of an energy management strategy for hybrid energy storage system in electric vehicle and real time optimization using a genetic algorithm. Appl Energy 2017;192:222–33. doi:10.1016/j.apenergy.2017.02.022.

[100] Sanaye S, Fardad A, Mostakhdemi M. Thermoeconomic optimization of an ice thermal storage system for gas turbine inlet cooling. Energy 2011;36:1057–67. doi:10.1016/j.energy.2010.12.002.

[101] Bahmani-Firouzi B, Azizipanah-Abarghooee R. Optimal sizing of battery energy storage for micro-grid operation management using a new improved bat algorithm. Int J Electr Power Energy Syst 2014;56:42–54. doi:10.1016/j.ijepes.2013.10.019.

[102] Baziar A. A Novel Self Adaptive Modification Approach Based on Bat Algorithm for Optimal Management of Renewable MG. J Intell Learn Syst Appl 2013;5:11–8. doi:10.4236/jilsa.2013.51002.

[103] Singh H, Srivastava L. Modified Differential Evolution algorithm for multi-objective VAR management. Int J Electr Power Energy Syst 2014;55:731–40. doi:10.1016/j.ijepes.2013.10.015.

[104] Tamilselvi S, Baskar S. Modified parameter optimization of distribution transformer design using covariance matrix adaptation evolution strategy. Int J Electr Power Energy Syst 2014;61:208–18. doi:10.1016/j.ijepes.2014.03.039.

[105] Lee W-S, Chen Y-T, Kao Y. Optimal chiller loading by differential evolution algorithm for reducing energy consumption. Energy Build 2011;43:599–604.

doi:10.1016/j.enbuild.2010.10.028.

[106] Acharjee P. Optimal power flow with UPFC using security constrained self-adaptive differential evolutionary algorithm for restructured power system. Int J Electr Power Energy Syst 2016;76:69–81. doi:10.1016/j.ijepes.2015.09.025.

[107] Ramli M a. M, Ishaque K, Jawaid F, Al-Turki Y a., Salam Z. A modified differential evolution based maximum power point tracker for photovoltaic system under partial shading condition. Energy Build 2015;103:175–84. doi:10.1016/j.enbuild.2015.06.058.

[108] Basu M. Multi-objective optimal reactive power dispatch using multi-objective differential evolution. Int J Electr Power Energy Syst 2016;82:213–24. doi:10.1016/j.ijepes.2016.03.024.

[109] Abou El Ela A a., Abido M a., Spea SR. Optimal power flow using differential evolution algorithm. Electr Power Syst Res 2010;80:878–85. doi:10.1016/j.epsr.2009.12.018.

[110] Nguyen TT, Vo DN, Dinh BH. Cuckoo search algorithm for combined heat and power economic dispatch. Int J Electr Power Energy Syst 2016;81:204–14. doi:10.1016/j.ijepes.2016.02.026.

[111] Piechocki J, Ambroziak D, Palkowski A, Redlarski G. Use of Modified Cuckoo Search algorithm in the design process of integrated power systems for modern and energy self-sufficient farms. Appl Energy 2014;114:901–8. doi:10.1016/j.apenergy.2013.07.057.

[112] Sekhar P, Mohanty S. An enhanced cuckoo search algorithm based contingency constrained economic load dispatch for security enhancement. Int J Electr Power Energy Syst 2016;75:303–10. doi:10.1016/j.ijepes.2015.09.018.

[113] Basu M, Chowdhury a. Cuckoo search algorithm for economic dispatch. Energy 2013;60:99–108. doi:10.1016/j.energy.2013.07.011.

[114] Berrazouane S, Mohammedi K. Parameter optimization via cuckoo optimization algorithm of fuzzy controller for energy management of a hybrid power system. Energy Convers Manag 2014;78:652–60. doi:10.1016/j.enconman.2013.11.018.

[115] Camargo MP, Rueda JL, Erlich I, Añó O. Comparison of emerging metaheuristic algorithms for optimal hydrothermal system operation. Swarm Evol Comput 2014;18:83–96. doi:10.1016/j.swevo.2014.04.001.

[116] Deihimi A, Keshavarz Zahed B, Iravani R. An interactive operation management of a micro-grid with multiple distributed generations using multi-objective uniform water cycle algorithm. Energy 2016;106:482–509. doi:10.1016/j.energy.2016.03.048.

[117] Sayyaadi H, Amlashi EH, Amidpour M. Multi-objective optimization of a vertical ground source heat pump using evolutionary algorithm. Energy Convers Manag 2009;50:2035–46. doi:10.1016/j.enconman.2009.04.006.

[118] Singh M, Dhillon JS. Multiobjective thermal power dispatch using opposition-based greedy

heuristic search. Int J Electr Power Energy Syst 2016. doi:10.1016/j.ijepes.2016.03.016.

[119] Hasikos J, Sarimveis H, Zervas PL, Markatos NC. Operational optimization and real-time control of fuel-cell systems. J Power Sources 2009;193:258–68. doi:10.1016/j.jpowsour.2009.01.048.

[120] Wang X, El-Farra NH, Palazoglu A. Optimal scheduling of demand responsive industrial production with hybrid renewable energy systems. Renew Energy 2016. doi:10.1016/j.renene.2016.05.051.

[121] Bizon N. Energy optimization of fuel cell system by using global extremum seeking algorithm. Appl Energy 2017;206:458–74. doi:10.1016/j.apenergy.2017.08.097.

[122] Schirrer A, Brandstetter M, Leobner I, Hauer S, Kozek M. Nonlinear model predictive control for a heating and cooling system of a low-energy office building. Energy Build 2016;125:86–98. doi:10.1016/j.enbuild.2016.04.029.

[123] Zhu J, Vaghefi SA, Jafari MA, Lu Y, Ghofrani A. Managing demand uncertainty with cost-for-deviation retail pricing. Energy Build 2016;118:46–56. doi:10.1016/j.enbuild.2016.02.025.

[124] Razmara M, Maasoumy M, Shahbakhti M, Robinett RD. Optimal exergy control of building HVAC system. Appl Energy 2015;156:555–65. doi:10.1016/j.apenergy.2015.07.051.

[125] Kim SH. Building demand-side control using thermal energy storage under uncertainty: An adaptive Multiple Model-based Predictive Control (MMPC) approach. Build Environ 2013;67:111–28. doi:10.1016/j.buildenv.2013.05.005.

[126] Mayer B, Killian M, Kozek M. Management of hybrid energy supply systems in buildings using mixed-integer model predictive control. Energy Convers Manag 2015;98:470–83. doi:10.1016/j.enconman.2015.02.076.

[127] Yun K, Cho H, Luck R, Mago PJ. Real-time combined heat and power operational strategy using a hierarchical optimization algorithm. Proc Inst Mech Eng Part A J Power Energy 2011;225:403–12. doi:10.1177/2041296710394287.

[128] Petrollese M, Valverde L, Cocco D, Cau G, Guerra J. Real-time integration of optimal generation scheduling with MPC for the energy management of a renewable hydrogen-based microgrid. Appl Energy 2016;166:96–106. doi:10.1016/j.apenergy.2016.01.014.

[129] Rossi I, Banta L, Cuneo A, Ferrari ML, Traverso AN, Traverso A. Real-time management solutions for a smart polygeneration microgrid. Energy Convers Manag 2016;112:11–20. doi:10.1016/j.enconman.2015.12.026.

[130] Sanjari MJ, Karami H, Gooi HB. Micro-generation dispatch in a smart residential multi-carrier energy system considering demand forecast error. Energy Convers Manag 2016. doi:10.1016/j.enconman.2016.04.092.

[131] Hida Y, Shibutani S, Amano M, Maehara N. District Cooling Plant with High Efficiency Chiller

and Ice Storage System. Mitsubishi Heavy Ind Ltd Tech Rev 2008;45:37–44.

[132] Maehara N, Shimoda Y. Optimum chiller system control methods: research of optimum control system for district cooling plant using PSO optimization methods (in Japanese). Trans Soc Heating, Air-Conditioning Sanit Eng Japan 2014;209:1–11.

[133] Takenaka Corporation. Development and aapplication of new energy management system for the electric power system reform (in Japanese) 2015. http://www.takenaka.co.jp/news/2015/09/04/index.html.

[134] SmartWatt. Case studies 2017. https://www.smartwatt.com/case-studies/.

[135] REC GREEN Energy Solutions Co. Ltd. New Project – Energy Optimization Solutions for HVAC System and Energy Efficient Products 2014. http://www.rec-gt.com/en/news/detail/20/?page=10.

[136] Hammerstrom D, Johnson D, Kirkeby C, Agalgaonkar Y, Elbert S, Kuchar O. Pacific Northwest Smart Grid Demonstration Project: Technology Performance Report Highlights. 2015.

[137] DeCarolis J, Hunter K, Sreepathi S. The TEMOA Project: Tools for Energy Model Optimization and Analysis. Int Energy Work 2010 2010:1–18.

[138] Hunter K, Sreepathi S, DeCarolis JF. Modeling for insight using Tools for Energy Model Optimization and Analysis (Temoa). Energy Econ 2013;40:339–49. doi:10.1016/j.eneco.2013.07.014.

[139] DeCarolis JF, Babaee S, Li B, Kanungo S. Modelling to generate alternatives with an energy system optimization model. Environ Model Softw 2016;79:300–10. doi:10.1016/j.envsoft.2015.11.019.

[140] Gurobi Optimization Inc. Gurobi optimizer 7.5 2017. http://www.gurobi.com/.

[141] Simpkins T, Cutler D, Anderson K, Olis D, Elgqvist E, Callahan M, et al. REopt: A Platform for Energy System Integration and Optimization. Vol 2 Econ Environ Policy Asp Altern Energy; Fuels Infrastructure, Biofuels Energy Storage; High Perform Build Sol Build Incl Sol Clim Control Sustain Cities Communit 2014;2:V002T03A006. doi:10.1115/ES2014-6570.

[142] Diorio N, Cutler D, Butt B. Increasing Resiliency Through Renewable Energy Microgrids. J Energy Manag 2017;2:22–38.

[143] National Renewable Energy Laboratory (NREL). BEopt 2017. http://beopt.nrel.gov/home.

[144] The Ministry of Land Infrastructure Transport and Tourism. Life cycle energy management tool (LCEM tool) 2014.

[145] Sarbu I, Sebarchievici C. General review of ground-source heat pump systems for heating and cooling of buildings. Energy Build 2014;70:441–54. doi:10.1016/j.enbuild.2013.11.068.

[146] Simpson C. Characteristics of Rechargeable Batteries. Natl Semicond 2011:1–12.

REFERENCES

[147] Duffie J a., Beckman W a., Worek WM. Solar Engineering of Thermal Processes, 4nd ed. 2013. doi:10.1002/9781118671603.

[148] Land AH, Doig AG. An Automatic Method of Solving Discrete Programming Problems. Econometrica 1960;28:497–520.

[149] Dakin RJ. A Tree Search Algorithm for Mixed Integer Programming Problems. Comput J 1965;8:250–5.

[150] Andersen ED, Andersen KD. Presolving in linear programming. Math Program 1995;71:221–45. doi:10.1007/BF01586000.

[151] Cornuéjols G. Valid inequalities for mixed integer linear programs. Math Program 2007;112:3–44. doi:10.1007/s10107-006-0086-0.

[152] Richard E. Bellman. Dynamic Programming. Princeton University Press; 1957.

[153] Ikeda S, Ooka R. Metaheuristic optimization methods for a comprehensive operating schedule of battery, thermal energy storage, and heat source in a building energy system. Appl Energy 2015;151:192–205. doi:10.1016/j.apenergy.2015.04.029.

[154] Holland J. Adaptation in natural and artificial systems. Cambridge, USA: MIT Press; 1975.

[155] Takahashi T, Kawai K, Nakai H, Ema Y. Development of the Automatic Modeling System for Reaction Mechanisms Using REX+JGG. Phys Procedia 2013;46:239–47. doi:10.1016/j.phpro.2013.07.060.

[156] Akimoto Y, Sakuma J, Ono I, Kobayashi S. Adaptation of expansion rate for real-coded crossovers. Proc 11th Annu Conf Genet Evol Comput - GECCO '09 2009:739. doi:10.1145/1569901.1570004.

[157] Uemura K, Nakashima N, Nagata Y, Ono I. A new real-coded genetic algorithm for implicit constrained black-box function optimization. 2013 IEEE Congr Evol Comput 2013:2887–94. doi:10.1109/CEC.2013.6557920.

[158] Kennedy J, Eberhart R. Particle swarm optimization. Proc ICNN'95 - Int Conf Neural Networks 1995;4:1942–8. doi:10.1109/ICNN.1995.488968.

[159] Shi Y, Eberhart R. A modified particle swarm optimizer. IEEE Int Conf Evol Comput Proceedings IEEE World Congr Comput Intell (Cat No98TH8360) 1998:69–73. doi:10.1109/ICEC.1998.699146.

[160] Higashi N, Iba H. Particle swarm optimization with Gaussian mutation. Proc 2003 IEEE Swarm Intell Symp SIS'03 (Cat No03EX706) 2003:72–9. doi:10.1109/SIS.2003.1202250.

[161] Stacey A, Jancic M, Grundy I. Particle swarm optimization with mutation. 2003 Congr Evol Comput 2003 CEC '03 2003;2:1425–30. doi:10.1109/CEC.2003.1299838.

[162] Miranda V, Fonseca N. EPSO-evolutionary particle swarm optimization, a new algorithm with

applications in power systems. IEEE/PES Transm. Distrib. Conf. Exhib., vol. 2, IEEE; 1995, p. 745–50. doi:10.1109/TDC.2002.1177567.

[163] Yang X-S. Cuckoo Search via Lévy flights. 2009 World Congr. Nat. Biol. Inspired Comput., IEEE; 2009, p. 210–4. doi:10.1109/NABIC.2009.5393690.

[164] Civicioglu P, Besdok E. A conceptual comparison of the Cuckoo-search, particle swarm optimization, differential evolution and artificial bee colony algorithms. vol. 39. 2011. doi:10.1007/s10462-011-9276-0.

[165] Yang X-S, Gandomi AH. Bat algorithm: a novel approach for global engineering optimization. Eng Comput 2012;29:464–83. doi:10.1108/02644401211235834.

[166] Storn R, Price K. Differential evolution-a simple and efficient adaptive scheme for global optimization over continuous spaces. J Glob Optim 1997;11:341–359.

[167] Takahama T, Sakai S. Constrained optimization by the ε constrained differential evolution with an archive and gradient-based mutation. IEEE Congr. Evol. Comput., IEEE; 2010, p. 1–9. doi:10.1109/CEC.2010.5586484.

[168] Watkins CJCH. Learning from Delayed Rewards. Doctral Thesis (King's Coll 1989.

[169] Ikeda S, Ooka R. Development of a metaheuristic nonlinear multi-objective optimization method for operating energy systems including CGS and energy storage systems. J Environ Eng Archit Inst Japan 2016;81:101–10.

[170] The Society of Heating Air-Conditioning and Sanitary Engineers of Japan. CASCADE III: Computer Aided Simulation for Cogeneration Assessment & Design. Tokyo, Japan: The Society of Heating Air-Conditioning and Sanitary Engineers of Japan; 2003.

[171] Meteorological Data System Co. Ltd. Expanded AMeDAS Weather Data (in Japanese) n.d. http://www.metds.co.jp/.

[172] The Ministry of Economy Trade and Industry. Report of power plants' generation costs (in Japanese) 2015.

[173] Deb K, Pratap A, Agarwal S, Meyarivan T. A fast and elitist multiobjective genetic algorithm: NSGA-II. IEEE Trans Evol Comput 2002;6:182–97. doi:10.1109/4235.996017.

[174] Ali M, Siarry P, Pant M. An efficient Differential Evolution based algorithm for solving multi-objective optimization problems. Eur J Oper Res 2011;217:404–16. doi:10.1016/j.ejor.2011.09.025.

[175] Crow ML. Computational Methods for Electric Power Systems, Second Edition (Electric Power Engineering Series). 2 edition. CRC Press; 2009.

[176] Toshiba Corporation. Smart Grid Progress in Japan & US. US-Japan Renew. Energy Policy Bus. Roundtable, 2012.

REFERENCES

[177]   Panasonic Corporation. Energy Solutions for Homes 2015. http://panasonic.net/es/solution-works/HouseEnergy/.

[178]   Ikeda S, Ooka R. Optimal Operation of Energy Systems Including Energy Storage Equipment under Different Connections and Electricity Prices. Sustain Cities Soc 2016;21. doi:http://dx.doi.org/10.1016/j.scs.2015.10.007.

[179]   The Society of Heating Air-Conditioning and Sanitary Engineers of Japan (SHASE). NewHASP/ACLD Ver.20091117. Japanese Association of Building Mechanical and Electrical Engineers; 2009.

[180]   Ikeda S, Ooka R. A New Optimization Strategy for the Operating Schedule of Energy Systems under Uncertainty of Renewable Energy Sources and Demand Changes. Energy Build 2016;125:75–85. doi:10.1016/j.enbuild.2016.04.080.

[181]   Bojić M, Cvetković D, Bojić L. Decreasing energy use and influence to environment by radiant panel heating using different energy sources. Appl Energy 2015;138:404–13. doi:10.1016/j.apenergy.2014.10.063.

[182]   Genchi Y, Kikegawa Y, Inaba A. CO2 payback-time assessment of a regional-scale heating and cooling system using a ground source heat-pump in a high energy-consumption area in Tokyo. Appl Energy 2002;71:147–60. doi:10.1016/S0306-2619(02)00010-7.

[183]   Han C, Yu XB. Performance of a residential ground source heat pump system in sedimentary rock formation. Appl Energy 2016;164:89–98. doi:10.1016/j.apenergy.2015.12.003.

[184]   Ozyurt O, Ekinci DA. Experimental study of vertical ground-source heat pump performance evaluation for cold climate in Turkey. Appl Energy 2011;88:1257–65. doi:10.1016/j.apenergy.2010.10.046.

[185]   Yan L, Hu P, Li C, Yao Y, Xing L, Lei F, et al. The performance prediction of ground source heat pump system based on monitoring data and data mining technology. Energy Build 2016;127:1085–95. doi:10.1016/j.enbuild.2016.06.055.

[186]   Capozza A, Zarrella A, De Carli M. Long-term analysis of two GSHP systems using validated numerical models and proposals to optimize the operating parameters. Energy Build 2015;93:50–64. doi:10.1016/j.enbuild.2015.02.005.

[187]   Luo J, Rohn J, Xiang W, Bertermann D, Blum P. A review of ground investigations for ground source heat pump (GSHP) systems. Energy Build 2016;117:160–75. doi:10.1016/j.enbuild.2016.02.038.

[188]   Gultekin A, Aydin M, Sisman A. Thermal performance analysis of multiple borehole heat exchangers. Energy Convers Manag 2016;122:544–51. doi:10.1016/j.enconman.2016.05.086.

[189]   Pardo N, Montero Á, Martos J, Urchueguía JF. Optimization of hybrid - ground coupled and air

source - heat pump systems in combination with thermal storage. Appl Therm Eng 2010;30:1073–7. doi:10.1016/j.applthermaleng.2010.01.015.

[190]   Ikeda S, Choi W, Ooka R. Optimization method for multiple heat source operation including ground source heat pump considering dynamic variation in ground temperature. Appl Energy 2017;193:466–78. doi:10.1016/j.apenergy.2017.02.047.

[191]   Bureau of Waterworks Tokyo Metropolitan Government. Public water temperature (in Japanese) 2016. http://www.waterworks.metro.tokyo.jp/suigen/topic/03.html.

[192]   Himeji city. Pipes pressure loss (in Japanese) n.d. http://www.city.himeji.lg.jp/var/rev0/0032/3805/3-3-3.pdf.

[193]   EBARA Corporation. Pump catalogue (in Japanese) n.d. https://www.ebook.ebara.com/handbook/pump/50Hz/html/index.html#page=33.

[194]   Carslaw HS, Jaeger JC. Conduction of Heat in Solids. 2nd ed. UK: Oxford University Press; 1959.

[195]   Ingersoll LR, Zobel OJ, Ingersoll AC. Heat conduction with engineering, geological, and other applications. Madison: University of Wisconsin Press; 1954.

[196]   The Society of Heating Air-Conditioning and Sanitary Engineers of Japan. Computer Aided Simulation for Cogeneration Assessment & Design III (in Japanese). Maruz Publ 2003.

[197]   Pickering B, Ikeda S, Choudhary R, Ooka R. Comparison of Metaheuristic and Linear Programming Models for the Purpose of Optimising Building Energy Supply Operation Schedule. CLIMA2016 Proc 12th REHVA World Congr Vol 6 Aalborg Aalborg Univ Dep Civ Eng 2016.

[198]   Engineering page. Typical overall heat transfer coefficients (U-values) n.d. http://www.engineeringpage.com/technology/thermal/transfer.html.

[199]   International Energy Agency (IEA). Cogeneration and District Energy. IEA Rep 2009:60. doi:10.1787/9789264077171-en.

[200]   Abedini M, Moradi MH, Hosseinian SM. Optimal management of microgrids including renewable energy scources using GPSO-GM algorithm. Renew Energy 2016;90:430–9. doi:10.1016/j.renene.2016.01.014.

[201]   Jirdehi MA, Tabar VS, Hemmati R, Siano P. Multi objective stochastic microgrid scheduling incorporating dynamic voltage restorer. Int J Electr Power Energy Syst 2017;93:316–27. doi:10.1016/j.ijepes.2017.06.010.

[202]   ICAX (International Heat Transfer). Heat Sharing Networks n.d.

[203]   Ikeda S, Ooka R. Hybrid method of metaheuristics with machine learning for optimal operation of district energy systems Part 1 - Day-ahead optimization for district heating and cooling system

including thermal energy storage. Trans Soc Heating, Air-Conditioning Sanit Eng Japan 2017;241:11–20.

[204] Shimoda Y, Mizuno M, Kametani S, Kawamura S. Evaluation of Distribution System Performance in District Heating and Cooling System. Build Simulation'99, Kyoto 1999.

[205] Rohsenow WM, Hartnett JP, Cho YI. Handbook of Heat Transfer. 3rd ed. McGraw-Hill Education; 1998.

[206] Watkins CJCH, Dayan P. Q-learning. Mach Learn 1992;8:279–92. doi:10.1007/BF00992698.

[207] Kofinas P, Doltsinis S, Dounis AI, Vouros GA. A reinforcement learning approach for MPPT control method of photovoltaic sources. Renew Energy 2017;108:461–73. doi:10.1016/j.renene.2017.03.008.

[208] Li F-D, Wu M, He Y, Chen X. Optimal control in microgrid using multi-agent reinforcement learning. ISA Trans 2012;51:743–51. doi:10.1016/j.isatra.2012.06.010.

[209] Kuznetsova E, Li YF, Ruiz C, Zio E, Ault G, Bell K. Reinforcement learning for microgrid energy management. Energy 2013;59:133–46. doi:10.1016/j.energy.2013.05.060.

[210] Raju L, Sankar S, Milton RS. Distributed optimization of solar micro-grid using multi agent reinforcement learning. Procedia Comput Sci 2015;46:231–9. doi:10.1016/j.procs.2015.02.016.

[211] Lee D, Ooka R, Ikeda S, Choi W. Development of optimization method for district heat-sharing network with thermal energy storage (Part 1) ANN model of stratified thermal storage based on physical model and measured data (in Japanese). Proc AIJ Annu Conf 2017 2017;41558:1173–4.

[212] Hitachi Plant Services Co. Ltd. OH Saver 2017. http://www.hitachi-hps.co.jp/business/office_commercial/ohsaver/index.html.

[213] IBM. IBM TRIRIGA Energy Optimization 2017. http://www-03.ibm.com/software/products/en/tririga-energy-optimization.

[214] Honeywell. UniSim Optimization Suite 2017. https://www.honeywellprocess.com/en-US/explore/products/advanced-applications/unisim/Pages/unisim-optimization-suite.aspx.

[215] NTT FACILITIES. SmartStream (in Japanese) 2017. http://www.ntt-f.co.jp/service/building/ss/.

[216] Azbil Corporation. Optimization controller for heat source machines (in Japanese) 2017. http://www.azbil.com/jp/product/building/system/controller/paraconductor/index.html.

[217] Mitsubishi Heavy Industries Thermal Systems Ltd. Ene-Conductor (in Japanese) 2017. https://www.mhi-mth.co.jp/products/detail/turbo_freezer_after_solution_enecon.html.

[218] SIEMENS. Energy Management and Energy Optimization in the Process Industry. 2011.

[219] Scheneider Electric. EcoStruxure Building Advisor 2017. https://www.schneider-electric.com/b2b/en/services/field-services/building-management-system/optimize/.

[220] Johnson Controls. Central Chiller Plant Optimization 2017.

http://www.johnsoncontrols.com/buildings/services-and-support/optimization-and-retrofit-services/central-plant-optimization.

REFERENCES

PUBLICATIONS

Peer-reviewed journals

[1]   Shintaro Ikeda, Ryozo Ooka, Hybrid Method of Metaheuristics with Machine Learning for Optimal Operation of District Energy Systems Part 1 – Day-ahead Optimization for District Heating and Cooling System Including Thermal Energy Storage, Transactions of the Society of Heating, Air-Conditioning and Sanitary Engineers of Japan, No. 214, pp.11–20, 2017 (in Japanese)

[2]   Shintaro Ikeda, Wonjun Choi, Ryozo Ooka, Optimization method for multiple heat source operation including ground source heat pump considering dynamic variation in ground temperature, Applied Energy, 193, pp.466-478, 2017

[3]   Shintaro Ikeda, Ryozo Ooka, Development of a Metaheuristic Nonlinear Multi-objective Optimization Method for Operating Energy Systems Including CGS and Energy Storage Systems, Journal of Environmental Engineering, Vol. 81, No. 719, pp.101–110, 2016 (in Japanese)

[4]   Shintaro Ikeda, Ryozo Ooka, A new optimization strategy for the operating schedule of energy systems under uncertainty of renewable energy sources and demand changes, Energy and Buildings, 125, pp.75–85, 2016

[5]   Shintaro Ikeda, Ryozo Ooka, Optimal operation of energy systems including energy storage equipment under different connections and electricity prices, Sustainable Cities and Society, 21, pp.1–11, 2016

[6]   Ryozo Ooka, Shintaro Ikeda, A review on optimization techniques for active thermal energy storage control, Energy and Buildings, 106, pp.225–233, 2015

[7]   Shintaro Ikeda, Ryozo Ooka, Metaheuristic optimization methods for a comprehensive operating schedule of battery, thermal energy storage, and heat source in a building energy system, Applied Energy, 151, pp.192-205, 2015

[8]   Shintaro Ikeda, Ryozo Ooka, Development of Metaheuristic Optimization Methods for Operating Energy Systems Including Residual Battery and Thermal Storage Tank, Journal of Environmental Engineering, Vol. 79, No. 705, pp.957–966, 2014 (in Japanese)

Conference proceedings (International)

[1] Shintaro Ikeda, Ryozo Ooka, A New Index for Decision-making : an Optimal Operation Strategy of Batteries and Photovoltaic Systems in Buildings, IAQVEC 2016, Songdo (South Korea), 2016.10

[2] Bryn Pickering, Shintaro Ikeda, Ruchi Choudhary, Ryozo Ooka, Comparison of Metaheuristic and Linear Programming Models for the Purpose of Optimising Building Energy Supply Operation Schedule, CLIMA 2016, Aalborg (Denmark), 2016.5

[3] Shintaro Ikeda, Ryozo Ooka, Optimal Adjustment Strategy for Operating Schedule of Energy System under Uncertainty of Renewable Sources and Demand Changes, CLIMA 2016, Aalborg (Denmark), 2016.5

[4] Shintaro Ikeda, Ryozo Ooka, Optimal operation of energy systems including thermal energy storage and battery under different connections, 6th IBPC, Turin (Italy), 2015.6

[5] Shintaro Ikeda, Ryozo Ooka, Optimal Operating Schedule of Shared Battery and TES in Two Different Types of Buildings under Unpredicted Demand Change, Greenstock, Beijing (China), 2015.5

[6] Shintaro Ikeda, Ryozo Ooka, Development of Optimization Method for Operating Heat Source Systems Including Thermal Energy Storage and a Storage Battery Using Cuckoo Search, Grand Renewable Energy 2014, Tokyo (Japan), 2014.8

Conference proceedings (Japan)

[1] Shintaro Ikeda, Ryozo Ooka, Lee Doyun, Wonjun Choi, Development of Model Predictive Control Method using ANN and Metaheuristics Part 2 Validation of the Benefits of ANN in Day-ahead Optimization for Energy Systems, Technical papers of annual meeting, the Society of Heating, Air-Conditioning and Sanitary Engineers of Japan, Kochi University of Technology, E-40, pp.161–164, 2017 (in Japanese)

[2] Lee Doyun, Ryozo Ooka, Shintaro Ikeda, Wonjun Choi, Development of Model Predictive Control Method using ANN and Metaheuristics Part 1 Accurate Prediction of Heat Source Water Temperature of GSHP using ANN, Technical papers of annual meeting, the Society of Heating, Air-Conditioning and Sanitary Engineers of Japan, Kochi University of Technology, E-39, pp.157–160, 2017 (in Japanese)

[3] Tetsuya Kawamura, Ryozo Ooka, Shintaro Ikeda, Development of Design Optimization Method for A Detached House Considering Thermal Performance Using Metaheuristics,

Technical papers of annual meeting, the Society of Heating, Air-Conditioning and Sanitary Engineers of Japan, Kochi University of Technology, E-41, pp.165–168, 2017 (in Japanese)

[4] Mingzhe Liu, Ryozo Ooka, Shintaro Ikeda, Wonjun Choi, Development of distributed water source heat pump system for renewable energy (Part6) Analysis of pressure loss in piping system based on CFD, Technical papers of annual meeting, the Society of Heating, Air-Conditioning and Sanitary Engineers of Japan, Kochi University of Technology, C-3, pp.9–12, 2017 (in Japanese)

[5] Tetsuya Kawamura, Ryozo Ooka, Shintaro Ikeda, Research on shape optimization of houses considering thermal performance using metaheuristic, Proceedings of AIJ annual conference at Hiroshima Institute of Technology, 41028, pp.85–86, 2017 (in Japanese)

[6] Mingzhe Liu, Ryozo Ooka, Wonjun Choi, Shintaro Ikeda, Study on energy saving potential of decentralized pump system for water transport in HVAC system, Part 3: Analysis of pressure loss in piping system based on CFD, Proceedings of AIJ annual conference at Hiroshima Institute of Technology, 41563, pp.1183–1184, 2017 (in Japanese)

[7] Shintaro Ikeda, Ryozo Ooka, Wonjun Choi, Development of optimization method for district heat-sharing network with thermal energy storage (Part 2) Hybrid method of metaheuristics and ANN for day-ahead optimization, Proceedings of AIJ annual conference at Hiroshima Institute of Technology, 41559, pp.1175–1176, 2017 (in Japanese)

[8] Doyun Lee, Ryozo Ooka, Shintaro Ikeda, Wonjun Choi, Development of optimization method for district heat-sharing network with thermal energy storage (Part 1) ANN model of stratified thermal storage based on physical model and measured data, Proceedings of AIJ annual conference at Hiroshima Institute of Technology, 41558, pp.1173–1174, 2017 (in Japanese)

[9] Shintaro Ikeda, Ryozo Ooka, Wonjun Choi, Self-learning algorithm for optimal operation of heat source system with multiple renewable sources, Proceedings of Japanese Joint Conference on Air-conditioning and Refrigeration (Tokyo), Tokyo University of Marine Science and Technology, 28, pp.123–126, 2017 (in Japanese)

[10] Shintaro Ikeda, Ryozo Ooka, Optimal Operation of Heat Source and Thermal Energy Storage in Two Systems: District Heating and Cooling and Heat-sharing Network,

Technical papers of annual meeting, the Society of Heating, Air-Conditioning and Sanitary Engineers of Japan, Kagoshima University, IS-6, pp.1–4, 2016

[11]   Mingzhe Liu, Ryozo Ooka, Shintaro Ikeda, Wonjun Choi, Masao Masuda, Development of distributed water source heat pump system for renewable energy (Part3) Energy saving potential of decentralized pump system for water transport in HVAC system, Technical papers of annual meeting, the Society of Heating, Air-Conditioning and Sanitary Engineers of Japan, Kagoshima University, B-55, pp.221–224, 2016 (in Japanese)

[12]   Ryozo Ooka, Mingzhe Liu, Wonjun Choi, Shintaro Ikeda, Study on energy saving potential of decentralized pump system for water transport in HVAC system, Part 1: Outline of experimental system, Proceedings of AIJ annual conference at Fukuoka University, 41617, pp.1301–1302, 2016 (in Japanese)

[13]   Shintaro Ikeda, Ryozo Ooka, Optimisation for Annual Operation Schedule of Energy System Including Storage Equipment and CHP, Proceedings of AIJ annual conference at Fukuoka University, 41682, pp.1431–1432, 2016 (in Japanese)

[14]   Mingzhe Liu, Ryozo Ooka, Wonjun Choi, Shintaro Ikeda, Study on energy saving potential of decentralized pump system for water transport in HVAC system, Part 2: Comparison of decentralized pump system and valve control central pump system, Proceedings of AIJ annual conference at Fukuoka University, 41618, pp.1303–1304, 2016 (in Japanese)

[15]   Shintaro Ikeda, Ryozo Ooka, Optimization methods: algorithms of metaheuristics Part 1—Basic theory and their categories, Proceeding of Architectural Research Meetings, Kanto Chapter, Architectural Institute of Japan, 4003, pp.9–12, 2015 (in Japanese)

[16]   Shintaro Ikeda, Ryozo Ooka, Optimization methods: algorithms of metaheuristics Part 2—Evolutionary algorithm, Proceeding of Architectural Research Meetings, Kanto Chapter, Architectural Institute of Japan, 4004, pp.9–12, 2015 (in Japanese)

[17]   Shintaro Ikeda, Ryozo Ooka, Optimization methods: algorithms of metaheuristics Part 3—Swarm intelligence, Proceeding of Architectural Research Meetings, Kanto Chapter, Architectural Institute of Japan, 4005, pp.9–12, 2015 (in Japanese)

[18]   Shintaro Ikeda, Ryozo Ooka, Development of Operating Optimization Method for Nonlinear Energy System Including CGS and Energy Storage under Dynamic Pricing, Technical papers of annual meeting, the Society of Heating, Air-Conditioning and Sanitary Engineers of Japan, Osaka University, D-48, pp.77–80, 2015 (in Japanese)

[19] Shintaro Ikeda, Ryozo Ooka, Multi-objective optimization for nonlinear energy system including storage equipment and several heat sources, Proceedings of AIJ annual conference at Tokai University, 41672, pp.1401–1402, 2015 (in Japanese)

[20] Shintaro Ikeda, Ryozo Ooka, Metaheuristic optimization methods for operating energy system including residual battery and thermal storage tank and comparison among results of these methods, Technical papers of annual meeting, the Society of Heating, Air-Conditioning and Sanitary Engineers of Japan, Akita University, F-58, pp.113–116, 2014 (in Japanese)

[21] Shintaro Ikeda, Ryozo Ooka, Development of Optimization Method for Operating Energy Systems Including a Residual Battery and a Thermal Storage Tank Using Cuckoo Search, Proceedings of AIJ annual conference at Kobe University, 41695, pp.1441–1442, 2014 (in Japanese)

ACKNOWLEDGEMENTS

Five years have passed since I first came to the laboratory and this period has left me with wonderful memories. I would like to express my gratitude to all the people who have supported me in producing this thesis.

First and the foremost, I really appreciate the support of my supervisor, Prof. Ryozo Ooka. I am sure that your continual good advice has greatly benefited me and my research. In addition, your support with applications and in participating in architectural society committees have helped me to grow. These experiences are indispensable for me as I develop as an academic researcher. I will continue to do my best to improve my skills and knowledge so that I can work with you again in the future.

I also thank Prof. Shinsuke Kato, who served as co-advisor for my postgraduate and doctoral courses. While at the laboratory, I have been impressed with your deep knowledge and insight, not only in architectural engineering but also in many other subjects, including electrical and mechanical science. This inspires me to develop a broad knowledge.

I extend my appreciation to my advising committee members, Prof. Kazuyuki Aihara, Prof. Yasunori Akashi, and Lecturer Hideki Kikumoto for giving their time and providing excellent comments and suggestions.

Prof. Kazuyuki Aihara, you are a leading scientist all over the world in the fields of mathematics, life-sciences, and informatics, and it is my honor that you read my thesis and delivered invaluable comments.

Prof. Yasunori Akashi, I thank you for providing me with priceless advice on how I could find practical applications. Your comments made my research more realistic and was a key factor behind my decision to apply the proposed methods to actual situations in both my master's and doctoral courses.

Lecturer Hideki Kikumoto, I greatly respect you because of your enthusiastic attitude towards both your research and the care you take towards the laboratory students. I will never forget the precious time during the laboratory seminar camp when we talked about many things, including your research and daily life.

ACKNOWLEDGEMENTS

Finally, I express my honest appreciation to my family, who always supported me and allowed me to do what I wanted to do. Thanks to your support, I could completely focus on my work and you have been a great source of encouragement. I will return the favor to my mother and my wife.

Thank you for all your encouragement.

February 2018